COMPARATIVE STUDIES OF COPPER BROMIDE LASERS

Laura Little

A Thesis Submitted for the Degree of PhD
at the
University of St Andrews

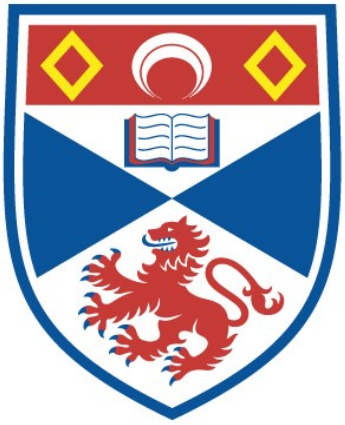

1998

Full metadata for this item is available in
St Andrews Research Repository
at:
http://research-repository.st-andrews.ac.uk/

Please use this identifier to cite or link to this item:
http://hdl.handle.net/10023/13895

This item is protected by original copyright

Comparative Studies of Copper Bromide Lasers

Laura Little

A thesis submitted in application for the degree of

Doctor of Philosophy

in the

School of Physics and Astronomy

University of St. Andrews

January 1998

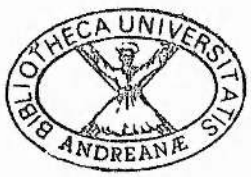

ProQuest Number: 10166921

All rights reserved

INFORMATION TO ALL USERS
The quality of this reproduction is dependent upon the quality of the copy submitted.

In the unlikely event that the author did not send a complete manuscript
and there are missing pages, these will be noted. Also, if material had to be removed,
a note will indicate the deletion.

ProQuest 10166921

Published by ProQuest LLC (2017). Copyright of the Dissertation is held by the Author.

All rights reserved.
This work is protected against unauthorized copying under Title 17, United States Code
Microform Edition © ProQuest LLC.

ProQuest LLC.
789 East Eisenhower Parkway
P.O. Box 1346
Ann Arbor, MI 48106 – 1346

TL
D59

Abstract

Comparative Studies of Copper Bromide Lasers

L. Little

School of Physics and Astronomy, University of St. Andrews

Submitted for the degree of Doctor of Philosophy

January 1998

This thesis reports the first comprehensive comparison of the operating regimes of the three major types of Cu halide laser, which oscillate on the 510.6 nm and 578.2 nm resonance-metastable transitions of atomic Cu in pulsed discharges at 10-50 kHz pulse recurrence frequency. The three lasers had similar active volumes (36.8-43.5 cm^3) and bores (12.5-13 mm), were excited using the same power supply and circuit and monitored using the same diagnostic apparatus. The CuBr-Ne laser produced an annular output beam, weighted towards the yellow transition, with a maximum average output power of 3.55 W and a maximum efficiency of 0.71 %. When H_2 gas was added to this laser at a level of ~5%, the output beam developed an axial (central) peak in intensity, the beam was less constricted, the balance of green and yellow powers was improved, the output power rose to a maximum of 11.4 W and the maximum efficiency reached 1.47 %. In both of these lasers, the CuBr vapour was generated by heating a sidearm of the discharge tube. The vapour was entrained in a flow of Ne buffer gas to seed the active volume. A Cu hybrid laser, where CuBr is generated in the tube in situ by reaction of the discharge products of a Ne-HBr buffer gas with Cu pieces in the tube, has been compared to the two conventional CuBr lasers. The Cu hybrid laser also produced an output beam with a central maximum, little or no constriction and a good balance of green and yellow powers. Maximum average output power reached 12.8 W and the maximum efficiency was 1.66%. In terms of specific average output power, the hybrid laser was clearly superior to the other two, with values of 82 $mW.cm^{-3}$ (CuBr), 262 $mW.cm^{-3}$ (CuBr-H_2) and 348 $mW.cm^{-3}$ (Cu hybrid). The specific output power of the Cu hybrid laser obtained

in these studies is a record value for any Cu laser (including elemental Cu lasers) of tube bore ≥12.5 mm. This result and the general dependences of output power on buffer gas pressure, additive (H_2, HBr) pressure, pulse recurrence frequency and charging voltage and capacitances are discussed in detail in terms of the fundamental processes and chemical reactions. The most important processes responsible for the high powers and efficiencies and the Gaussian-like beam profiles in the presence of hydrogen are dissociative attachment of HBr in the interpulse period and at the beginning of the pulse, and the reduction of Cu_xBr_x polymers and monomers by H_2 to free Cu atoms in the active volume. This is the first time that the importance of hydrogen reduction in these lasers has been identified. Without it, the filling in of the annular output beam cannot be explained.

The mechanism of Cu seeding of the hybrid laser has also been studied in detail, as it is the most obvious difference between the Cu hybrid and conventional CuBr lasers. The basic reactions of the seeding process are described, and it is found that in addition to Cu_3Br_3 and Cu_4Br_4 polymers there must be a substantial amount of CuH in the discharge to account for the large density of Cu atoms in free form and locked up in molecular forms. This is the first time that CuH has been suggested as a major Cu-bearing species. The process of Cu dendrite formation in the tube is also discussed.

Finally, the properties of the hybrid laser have been considered from the point of view of scaling to very high average output powers. It has been shown that average output powers of 1 kW are possible using current technology.

Declarations

I, Laura Little, hereby certify that this thesis, which is approximately 58,000 words in length, has been written by me, that it is the record of work carried out by me and that it has not been submitted in any previous application for a higher degree.

Date 30/1/98 Signature of candidate

I was admitted as a research student in November 1993 and as a candidate for the degree of Ph.D. in November 1993; the higher study for which this is a record was carried out in the University of St. Andrews between 1995 and 1998.

Date 30/1/98 Signature of candidate

I hereby certify that the candidate has fulfilled the conditions of the Resolution and Regulations appropriate for the degree of Ph.D. in the University of St. Andrews and that the candidate is qualified to submit this thesis in application for that degree.

Date 30/1/98 Signature of supervisor

Copyright

In submitting this thesis to the University of St. Andrews I understand that I am giving permission for it to be made available for use in accordance with the regulations of the University Library for the time being in force, subject to any copyright vested in the work not being affected thereby. I also understand that the title and abstract will be published, and that a copy of the work may be made and supplied to any bona fide library or research worker.

Date 30/1/98 signature of candidate

Acknowledgements

It is a great pleasure to thank my husband and supervisor Dr Christopher E Little, first, for agreeing to Head of School's request to take over the supervision of my work on the death of an earlier supervisor and second, for supporting me through a change in topic (from high power microwaves to high power lasers) rendered necessary through a lack of appropriate equipment. For these things, and for his never failing love and support as a husband, I am eternally grateful.

I would also like to thank my mother and father, Janet and Edward Brown, for being a constant source of love and inspiration for me throughout my life. Their support for my every endeavour through the years has been invaluable and it is thanks to them that I have reached this stage in my education today.

I thank also my sister Karen whom I have followed through the educational system for most of my life. As a sister she is the best I could ever have wished for.

Last, but never least, I thank my late cat Towsie (1981-1996) who was my constant companion through fifteen years of study and thought my Ph.D. notes made a good place to sleep, especially when I was reading them!

Dedicated to my loving husband Chris

Contents

Symbols and Acronyms

a	Radius of inner conductor
A_R	Exposed Cu surface area
b	Radius of coaxial current return
BSE	Based on stored energy
CBL	Copper bromide laser
CHL	Copper halide laser
C_{large}	Large capacitors (storage 0.97 nF/peaking 0.45 nF)
C_{medium}	Medium capacitors (storage 0.66 nF/peaking 0.33 nF)
C_p	Peaking capacitance
C_s	Storage capacitance
C_{small}	Small capacitors (storage 0.52 nF/peaking 0.24 nF)
CVL	Copper vapour laser (elemental)
D	Discharge tube bore
d_a	Mean distance from anode
DP	Double pulse
EEDF	Electron energy distribution function
E_{max}	Maximum applied electric field
FWHM	Full-width half-maximum
g_l	Statistical weight of lower laser level
g_u	Statistical weight of upper laser level
HT	High temperature
HV	High voltage
I	Laser beam intensity
I_0	Intensity of laser beam on entering a section of gain medium
IC	Interacting circuit
ICO	Injection-controlled oscillator
ID	Inner diameter

$I_g(t)$	Green intensity waveform
i_{in}	Input current
$I_l(t)$	Total intensity waveform
IP	Interacting peaking
$i_t(t)$	Discharge current waveform
$i_{t\,pk}$	Peak discharge current
$I_y(t)$	Yellow intensity waveform
k	Boltzmann's constant
L	Length of active volume
L_h	Discharge tube inductance
L_s	Saturation length
LT	Low temperature
M_{Br}	Mass of Br atom
MOPA	Master-oscillator power-amplifier
MVL	Metal vapour laser.
μ_0	Permeability of free space
n_{Br}	Number density of liberated Br atoms
n_{Cu}	Number density of liberated Cu atoms
n_{CuBr}	Number density of CuBr molecules
$n_{Cu_3Br_3}$	Number density of Cu_3Br_3 molecules
n_{CuH}	Number density of CuH molecules
n_e	Number density of free electrons
n_{H_2}	Number density of H_2 molecules
n_{HBr}	Number density of HBr molecules
n_l	Number density of Cu atoms in the lower laser level
n_{Ne}	Number density of Ne atoms
n_u	Number density of Cu atoms in the upper laser level
Δn_{ul}	Population difference
OD	Outer diameter

P	Average output power
p_{Br}	Atomic bromine pressure
p_{CuBr}	CuBr pressure
$p_{Cu_3Br_3}$	Cu_3Br_3 pressure
p_{H_2}	H_2 pressure
p_{HBr}	HBr pressure
P_{in}	Input power
P_{max}	Maximum average output power
p_{Ne}	Ne pressure
PRF	Pulse recurrence frequency
P_s	Specific average output power
$P_{s\,max}$	Maximum specific average output power
p_{total}	Total gas pressure
R_{HBr}	HBr flow rate
R_{Ne}	Ne flow rate
σ_{ul}	Stimulated emission cross-section
t	Time
t_{da}	Delay between onset of the discharge current pulse and onset of the current avalanche proper
t_{dg}	Delay between onset of the discharge current pulse and lasing in the green
t_{dl}	Delay between onset of the discharge current pulse and onset of lasing
t_{dy}	Delay between onset of the discharge current pulse and lasing in the yellow
T_e	Electron temperature
t_g	Duration of green intensity pulse
T_g	Gas temperature
t_l	Duration of total intensity pulse
t_{ra}	Total risetime of current avalanche
t_{rg}	Total risetime of green intensity pulse

t_{ri}	Total risetime of discharge current pulse
t_{rl}	Total risetime of total intensity pulse
t_{ry}	Total risetime of yellow intensity pulse
T_s	Sidearm wall temperature
T_w	Discharge tube wall temperature
t_y	Duration of yellow intensity pulse
$\bar{v}_{Br}$	Average velocity of a Br atom
V_{ch}	Charging voltage
$V_{ch}(t)$	Charging voltage waveform
V_{in}	Input voltage
$V_t(t)$	Laser tube voltage waveform
$V_{t\,pk}$	Peak laser tube voltage
w	Weight of Cu metal
w_a	Weight of Cu metal after lasing
w_b	Weight of Cu metal before lasing
Δw	Change in weight of Cu metal during lasing
η	Efficiency (BSE)
η_{max}	Maximum efficiency (BSE)
z	Longitudinal distance travelled by beam within gain medium

Chapter 1

Introduction

1.1 Introduction

Of all atomic metal lasers oscillating on resonance-metastable transitions, those employing copper (Cu) metal have consistently demonstrated the best output characteristics. Atomic copper lasers oscillate in the green (510.6 nm) and yellow (578.2 nm) and have a large range of diverse applications from materials processing to port wine stain removal. The first atomic copper lasers, known as elemental copper vapour lasers (CVLs), have been outperformed in many respects by copper halide lasers (CHLs) of which the most powerful and efficient are the copper bromide (CuBr) lasers (CBLs). CBLs include conventional CuBr lasers (with or without hydrogen (H_2) additive) and copper hybrid lasers. The Cu hybrid laser is the most efficient of them all, having demonstrated 200 W average output power with 1.9 % efficiency and 120 W with 3.2 % efficiency.

The main work presented in this thesis is a comprehensive experimental comparison of conventional CuBr and Cu hybrid laser technologies in the same experimental rig. This is the first time that such a comparison has been attempted. Conclusions are drawn regarding the mechanisms responsible for the observed behaviours of the lasers. Results are also presented of the first quantitative experimental study of the metal seeding mechanism in a Cu hybrid laser. As Cu hybrid lasers are the highest efficiency high average power visible lasers (510.6 and 578.2 nm), the prospects for raising the average output power into the kilowatt regime by scaling these devices in active volume are also discussed here for the first time.

The current chapter begins with some background information relating to CVLs

and CBLs, followed by brief histories of their developments. The fundamental conditions for lasing to occur in an atomic Cu laser (or in any suitable gain medium) are subsequently introduced. The specific case of transient population inversion in atomic Cu lasers is then considered. There follows a discussion of a number of kinetic processes which occur (and sometimes compete) in the discharges of atomic Cu lasers. In controlling to what extent and for how long the fundamental conditions for lasing are met, these mechanisms are directly responsible for the observed emission characteristics of the lasers. Their role in determining the operating features of a CVL with Ne buffer gas is considered. Finally, the differentiating features of the three main types of CBLs (conventional CBLs, CBLs with H_2 additive and Cu hybrid lasers) are discussed in terms of how the atomic and/or molecular species added to these lasers affect the discharge kinetics.

1.2 Background - Atomic Copper Lasers

Atomic Cu lasers operate with a high-gain plasma medium established by applying successive high voltage (HV) electric pulses across a fused silica chamber enclosing a buffer gas-atomic Cu vapour mixture. The buffer gas is usually He or Ne. Alongside atoms and ions of the Cu and buffer gas, other atomic and molecular species may be present in the plasma medium depending on the method used to generate the atomic Cu and/or as a means of controlling the plasma kinetics.

The necessary vapour pressures of atomic Cu are ordinarily obtained in one of two ways: vaporisation of source Cu metal in the discharge chamber at relatively high temperatures (1500-1600 °C) or electron impact dissociation within the discharge volume of a molecular Cu donor species at greatly reduced temperatures (400-600 °C). CVLs exploit the first technique. Of those lasers based on the second technique, CHLs are the more commonplace employing copper bromides, chlorides and iodides as Cu donors. A minimum of two HV pulses is required for lasing, the first to dissociate the Cu donor molecules and the second to excite the liberated Cu atoms so formed. Of the CHLs investigated, CBLs have generated the highest powers and efficiencies to date.

Conventional CBLs contain solid CuBr salt, usually within a sidearm of the discharge tube. This is heated to form a CuBr vapour, whose principal constituents are Cu_3Br_3 polymers, which mixes freely with the rare buffer gas in the main body of the discharge tube. Conventional CBLs operate with start-up times of the order of 5-10 min. This is fast compared with the 1-2 hr start-up times of CVLs but slow in comparison to Cu hybrid lasers which have been shown to lase within 1 min from a cold start.

In conventional CBLs with no H_2 additive (*i.e.* containing a rare buffer gas only), average powers and efficiencies are relatively low and akin to those of CVLs with similar active volumes. The emission has a decidedly annular distribution. Conventional CBLs with added H_2 form a second category. In these devices, the buffer gas is composed of a rare gas-H_2 mixture. The H_2 is added at the gas inlet and is present in relatively small (up to 5 %) concentrations. Amongst other things, this approach has led to a doubling of the output powers and efficiencies typically attained in conventional CBLs with no H_2 and to improvements in beam quality which include the filling in of the annularity and the development of a bell-shaped or pseudo-Gaussian beam profile.

A third class of CBL is the Cu hybrid laser. In these lasers the conventional CuBr salt is replaced by source Cu metal located in the discharge tube itself. The buffer gas comprises a rare gas to which relatively small partial pressures of hydrogen bromide (HBr) have been added. The discharge dissociation products of the HBr gas react with the Cu metal to form first CuBr then Cu_3Br_3 vapour on demand in the discharge tube. Though a relatively recent development, Cu hybrid lasers have already demonstrated record efficiencies together with output powers which surpass those generated in CBLs with H_2 additive and which approach those of the most powerful single tube CVLs. High specific output energies and repetition rates have also been realized.

Like conventional CBLs with H_2 additive, Cu hybrid lasers demonstrate superior beam quality, but the Cu hybrid laser offers further advantages. HBr is a gas at room temperature, is simple to control and donates bromine and hydrogen to the discharge in a convenient one-to-one ratio. Lasing has been achieved within 45 s from a cold start-up in Cu hybrid lasers because heating of the Cu metal to the 400-600 °C necessary for the

Cu/HBr reaction to occur is by waste heat from the discharge and takes place in under 1 min. Lasing then occurs almost immediately on addition of HBr. The time to cessation of lasing is also of the order of 1 min. As CuBr is formed via the Cu/HBr reaction, rapid, simple control of the CuBr vapour pressure is achieved by varying the HBr pressure only. As a result of the immediacy of the Cu/HBr reaction, control of the laser output is rapid with response times of typically 30-40 s (*cf.* the lengthy, somewhat inaccurate procedure of controlling the heat applied to a sidearm).

There are however two drawbacks to Cu hybrid laser technology. First, these lasers contain a toxic gas. Second, CVLs and conventional CBLs (with or without H_2 additive) have all been operated as both flowing-gas and sealed-off systems. Cu hybrid lasers, although they have achieved high output powers and record efficiencies, have thus far been operated as flowing-gas systems only. The second disadvantage is unlikely to last.

Although investigations of CBL technologies have multiplied since the first demonstration of a conventional CBL in 1975 [1], and have in many instances led to efficient high-power, high beam quality devices, CVLs remain the subject of most atomic Cu laser studies and continue to dominate the commercial markets. There are a number of reasons for this. CVLs represent a known and proven technology of over 30 yr development, have a high green:yellow ratio, may be operated easily under sealed-off conditions and employ no toxic gases. The recent addition of HBr to a sealed-off, elemental CVL [2] has helped to overcome some of the drawbacks in its beam quality, but with the disadvantage that, like the Cu hybrid laser, this particular model now contains a toxic gas.

1.3 Copper Vapour Laser Development

Self-terminating atomic metal lasers have been subject to experimental investigation since 1965 when Fowles and Silfvast first obtained lasing in atomic lead (Pb) [3]. This was an elemental metal vapour laser (MVL), in which source Pb metal was heated to form an atomic Pb vapour which seeded a buffer gas discharge with free Pb atoms for lasing on

high-gain, resonance-metastable, self-terminating transitions. The first CVL was also demonstrated in 1965-66 by Gould, Bennett and Walter of the US company TRG Inc. [4, 5]. The Cu metal was heated by an oven in which the entire discharge tube was enclosed.

As with most lasers, the first decade in CVL development saw a drive for higher average output powers coupled with size reduction so that commercial applications could be found. A major step forward in both respects was made in 1972 when Isaev at al. used a high PRF (10 kHz) discharge to self-heat a CVL [6, 7]. This self-heating enabled the external heating components to be dispensed with while lasing was attained at very much higher overall efficiencies.

In the mid 1970's, there was a moderate degree of interest in CVL application to the investigation of Raman spectra in crystals [8], to laser projection microscopes [9] and to optical pumping of dye lasers [10]. A breakthrough came in 1976 when the US isotope separation programme at the Lawrence Livermore National Laboratory (LLNL) identified the CVL as the most suitable device for pumping their dye lasers [11]. Concerns remained regarding the maximum powers attainable from CVLs but these were quelled some two years later when Smilanski et al. demonstrated the possibility of volume scaling (by bore) the devices [12]. By the early 1980's, CVLs were routinely generating output powers of the order of 100 W, *e.g.* [13], compared to typically 5 W, *e.g.* [14], some 4-5 years earlier.

Since the early 1980's, improved understanding of the kinetics of CVLs have seen powers of 550 W obtained from single oscillator tubes [15], 650 W from a single tube amplifier [16] and 1.4 kW from a master-oscillator power-amplifier (MOPA) chain comprising a 25 W MO and 3 PAs [16]. Elemental CVLs are now used routinely in applications such as high frequency pumping of dye lasers for nuclear isotope enrichment or laser guide stars, materials processing, UV ablation, port wine stain treatment and high-speed flash photography. The recent addition of HBr to a CVL [2], which enables these lasers to emulate to a large extent the output powers and beam quality of the lower temperature Cu hybrid laser (which already uses this technique), may open a new era in CVL development.

1.4 Conventional Copper Halide Laser Development

Although copper halides were used to generate light in electrodeless lamps in the early 1950's [17], the application of these salts to atomic Cu lasers did not occur until some two decades later. Then in 1973, Weaver et al. reported superradiant emission in an atomic Cu laser set-up in which the free Cu atoms were donated solely by copper iodide (CuI) molecules entrained in the buffer gas [18]. Later that year, Chen et al. reported lasing proper in a copper chloride (CuCl) system [19] and in 1974, Liberman et al. not only reported laser emission from their CuI system but also demonstrated continuous pulsing of the device at high multikilohertz PRFs [20]. Although initial reports were of a CVL variant, the CHL's peculiar properties were soon to place it in a class of its own.

The first CHLs mostly made use of CuCl or CuI as the donor salt, however one CuBr device was reported as early as 1975 [1] and has also emerged as the first self-heated CBL in which the discharge itself was used to heat pieces of solid CuBr distributed along the base of the discharge tube. As the requisite operating temperatures for CHLs are only ~ 500 °C, a relatively low discharge current density and a minimum of thermal insulation were sufficient to replace the external heating. The first transverse excitation of a CHL was also reported in that year [21].

The period 1976-77 saw a sudden proliferation in the number of investigations of atomic Cu lasers in which non-halide molecules were the donor species. The first of these made use of copper oxide [22]. Sustained operation at high PRFs was reported in a self-heated tube at temperatures of 1200-1300 °C. This temperature range represented a marginal improvement over elemental CVLs but was still no match for the 400-600 °C operating wall temperatures of CHLs. Other researchers tried copper acetylacetonate [23], copper acetate [24] and Cu_2O [25] but although a small number of investigations into these devices were carried out in subsequent years, by large, interest remained with the higher power and efficient copper halide lasers.

The year 1977 was also an important time in CHL technology. A comparison of the properties of CuCl, CuBr and CuI [26] revealed CuBr as the donor to provide the highest output powers. This discovery precipitated a shift away from the traditional CuI

and CuCl systems towards CuBr as the donor species. In another important development of that year, Vetter and Nerheim added hydrogen chloride (HCl) to the buffer gas of a double pulse (DP) CuCl laser and in so doing produced an increase in the number density of ground state Cu atoms in the discharge and a 15 % increase in laser energy [27]. This was the first example of a CHL with hydrogen additive, but the work was not pursued at the time.

As the drive for higher average powers continued in order to make the CHL a viable alternative to the CVL in laser applications, MOPA systems [28] and scaled models of existing CHLs [29] were developed. Experiments with sealed-off CuBr laser tubes showed window heating to be an important factor in increasing their service lifetimes [30].

An observation which is seldom remarked upon but has not yet been properly explained, was that made by Winiarczyk and Krause in 1982 of two temperature regimes of operation in a DP CuCl laser [31]. Further experiments were conducted in which first sodium (Na) and potassium (K) [32] and then sodium chloride (NaCl), potassium chloride (KCl) and caesium chloride (CsCl) [33] were added to the CuCl laser tube, but although interesting changes in the temperature response of both modes were observed, no real explanation for their existence was offered and no such phenomenon has been reported in any other research until the current investigation.

In the interval 1983-1984, enhancements to the average power and lifetime of conventional CHLs continued to be made but were ultimately limited by fundamental factors such as discharge constriction. Collaborative work between the groups of Sabotinov (Bulgarian Academy of Sciences) and Petrash (Lebedev Institute of Physics, U.S.S.R.) had identified the atomic and molecular species present in a sealed-off CBL discharge tube after it had lased for some time [34] and had highlighted the problem of a rising bromine concentration [35]. While purging a sealed-off CBL tube of impurities in 1985, Astadjov at al. noticed that the laser beam became increasingly annular during the clean-up and that the output power reduced [36]. The annular beam pattern was found to be a characteristic feature of 'clean' CHLs and the beneficial impurity which causes the

centre hole to fill in was identified by Astadjov et al. as hydrogen [36]. The disappearance of the on-axis minimum as hydrogen is added to a CHL was termed the "hydrogen effect" by these investigators.

There was little in the pre-1985 literature to suggest that the conventional CHL output was annular indicating that most early CHLs probably contained some measure of hydrogen contamination in one form or another. However, in their 1981 report on a MOPA CuBr system Kuroda et al. [37] made the important observation that the gain distribution and extractable energy density were concentrated in a narrow annular region near the discharge tube wall, so one can assume that these investigators at least had an exceptionally clean laser tube. H_2 addition was found to improve the output power, efficiency and beam profile of conventional CHLs so dramatically that CHLs with hydrogen additive were placed in a class of their own. The 15 % increase in laser energy observed by Vetter and Nerheim when they added HCl to their DP CuCl laser in 1977 [27] was attributed to the addition of hydrogen, albeit in molecular form.

From 1985 onwards there have been a number of advances in conventional CHL technology. One area of investigation has been the addition of new elements and salts to the active regions of CHLs in an attempt to speed up the relaxation rate of the laser gain medium and to enable operation at higher PRFs. An example of this is the addition of caesium (Cs) to a CuCl laser by Saito and Taniguchi in 1985 [38]. These investigators found that the presence of Cs enabled them to achieve more rapid system relaxation through transfer of energy from the metastable states of atomic Cu to a resonance state of Cs. A further example is the addition of silver bromide (AgBr) salt to a CuBr laser by Oouchi et al. in 1989 [39].

The electrical excitation of CHLs has also received attention. In 1988, Vuchkov et al. published details of a new excitation circuit which they termed an interacting peaking (IP) circuit and which they claimed to have improved the efficiency of one of their CuBr-H_2 devices [40]. Following on from that study those same investigators modelled a CuBr-H_2 laser which employed two IP circuits in the excitation circuitry [41]. In 1991, Vuchkov et al. devised a further circuit for a CuBr-H_2 laser comprising two interacting

circuits (IC) [42]. These developments led to the demonstration in 1997 of a 120 W CuBr-H_2 laser [43] and a version of this device with a central electrode has since been constructed [44].

1.5 Copper Hybrid Laser Development

While studies of conventional CBLs, with and without H_2 additive, have been ongoing, other investigators have preferred to concentrate on the development of a third type of CBL known as the Cu hybrid laser. As mentioned earlier, the essential difference between Cu hybrid lasers and conventional CBLs is the means of introducing Cu_3Br_3 vapour to the rare gas discharge. In conventional CBLs this merely entails the heating of solid CuBr situated at a convenient location within the laser tube. In the Cu hybrid laser, HBr gas is entrained in the flowing buffer gas and the discharge dissociation products of the HBr react with Cu metal in the discharge tube to form Cu_3Br_3 vapour as required in the active volume of the laser tube.

Although the Cu hybrid laser has only recently emerged as an independent class of CBL, the origins of the work can be traced back to the first demonstration of lasing in copper oxide by Anderson et al. in 1976 [22]. There was one crucial difference between this laser and other atomic Cu lasers of that time. Aside from the different donor species, in one approach, the discharge dissociation products of O_2/air were reacted with solid Cu metal in the discharge tube to produce a supply of copper oxide, and thus of atomic Cu for lasing, on demand. This was effectively a Cu hybrid laser in which oxygen instead of halogen or hydrogen halide gas was added.

In a further example of hybrid technology, in 1982, Vuchkov et al. achieved lasing in atomic Cu by adding a halide of another metal to a buffer gas discharge in a laser tube containing only Cu metal [45]. In 1985, Saito and Taniguchi experimented with a laser tube in which aluminium chloride (AlCl) in a reservoir reacted with Cu granules at the mouth of the reservoir to form $CuAl_mCl_n$ in the laser tube [46]. This too was effectively a Cu hybrid laser.

Then, in 1989, Livingstone and Maitland described a laser tube in which halogen

gas entrained in a rare buffer gas (Ne or He) reacted with large cylindrical segments of Cu which were interspersed with alumina rings to form the discharge tube itself [47]. The halogens tried were bromine (Br_2) and chlorine (Cl_2). In 1991, those same investigators repeated their experiments with hydrogen bromide (HBr) [48]. Though average powers of up to 22 W were observed there were stability problems caused by discharge arcing to the metallic walls.

In 1992, in a set of independent investigations at the University of St. Andrews, Jones and Little obtained lasing on the cyclic transitions of atomic lead (Pb) by passing HBr entrained in Ne buffer gas over molten Pb in a discharge tube of a different kind [49]. Their laser design was a scaled down version of a system employed by Little and Piper in their studies of strontium ion lasers at Macquarie University, Sydney, Australia in the late 1980s [50]. In 1992, this configuration was re-used to obtain stable lasing for the first time in a CBL in which HBr entrained in Ne buffer gas was flowed over Cu metal in the discharge tube [51]. Little christened these devices (in which HBr was reacted with source metal in the discharge tube) "HyBrID" lasers, the acronym HyBrID meaning *hy*drogen *br*omide *i*n *d*ischarge, but the name is now often used in connection with any atomic metal laser in which an active species is passed over source metal in the laser tube to produce volatile metal donor molecules on demand. Jones and Little went on to obtain lasing in iron (Fe) [52], manganese (Mn) [53] and bismuth (Bi) [54] hybrid lasers using the same laser tube configuration.

The Cu hybrid laser tube design employed by Little's group, has since been scaled in active bore and length [55]. In collaborative work with Sabotinov's group at the Bulgarian Academy of Sciences, the new excitation circuitry developed there for CBLs with H_2 additive was applied to the Cu hybrid laser [56]. As a consequence of this work, by 1993, a Cu hybrid laser of 60 mm bore and 2 m active length had attained output powers of up to 201 W and the highest recorded efficiencies of all atomic Cu lasers [57]. In 1994, the low remanent electron density in the Cu hybrid laser was equated with its good output characteristics [58] and the kinetics of the Cu hybrid laser were considered in detail for the first time [59]. A record specific average output power for small bore atomic

Cu lasers was reported in a Cu hybrid laser [60].

The period 1995-96 saw worldwide interest in Cu hybrid laser technology developing. After studying Little's 200 W Cu hybrid laser at St. Andrews, Pique returned to France to build his own [61]. Hybrid lasers were studied in China [62] and in Israel [63]. In the latter case excitation used magnetic pulse compression. A collaboration between the groups of Little and Webb (Oxford University) resulted in the measurement of the electron density, n_e, in the Cu hybrid laser which confirmed the theory that n_e was very small in the afterglow [64]. A hybrid MOPA system was demonstrated for the first time in a collaboration between the groups of Little and Piper (Macquarie University, Sydney, Australia) [65]. Coutance et al. found Cu_xBr_x polymers in their hybrid laser [66] and the groups of Little and Petrash (Lebedev Institute of Physics, Moscow, U.S.S.R.) achieved second harmonic generation in a BBO crystal pumped by a 20 W St Andrews Cu hybrid laser [67]. The current work continues the investigation of both conventional CuBr and Cu hybrid technologies.

1.6 Fundamental Conditions for Lasing

The energy level diagram for atomic Cu is shown in Figure 1.1. The Cu laser is a transient three-level system. The ground level is $^2S_{1/2}$ as there is a single $4s$ electron in the outer shell of a neutral Cu atom, just outside a complete $3d$ subshell. Ignoring the possibility of ionization or excitation to higher energy levels, Cu atoms may be pumped to the resonance ^2P levels, which are the lowest excited levels with an optically allowed transition to the ground level, or to the intermediate, metastable, ^2D levels which have no optical path connecting them with the ground level.

The $3d^{10}4p\ ^2P_{3/2}$ and $3d^{10}4p\ ^2P_{1/2}$ resonance levels lie at 3.81 and 3.78 eV above the ground level respectively. A neutral Cu atom may be excited to either one of these levels depending on the spin of its outer electron. Alternatively, the Cu atom may be excited to one of the $3d^94s^2\ ^2D_{3/2}$ or $3d^94s^2\ ^2D_{5/2}$ levels at 1.6 and 1.4 eV above the ground level respectively. The actual level to which an atom is excited will depend on the energy of the colliding electron together with the cross-section for excitation to each

level. As the cross-section for excitation from the ground level to a higher energy level is proportional to the probability of radiative decay in the opposite direction, strong excitation to the resonance levels is expected alongside weak pumping of the metastable levels.

Excited Cu atoms occupying a resonance level are presented with two possible decay routes: direct optical transition to the ground level or optical transition to a metastable level followed by metastable decay to the ground level. The former route has the shortest lifetimes (~ 10 ns) with wavelengths 325 nm or 328 nm from the $^2P_{3/2}$ or $^2P_{1/2}$ levels. The latter path is more complex. Although the first half of the procedure (optical transition to a metastable level) is straightforward, with lifetimes of 500 ns and 610 ns from $^2P_{3/2}$ and $^2P_{1/2}$, the subsequent decay of the metastable atom can occur in only one of two ways, both of which are much slower: collision with (and transfer of energy to) another particle or the discharge chamber wall or electron impact excitation of the metastable atom to a higher energy level followed by decay by alternative routes.

In practice, the dominant decay route, resonant transition to the ground level, is impeded by an additional process known as radiation trapping. When the number density of free Cu atoms, n_{Cu}, exceeds a critical value (~ 3 x 10^{17} m^{-3} for a CVL of 20 mm bore radius [68]), the proximity of the atoms ensures that any photon emitted during decay from a resonance level to the ground level is immediately absorbed by a neighbouring ground level atom which is photo-excited to the resonance level. Continuing and/or increasing excitation will augment the numbers of Cu atoms in the resonance levels which cannot be reduced by resonant decay to the ground level because the effective lifetime has been increased from ~ 10 ns to >> 1 μs (long *cf.* current pulse).

This inability of the Cu atoms to make a direct transition to the ground level once excited to a resonance level enables a state of *population inversion* to be created between the resonance and metastable states. We consider next the creation of this inversion as it is one of two fundamental conditions for lasing to occur. In an atomic Cu laser, residual numbers of free electrons remain in the afterglow of an excitation pulse. At the onset of the next pulse, these electrons are accelerated by the rising laser tube voltage. When the

voltage is such that electron energies transcend a threshold value, there is a finite and increasing probability of a collision with another gas species resulting in the release of an additional electron. Electron avalanche occurs and the gas breaks down. The discharge current pulse begins to rise and the tube voltage begins to fall. During this time, the peak electron temperature, T_e, is high, ensuring efficient pumping of the ^2P *upper laser* levels. Provided that T_e remains above ~ 2 eV, direct excitation from the ground level to the ^2D, metastable, *lower laser* levels is relatively unlikely so that during the first 50 ns or so of the discharge current pulse, rapid pumping of the resonance levels readily establishes an excess of Cu atoms in the upper levels relative to the corresponding lower levels and a state of population inversion exists between the resonance and metastable levels. The only effective means of decay from the resonance levels is then via the second route *i.e.* by optical transition to the $^2D_{5/2}$ or $^2D_{3/2}$ metastable levels by stimulated emission.

An atom in the $^2P_{3/2}$ energy level can make an optical transition to the $^2D_{5/2}$ level releasing a photon of green (510.6 nm) light in the process. An atom in the $^2P_{1/2}$ level can make an optical transition to the $^2D_{3/2}$ level emitting a photon of yellow (578.2 nm) light in so doing. There is also a $^2P_{3/2}$ to $^2D_{3/2}$ transition with a 570.0 nm wavelength, but it does not lase, due to the smaller gain and competition for the same upper level as the 510.6 nm transition.

The second criterion which must be fulfilled for efficient extraction of laser energy is *gain saturation.* When a laser beam of a particular wavelength passes through a section of gain medium, its evolving intensity, I, may be shown to be an exponential function of the population difference,

$$\Delta n_{ul} = \left[n_u - \frac{g_u}{g_l} n_l \right], \qquad \text{----------(1.1)}$$

between the relevant upper and lower laser levels, the distance travelled in the longitudinal direction, z, and the stimulated emission cross-section, σ_{ul}. Hence, at any distance z,

$$I = I_0 e^{\sigma_{ul}\left[n_u - (g_u/g_l)n_l\right]z}. \qquad \text{----------(1.2)}$$

In the above expressions, n_u and n_l are the number densities of Cu atoms in the upper and lower laser levels respectively, g_u and g_l are the statistical weights of the upper and lower levels respectively and I_0 is the intensity of the beam as it enters the section of gain medium. For amplification to occur, the exponent in equation (1.2) must be positive and sufficiently large.

Assuming this to be the case then at some distance z into the gain medium the beam will reach an intensity at which the energy in the upper level is no longer sufficient to enable the beam to keep growing. This is known as the saturation intensity and the length at which it occurs is the saturation length, $z = L_s$. At the saturation intensity, the rates of spontaneous and stimulated emission are equal, the inversion density is halved, the beam experiences linear growth in intensity and the maximum energy is extracted from the system.

1.7 Transient Population Inversions

Population inversion was introduced in Section 1.6 as a fundamental condition for lasing as it enables a sufficient difference in the number densities of resonance and metastable Cu atoms to be created so that not all photons released during a resonance to metastable transition are immediately re-absorbed in a transition taking place in the opposite direction. In practice n_u does not have to exceed n_l because the population difference, Δn_{ul}, is weighted according to the probability of making a downwards or upwards transition. From equation (1.1), A population inversion is possible when,

$$n_u > \frac{g_u}{g_l} n_l, \qquad \text{----------(1.3)}$$

For Cu, g_u and g_l are 4 and 6 respectively for the green transition and 2 and 4 respectively for the yellow transition meaning that lasing can occur on the green or

yellow lines when n_u exceeds 0.67 or 0.5 times n_l respectively.

The metastable nature of the lower laser levels limits the lifetime of the emission pulse. There is no allowed optical transition from a lower laser level to the ground level and the atom must remain in that state until a collision with a second particle or with the container wall enables it either to lose the energy necessary to return to the ground level or to gain sufficient energy to make an upwards transition to a higher energy level from whence it can decay to ground level more easily. In atomic Cu lasers, the metastable $^2D_{5/2}$ and $^2D_{3/2}$ levels are quickly populated by electron impact and by optical decay from higher energy levels (especially the ^2P upper laser levels). Conversely, metastable decay takes place over relatively large timescales (10's μs) compared with de-excitation of the upper $^2P_{3/2}$ and $^2P_{1/2}$ levels.

Lasing on either one of the 510.6 and 578.2 nm lines will occur only for as long as the population inversion between the appropriate upper and lower laser levels is sustained. As a result of the difference in the decay rates of the upper and lower levels, the population inversion is usually eliminated within 30-50 ns of its onset and atomic Cu lasers lasing on resonance-metastable transitions are therefore self-terminating. Continuous wave (CW) excitation is not possible as a delay is necessary between successive excitation periods to enable relaxation of the lower laser level populations.

As a consequence of the self-terminating nature of the emission from an atomic Cu laser and of an inversion which lasts for only a short period (~ 30 ns in a CVL), the small signal gain of the plasma medium must be correspondingly very high at 10's % cm^{-1} (50000 m^{-1}) for useful light to be extracted in the short time allowed. For a 1 m active length, each round-trip of the cavity takes ~ 10 ns so that the beam makes ~ 3 round trips during the inversion. A high-loss cavity is required to couple most of the power out and is usually comprised of a high reflector and glass flat (to extract the energy).

1.8 Kinetic Processes in Atomic Copper Lasers

A number of kinetic processes occur in the low density plasma gain medium of an atomic Cu laser. The precise character (distribution, strength and efficiency) of the laser

emission, and the maximum rate at which it can be pulsed, are the cumulative effect of the influences exerted by these mechanisms. The importance of each kinetic process varies according as the system is in an excitation or relaxation phase of the pulse train.

The basic kinetics of atomic Cu lasers are most readily demonstrated in a CVL with no additives in which Cu is introduced directly in atomic form and Cu and buffer gas (usually Ne) atoms and ions are the only species present. In such a CVL there is no effective electron-ion recombination in the interpulse period, so that the electron density, n_e, is usually quite high (30 % of the peak) at the beginning of the excitation pulse. This is reflected in a low discharge channel impedance, poor circuit-laser matching and 'low' efficiencies of ~ 1 %.

In the initial stages of the excitation pulse, the metastable and resonance levels compete for the greatest share of the pumping which occurs via electron impact. At peak electron temperatures, T_e, of ≤ 2 eV, pumping of the metastable energy levels is more effective. In the range 2-5 eV the resonance levels receive the greater share of the excitation. It is therefore important that the voltage risetime is short so that electron temperature reaches the 'optimum' regime of 2-5 eV as quickly as possible at the onset of the excitation pulse before the electrons have made too many impacts. It is also important that the electron density at the onset of the excitation pulse is not so high that numerous collisions are made during the short period when $T_e \leq 2$ eV. In a CVL where the pre-pulse electron density is high, early pumping of the metastable states leads to a reduction in both the peak population inversion and the timescales over which it can be sustained. For this reason (amongst others) CVLs have relatively short laser pulse durations compared to other types of Cu laser.

Usually before the current pulse has peaked both the population inversion and laser intensity pass through their maxima and begin to fall again. This saturation occurs for three reasons. First, the lack of an optical decay channel for the metastable lower laser levels causes their number to accrue with time. Second, as the laser tube voltage approaches its peak, excitation of the resonance (upper level) atoms to higher energy levels occurs (stepwise excitation) while the ground state Cu density falls due to

excitation and ionization. Third, electron temperature T_e falls as the tube voltage collapses.

The above processes account for the power and duration of the laser pulse but not for the beam profile. The threshold atomic Cu vapour pressure for radiation trapping of the resonance state is of the order of 10^{-5} torr [68]. In CVLs, whose optimum Cu vapour pressure is typically of the order of 0.1-1 torr, the threshold density is readily exceeded over the entire cross-section of the discharge tube, but the beam is at most uniform and may even display an on-axis minimum. This is a result of the atomic Cu distribution in the discharge which is a function of three separate phenomena: local variation in n_{Cu}, gas heating and radial cataphoresis.

The Cu vapour originates near the discharge tube wall. As the centre of the discharge tube is initially depleted of Cu, the newly formed Cu vapour diffuses into the central region. This diffusion is countered to some extent by gas heating which is a maximum on-axis. The thermal gradient so produced promotes diffusion of Cu and Ne atoms towards the laser tube wall so that both n_{Cu} and the number density of Ne atoms, n_{Ne}, display distinct on-axis minima (50 % typically due to gas heating alone).

When a voltage is applied across the discharge tube, gas breakdown occurs primarily along the tube axis where gas temperature is a maximum and n_{Ne}, smaller in the vicinity of the axis, presents less impedance to the discharge current. The cumulative effect of repetitive pulsing is an increasing gas temperature and an even greater tendency for the discharge current to adhere to the discharge centre and so on. In a discharge containing only atoms of Cu and Ne, the Cu atoms are by far the more readily ionized and in sufficient numbers, n_{Cu} can be strongly affected by radial cataphoresis. Cataphoresis is the selective movement of charged particles along electric field lines, and in atomic Cu lasers, n_{Cu} can become severely depleted on-axis because of this effect. As the Cu migrates away from the centre of the tube, excess Cu at the wall condenses out of the discharge. As a result, the density of atomic Cu always has an on-axis minimum due to a combination of the cumulative effect of cataphoresis and gas heating by successive pulses. The higher n_{Cu} at the wall means that this region of the discharge goes into gain

first on application of the excitation pulse, and the beam profile is annular or uniform at best. The atomic Ne density, which is depleted by gas heating only, has a less pronounced on-axis minimum (50 % compared to 70-80 %).

The generally low impedance of the CVL discharge channel also provides for a large plasma skin effect so that in a large-bore tube (> 40 mm), a large proportion of the current also travels through the discharge along a narrow path adjacent with the tube wall. This further enhances the annular beam profile.

In the interpulse period, the relaxation of the metastable Cu atoms, the recombination of free electrons and Cu ions and the replenishment of depleted ground state Cu atoms occur. The lifetimes of the metastable states are 1-10 μs by superelastic electron collisions. The metastable density equilibrates at T_e several microseconds into the afterglow, and then follows the relaxation of T_e towards the gas temperature, T_g, as the electrons cool by elastic collisions with buffer gas atoms. Three-body recombination of Cu^+ ions and free electrons,

$$e + e + Cu^+ \rightarrow e + Cu,$$

increases with time as it is proportional to $T_e^{-9/2}$. However, the ground state Cu atoms are not wholly replenished during relaxation for two main reasons. First, T_e and T_g cannot fully relax during the interpulse period. Second, depletion of Cu is assisted by cataphoresis, whereas replenishment occurs by simple diffusion of Cu atoms from the discharge tube wall to the discharge centre with no assistance from an electric field. The rates of Cu depletion and replenishment are therefore unequal and favour depletion. Depletion of Cu by gas heating and cataphoresis together with a build-up of metastable lower level populations are all cumulative effects which worsen at higher PRFs at which the relaxation periods are shorter. These processes therefore limit the attainable average laser output power.

1.9 Operating Features and Current Understanding of Copper Bromide Lasers

In Section 1.8, the fundamental kinetic processes occurring in the discharge volumes of atomic Cu lasers were introduced in the context of an elemental CVL with Ne buffer gas. In CBLs, these basic kinetic processes are affected by the atomic and/or molecular structures and properties of added species, *e.g.* CuBr, H_2 and HBr, and by alternative methods of atomic Cu generation. In this section, the operating features of CBLs are introduced along with existing theories on which processes (involving the added species) combine to produce the observed performance.

Conventional CBLs with no added hydrogen

In conventional CBLs with no H_2 additive, laser action, *i.e.* output powers and efficiencies, is similar to that of elemental CVLs but peak output power occurs at higher PRFs. The beam is at all times confined to an annular region adjacent to the tube wall and at no time displays uniform lasing. Although lasing occurs over a wide range of buffer gas pressures, the requisite Cu_3Br_3 pressure increases with increasing buffer gas pressure which is limited by discharge constriction and instability. The optimum Cu_3Br_3 pressure for lasing is ~ 0.33 torr, and occurs at a CuBr source temperature of ~ 490 °C [69].

The Cu atoms are introduced into the discharge in the form of Cu_3Br_3 vapour so that the additional species present are likely to be CuBr (monomer or polymer), Br, Br^- and Br_2. The last of these is only weakly bound (< 2 eV) and so probably not present in significant concentrations. The first process to occur on Cu_3Br_3 addition is diffusion of Cu_3Br_3 to the discharge tube centre followed by depolymerization of Cu_3Br_3 and dissociation of CuBr by electron impact processes:

$$e + Cu_xBr_x \rightarrow Cu_{x-1}Br_{x-1} + CuBr + e,$$

$$e + CuBr \rightarrow Cu + Br + e,$$

$$e + CuBr \rightarrow Cu + Br^-.$$

Along with free Cu atoms for lasing, these reactions can generate free bromine atoms. As Br is highly electronegative it can capture free electrons thereby preventing them from moving far from their place of origin (near the centre of the discharge tube). In the third reaction (dissociative attachment of CuBr) the electron impact generates Br^- directly. As the number density of Cu_3Br_3, $n_{Cu_3Br_3}$, is raised, the increased Br/Br^- levels exert an increasing influence over the electrons and impel the discharge to adhere ever more closely to the centre of the discharge where most of the electrons are trapped. Discharge constriction results. High bromine concentrations eventually lead to high impedance and discharge 'twisting', which terminate lasing if the Cu_3Br_3 density is too high.

The behaviour at increased Ne pressure is consistent with third-body assisted reassociation of Cu and Br,

$$Cu + Br + m \rightarrow CuBr + m.$$

Higher Ne buffer gas pressures yield increased densities of CuBr by reassociation and more Cu_3Br_3 is necessary to maintain the atomic Cu concentrations. The increased bromine concentrations lead to discharge instabilities eventually, however, and the peak T_e in the pulse is reduced by the larger number density of Ne atoms so at high p_{Ne}, output power falls.

The beam is annular due to Cu depletion on-axis caused by gas heating and radial cataphoresis. Cataphoresis is more effective than in CVLs due to a higher degree of ionization because of discharge constriction (high current density). In addition, during the relaxation phase, atomic Cu is transported back to the discharge centre not as free Cu atoms, as in CVLs, but as part of the heavier, and slower, CuBr/Cu_3Br_3 molecules. The effectiveness of atomic Cu replenishment by diffusion in the relaxation phase is therefore reduced and when combined with the usual effects of gas heating and cataphoresis results in a permanently annular beam profile.

In spite of the decidedly annular emission pattern, output powers and efficiencies

similar to those of elemental CVLs are still attainable in conventional CBLs with no H_2 additive for two reasons, mainly because of the higher PRFs of the CBL. High PRFs increase n_{Cu} initially as the cumulative dissociation increases. Second, the higher impedance of the CBL allows better matching of the laser to the circuit and higher voltages can be applied to the discharge.

Conventional CBLs with added hydrogen and Cu hybrid lasers

Hydrogen addition to conventional CBLs typically doubles their output powers and efficiencies. Cu hybrid lasers generally achieve even better performance. Despite this, neither device has so far been found to demonstrate improvements in optimum PRF over conventional CBLs with no added H_2. In both lasers, the annular beam profile fills in at small H_2/HBr pressures, becoming bell-shaped or pseudo-Gaussian at higher pressures. Much of the discharge constriction of conventional CBLs with no H_2 additive is also removed, the beam expanding to full bore size at even very small H_2/HBr pressures and beyond. Improved laser-circuit matching is reflected in the increased efficiencies of the devices with H_2 and is evinced by an increase in tube wall temperature at the same PRF and charging voltage, and by a much lower voltage back swing on the thyratron anode following the excitation pulse. The laser pulse duration is also increased with H_2 addition.

A disadvantage of both H_2-CBLs and Cu hybrid lasers is that the output power reduces with time due to the growth of vertical Cu dendrites (up to 4 mm high) in the active region. Collapse of the dendrites at 20-30 min intervals periodically reinstates the laser output powers. Dendrites form on hot surfaces especially when the H_2/HBr concentration is too high or the wall temperature is too hot. In small bore lasers the problem is much worse.

Mass spectrometric studies of the gas at the outlets of CuBr-H_2 and Cu hybrid lasers have revealed that the species composing their gas mixtures are the same in both types of laser, though present in different concentrations. This is not surprising as the same atomic species are added, albeit in different forms. An important finding is that HBr is present at the outlet of both lasers, but in addition to HBr we can expect to find in the

discharge not only CuBr (monomer or polymer), Br, Br^- and Br_2, all of which are present in conventional CBLs with no additives, but also CuH, H, H^- and H_2.

The efficacy of hydrogen addition has been attributed by some authors to alterations to the electron energy distribution function (EEDF) caused mainly by the attachment of free electrons to atoms of hydrogen (vibrational excitation of H_2 and alterations in n_{Cu} were said to be other factors) [70]. The formation of H^- was claimed to 'shield' the ionization of Cu atoms so preventing depletion of atomic Cu.

The accepted theory is that proposed by Isaev et al. in a more recent publication [71]. These authors concluded that HBr is the species responsible for the improved performance of CBLs with H_2 additive and Cu hybrid lasers. HBr was said to alter the discharge kinetics chiefly via a process of dissociative attachment,

$$HBr + e \rightarrow H + Br^-.$$

This process has a peak cross section of 2.7×10^{-16} cm^2 for an electron energy of 0.28 eV and is believed to act with even greater speed than dissociative attachment of CuBr to remove free electrons in the early afterglow in the form of Br^- ions. A density of $\sim 10^{14}$ cm^{-3} HBr in the active volume is sufficient to remove the electrons with the characteristic time of ~ 5 μs which is measured in Cu hybrid lasers [64]. The rapid formation of Br^- in turn leads to fast (100 ns) two-body recombination of Cu^+ and Br^- ions to yield Cu and Br atoms,

$$Cu^+ + Br^- \rightarrow Cu^* + Br,$$

which replenishes the ground-state n_{Cu} in the central region of the discharge much more quickly than in CBLs with no H_2. Further, as the recombination process occurs over short timescales (100 ns), there is a reduction in the average Cu^+ lifetime and less Cu depletion by radial cataphoresis.

When the prepulse electron density is small, and both the electric field and

discharge current are still low, electron attachment to electronegative bromine atoms by dissociative attachment of HBr impedes and delays the electron avalanche [71]. As the electric field strength rises, higher electron energies are realized at which the cross-section for electron attachment falls with respect to the rate constant for ionization, and the avalanche proper begins. Evidence for these processes lies in the fact that discharge impedance increases on first application of the electric field while the current remains low. This delay means that when avalanche proper does commence, the electric field is again close to peak, and the current increase is fast (~ 70 ns from 10 % to 90 % of peak current in a 60 mm bore, 200 cm active length discharge tube).

As a consequence of electron attachment processes at the start of the current pulse in CuBr-H_2 and Cu hybrid lasers, at low electron energies (corresponding to $T_e < 2$ eV) ionization is balanced by attachment, and electron numbers remain low [71]. This prevents early population of the metastable lower laser levels. When the electron avalanche does begin, the electric field is near maximum so that T_e is within the 2-5 eV range most suited to pumping of the upper laser levels [71]. A larger inversion can therefore be sustained which is reflected in the higher (effectively doubled) specific output pulse energies and efficiencies of the CuBr-H_2 and Cu hybrid lasers and the longer laser pulse durations. Therefore, both the kinetics and the electrical characteristics of Cu lasers are improved by the addition of hydrogen halides or donors of their constituent atoms. Cu hybrid lasers also differ from CVLs and CBLs in the mechanism of generating the atomic Cu. As well as improving the kinetics of laser generation, HBr additive in a Cu hybrid laser controls the density of free Cu atoms in the discharge.

A number of mechanisms have also been proposed for the accelerated rates of Cu loss observed in atomic Cu lasers with HBr: hydrogen reduction of CuBr on the Cu surface followed by condensation of Cu vapour, thermal dissociation of CuH formed near the wall and condensation of CuBr on the wall. Results suggest hydrogen reduction of CuBr on the Cu surface and/or thermal decomposition as the principal mechanisms. The Cu surface may catalyse the reduction process by adsorption of hydrogen or by being at a greater temperature than the alumina due to inadequate thermal coupling between the

alumina and the Cu metal pieces. These processes, together with electric field and/or the plasma assistance, may also be responsible for dendrite growth .

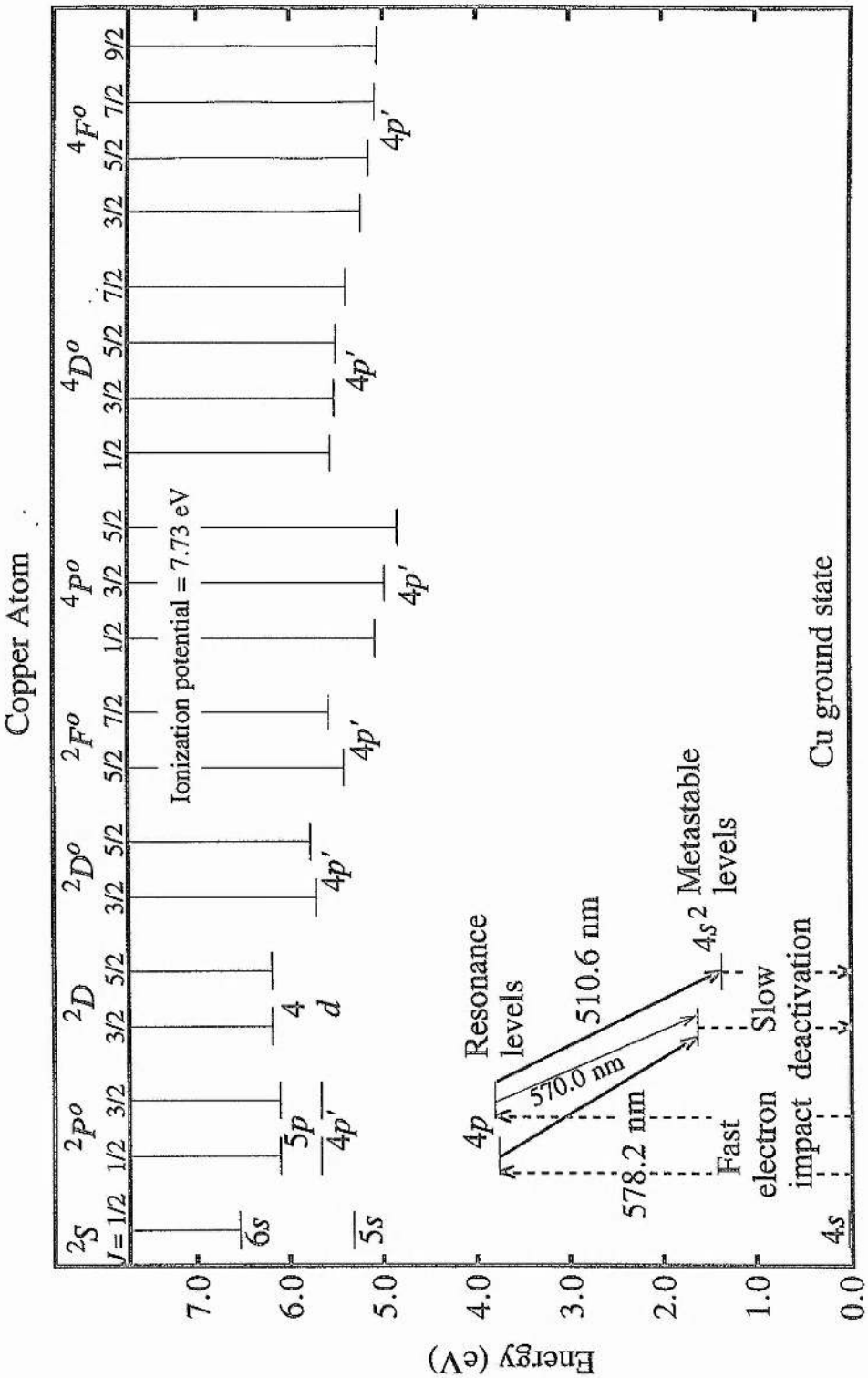

Fig. 1.1

Energy level diagram of atomic copper.

Chapter 2

Description of Lasers and Experimental Set-Up

2.1 Introduction

In this chapter, the three laser tubes (CuBr-Ne, CuBr-Ne-H_2 and Cu hybrid) studied are described fully together with their excitation circuitry, gas handling system and diagnostics set-up. The ancillary equipment was unaltered in the characterisation of each laser in order that direct comparisons could be made between their behaviours. A brief description is also given of the scanning and measurement techniques employed.

2.2 The Laser Configurations Studied

CuBr-Ne Laser

The CuBr-Ne laser investigated is shown schematically in Fig. 2.1. The plasma gain medium was confined within an alumina ceramic tube comprising two separate adjoining alumina cylinders both of 13.0 ± 0.25 mm bore but of unequal lengths. The longer cylinder was 300 mm in length while the shorter cylinder was 27.8 mm in length. The wall thickness was 2 mm in each case. The alumina was sleeved within a fused silica cylinder incorporating a sidearm at one end. The main body of the fused silica tube was of length 341 mm, inner diameter (ID) 19 mm and outer diameter (OD) 22 mm. The sidearm was of inside length 69 mm, ID 15 mm and OD 18 mm and was pre-filled with copper (I) bromide powder of 99.999 % purity before assembling the alumina. The fused silica tolerances were ± 1 mm except for the diameter tolerances which were ± 0.25 mm. Wall thicknesses were 1-1.5 mm.

A small, semicircular incision of radius 4 mm was made in the abutting edge of the shorter alumina cylinder and the alumina assembly arranged within the silica tubing such that the semicircular cavity so formed was located directly above and adjacent to the sidearm opening. The longer segment of alumina was supported within the fused silica by a Cu cylinder at either end. Each cylinder was fabricated from a Cu strip of length 65 mm, width 5 mm and thickness 0.25 mm. The shorter segment was supported by an identical Cu cylinder at the anode facing end and by gold wire at the abutting end to avoid reaction of Cu_3Br_3 vapour from the sidearm with the alumina support during lasing.

The silica was sealed to stainless steel, water-cooled endflanges by Viton *O* rings. Each endflange was cut to Brewster's angle at the exits to which quartz windows were also sealed by Viton *O* rings. The electrodes were simple molybdenum (Mo) cylinders, rolled from strips of 99.95 % pure Mo sheet metal of length 100 mm, width 25 mm and thickness 0.25 mm. These were push-fitted into the endflanges such that their ends projected by a few millimetres only, each just touching the alumina ceramic tube when the laser was fully assembled. As the electrodes adjoined the alumina, the active volume of the laser was simply the inside volume of the alumina assembly and was 43.5 cm^3 in this case. The discharge current was stable because the small electrode projections enabled a large contact area to be established between each electrode and its respective endflange and because additional water cooling was supplied to the cathode endflange which was the hotter of the two during normal operation. Wall temperatures fell under conditions of electrical excitation and buffer gas where the system was improperly matched so that insulation was necessary. The main body of the fused silica tube was wrapped in a thin layer of Saffil insulation so that the outside (silica) wall temperature was in the range 400-600 °C when lasing.

The sidearm was encased in a heating element comprising resistive wire wound on a silica cylinder. The heater terminals were connected to a 240 V, current limited Claude Lyons Regavolt™ variable transformer (Variac) via an ammeter placed in the current path. The heater terminal resistance was measured as 12 Ω which together with the current limit of 10 A on the Variac determined the maximum voltage of 120 V which

could be applied. A layer of Saffil insulation was also wrapped around the heating element so that no part of either the heater or the sidearm was exposed.

After evacuating the system for several hours, the CuBr powder was prepared prior to operating the laser. With Ne gas flowing through the laser tube at a flow rate, R_{Ne}, of ~ 1.5 litre.atm.hr^{-1} and a pressure, p_{Ne}, of ~ 37.5 torr, the CuBr was first heated to temperatures above 100 °C but below the vaporisation temperature of CuBr. This enabled the release of impurities (particularly H_2O) from the CuBr powder. (Although the powder is quoted as being 99.999 % pure by the manufacturer, some moisture from the air is inevitably absorbed by the CuBr during assembly of the laser tube. As H_2O bonds well with CuBr, to is not possible to remove all of it even by heating to 100 °C so that there is always some level of H_2 contamination in the CuBr-Ne laser tube.) The Variac was switched off. After the sidearm had cooled to room temperature and the system had been evacuated for a further 30 min., the laser tube was back-filled with Ne gas to approximately 600 torr. The Variac voltage and heater temperature were gradually increased until the CuBr powder melted, the high p_{Ne} preventing sputtering of liquid CuBr into the active region of the laser tube. Following this, the Variac was again switched off and the sidearm allowed to cool. The CuBr melt, when solidified, occupied approximately one fifth to one third of the total sidearm volume. The system was evacuated for several hours before lasing.

The Ne buffer gas was flowed through the laser via gas inlet and outlet vacuum connections fitted into the water cooled endflanges. Although R_{Ne} was varied from 0.3 to 13.5 litre.atm.hr^{-1} (approximately 30-1350 litre.kPa.hr^{-1}) during the characterization experiments it was generally maintained at ~ 1 litre.atm.hr^{-1}. Multikilohertz excitation of the electrodes enabled a stable plasma gain medium of electric discharge origin to be established and confined within the walls of the alumina tubing. Heating of the sidearm then released Cu_3Br_3 vapour into the active region of the laser tube where this was dissociated in the pulsed discharge to yield free Cu atoms for lasing on the 510.6 and 578.2 nm cyclic transitions of atomic Cu.

CuBr-Ne-H_2 Laser

The CuBr-Ne-H_2 laser tube was identical in construction to the CuBr-Ne laser shown in Fig. 2.1, but when operated as a CuBr-Ne-H_2 laser, relatively small concentrations of H_2 gas were mixed with the Ne buffer gas prior to entering the laser tube at the anode end. A very fine needle valve was necessary to regulate H_2 flow because of the small diameter of the H_2 molecule. It was not found practical to characterise the CuBr-Ne and CuBr-Ne-H_2 lasers concomitantly, for once the system had been exposed to H_2 gas it continued to display characteristics of CuBr-Ne-H_2 laser operation no matter how thoroughly the system was subsequently purged with Ne gas. Disassembly, cleaning and reassembly with fresh materials was necessary to remove all traces of H_2.

Cu Hybrid Laser

The Cu hybrid laser studied was similar in configuration to that described in [49] and is shown schematically in Fig. 2.2. An alumina ceramic tube of length 300 mm, ID 12.5 ± 0.25 mm and OD 17 mm was sleeved by a simple fused silica cylinder of ID 19 mm and OD 22 mm, available in two lengths (340 and 400 mm) and incorporating no sidearm. The alumina tube was supported inside the fused silica by two Cu cylinders encircling either end of the alumina and fashioned from Cu strips of length 65 mm, width 5 mm and thickness 0.25 mm. In the characterisation experiments reported in Chapter 5, the longer length of fused silica tubing was used. Twelve pieces of high purity (99.99 %) Cu sheet metal were placed end-to-end along the floor of the alumina tube in groups of two at 50 mm intervals. Each piece was typically of length 10 mm, width 5 mm and thickness 0.25 mm. The edge of the first Cu piece was positioned close to the anode facing edge of the alumina tube. The Cu pieces were flat and were thus suspended some small distance above the floor of the cylindrical alumina tube at their centres. In the metal seeding experiments discussed in Chapter 7, the shorter length of fused silica was employed and the flat Cu pieces were replaced in some instances by single Cu cylinders of outer diameter equal to the inner bore of the alumina tube. Double thicknesses of Cu cylinders were used in order that surface area would not diminish during lasing. Inspection of the

Cu metal after lasing verified that this approach worked.

The fused silica cylinder was sealed to the same metal endflanges described for the CuBr-Ne laser and in the same manner. The electrodes were again cylinders of 99.95 % pure molybdenum which were push-fitted into the endflanges so as to touch the alumina when assembled. With the longer length of fused silica tube and the shorter ceramic cylinder, the electrodes necessarily projected a greater distance than in the CuBr-Ne and CuBr-Ne-H_2 lasers. Each electrode was fabricated from a molybdenum sheet of dimensions 70 x 100 x 0.25 mm and projected by approximately 50 mm from each endflange. The overlapping edge on the inside of the rolled molybdenum cathode was upturned to encourage electron attachment. In the metal seeding experiments, during which the shorter fused silica tube was employed, the electrode lengths were modified to accommodate this change. The electrodes were fabricated from molybdenum sheets 40 x 100 x 0.25 mm in dimension and projected approximately 20 mm from each endflange. Thermal insulation was a thin layer of Saffil wrapped around the exposed area of the fused silica tube. Greatest stability was achieved with the shortest length of fused silica tube, the shortest possible molybdenum electrode projections, a minimum of thermal insulation (1-2 mm) and with additional water cooling on the cathode endflange.

A Ne-HBr gas mixture was flowed at typically 0.5-2.0 litre.atm.hr^{-1} (approximately 50-200 litre.kPa.hr^{-1}) through the laser via the gas inlet and outlet vacuum connections fitted into the water cooled endflanges. This again enabled an electric discharge to be established between the electrodes by repetitive pulsing of the laser. The electric discharge dissociation products of the HBr reacted with the Cu metal in the discharge tube to create CuBr/Cu_3Br_3 which was then dissociated by electron impact to yield free Cu atoms for lasing on the 510.6 and 578.2 nm cyclic transitions of atomic Cu. As the electrodes adjoined the alumina, the active volume of the laser was again the inside volume of the alumina tube and was 36.8 cm^3 in this case. The small difference in active volume between the conventional CuBr-Ne laser tube and the Cu hybrid version does not affect the comparisons as the alumina ceramic tube bores were approximately equal in both cases.

2.3 The Excitation Circuitry

A conventional resonant charging, capacitance transfer circuit provided electrical excitation to all three laser tubes and is illustrated schematically in Fig. 2.3. A high voltage supply (Converter Power Inc. model RCS-6000) charged a storage capacitor via an inductor and diode. Charging voltages were in the range 4 to 16 kV. The energy in the storage capacitor was switched by an EEV CX1535 thyratron at PRFs up to 50 kHz into a peaking capacitor in parallel with both the laser tube and a bypass inductor. This caused the gas mixture in the laser tube to break down to form an electric discharge and the plasma gain medium for lasing. The current loop containing the laser discharge and peaking capacitor was completed by an outer current return which was coaxial with the laser tube to ensure a low loop inductance, so that discharge current pulses with short risetimes could be generated. The current return comprised two aluminium strips connected to the anode endflange and connected by earth braid at the cathode end of the laser tube. The strips fanned out by an extra 30 mm towards the cathode end to prevent melting of the aluminium in this region of increased heat. Current pulses of up to 500 A peak were produced with typically 30 to 100 ns risetimes.

Three combinations of the storage/peaking capacitances, C_s/C_p, were used in an effort to optimise the transfer of energy from the electric circuit to the discharge: 0.81 nF (0.66 nF at operating temperature)/0.41 nF (0.33 nF at operating temperature); 0.62 nF (0.52 nF at operating temperature)/0.30 nF (0.24 nF at operating temperature); 1.16 nF (0.97 nF at operating temperature)/0.57 nF (0.45 nF at operating temperature). The capacitors fell in capacitance when the system was operating due to a non-linear temperature response. As only the capacitance at the operating temperature is important, in the following chapters any capacitance quoted shall be understood to be an operating value. The three combinations of C_s/C_p are therefore 0.52/0.24 nF, 0.66/0.33 nF and 0.97/0.45 nF and shall henceforth be denoted C_{small}, C_{medium} and C_{large} respectively.

2.4 The Gas Handling System

The gas handling system is illustrated schematically in Fig. 2.4. The Ne buffer gas and

additive gas (H_2 or HBr) were mixed via needle valves before entering the laser tube through the gas inlet vacuum connection on the anode endflange upstream of the anode itself. The gases were exhausted downstream of the cathode via the gas outlet vacuum connection on the cathode endflange, a halogen filter and a rotary vacuum pump (Edwards model E2M12). The needle valves were used to control individual gas flow rates and the outlet valve to control total gas pressure. Total pressure was monitored on a 0-1000 mbar Diavac pressure gauge model DV1000.

When the laser tube shown in Fig. 2.4 was used as a CuBr-Ne laser, Ne buffer gas alone flowed through the system and the H_2 cylinder remained sealed off throughout. When replaced by the Cu hybrid laser tube, an HBr cylinder was connected in place of the H_2 cylinder. Ne buffer gas and HBr additive were then mixed via the needle valves prior to entering the laser tube at the anode end. The needle valve employed to control HBr flow was not required to be as fine as that used to regulate H_2 flow because of the larger diameter of the HBr molecule.

Prior to performing any gas flow rate calibrations or experiments with the laser tubes, the relevant gas mixture was allowed to flow freely through the system to enable the cylinder outlet pressures to settle at their steady state values. In the case of the CuBr-Ne laser the steady state Ne pressure was 413 torr (0.55 bar or 8 $lb.in^{-2}$). For the CuBr-Ne-H_2 laser the equilibrium Ne pressure fell to 207 torr (0.28 bar or 4 $lb.in^{-2}$) and the H_2 pressure was typically 259 torr (0.34 bar or 5 $lb.in^{-2}$). For the Cu hybrid laser the Ne and HBr steady state pressures were 413 torr (0.55 bar or 8 $lb.in^{-2}$) and 450 torr (0.6 bar or 9 $lb.in^{-2}$) respectively. Following this, the system was evacuated for a short period (10-15 min.) before filling with Ne at the desired pressure and flow rate and exciting the laser.

2.5 The Optical Cavity

The optical cavity was a nonoptimized plane-parallel resonator comprising a flat high-reflector (Tec-Optics, > 99.5 % at 400-700 nm) at the cathode end of the laser tube and an uncoated quartz flat as output coupler. These are shown schematically in Fig. 2.5. The cavity was ~ 1.05 m in overall length. Beam alignment was very easy due to the high gain

of the laser system.

2.6 The Diagnostics Set-Up

The diagnostics set-up is also shown in Fig. 2.5. Measurements of average output power, P, were made using a Photon Control power meter capable of measuring over a 3 mW to 300 W range. The laser pulse was observed by reflecting a sample of the beam cross-section onto a fast (< 1 ns) Ge photodiode connected to an oscilloscope (Tektronix model 2445A). Green and yellow filters were placed in front of the photodiode where appropriate to enable separate data for the 510.6 nm (green) and 578.2 nm (yellow) pulses to be procured. A Shackman 7000 camera provided oscillograms of the total, green and yellow emission intensity waveforms. The temporal behaviours of the green and yellow pulses are readily seen in these but because the filters were of different reflectivity the units of intensity are essentially arbitrary and the green and yellow amplitudes cannot be compared directly.

The discharge current waveform, $i_t(t)$, was sampled by a model 2-0.1W Stangenes current transformer which encircled the current return near the ground point (Fig. 2.5). Charging and laser tube voltage waveforms, $V_{ch}(t)$ and $V_t(t)$, were monitored by means of HV probes (Tektronix P6015A) connected across the charging capacitors and laser tube respectively. The output signals from the current transformer and the HV probes were displayed on separate channels of the Tektronix model 2445A oscilloscope. The Shackman 7000 camera provided oscillograms of these waveforms also.

In the cases of the CuBr-Ne and CuBr-Ne-H_2 lasers, the sidearm wall temperature was also important as the parameter controlling the partial pressure of Cu_3Br_3 diffusing into the main body of the laser tube. A thermocouple was routed through a plug of insulation at the base of the fused silica heater cylinder to an area of sidearm wall adjacent to the CuBr melt (Fig. 2.1). Care was taken to ensure that the thermocouple did not touch the heating element itself. The Saffil insulation surrounding the sidearm reduced air circulation around the thermocouple whose output was displayed on a 0-1000 °C Wild-Barfield galvanometer.

In the case of the Cu hybrid laser, the wall temperature of the simple fused silica cylinder was of primary importance due to the different Cu seeding mechanism in this type of laser. A thermocouple was routed through the Saffil insulation to the fused silica tube to enable measurements of wall temperature to be made. The Saffil covering again reduced air circulation in the vicinity of the thermocouple which might otherwise have led to false temperature readings. The thermocouple output was again displayed on the 0-1000 °C Wild-Barfield galvanometer. Temperatures from 500 to 800 °C were typical.

2.7 Experimental Procedures

In characterising each laser, the independent electrical excitation variables were PRF and charging voltage, V_{ch}. The variable gas parameters were flow rate and pressure. In the CuBr-Ne and CuBr-Ne-H_2 lasers the Cu_3Br_3 pressure, $p_{Cu_3Br_3}$, was also variable via the sidearm wall temperature, T_s, which was controlled by means of the heater voltage. In the CuBr-Ne-H_2 and Cu hybrid lasers, control of the H_2 pressure, p_{H_2}, and the HBr pressure, p_{HBr}, respectively was also possible via needle valves. The quantities measured were average output power, discharge current, laser tube voltage, and emission intensity (total, green and yellow). Metal seeding experiments were conducted with the Cu hybrid laser only in which additional independent variables were exposed Cu area, A_R, and lasing time, t. The Cu metal configuration was also varied. Observations of average output powers, Cu weights before and after lasing, w_b and w_a, and the change in Cu weight, Δw, at specific locations in the discharge tube were made.

Variation of the electrical excitation parameters was achieved with ease. PRFs and charging voltages were set accurately by adjusting the output signals at the trigger generator and HV supply respectively whilst monitoring the discharge current pulse and charging voltage traces on the oscilloscope. Total gas pressures, p_{total}, were controlled by adjustment of the outlet valve and could be obtained directly from the pressure gauge (Fig. 2.4). Flow rates and partial pressures of Ne, H_2, HBr and Cu_3Br_3 were adjusted by means of the inlet and outlet valves and the sidearm heater voltage but could not be monitored directly. Instead, knowledge of these quantities was based on needle valve

calibrations and estimations.

In the case of the CuBr-Ne laser, p_{Ne} and p_{total} were assumed synonymous ($p_{Cu_3Br_3}$ is only of the order of 0.33 torr) and could be obtained directly from the pressure gauge. Ne flow rates were determined by needle valve calibrations. Pressure versus time was recorded when Ne gas was released into the evacuated system at selected needle valve settings. The gradients of the resulting plots of pressure versus time together with knowledge of the free volume of the total gas circuit enabled a graph of flow rate versus needle valve setting to be plotted and used to determine any subsequent rates of flow. The relatively small $p_{Cu_3Br_3}$ could at best be estimated based on knowledge of the temperature of vaporisation of CuBr and the flow rate of Cu_3Br_3 was of little importance to this study.

In the CuBr-Ne-H_2 laser, as a consequence of mixing the constituent gases prior to their entering the laser tube, the flow rates and partial pressures of the Ne and H_2 were controlled by means of the inlet needle valves but neither gas could not be monitored directly. The Ne flow rates were obtained in the same fashion as for the CuBr-Ne laser. It was difficult to calibrate the H_2 needle valve for flow rate for H_2, being a very small molecule, was difficult to control and its flow rate at any particular needle valve setting appeared to change slowly over a period of time perhaps due to temperature effects. H_2 flow rates were unimportant in the investigation, except as a means of determining H_2 partial pressures. As most of the CuBr-Ne-H_2 laser experiments were conducted at a single R_{Ne}, it was only necessary to plot p_{H_2} versus p_{Ne} at this one particular rate. To obtain this plot, p_{H_2} was optimised for peak output power at a number of total pressures. At each pressure, lasing was terminated on achieving optimisation, and the Ne inlet line sealed off so that the pressure could settle at the optimum partial pressure of H_2. At each p_{total}, this plot was used to find first p_{H_2} and then p_{Ne}, the difference of the two.

In the case of the Cu hybrid laser, Ne flow rates were obtained by needle valve calibrations as before. HBr flow rates were obtained in a similar manner but instead of recording pressure versus time as HBr flowed into an evacuated gas circuit, the laser was pre-filled to 37.5 torr with static Ne gas before admitting the HBr gas. To obtain the

partial pressures of each gas, the total gas pressure was multiplied by the ratio of the flow rate of each gas to the sum of both flow rates. In this way the partial pressures of Ne and HBr were obtained for any combination of the inlet and outlet valve settings.

For consistency in comparing the three laser systems, a reference set of values was defined for the main independent variables. The reference values of p_{total}, R_{Ne}, PRF and V_{ch} were 37.5 torr, 0.8 litre.atm.hr^{-1}, 20 kHz and 10 kV respectively. These values were chosen to give relatively strong and stable lasing in each regime of lasing at an input power of ~ 1 kW which did not put undue stress on the thyratron. The modulator could deliver a maximum input power of 2 kW to the laser tube so that setting the reference parameters for 1 kW input power allowed for increases in input power when using the largest capacitors or when operating at high PRFs. The low flow rate and medium pressure selected helped to reduce window contamination during the experiments which might otherwise have distorted the results. In general, while one parameter was varied the others were set to their reference values. Other values were only used in special circumstances. The 0.66/0.33 nF capacitors were used to illustrate most of the general trends in lasing.

In the following chapters the values of the independent variables should be assumed to be reference unless stated otherwise. The reference values will not be restated except where particular emphasis is required. To avoid any confusion all values of the independent variables are quoted in any figure used to illustrate the results.

When scanning the main independent variables (p_{total}, R_{Ne}, PRF and V_{ch}) fast experimental techniques were adopted. With the exception of the parameter being varied, all other independent variables were fixed at their reference values except where special circumstances dictated otherwise. The additive gas pressures, $p_{Cu_3Br_3}$, p_{H_2} and p_{HBr} (according as the CuBr-Ne, CuBr-Ne-H_2 or Cu hybrid laser was being investigated) were optimised for peak power at the reference value of the independent variable being scanned. The variable was then lowered or increased to either side of its reference value and measurements taken within 30 s of the change so that thermal effects could not influence the results. On return to the reference value, the additive gas pressures were

readjusted and the measured quantity allowed to settle before repeating the procedure for another value of the independent variable. A full description of an experimental technique is only provided in the following chapters if it varies significantly from the above scenario.

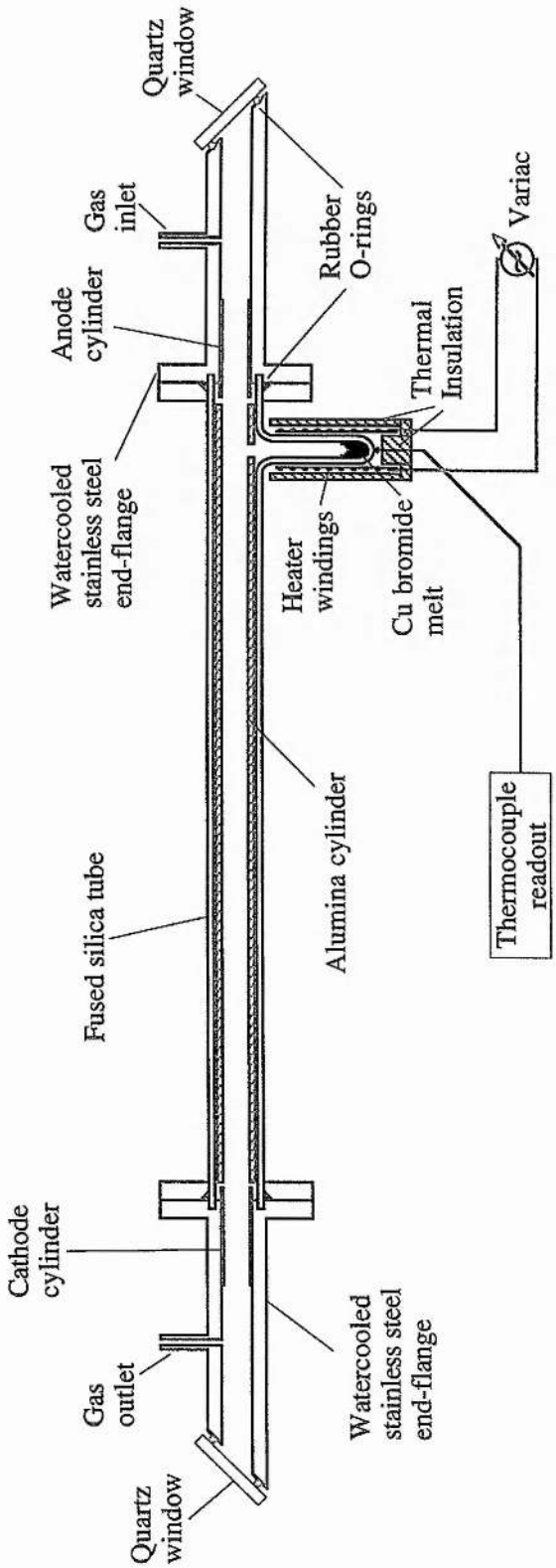

Fig. 2.1

Schematic diagram of the CuBr-Ne/CuBr-Ne-H_2 laser tube.

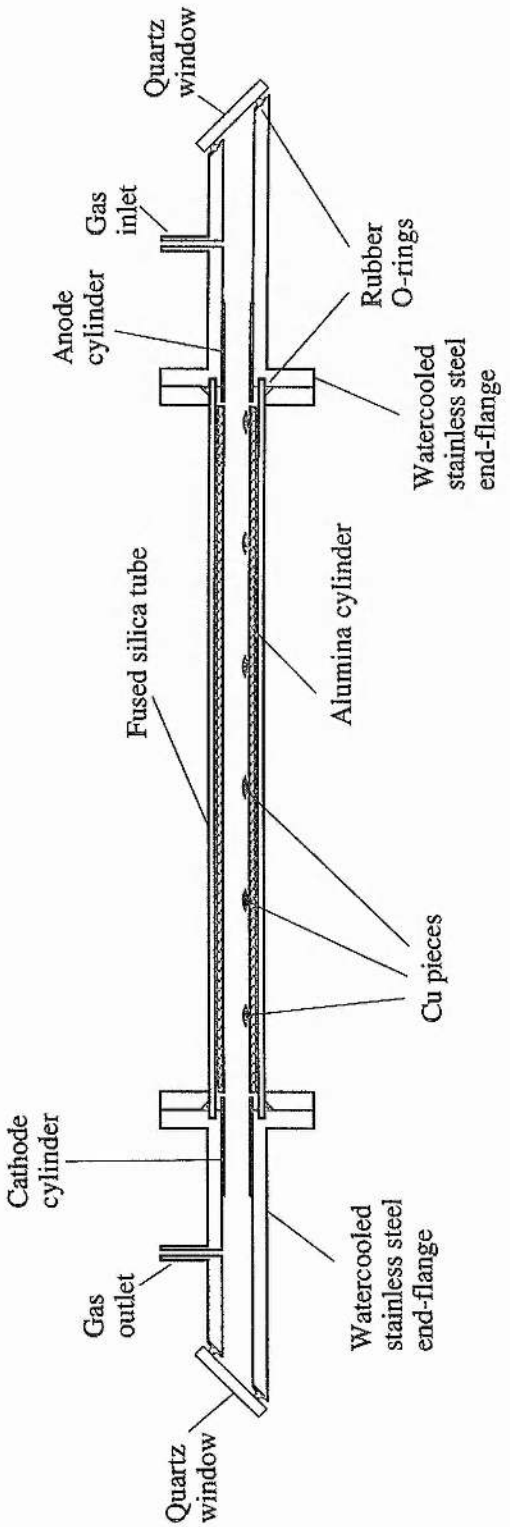

Fig. 2.2

Schematic diagram of the Cu hybrid laser tube.

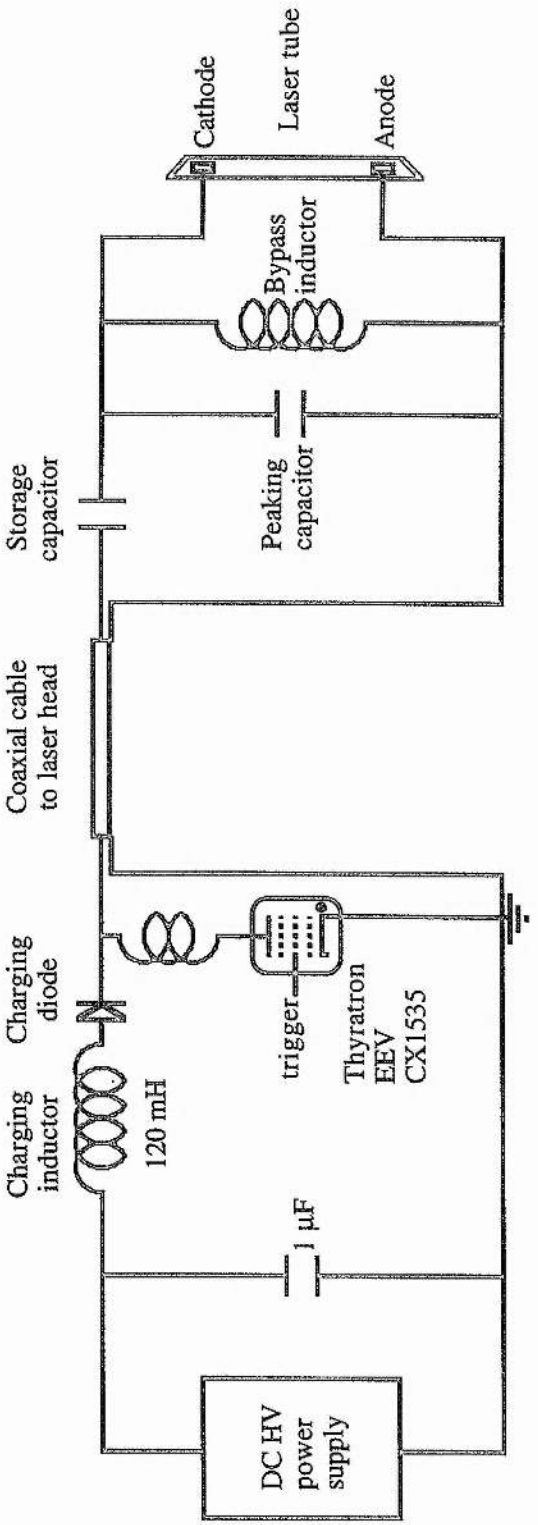

Fig. 2.3

Schematic diagram of the resonant charging, capacitance transfer excitation circuitry.

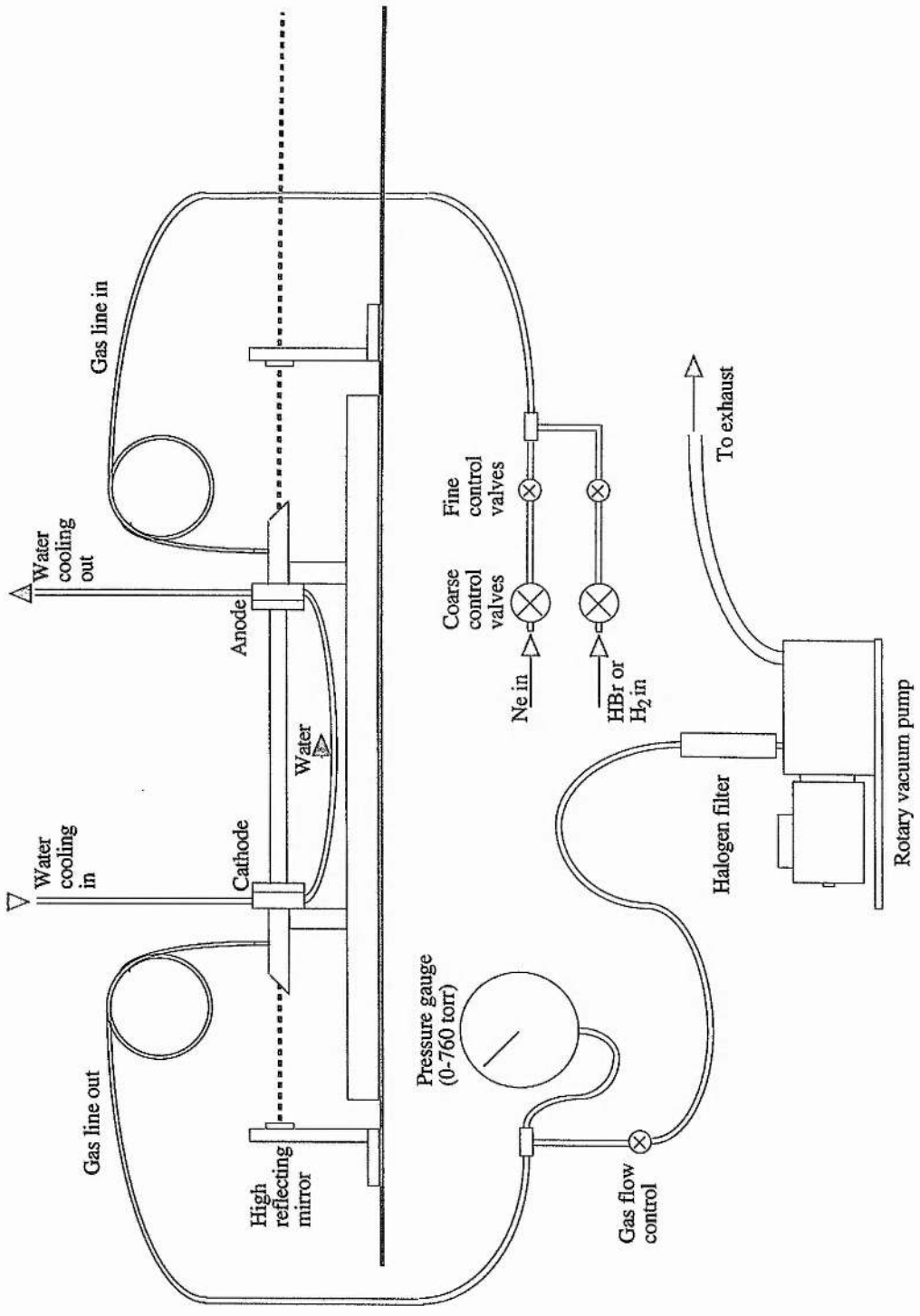

Fig. 2.4
Schematic diagram of the laser tube and gas handling system.

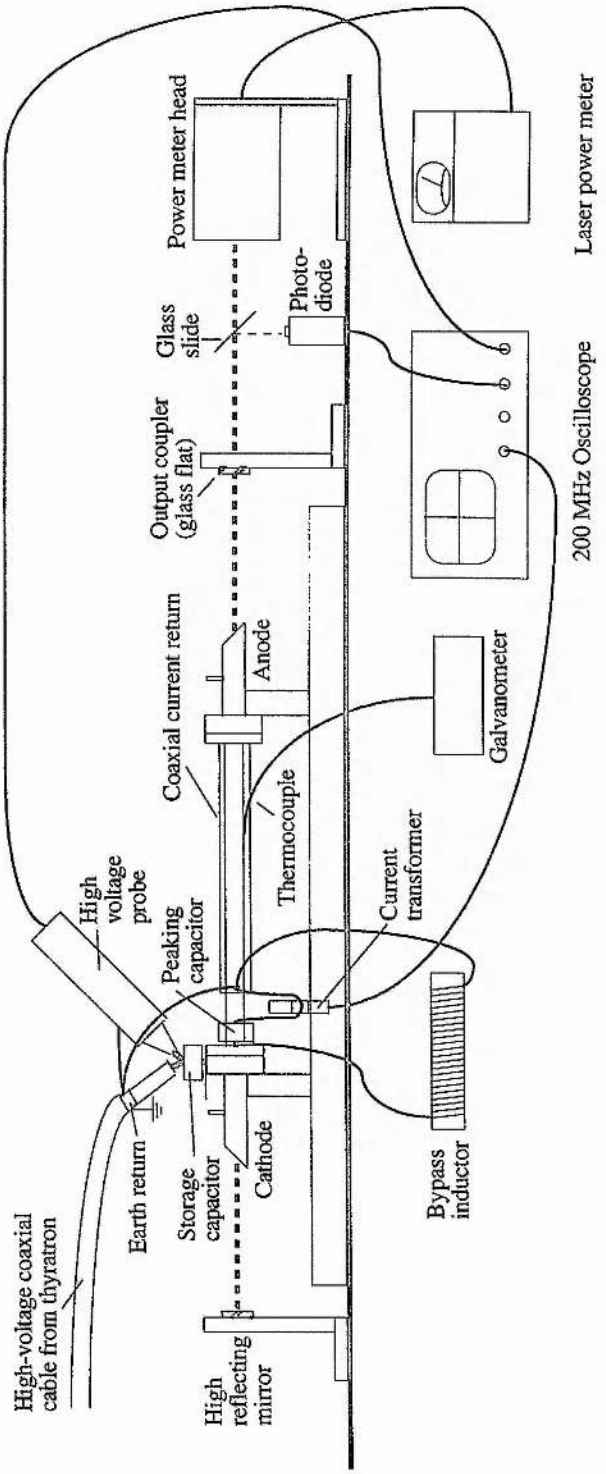

Fig. 2.5

Schematic diagram of the optical cavity and diagnostics set-up.

Chapter 3

Characterization of the CuBr-Ne Laser

3.1 Introduction

In conventional CBLs, heating of solid CuBr, or of a compound containing CuBr, in the main discharge tube, or in one or several sidearms, enables Cu_3Br_3 vapour to diffuse into the discharge volume where electron impact dissociation of the Cu salt produces the free Cu atoms required for the laser transitions. In this chapter, the operating characteristics of a small, self-heated conventional CBL accommodating a single sidearm reservoir of CuBr melt are described. Two regimes of operation are reported, labelled low-temperature (LT) and high-temperature (HT) because of their relationship to sidearm wall temperature, T_s. The active volume and discharge tube bore were 43.5 cm^3 and 13 mm respectively and the buffer gas was Ne. A full description of the laser was given in Chapter 2.

The current chapter begins with some general observations regarding the behaviour of the CuBr-Ne laser. The exact dependence of average output power, P, on T_s for two values of the buffer gas pressure, p_{Ne}, is subsequently reported, both as evidence for the existence of two temperature regimes of operation, and as an illustration of the efficacy of each regime under optimal and non-optimal conditions of buffer gas pressure.

Comparison of the laser response at low T_s with reports of CBL performance made by other authors points to the LT regime as the authentic mode of operation for this type of laser, and as such it has been characterised extensively. Trends in P and efficiency (BSE), η, with scanning of the parameters of the electrical excitation and/or gas mixture are described in detail for this regime. Oscillograms reveal the temporal behaviour of the discharge current, $i_t(t)$, the laser tube voltage, $V_t(t)$ and the total, green

and yellow emission intensities, $I_l(t)$, $I_g(t)$ and $I_y(t)$, under close to optimum conditions for lasing.

The HT regime of operation was characterised less extensively as it was not the working regime of the CuBr-Ne laser. Nonetheless, it was important to conduct a summary investigation of its behaviour in order to account for its existence. Some equivalent aspects of HT performance are therefore reported. In later chapters (4 and 6) these are seen to mimic, in part, the results for the CuBr-Ne-H_2 laser, suggesting that this particular regime has its origin in hydrogen-containing impurities. Finally, in the discussion section of this chapter (Section 3.6) explanations are proffered for the responses of both regimes to the test conditions. As the descriptions of each experiment, together with their outcomes, (Sections 3.2 to 3.5) are detailed, the reader may find it convenient to read the discussion first.

3.2 General Observations

Lasing in the 13 mm bore CuBr-Ne laser always commenced within 5-10 min from a cold start. At T_s of the order 150-300 °C (depending on p_{Ne}), sufficient vapour pressures, $p_{Cu_3Br_3}$, of Cu_3Br_3 were produced to change the sidelight spectrum from the bright orange-red hue associated with pure Ne to a uniform pale green colour, as copper transitions increased in intensity and those of Ne decreased, and the LT regime was established. The rate determining factor for lasing was the heating of the sidearm. Discharge heating of the main body of the laser tube occurred over timescales of 1 min or less.

Lasing was of reasonable strength and stability in both temperature regimes at low-medium buffer gas pressures and flow rates, R_{Ne}, of around 10-30 torr and 0.5-1.5 litre.atm.hr^{-1} respectively. Under these conditions, and at reference values of PRF and charging voltage, V_{ch}, (*i.e.* 20 kHz and 10 kV), laser action at low T_s was low in power and confined to a narrow green annular region adjacent to the alumina wall. The laser discharge was very stable. With increasing T_s and $p_{Cu_3Br_3}$, the annulus increased in thickness and intensity but acquired a degree of constriction. At T_s some 50-100 °C

higher than that at which lasing was first observed, average output power peaked. The outer diameter of the annulus had narrowed from its original 12-13 mm to approximately 7-8 mm and displayed a higher proportion of yellow. No significant alteration in V_{ch} had occurred on adding the Cu_3Br_3 implying little change in discharge impedance and circuit-laser matching. The LT regime was broad in temperature extent remaining at ≥ 95 % of its peak value over an ~ 20 °C range.

On increasing T_s above optimum for the LT regime the average power started to fall. This stage of operation was characterised by appreciable discharge instability causing swings in sidearm temperature and small, unpredictable power fluctuations. The beam remained annular but became more constricted (3-4 mm OD) and increasingly yellow with rising T_s. The discharge was pale blue in colour as bromine transitions were strong in the sidelight spectrum. The charging voltage dropped indicating that the discharge channel impedance was rising and improvements in circuit-laser matching were taking place. Readjustment of the modulator voltage was required to maintain V_{ch} at 10 kV. The LT regime ended as average power passed through a minimum. At temperatures beyond this, the system began to stabilise again as the laser entered the HT regime of operation.

In the HT regime, the rise to a new peak power with increasing T_s was relatively sudden and circuit-laser matching continued to improve. The HT regime was the less stable of the two exhibiting a significant degree of current 'hopping' caused by discharge attachment jumping between different points on the electrodes. This caused a local instability of ≤ ± 0.5 W around the increasing power (up to 3-4 W). At low powers, the beam was yellow/green, annular and 3-4 mm in diameter. At peak power the discharge, beam and average power stabilised to some extent (and did so completely under optimal conditions of Ne pressure, flow rate and electrical excitation). The beam cross-section was less constricted (~ 5 mm OD) and less annular and the discharge was a uniform deep blue. At low-medium p_{Ne} and R_{Ne}, the peak average power was almost double that of the LT regime, but high power and stability lasted over a much narrower temperature range (usually only 5-10 °C).

Further increase in T_s caused the power to fall off and the discharge to change in

colour from uniform blue to deep turquoise as more bromine vapour was added. 'Standing waves' of sidelight intensity appeared along the length of the discharge. The beam was yellow, 2-3 mm in diameter and showed little or no annularity. In the initial stages of power fall off, the beam intensity tended to ebb then reinstate itself in bursts. Within a few degrees centigrade from the onset of instability, oscillation ceased. This was followed almost immediately by the collapse of the discharge current pulse and the establishment of a wall discharge *i.e.* the impedance of the gas was higher than the inside surface of the tube. Turning off the Cu_3Br_3 supply restored the discharge current pulse and compelled the average output power to rise and to fall in the reverse pattern. The sidelight spectrum returned to that of Ne. When the tube was relatively new, cessation of lasing took place over timescales similar to those at start-up (5-10 min).

A peculiar dependence of the discharge current waveform on T_s was also observed. The first alteration in $i_t(t)$ occurred almost immediately on addition of even the smallest $p_{Cu_3Br_3}$ to the discharge when a step was observed to move down the leading edge of the discharge current pulse. The height of the step at any instant provided a good indication of the levels of Cu_3Br_3 added.

Simultaneously with the decreasing step height and increasing output power, the peak discharge current, $i_{t\,pk}$, began to rise. As T_s reached optimum for the LT regime, the leading edge step on the primary current pulse fell to around the 10-20 % height and peak current passed through a maximum simultaneously with output power.

A further rise in T_s caused the step height to fall below the 10-20 % level, and both the peak discharge current and average output power to reduce, passing through minima simultaneously. The sudden rise in output power as T_s entered the HT regime coincided with the total collapse of the step and a partial recovery in $i_{t\,pk}$. As output power rose with increasing T_s in the HT regime the current pulse continued to increase in amplitude. Peak power in the HT regime occurred simultaneously with the current pulse reaching its maximum amplitude. Both were higher than at optimum T_s in the LT regime. During fall off in power with increasing T_s in the HT regime, the current also reduced in amplitude. At cessation of lasing, when $i_{t\,pk}$ was still ~ 100 A, the current pulse collapsed

without warning and the wall discharge, spoken of earlier, resulted.

At the onset of the HT regime, a step was observed to appear near the top of the leading edge of a smaller current pulse appended to the trailing end of the main pulse. This step continued to move down the leading edge as power increased in the HT mode, reaching zero (or just below) when the power peaked. The smallness of this step is a tribute to the efficacy of the process of electron attachment to atomic bromine which is responsible for removing the prepulse electrons that carry the step current [72].

The CuBr laser was operated continuously for up to 12 hr on a number of separate occasions. Peak average power in the HT regime lessened over intervals of a few hours or more due to small numbers of Cu dendrite formations in the active region, primarily around the semicircular aperture in the ceramic above the sidearm opening and notably when this area of the tube was running too hot. The dendrites grew vertically from the abutting edges of the ceramic sections and were observed to melt periodically in the intense heat of the discharge thereby reinstating the average power from time to time.

With increasing use of the laser tube, CuBr deposits built up around the sidearm opening and elsewhere. The heat from the discharge was sufficient to cause lasing at these sites even when no sidearm heater voltage was applied. It thus became increasingly difficult with time to alter or terminate lasing by simple control of T_s. Operation at very low pressures posed additional problems. The discharge extended almost to the cathode window causing quantities of contaminants (especially bromine) to be deposited there. The cathode also became very hot. At low pressures and/or at peak power in the HT regime, the discharge penetrated the sidearm causing large temperature and power swings. Window contamination was also a problem at high buffer gas pressures and flow rates and at high PRFs and charging voltages at which increased Cu_3Br_3 pressures were found necessary to attain peak power in both regimes, but gave rise to increased discharge constriction and turbulence.

To effect control over P, it was necessary to maintain the laser tube wall temperature, T_w, at levels above the vaporisation temperature of CuBr. This inhibited condensation of Cu_3Br_3 on the tube wall so that $p_{Cu_3Br_3}$ in the discharge could be

governed solely by the sidearm heater voltage. Increasing the insulation thickness near the sidearm opening discouraged deposition of CuBr powder in that location but encouraged Cu metal deposition in the form of dendrites in this same area if temperatures became too hot. A temperature balance had to be achieved. To curb window contamination, the laser was operated at low-medium values of pressure and flow rate where possible *i.e.* 37.5 torr and 0.8 litre.atm.hr^{-1}. In exceptional cases, fast experimental techniques ensured that lasing times under extreme conditions of pressure and/or flow rate were minimal. In spite of these precautions, a fine scattering of Cu and CuBr particles was usually visible across the entire inner surface of the alumina on cessation of lasing.

3.3 Dependence of Average Output Power on Sidearm Wall Temperature

The medium sized (0.66/0.33 nF) capacitors, C_{medium}, were chosen to begin the investigation. With these connected, the precise dependence of average output power on T_s was obtained at two separate buffer gas pressures, 19 and 34 torr. The main aim of this study was to establish conclusively the presence of two temperature regimes of operation. The pressures tried are shown in parts 3.4 and 3.5 of this chapter to be around optimum for the HT and LT regimes respectively with the medium capacitors.

The sidearm wall temperature was raised from 100-445 °C and average power recorded at intervals of approximately 5-20 °C. Average output power versus sidearm wall temperature at 19 and 34 torr is shown in Fig. 3.1. Each plot clearly shows two temperature regimes of operation. In moving from 19 to 34 torr, T_s necessary to attain peak power increases by ~ 120 °C in the LT regime and by ~ 130 °C in the HT regime. The LT regime is strengthened on moving to the higher pressure, attaining peak powers of 1.6 W and 2.05 W at 19 and 34 torr respectively. The wide range of temperatures covered by this regime at both pressures illustrates its expediency as a source of visible light.

Although the peak average power of 3.15 W obtained in the HT regime at 34 torr p_{Ne} exceeds that of the LT regime, the HT output is very much weaker in terms of

temperature range and is clearly favoured by the lower pressure at which peak powers are not only higher (4.3 W in this example) but the working temperature band is wider. Power fall-off and instability between regimes are also less pronounced at the lower pressure.

The sidearm wall temperatures shown in Fig. 3.1 are not truly representative of the temperatures experienced by the CuBr melt. The recorded temperatures are reliant upon the thermal conduction properties of the fused-silica, the degree of thermal coupling established between thermocouple and sidearm wall and the proximity of the thermocouple to the main body of the laser tube (*i.e.* to the discharge). Optimum $p_{Cu_3Br_3}$ has been measured in special experiments by other investigators to be 0.33 torr in 15 torr Ne corresponding to a reservoir temperature of 490 °C [69]. The somewhat low value of recorded sidearm wall temperature of ~ 360 °C at which the LT regime optimises in the present laser therefore probably corresponds to an actual CuBr melt temperature of around 490 °C.

3.4 Low Temperature (LT) Results

3.4.1 Average Output Power Versus Buffer Gas Pressure

The buffer gas pressure plays a number of roles in CBLs. For conventional CBLs with no additive gases, principal among them is to speed the fall in electron temperature, T_e, after the excitation pulse, which an increasing p_{Ne} affords due to a rising frequency of elastic electron collisions. This allows the plasma to relax quickly between pulses and thus to enable high PRFs to be attained. The Ne atoms do not greatly influence the peak T_e during the current pulse. Peak T_e is determined by the number density of free Cu atoms, n_{Cu}, and of CuBr molecules, n_{CuBr}, because the excited states of Ne are far above (> 16.7 eV) the low-lying energy levels (electron energy loss channels) of Cu and CuBr. Nevertheless, at high p_{Ne}, T_e can be expected to be reduced during the pulse as a result of inelastic electron-Ne collisions.

With the 0.66/0.33 nF capacitors connected, average output power in the LT regime was investigated as a function of buffer gas pressure over a 11.3 to 97.5 torr Ne

pressure range. The resulting plot in shown in Fig. 3.2. The LT regime clearly favours low-medium p_{Ne}. Average power rises steeply and linearly with increasing pressure to 25 torr then levels off to a peak at 30 torr. Beyond 30 torr the decrease in average power is linear but gradual. A fall in power of 32 % was recorded at the maximum pressure of 97.5 torr attempted.

Alterations to the beam and discharge at $T_s \leq$ optimum for the LT regime were observed during the pressure scanning. At low p_{Ne} the beam was yellow/green, annular and somewhat constricted (the exact degree depending on T_s). Both the fraction of yellow in and degree of constriction of the beam increased with increasing p_{Ne}. The discharge was stable over the entire pressure range from 11.3 to 97.5 torr but an increasing yellow component of sidelight spectrum together with increasing constriction echoed the changes to the beam at the higher pressures. It was also noted that higher p_{Ne} required higher partial pressures of Cu_3Br_3 for peak average power.

Pressure scanning also affected the final phase of the LT regime. At low pressures, the power stabilised or fell by a few tenths of a watt only before the HT regime was established. The beam, though constricted (4-5 mm OD), was steady and the discharge a very pale blue. With increasing p_{Ne} from ~ 30 to 55 torr the beam became increasingly yellow, constricted (3-4 mm OD), of changeable directionality and displayed an increasing component of high-divergence output. The power dropped to ever lower levels and 'standing waves' were observed in a deep blue sidelight spectrum. Beyond ~ 55 torr the output beam adopted the form of a 'rotating' yellow centre of approximately 3-4 mm OD encircled by a 'rotating' green component of high divergence. 'Standing waves' of sidelight emission grew in intensity and frequency. The power fell to 0 W and it was not possible to establish an HT regime. Note that 'twisting' of the discharge was a characteristic of even the very first Cu halide lasers [73]. It was attributed to the influence of electron attachers in the discharge.

3.4.2 Average Output Power Versus Buffer Gas Flow Rate

Flow rate influences oscillation via uniformity of the gain medium and gas cooling. The

dependence of average output power on buffer gas flow rate was studied for R_{Ne} in the range 0.3 to 13.6 litre.atm.hr^{-1}. The 0.66/0.33 nF capacitors were connected. Fig. 3.3 illustrates the result. Optimum flow rate is 2 litre.atm.hr^{-1}, but average power is still 89.5 % of its peak value at the maximum flow rate of 13.6 litre.atm.hr^{-1} considered. By contrast, P is a steep, almost linear function of flow rate with increasing R_{Ne} to the optimum rate of 2 litre.atm.hr^{-1}.

Sidearm wall temperatures at peak P were noted to be in the range 315 to 620 °C depending on R_{Ne}, implying that the requisite $p_{Cu_3Br_3}$ is also a function of flow rate. At low flow rates T_s was virtually constant but beyond ~ 3 litre.atm.hr^{-1} the required temperature rose substantially. Increasing flow rate in the LT regime produced similar changes in beam and discharge as were noted on raising the pressure and under reference conditions of p_{total}, PRF and V_{ch} it was not possible to establish an HT regime beyond ~ 2.2 litre.atm.hr^{-1}.

3.4.3 Average Output Power Versus PRF for Three Values of the Storage/Peaking Capacitors

The PRF is important in many respects. It is a factor in the specific input powers supplied to the laser and therefore contributes to gas heating. It also determines the relaxation time available between successive pulses and so controls cumulative effects such as depletion of Cu from the discharge centre caused by gas heating and cataphoresis.

Average output power was considered as a function of PRF for all three of the capacitor pairs, C_{small} (0.52/0.24 nF), C_{medium} (0.66/0.33 nF) and C_{large} (0.97/0.45 nF), employed in these investigations. For each set of capacitors, the PRF was varied in increasing multiples of approximately 2.5 kHz alternately higher then lower than its reference value of 20 kHz. T_s was adjusted for peak power at 20 kHz only. The input powers under reference conditions of p_{Ne}, R_{Ne}, PRF and V_{ch} were 0.85 kW, 1 kW and 1.23 kW for the small, medium and large capacitors respectively.

Average power versus PRF is shown in Fig. 3.4 for each of C_{small}, C_{medium} and C_{large}. The optimum PRFs are 23, 22.5 and 20 kHz for C_{small}, C_{medium} and C_{large}

respectively so that there is a tendency for PRF to decrease with increasing capacitance. The highest P is observed at 22.5 kHz with C_{medium} connected. For C_{large} only, PRFs below 10 kHz were attempted and there is a suggestion of an earlier peak in average power curve at around the 10 kHz point. This earlier peak occurs at exactly half the PRF of the main peak and might indicate the presence of acoustic resonances in the tube. Such resonances have been discovered in similar systems [74]. There is also a slight dip in the curve for C_{medium} at 20 kHz probably due to resonances blocking the release of Cu_3Br_3 from the sidearm at this PRF. If this dip were not present then the curve for C_{medium} would probably peak at ~ 21 kHz.

It was noted that at reference conditions of V_{ch} and at low PRFs the beam was annular and green at $T_s \leq$ optimum for the LT regime. As the PRF was increased, larger T_s were necessary for peak power to occur, and the fraction of yellow in and degree of constriction of the beam rose. Beyond optimum PRF the beam became low power, annular and bright yellow. In the final phase of the LT regime ($T_s >$ optimum) there was improved matching and less of a fall in average power at optimum PRF than at less than optimum PRFs.

3.4.4 Average Output Power and Efficiency Versus Charging Voltage for Three Values of the Storage/Peaking Capacitors

The charging voltage is also an important quantity. It too determines the specific input powers supplied to the laser and so contributes to gas heating. Generally, the higher the charging voltage, the higher the voltage finally applied to the discharge tube. Thus, the charging voltage also controls the peak T_e in the discharge and, together with current pulse risetime, determines the efficiency of pumping to the upper and lower laser levels.

With each set of capacitors connected in turn, the PRF was fixed in the vicinity of its optimum value (obtained from Fig. 3.4) and V_{ch} varied in increasing multiples of approximately 1 kV alternately higher then lower than 10 kV. T_s was optimised at 10 kV only. Average power versus V_{ch} is shown in Fig. 3.5 for each of C_{small}, C_{medium} and C_{large}.

The plots for C_{small} and C_{medium} clearly peak in the vicinity of 12 kV. For C_{large}, average power has still to peak at a maximum applied V_{ch} of 11 kV, but P is still rising linearly at 11 kV whereas the other capacitors already show signs that P is saturating at this charging voltage so that the peak for C_{large} is likely to occur at some V_{ch} beyond optimum for either of the other two capacitor sets.

The plots of Fig. 3.5 also reveal the maximum power, P_{max}, extractable from the 13 mm bore CuBr-Ne laser LT regime. Maximum power is 3.55 W and was observed at 22.5 kHz and 12 kV with the medium sized capacitors connected. It is not possible to tell from these plots what the exact dependence of V_{ch} on capacitance would look like because the PRF is also varied.

Analysis was performed on the charging voltage data of Fig. 3.5 so as to obtain information about the efficiency based on stored energy (BSE), η, in the LT regime of lasing. For each point plotted in Fig. 3.5, the efficiency was calculated from,

$$\eta\ (\%) = 100\left(\frac{Laser\ Pulse\ Energy}{Input\ Energy}\right) = 100\left(\frac{P/PRF}{C_s V_{ch}{}^2/2}\right), \qquad \text{----------(3.1)}$$

where P and V_{ch} have their usual meanings and C_s is the storage capacitance.

Efficiency versus charging voltage at close to optimum PRF is plotted in Fig. 3.6 for all three capacitor sets. Efficiency is seen to peak at 7 kV for the small capacitors and at 7.5 kV for the medium and large capacitors. Peak efficiencies occur at V_{ch} just above those at which lasing is first observed so that the initial rise to peak η is linear and very steep. In the vicinity of the peaks, the curves spread out as each attains a different level. The highest efficiency of 0.71 % is obtained when C_{small} is connected. The medium and large sized capacitors give peak η of around 0.56 % and 0.25 % respectively. Beyond optimum V_{ch}, the efficiency falls almost linearly with increasing charging voltage though more gradually than before. The curves appear to be converging towards a V_{ch} beyond 15 kV. Average power was observed to peak/saturate at similar V_{ch} for both C_{small} and C_{medium}. The plots of Fig. 3.6 show that the efficiencies for both are almost identical at

12 kV which explains why C_{medium} gave the greater power. From the plot for C_{medium} we find that η at that V_{ch} corresponding to P_{max}, *i.e.* 12 kV, is only 0.33 %, while P at that V_{ch} corresponding to η_{max} (for C_{medium}), *i.e.* 7.5 kV, is only 2.30 W.

3.4.5 Average Output Power and Efficiency Versus Charging Voltage at Three Values of the PRF

With the 0.66/0.33 nF capacitors connected, average output power and efficiency were investigated as a function of charging voltage at two additional PRFs, 15 and 30 kHz, to either side of the optimum PRF of 22.5 kHz. The input powers at the reference V_{ch} of 10 kV were 0.73, 1.0 and 1.56 kW at 15, 22.5 and 30 kHz respectively.

Average output power versus charging voltage is plotted in Fig. 3.7. Peak average power occurs beyond 15 kV, and at 12 kV and 7 kV for PRFs of 15, 22.5 and 30 kHz respectively so that the general trend is for optimum V_{ch} to reduce with increasing PRF. As might be expected from the earlier plots of average output power versus PRF (Fig. 3.4), the highest average power is seen at 22.5 kHz.

The efficiency η at each V_{ch} was calculated from the data of Fig. 3.7 using equation (3.1) above. Efficiency versus charging voltage is plotted in Fig. 3.8. Efficiency peaks at 8, 7.5 and 5 kV at 15, 22.5 and 30 kHz respectively. The curves show the same general trend with increasing V_{ch} as in previous examples, *i.e.* a steep rise to peak η at low V_{ch} with a more gradual and almost linear decline beyond optimum V_{ch}. There is no tendency to converge at low V_{ch} but at ~ 13 kV the curves for 15 and 22.5 kHz clearly cross. Highest efficiency is observed at 22.5 kHz.

3.4.6 Features of the Discharge Current, Laser Tube Voltage and Total, Green and Yellow Intensity Waveforms

To complete the study of the LT regime of oscillation, oscillograms of discharge current, laser tube voltage, and emission intensity were taken, together with the charging voltage waveform, $V_{ch}(t)$, under approximate conditions for P_{max} in the LT regime. The 0.66/0.33 nF capacitors were connected while p_{total}, R_{Ne}, V_{ch} and PRF were 37.5 torr,

0.8 litre.atm.hr^{-1}, 10 kV and 22.5 kHz respectively.

The discharge current, laser tube voltage and charging voltage waveforms are shown in Fig. 3.9. Oscillogram (a) shows $i_t(t)$ and $V_{ch}(t)$. The step on the leading edge of the current pulse is clearly at ~ 10 % of the peak current of ~ 215 A. Oscillogram (b) displays the $V_t(t)$ and $V_{ch}(t)$ waveforms. $V_t(t)$ reaches ~ 75 % of $V_{ch}(t)$, *i.e.* 7.5 kV. Comparing oscillograms (a) and (b) reveals a ~ 20 ns delay between first rise of $V_t(t)$ and the subsequent rise of $i_t(t)$. The delay in the current avalanche, t_{da} , relative to the onset of the current pulse, is ~ 27 ns and $V_t(t)$ has almost peaked when it begins. Likewise $V_t(t)$ is almost zero when $i_t(t)$ peaks. The total current pulse risetime, t_{ri}, is ~ 67 ns yielding a figure for the avalanche risetime, t_{ra}, of ~ 40 ns.

Fig. 3.10 shows the total intensity waveform, $I_l(t)$. Lasing begins on the leading edge of the current pulse. Although the intensity rises sharply within the first few nanoseconds, the risetime to peak intensity, t_{rl}, is still ~ 16 ns. Fall off in intensity beyond the main peak, is slightly more gradual. Peak intensity occurs well before the current pulse has peaked but at approximately the same time as peak $V_t(t)$ and smaller peaks are displayed to either side of the principal peak. The total intensity pulse duration, t_l, is ~ 49 ns. The delay in $I_l(t)$, t_{dl}, relative to the onset of the current pulse is also ~ 27 ns *i.e.* lasing commences at approximately the same time as the current avalanche.

Fig. 3.11 shows the green and yellow intensity waveforms, $I_g(t)$ and $I_y(t)$. The green and yellow pulses begin at different times. The start of the green pulse is coincident with the beginning of the total intensity pulse and its main peak occurs ~ 6 ns into the pulse. Smaller peaks occur at regular intervals of ~ 7 ns beyond the primary peak. The total duration of the green pulse, t_g, its risetime, t_{rg}, and its delay, t_{dg}, relative to the onset of the current pulse, are 41, 6 and 27 ns respectively.

The yellow pulse begins ~ 3 ns after the green pulse and its main peak occurs ~ 19 ns into the total intensity pulse. It displays smaller peaks to either side of the main peak which are again equally spaced at ~ 7 ns. Whereas the green pulse fades fairly quickly after the first 6 ns, the yellow pulse displays a more central peak. The total duration of the yellow pulse, t_y, its risetime, t_{ry}, and its delay, t_{dy}, relative to the onset of the current

pulse, are 46, 16 and 30 ns respectively. The above information relating to the discharge current, laser tube voltage and total, green and yellow intensity waveforms close to conditions for P_{max} is summarised in Table 3.1.

3.5 High Temperature (HT) Results

3.5.1 Average Output Power Versus Buffer Gas Pressure

Average output power was studied as a function of buffer gas pressure in the range 7.5 to 52.5 torr for the HT regime. The 0.66/0.33 nF capacitors were used for consistency with the LT results. The results of these measurements are shown in Fig. 3.12. In the HT regime, average power increases with increasing pressure to around 20-25 torr where the average power peaks. Beyond ~ 30 torr, average power drops sharply with increasing pressure to ~ 55 torr. At p_{Ne} higher than 55 torr, no HT mode can be established.

As in the LT regime, the beam and discharge were noted to undergo a number of alterations with increasing pressure. At $T_s \leq$ optimum for the HT regime, and at low p_{Ne} ($\leq$ 30 torr), the beam was yellow/green, annular and of approximately 3-4 mm OD at the onset of the regime. The beam was noted to lose some of its constriction, widening to approximately 5 mm OD, on approach to peak (optimum T_s). There was a good balance of green and yellow in the beam and the discharge was stable. With increasing pressure from around 30 to 52.5 torr output power dropped, the beam became increasingly yellow and constricted (3-4 mm OD), the discharge turned deep blue and 'standing waves' appeared in the sidelight spectrum. At 52.5 torr the beam exhibited a yellow centre surrounded by a green component of high-divergence output, 10-15 mm in OD, which lacked directionality even at peak power.

In the final phase of the HT regime, the discharge was a deep turquoise and the number, intensity and speed of 'standing waves' of sidelight emission, and their associated flicker, increased with increasing p_{Ne}. The beam was green and constricted (2 mm OD at low p_{Ne}, becoming yellowed at medium p_{Ne} and developing a very wide annulus of high-divergence at the highest pressures considered. At 52.5 torr, there was a great deal of turbulence in the active region as evinced by light scattering from dust

particles at the windows (especially at the cathode window) and a wildly 'rotating' beam output with a large component of high-divergence output. T_s swings of up to 100 °C were observed caused by discharge penetration of the sidearm volume and forcing dramatic swings in output powers. The discharge occasionally reached the windows.

3.5.2 Average Output Power Versus Buffer Gas Flow Rate

Average output power versus buffer gas flow rate is plotted in Fig. 3.13 for the range 0.3 to 2.5 litre.atm.hr^{-1}. The 0.66/0.33 nF capacitors were again connected. In the HT regime, power rises quite steeply at low flow rates, peaking at ~ 1 litre.atm.hr^{-1}. Beyond this power drops sharply with increasing flow rate from 1 to ~ 2.2 litre.atm.hr^{-1}. At R_{Ne} above 2.2 litre.atm.hr^{-1} it is not possible to establish an HT regime. The highest power of 3.2 W was much lower than the maximum average power of 4.73 W observed during the pressure run. This is because the flow rate scanning was performed at 37.5 torr for consistency with the LT regime experiments. At this pressure, we see from Fig. 3.12 that the average power is already well into its decline.

Similar changes to the characteristics of beam and discharge were found on increasing the flow rate at low pressure as when increasing the pressure at low R_{Ne}. Greatest stability was achieved at around 1 litre.atm.hr^{1}. From 1 to 2.2 litre.atm.hr^{1} the usual signs of turbulence set in at all T_s. Reducing R_{Ne} when p_{Ne} was high and vice versa helped to stabilise the HT regime.

3.5.3 Average Output Power Versus PRF

Average power is plotted as a function of PRF in Fig. 3.14 for the 0.66/0.33 nF capacitors. PRFs in the range 10-30 kHz were considered. R_{Ne} and V_{ch} were reference at 0.8 litre.atm.hr^{-1} and 10 kV respectively, but because (unlike the LT regime) output powers deteriorate significantly at the reference total gas pressure of 37.5 torr, a p_{total} of 19 torr was chosen in order to obtain a more realistic portrayal of P. Fig. 3.14 shows that the HT dependence on PRF is of a near parabolic nature with the peak average power occurring at 20 kHz. Peak power is now seen to be comparable to that obtained from the

HT regime during the average power versus pressure run.

The usual signs of instability were noted as PRF was increased beyond optimum. Higher T_s were necessary for peak power and the regime endured over narrower temperature bands. The beam became increasingly yellow with rising PRF at low p_{Ne} and reference R_{Ne} and V_{ch}.

3.5.4 Average Output Power and Efficiency Versus Charging Voltage

Average output power versus charging voltage was also investigated at the optimum PRF of 20 kHz (obtained from Fig. 3.14) and the resulting dependence is shown in Fig. 3.15. p_{total} was again 19 torr so that a true figure for the maximum average output power, P_{max}, of which this regime was capable, could be obtained. Fig. 3.15 shows a steep and almost linear rise in P with increasing charging voltage at low V_{ch}. In the HT regime a P_{max} of 5.7 W occurs at a charging voltage of 13.5 kV which demonstrates the efficacy of this regime under optimal conditions.

From the data of Fig. 3.15, efficiency has been calculated for each charging voltage considered. Efficiency versus V_{ch} is plotted in Fig. 3.16. The maximum efficiency, η_{max}, is 0.64 % at 10 kV under the conditions studied. At 13.5 kV, at which the average output power peaks, η is only 0.46 %. The curve demonstrates the same steep, linear rise to peak efficiency, characteristic of all of these curves, followed by a linear, more gradual fall off in efficiency beyond optimum V_{ch}.

3.5.5 Features of the Discharge Current, Laser Tube voltage and Total, Green and Yellow Intensity Waveforms

To complete the study the HT regime of oscillation, oscillograms of discharge current, laser tube voltage, and emission intensity were taken, together with the charging voltage waveform, $V_{ch}(t)$, under approximate conditions for P_{max}. The medium sized capacitors were used and p_{total}, R_{Ne}, V_{ch} and PRF were 19 torr, 0.8 litre.atm.hr^{-1}, 10 kV and 22.5 kHz respectively. The oscillograms were taken at a $p_{Cu_3Br_3}$ at which the power and current were just beginning to rise because of difficulty in keeping T_s and output power

stable at maximum. One oscillogram of the current pulse at peak power was obtained and is shown in Fig. 3.17.

The discharge current, laser tube voltage and charging voltage waveforms, $i_t(t)$, $V_t(t)$ and $V_{ch}(t)$, at the reduced power are shown in Fig. 3.18. Oscillogram (a) shows $i_t(t)$ and $V_{ch}(t)$. The step on the leading edge of the current pulse has clearly collapsed in the HT regime. Fig. 3.18 (b) displays the $V_t(t)$ and $V_{ch}(t)$ waveforms. These show that even at very low powers $V_t(t)$ almost equals $V_{ch}(t)$ in amplitude at ~ 9.5 kV. The true value at peak power can reach 12 kV. Comparing oscillograms (a) and (b) reveals a 50 ns delay between the first rise of $V_t(t)$ and the subsequent rise of $i_t(t)$. As the step on the current pulse has collapsed, the pulse is in avalanche from the outset and the delay in the avalanche, t_{da} , relative to the onset of the current pulse is 0 ns. $V_t(t)$ has again almost peaked when the avalanche begins and is almost zero when $i_t(t)$ is maximum at ~ 215 A. The total current pulse risetime, t_{ri}, and thus the avalanche risetime, t_{ra}, are both in the region of 40 ns. As shown in Fig. 3.17, at peak power the discharge current climbed to 260 A.

Fig. 3.19 shows the total intensity waveform, $I_l(t)$, and its ground level. Lasing occurs only on the leading edge of the current pulse and commences simultaneously with the avalanche. The total intensity pulse exhibits several smaller peaks, to either side of its primary peak. The intensity rises sharply initially, arriving at its main peak with a risetime, t_{rl}, of ~ 13 ns. Peak intensity again occurs before the current pulse has peaked, but almost coincides with the peak of $V_t(t)$. Fall off in intensity beyond the main peak is more gradual. The total intensity pulse duration, t_l, is ~ 46 ns. The delay in $I_l(t)$, t_{dl}, relative to the onset of the current pulse, is of course 0 ns, *i.e.* lasing commences at the same time as the current avalanche.

Fig. 3.20 shows the green and yellow intensity waveforms, $I_g(t)$ and $I_y(t)$, together with their ground lines. The figure shows that the green transition has recovered at the onset of the HT regime. General observations have revealed that the beam has a higher green:yellow intensity ratio at peak power so that we might expect the green intensity to increase further before falling again as optimum T_s is exceeded.

The green transition again commences coincidently with the beginning of the total intensity pulse. There is a large initial peak ~ 3 ns into the total intensity pulse, followed by smaller peaks, all of considerable amplitude, at regular intervals of ~ 7 ns. The total duration of the green pulse, t_g, its risetime, t_{rg}, and its delay, t_{dg}, relative to the onset of the current pulse, are 40, 3 and 0 ns respectively. The yellow pulse begins within 1 ns of both the total and green intensity pulses. Its main peak occurs ~ 11-12 ns into the total intensity pulse. Minor peaks are again observed at ~ 7 ns intervals. The total duration of the yellow pulse, t_y, its risetime, t_{ry}, and its delay, t_{dy}, relative to the onset of the current pulse, are 45, 11 and < 1 ns respectively. The above information relating to the discharge current, laser tube voltage and total, green and yellow intensity waveforms at close to optimum conditions for P_{max} is summarised in Table 3.2.

3.6 Discussion

3.6.1 LT Regime

It is appropriate to comment on the general observations first. The beam in the CuBr-Ne laser working (LT) regime is annular at all times. With increasing T_s on approach to peak power, the annulus becomes more intense and covers a greater percentage of the beam cross-section, but the cross-section itself is smaller because of discharge constriction. When T_s is raised beyond a critical value, the beam power reduces and the constriction continues to worsen. There is also an increase in the ratio of yellow to green in the beam with increasing T_s throughout.

These observations can be explained in large part in terms of the effects of increased Cu_3Br_3 concentrations on the discharge. The beam is annular at all times due to depletion of atomic Cu from the centre of the discharge by gas heating and radial cataphoresis in the presence of strong discharge constriction. In the case of gas heating, the ideal gas laws show that number densities of all species (Cu, Ne, CuBr etc.) must be greater near the wall by a factor of ~ 2 (axial gas temperature, T_g, is ~ 2000 °C, wall T_g is ~ 500 °C). Cataphoresis is pronounced because the process of recombination of Cu^+ and electrons is slow in the absence of HBr and the lifetimes of Cu^+ ions are relatively

long. Cataphoretic depletion affects primarily Cu atoms as they are the major positive ion species.

As n_{Cu} is highest near the wall, this section of the discharge goes into gain first when Cu_3Br_3 is first added, hence the annular beam intensity pattern. The beam constricts further as $p_{Cu_3Br_3}$ is increased and peak power is approached because the free Br density, n_{Br}, increases. Constriction of the beam is primarily caused by electron attachment to free bromine atoms. When a current passes through the tube electrons are created mainly on axis and can either recombine (with say Cu^+) or attach to Br. In the case of Br^- formation, they do not shift far from their place of origin and when the next pulse passes through the tube it proceeds where the charge carriers are located: the centre again. Over successive pulses the discharge concentrates in the centre, leading to constriction, greater gas heating and a lower impedance on axis. This in turn leads to further constriction and so on.

At low T_s, the number density of Cu_3Br_3 molecules, $n_{Cu_3Br_3}$, is also low so that n_{Br} is too small to cause significant electron attachment. The free electrons have longer lifetimes and path lengths and are free to spread out so that successive pulses are not constricted to the centre of the discharge. The discharge does not contract or become unstable and the output beam annulus is full bore size at most Ne pressures. The annulus is thin and not very intense because n_{Cu} is also low. As n_{Br} increases further, the constrictive effects also increase so that there is eventually no lasing adjacent to the wall. The annulus is thicker and more intense because of the larger n_{Cu} which a larger n_{Br} implies.

The output power eventually turns over at a critical $p_{Cu_3Br_3}$ because inelastic collisions between free electrons and Cu_3Br_3 molecules (and their discharge dissociation products *e.g.* Cu and CuBr) alter the electron energy distribution function (EEDF) more and more and reduce the peak T_e below the range for efficient inversion creation. The Cu_xBr_x molecules and Cu atoms have many low lying energy states so that inelastic collisions with Cu_xBr_x and Cu deplete the electrons of some of their energy and the average energy or electron temperature, T_e, falls below ~ 2 eV at which pumping of the

lower level metastable states becomes more efficient and pumping of the upper laser levels is less efficient. The inversion is reduced and lower powers are generated until, at the highest $p_{Cu_3Br_3}$, oscillation cannot be sustained. Constriction and instability (due to electron capture by Br atoms) continue to increase. The increasing intensity of the yellow transition relative to the green is also a function of peak T_e, for as this is reduced, the pumping of the lower energy yellow transition upper level becomes the more efficient relative to pumping of the green. Discharge constriction, instability and intensity of yellow are all amplified at higher p_{Ne}, R_{Ne}, PRFs and V_{ch} because, as we have seen, greater $p_{Cu_3Br_3}$ is involved.

The pressure of $p_{Cu_3Br_3}$ that can be tolerated increases with increasing p_{Ne} because the impedance (breakdown voltage) of the tube increases. Cataphoretic depletion of Cu gets worse at higher p_{Ne} because the back diffusion of Cu atoms to the axis becomes slower. Higher levels of Cu_3Br_3 are necessary at the higher p_{Ne} to maintain the ground state n_{Cu} at its original level. This causes the fall in peak T_e to insufficient levels for lasing to occur at higher $p_{Cu_3Br_3}$. The required $p_{Cu_3Br_3}$ also increases with increasing R_{Ne} (especially at the higher rates of flow) 1) in order to sustain n_{CuBr} in the discharge and 2) because increased gas cooling can condense quantities of the Cu_3Br_3 vapour out of the discharge and on to the (cooler) discharge tube wall or endflanges.

At higher PRFs, the relaxation periods are shorter and gas heating increases due to the delivery of increased input powers to the discharge. Cataphoretic depletion may also be enhanced if the time available between pulses for recombination of Cu^+ is reduced. The cumulative effect of these is a pronounced depletion of n_{Cu} in the centre of the tube so that higher $p_{Cu_3Br_3}$ is necessary to redress the balance at high PRFs also.

Higher V_{ch} also generate increased input powers and deplete n_{Cu} in the centre of the tube by gas heating. As a major factor controlling the electron energy, it may also cause increased ionization of liberated Cu atoms, encouraging greater cataphoresis and inefficient pumping of the upper laser levels if too high. In either case the net effect should be an increase in the $p_{Cu_3Br_3}$ requirements in order to sustain the ground state n_{Cu}. The fact that the beam was very yellow at and beyond optimum V_{ch} supports this

conclusion, as the green:yellow intensity ratio falls as peak T_e falls *i.e.* increased numbers of elastic collisions between electrons and Cu/Cu_xBr_x are taking place.

The occurrence of a lumpy, non-crystalline, dendritic deposit around the aperture in the ceramic located above the sidearm opening supports the fact that the copper bromide exists mainly in the polymeric form Cu_3Br_3 near the wall at least. Loonam suggested that thermal deposition of copper from monomeric CuI is unlikely to occur, given that the entropies for the reaction are similar on either side of the equation [75]. He further suggested that if deposition does occur then one may take this to be evidence of the presence of the trimeric molecule Cu_3I_3 as the thermal deposition of Cu_3I_3 permits a considerable increase in entropy [75]. The same reasoning can be applied to CuBr.

Finally, it was noted that with increasing T_s to optimum levels for the LT regime there was little change in circuit-laser impedance matching whereas in the final phase the fall in power was accompanied by a distinct increase in laser impedance. Failure of the LT regime clearly features increased bromine concentrations (sidelight spectrum is blue and discharge/beam instabilities are occurring which are normally associated with an increasing $n_{Cu_3Br_3}$).

Moving on to the actual characterization of the LT regime, average power is found to peak at 25-30 torr, to fall off sharply with decreasing pressure below 25 torr and to decrease gradually with increasing pressure beyond 30 torr. This dependence of average power on buffer gas pressure may be accounted for thus. Optimum p_{Ne} is a balance between a sufficient number density for high elastic electron collision rates (plasma recovery between pulses) and not so high a density that peak T_e is reduced to below that required for efficient upper level pumping. In the CuBr-Ne laser LT regime, the optimum Ne pressure is rather low, indicating that it is more difficult to maintain peak T_e than in the Cu hybrid laser, for example (Chapter 5, Fig. 5.4).

The peak in the flow rate curve occurs at ~ 2 litre.atm.hr^{-1}. The rise to peak power is steep, but although there is a gradual fall in power beyond the peak, the response is relatively flat up to the maximum R_{Ne} considered. At low flow rates the longitudinal distribution of n_{CuBr} and n_{Cu} are poorer. As R_{Ne} is raised, the distributions become

more uniform, but Cu_3Br_3 needs to be supplied at a higher rate from the sidearm. Thus T_s must be increased concurrently with R_{Ne}. Beyond a critical flow rate increased gas cooling and turbulence means that lasing remains strong, the turbulence promoting a more uniform distribution of liberated Cu, but the vapour pressure of Cu_3Br_3 becomes more difficult to control so that there is some fall in power. At the highest flow rates, gas cooling begins to cause condensation of Cu_3Br_3 out of the discharge and onto the ceramic and sidearm opening, and loss of the lasant Cu atoms.

Initially with increasing PRF, output pulse energy falls only slightly so average output power rises. At higher PRFs, gas heating and cataphoresis increase. As gas temperature rises, powers reduce because of increasing Cu depletion. At the same time, the interpulse relaxation times become shorter so the diffusion of Cu atoms back to the tube axis to counter cataphoresis becomes less effective. The above discussion also applies to a rising V_{ch} (higher gas heating and increased Cu ionization/cataphoresis). In the case of PRF increase there is the additional factor of cumulative depletion of Cu which increases with increasing PRF as relaxation times diminish. As PRF and V_{ch} increases ultimately produce similar effects, we would expect to find an inverse relationship between their optimum values for lasing. This is indeed the case. An increase in one variable makes an increase in the other less tolerable.

An increase in the free electron density remaining at the end of each interpulse period means that the gas can also withstand lower voltages before it breaks down. Although the dependence of charging voltage on capacitance was not obtained, optimum voltage is expected to decrease with increasing capacitance. As a larger capacitance gives increased input energy for the same charging voltage, the voltage must be reduced if the PRF is fixed to prevent gas overheating. This was reflected in a tendency for optimum PRF to decrease with increasing capacitance. At greater capacitance, larger input energies were supplied to the discharge for the same V_{ch} so that cumulative gas heating and cataphoresis effects worsened and PRFs had to be lowered to enable sufficient relaxation times between pulses for n_{Cu} to recover.

The dependences of average output power on V_{ch} have revealed the maximum

power of which the device is capable to be 3.55 W at 22.5 kHz and 12 kV in the LT regime with the medium sized capacitors connected. The maximum specific average output power is therefore 82 $mW.cm^{-3}$ (for a 43.5 cm^3 active volume). In addition, the specific average input powers at P_{max} and at η_{max} (for C_{medium}) have been calculated, using the formula

$$Specific\ P_{in} = \frac{C_s V_{ch}^2 PRF}{2\pi(D/2)^2 L}, \qquad \text{----------(3.2)}$$

where P_{in} is the input power to the laser tube and $\pi(D/2)^2 L$ is the active volume of the laser tube. These are listed alongside other information pertaining to P_{max} and η_{max} in Table 3.3. We see that P_{max} exceeds P at η_{max} by a factor of 1.54 while η_{max} exceeds η at P_{max} by a factor of 1.7.

At very low V_{ch} the electron energies were too low (*i.e.* low peak T_e) to enable efficient pumping of the upper laser levels and the frequency of metastable lower level pumping increased. The efficiency for lasing peaked at slightly higher V_{ch} at which the electron temperature was high enough so as not to cause significant population of metastable states but low enough so as not to cause too much ionization of Cu either. Most energy therefore went into pumping of the upper laser levels and efficiency was high. The highest efficiency of 0.71 % was obtained with the small capacitors connected at the relatively low V_{ch} of 7 kV. Beyond optimum charging voltage the efficiency dropped linearly with increasing V_{ch} because of increasing ionization relative to excitation although an increase in the numbers of both relative to pumping of the metastable states ensures that the power still rises. The power peaked only when the rate of ionization exceeded that of excitation. Hence the observation that efficiency and power peaked at low and high V_{ch} respectively. Excepting electrical information relating to P_{max} and η_{max} which is listed in Table 3.3, the additional trends in performance revealed by the quantitative characterisation of the LT regime are summarised in Table 3.4.

The behaviour of the current pulse is also worth remarking on. The step moving

down the leading edge with increasing $p_{Cu_3Br_3}$ is indicative of an increasing removal of prepulse free electrons, most probably due to attachment to Br atoms. The end of the step signifies the beginning of electron avalanche and 'breakdown' of the discharge tube. The maximum power was reached when the step was 10-20 % of the peak current. This shows that some residual free electron density, n_e, is desirable for a uniform discharge to be established in the tube. Attachment probably accounts for the increasing discharge impedance during fall off in the LT regime as $p_{Cu_3Br_3}$ was raised, as bromine entrapment of electrons increased.

Lasing always occurred on the leading edge of the current pulse and commenced simultaneously with the avalanche, *i.e.* at the end of the current step. During the current step, the voltage can increase without breakdown of the tube, presumably due to attachment processes which counter any initial increase in electron density. However, as T_e increases, attachment to Br (by dissociative attachment) becomes less likely, and finally the avalanche begins. At avalanche, the voltage pulse had almost peaked and T_e was optimum for efficient excitation of the upper laser levels. Hence, lasing began almost immediately at onset of the avalanche. The small peaks in the laser intensity pulses are all spaced at ~ 7 ns. These correspond to round-trips of photons in the cavity. In 7 ns light travels ~ 2.1 m. The length of the optical cavity was 1.05 m in these experiments.

The yellow pulse lasts longer than the green because the faster excitation of the green pulse initially (higher gain) causes its lower level to become overpopulated first. There is a delay of a few nanoseconds before the yellow pulse begins because the green goes into gain first.

3.6.2 HT Regime

The sudden rise in power as the HT regime was entered is thought to result from a release of sufficient concentrations of hydrogen (atomic or molecular) from the sidearm reservoir to enable the effect to occur. Certainly, the discharge impedance increased throughout, a point noted by Astadjov et al. [70] in their studies of CBLs with H_2 additives. Although the beam was further constricted and very yellow after its fall in power during the final

phase of the LT regime, it became slightly less annular and constricted near peak power in the HT regime, effects which have again been observed with hydrogen addition. Laser output powers were also much higher as one might expect if this was the case. One further indication of a "hydrogen effect" was a better balance of green and yellow in the beam at peak which has also been noted in previous investigations of CBLs. Assuming H_2 addition, the reasons for these phenomena are considered fully in Chapter 4 where the results of the CuBr-Ne-H_2 laser are discussed.

The tendency for the beam to become more yellow and constricted with increasing p_{Ne}, R_{Ne}, PRF and V_{ch} is enhanced in the HT regime. Not only is the optimum $p_{Cu_3Br_3}$ greater than in the LT regime, but it again increases with increase in each of p_{Ne}, R_{Ne}, PRF and V_{ch}. Therefore the effects are again caused by increased electron capture by atoms of bromine (constriction) and by a reduction in T_e by an increase in the inelastic collision rate of electrons with Cu_xBr_x and Cu (a lower peak T_e implies a smaller green:yellow intensity ratio). The temperature band over which the regime operated was much narrower but showed the same tendency to increase in the vicinity of optimum p_{Ne}. The HT regime was much less stable that the LT regime, presumably also due to the larger $p_{Cu_3Br_3}$ and the sporadic nature of the release of the H_2-bearing impurities.

Dendritic deposits were observed which differed from those created when operating solely in the LT regime. These grew in the same position as before (around the aperture in the ceramic) but were more numerous and grew into the discharge showing a more crystalline structure with rounded edges where the dendrite had melted on too close approach to the discharge. These dendrite characteristics are common in CBLs with H_2 additive and in Cu hybrid lasers, so are again indicative of the presence of hydrogen.

Power increased with increasing p_{Ne} to around 15 torr, peaked in the region of 15-30 torr, then dropped sharply with increasing pressure to around 55 torr beyond which average power fell to zero. There is an indication here that the optimum pressure is again low, but power collapses at higher p_{Ne} where the levels of $p_{Cu_3Br_3}$ are too great to sustain the discharge. At pressures close to collapse of the regime, *e.g.* 50 torr, the beam was often composed of a highly focused, narrow diameter, inner beam enclosed within a

thicker, swirling annulus caused by refractive index effects in the twisting discharge. The gas acts like a lens due to the radial variation in number density. The lens effect is stronger in the HT regime where the elevated bromine concentration causes greater constriction.

The peak in the flow rate curve occurred at the low flow rate of ~ 1 litre.atm.hr^{-1}. The rise to and fall from peak power are equally steep. No HT regime could be established beyond ~ 2.2 litre.atm.hr^{-1}. At the reference pressure at which the flow rate curve was obtained, the powers were already low, according to the pressure dependence of Fig. 3.12, because of increased $p_{Cu_3Br_3}$. The further increase necessary at the higher flow rates together with extra turbulence induced by the gas flow itself accounts for the sudden turn over in response in the flow rate dependence. It may also be that the power was limited by slow release times of the H_2-bearing impurities from the sidearm. Reducing the flow rate when the pressure was high and vice versa helped to stabilise the HT regime which supports these arguments.

The charging voltage run revealed the HT regime to be capable of producing 5.7 W at 13.5 kV with the 0.66/0.33 nF capacitors connected. The efficiency peaked at low charging voltages and was much reduced at that charging voltage where maximum power was observed. Peak efficiency was 0.64 % at 10 kV. The maximum specific average output power is therefore 131 mW.cm^{-3} (for a 43.5 cm^3 active volume). In addition, the specific average input powers at P_{max} and at η_{max} (for C_{medium}) have been calculated, using equation (3.2). These are listed alongside other information pertaining to P_{max} and η_{max} in Fig. 3.5. We see that P_{max} exceeds P at η_{max} by a factor of 1.4 while η_{max} exceeds η at P_{max} by a factor of 1.4 also. Excepting electrical information relating to P_{max} and η_{max} which is listed in Table 3.5, the additional trends in performance revealed by the quantitative characterisation of the HT regime are summarised in Table 3.6.

There were further changes in the current with increasing T_s. The HT regime corresponded with the total collapse of the prepulse current step. Only after the step disappeared did the power and discharge current recover and the HT regime was entered. The current was again noted to follow the trends in power (*i.e.* peak current at peak output

power etc.). This dependence of current suggests that in order for the HT regime to occur, there must be 'no' free electrons at the beginning of each excitation pulse. During its final phase, the laser power fall was accompanied by turbulence and 'standing waves' of sidelight intensity which became stronger and more frequent in the discharge with increasing T_s. The beam was intensely yellow (*i.e.* low peak T_e) and narrow (OD 2-3 mm) (*i.e.* strong discharge constriction) but showed little or no annularity, *i.e.* the output beam was peaked towards the axis. A wall discharge occurred almost immediately on cessation of lasing in this regime indicating very high Cu_3Br_3 levels.

3.7 Conclusion

A maximum average output power of 3.55 W was extracted from a CuBr-Ne laser tube of 43.5 cm^3 active volume and 13 mm bore. This corresponds to a specific average power of 82 $mW.cm^{-3}$. Average power is shown to peak at buffer gas pressures in the region of 30 torr. The system is further shown to favour the higher buffer gas flow rates, peaking at around 2 $litre.atm.hr^{-1}$. Optimum PRF is within the range 20 to 24 kHz for the combinations of storage and peaking capacitors tried.

The peak power of 3.55 W was observed at 22.5 kHz and 12 kV with the 0.66/0.33 nF capacitors connected. This corresponds to an efficiency (BSE) of 0.33 %. At 7.5 kV, the average power was 2.30 W and the efficiency reached 0.56 %. The highest efficiency of 0.71 % was obtained at 22.5 kHz and 7 kV with the 0.52/0.24 nF capacitors connected.

Whilst establishing the characteristics described above, a second regime of operation was discovered at higher sidearm temperatures. Average powers were higher over smaller spans of buffer gas pressure and flow rate but less stable and the regime existed over a much narrower range of sidearm temperatures. The regime is believed to result from the release of hydrogen-containing impurities (probably H_2O) from the CuBr in the sidearm at elevated temperatures. A similar phenomenon has been reported [31] but not explained by other investigators. The characteristics of CBLs with purposefully added H_2 are discussed in the next chapter.

Quantity	CuBr-Ne Laser LT Regime
V_{ch} (kV)	10
$V_{t\,pk}$ (kV)	7.5
$i_{t\,pk}$ (A)	215
t_{ri} (ns)	67
t_{ra} (ns)	40
t_{da} (ns)	27
t_l (ns)	49
t_{rl} (ns)	16
t_{dl} (ns)	27
t_g (ns)	41
t_{rg} (ns)	6
t_{dg} (ns)	27
t_y (ns)	46
t_{ry} (ns)	16
t_{dy} (ns)	30

Table 3.1
Characteristics of $V_{ch}(t)$, $V_t(t)$, $i_t(t)$, $I_l(t)$, $I_g(t)$ and $I_y(t)$ at close to optimum conditions for P_{max} in the 13 mm bore CuBr-Ne laser LT regime.

(p_{total}, R_{Ne} and V_{ch} reference at 37.5 torr, 0.8 litre.atm.hr^{-1} and 10 kV respectively. PRF close to optimum at 22.5 kHz. C_s/C_p 0.66/0.33 nF.)

Quantity	CuBr-Ne Laser HT Regime
V_{ch} (kV)	10
$V_{t\,pk}$ (kV)	9.5 (~ 12 kV at peak)
$i_{t\,pk}$ (A)	215 (260 A at peak)
t_{ri} (ns)	40
t_{ra} (ns)	40
t_{da} (ns)	0
t_l (ns)	46
t_{rl} (ns)	13
t_{dl} (ns)	0
t_g (ns)	40
t_{rg} (ns)	3
t_{dg} (ns)	0
t_y (ns)	45
t_{ry} (ns)	11
t_{dy} (ns)	< 1

Table 3.2

Characteristics of $V_{ch}(t)$, $V_t(t)$, $i_t(t)$, $I_l(t)$, $I_g(t)$ and $I_y(t)$ as power begins to rise towards P_{max} in the 13 mm bore CuBr-Ne laser HT regime.

(R_{Ne} and V_{ch} reference at 0.8 litre.atm.hr^{-1} and 10 kV respectively. p_{total} and PRF close to optimum at 19 torr and 22.5 kHz respectively. C_s/C_p 0.66/0.33 nF.)

Quantity	CuBr-Ne Laser LT Regime
Tube bore (mm)	13
Tube length (cm)	32.8
Active volume (cm^3)	43.5
P_{max} **(W)**	3.55
Maximum specific P **($mW.cm^{-3}$)**	82
η **at** P_{max} **(%)**	0.33
C_s/C_p **for** P_{max} **(nF)**	0.66/0.33
PRF for P_{max} **(kHz)**	22.5
V_{ch} **for** P_{max} **(kV)**	12
Specific P_{in} **at** P_{max} **($W.cm^{-3}$)**	24.6
η_{max} **with** C_{medium} **(%)**	0.56
P **at** η_{max} **(W)**	2.30
V_{ch} **at** η_{max} **(kV)**	7.5
Specific P_{in} **at** η_{max} **($W.cm^{-3}$)**	9.6

Table 3.3

P_{max}, η_{max}, electrical excitation and related quantities for the 13 mm bore CuBr-Ne laser LT regime.

(p_{total} and R_{Ne} reference at 37.5 torr and 0.8 litre.atm.hr^{-1} respectively.)

P	Peaks at a single $p_{Cu_3Br_3}$ (~ 0.33 torr in 15 torr Ne)
	Peaks at a single p_{Ne} (30 torr for reference R_{Ne}, PRF and V_{ch} and for C_{medium})
	Peaks at a single R_{Ne} (2 litre.atm.hr^{-1} for reference p_{total}, PRF and V_{ch} and for C_{medium})
	Peaks at high V_{ch}
$p_{Cu_3Br_3}$ **for Peak *P***	Increases with increasing p_{Ne}, R_{Ne}, PRF and V_{ch}
PRF for Peak *P*	Decreases with increasing C_s/C_p
V_{ch} **for Peak *P***	Decreases with increasing PRF
η	Maximum at C_{small}
	Maximum at 22.5 kHz
	Maximum at 7 kV
	Peaks at low V_{ch}
V_{ch} **for Peak** η	Decreases with increasing PRF

Table 3.4
Additional characteristics of the 13 mm bore CuBr-Ne laser LT regime.

Quantity	CuBr-Ne Laser HT Regime
Tube bore (mm)	13
Tube length (cm)	32.8
Active volume (cm^3)	43.5
P_{max} **(W)**	5.7
Maximum specific P **($mW.cm^{-3}$)**	131
η **at** P_{max} **(%)**	0.46
C_s/C_p **for** P_{max} **(nF)**	0.66/0.33 (unoptimised)
PRF for P_{max} **(kHz)**	20
V_{ch} **for** P_{max} **(kV)**	13.5
Specific P_{in} **at** P_{max} **($W.cm^{-3}$)**	27.7
η_{max} **with** C_{medium} **(%)**	0.64
P **at** η_{max} **(W)**	4.1
V_{ch} **at** η_{max} **(kV)**	10
Specific P_{in} **at** η_{max} **($W.cm^{-3}$)**	15.2

Table 3.5

P_{max}, η_{max}, electrical excitation and related quantities for the 13 mm bore CuBr-Ne laser HT regime.

(p_{total} close to optimum at 19 torr. R_{Ne} reference at 0.8 litre.atm.hr^{-1}.)

P	Peaks at a single $p_{Cu_3Br_3}$ (>> 0.33 torr in 15 torr Ne)
	Peaks at a single p_{Ne} (~ 20-25 torr for reference R_{Ne}, PRF and V_{ch} and for C_{medium}. No HT regime beyond ~ 55 torr under these conditions.)
	Peaks at a single R_{Ne} (~ 1 litre.atm.hr^{-1} for reference p_{total}, PRF and V_{ch} and for C_{medium}. No HT regime beyond ~ 2.2 litre.atm.hr^{-1} under these conditions.)
	Peaks at high V_{ch}
$p_{Cu_3Br_3}$ **for Peak** P	Increases with increasing p_{Ne}, R_{Ne}, PRF and V_{ch}
η	Peaks at low V_{ch}

Table 3.6
Additional characteristics of the 13 mm bore CuBr-Ne laser HT regime.

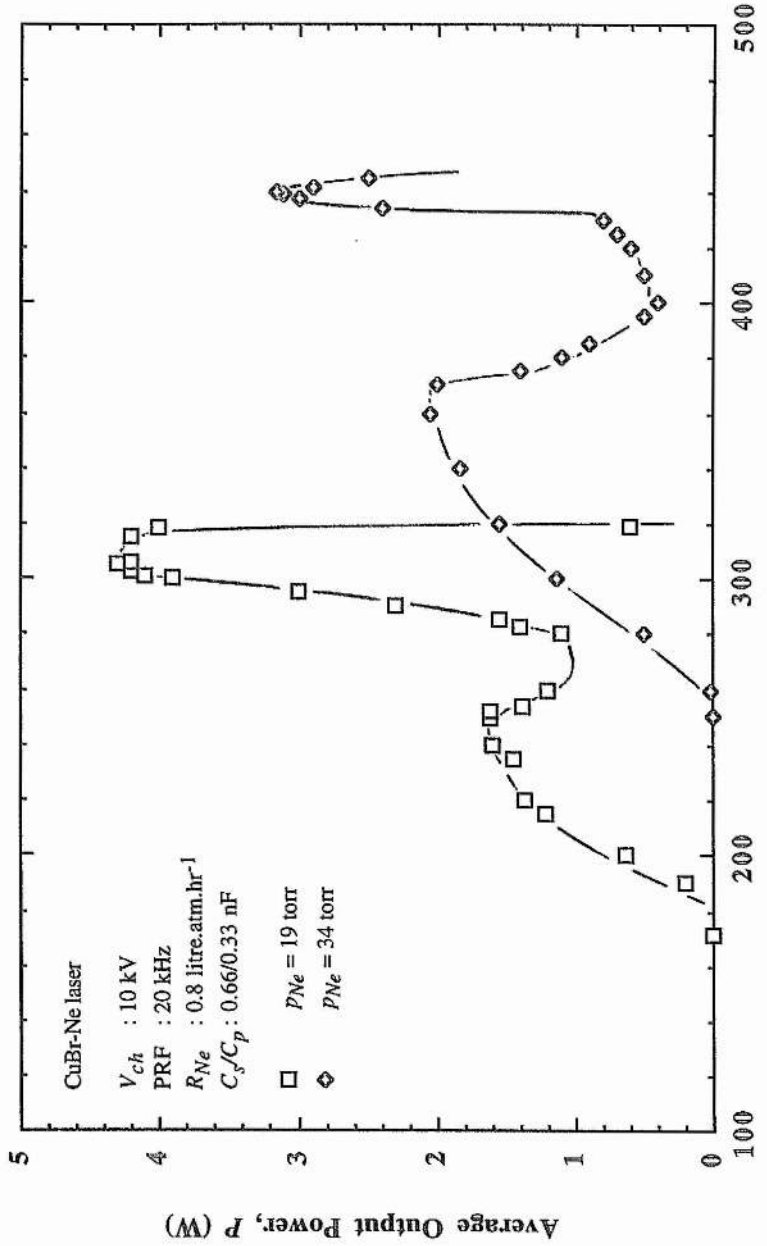

Fig. 3.1
Average output power, P, versus sidearm wall temperature, T_s, in the CuBr-Ne laser at two values of the buffer gas pressure, p_{Ne}.

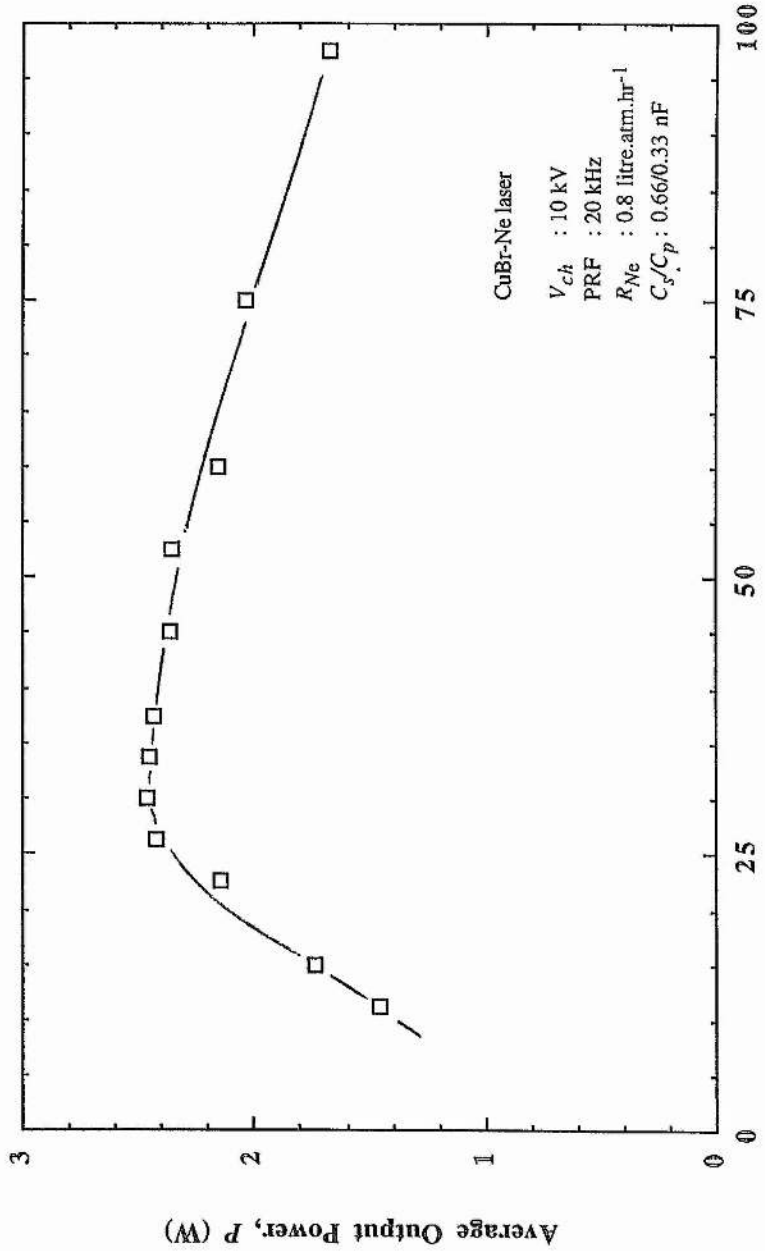

Fig. 3.2
Average output power, P, versus buffer gas pressure, p_{Ne}, in the CuBr-Ne laser LT regime.

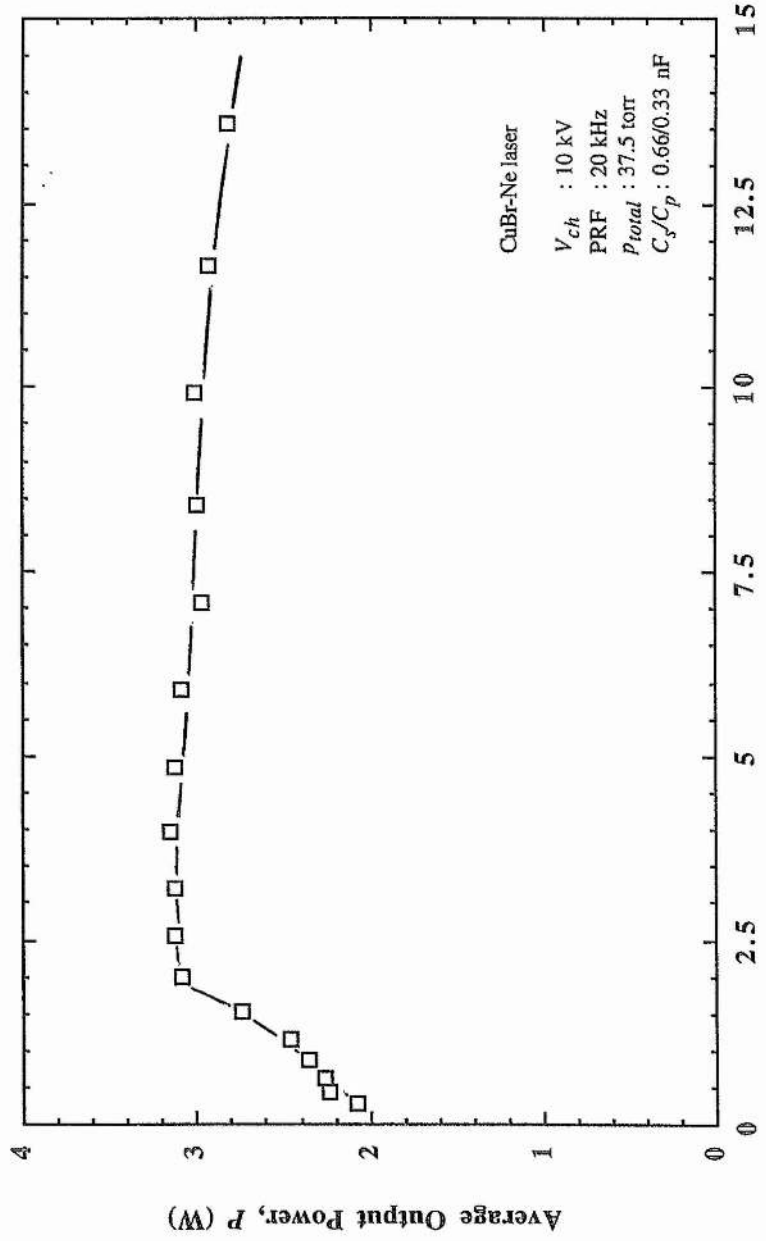

Fig. 3.3
Average output power, P, versus buffer gas flow rate, R_{Ne}, in the CuBr-Ne laser LT regime.

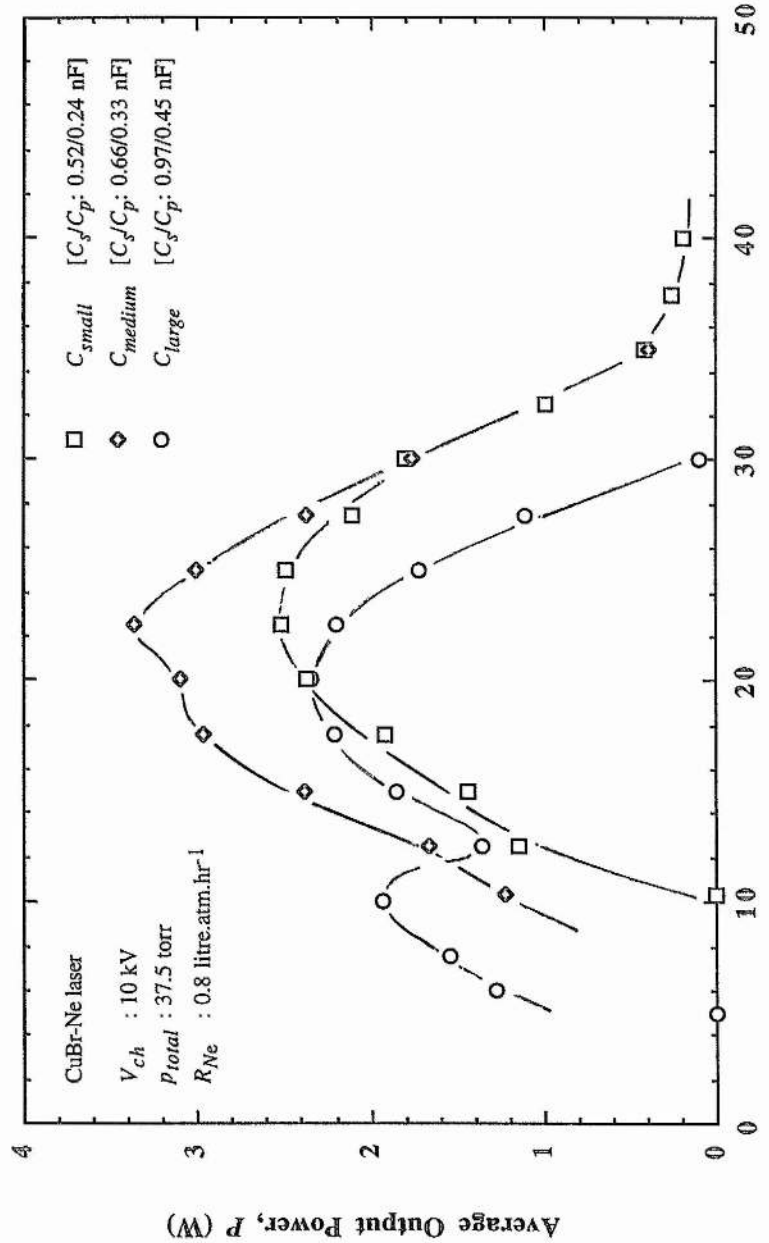

Fig. 3.4
Average output power, P, versus PRF in the CuBr-Ne laser LT regime for three values of the storage/peaking capacitors.

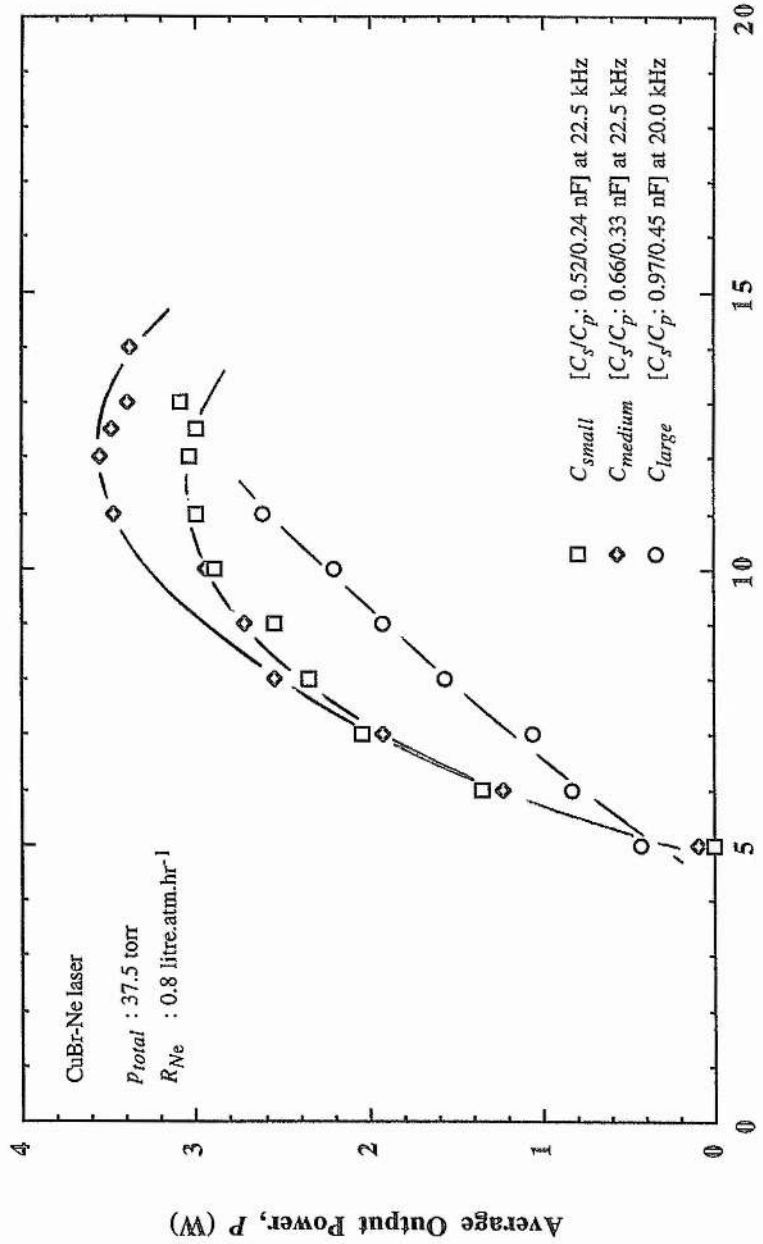

Fig. 3.5
Average output power, P, versus charging voltage, V_{ch}, in the CuBr-Ne laser LT regime for three values of the storage/peaking capacitors, and at close to optimum PRF for each.

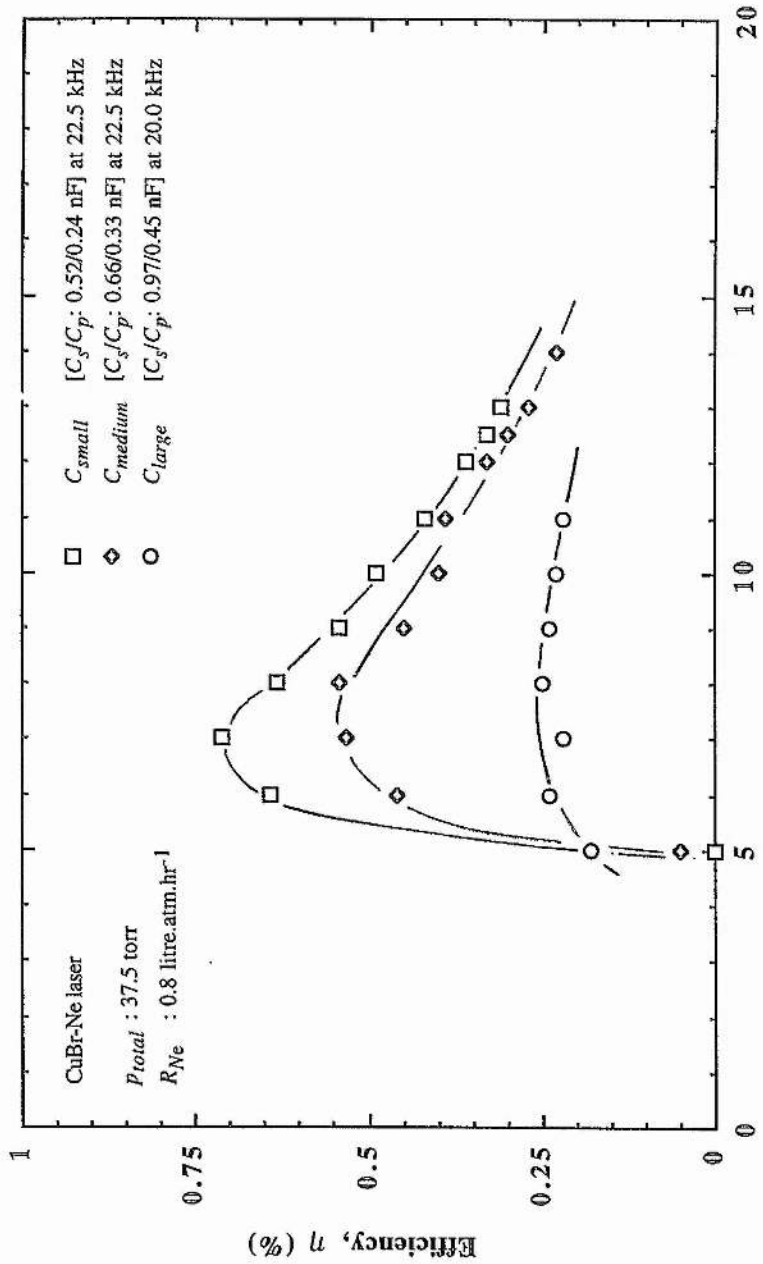

Fig. 3.6

Efficiency, η, versus charging voltage, V_{ch}, in the CuBr-Ne laser LT regime for three values of the storage/peaking capacitors, and at close to optimum PRF for each.

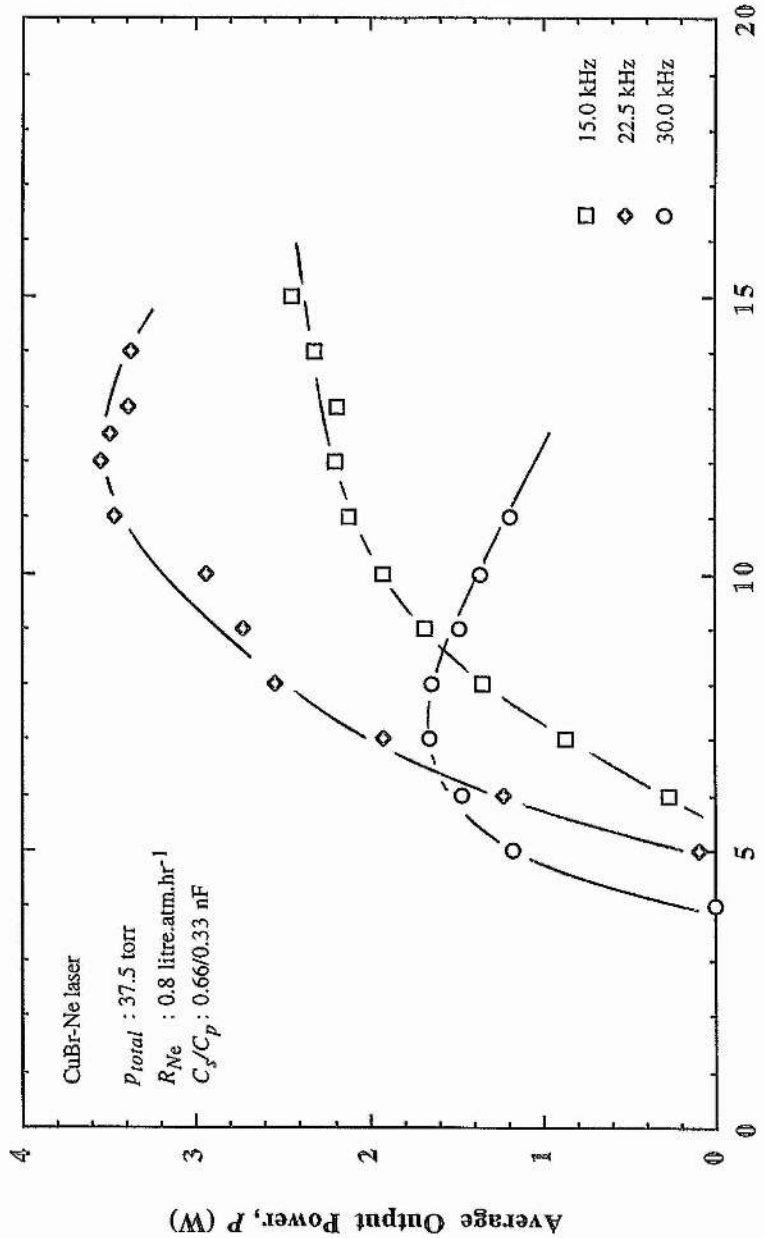

Fig. 3.7
Average output power, P, versus charging voltage, V_{ch}, in the CuBr-Ne laser LT regime at three values of the PRF.

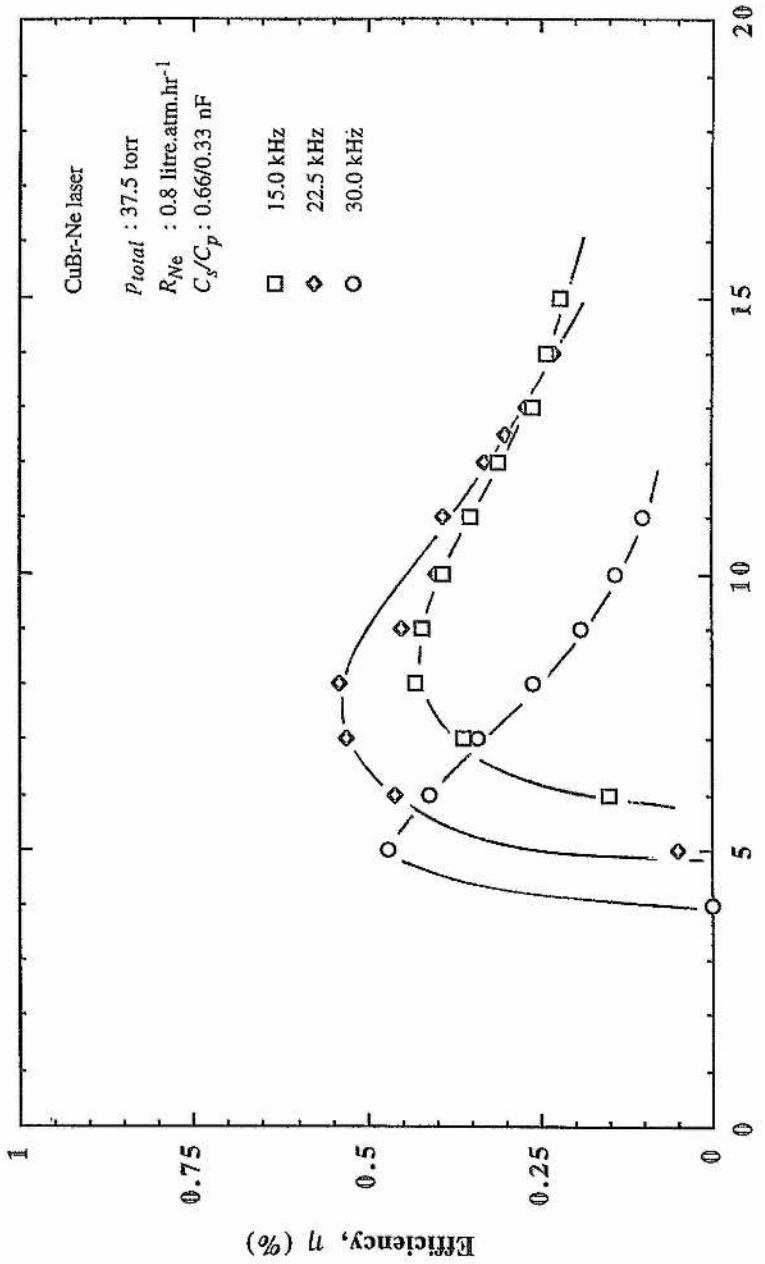

Fig. 3.8
Efficiency, η, versus charging voltage, V_{ch}, in the CuBr-Ne laser LT regime at three values of the PRF.

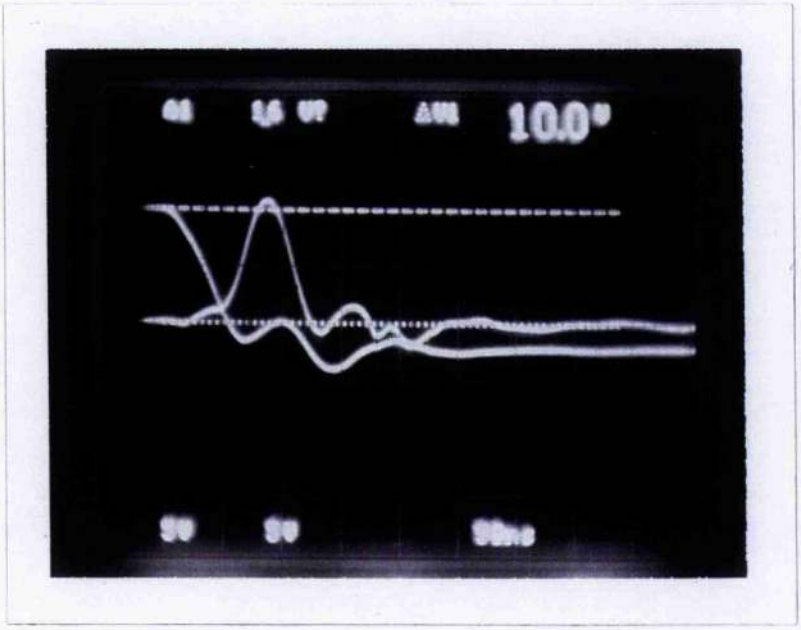

(a) $V_{ch}(t)$ and $i_t(t)$

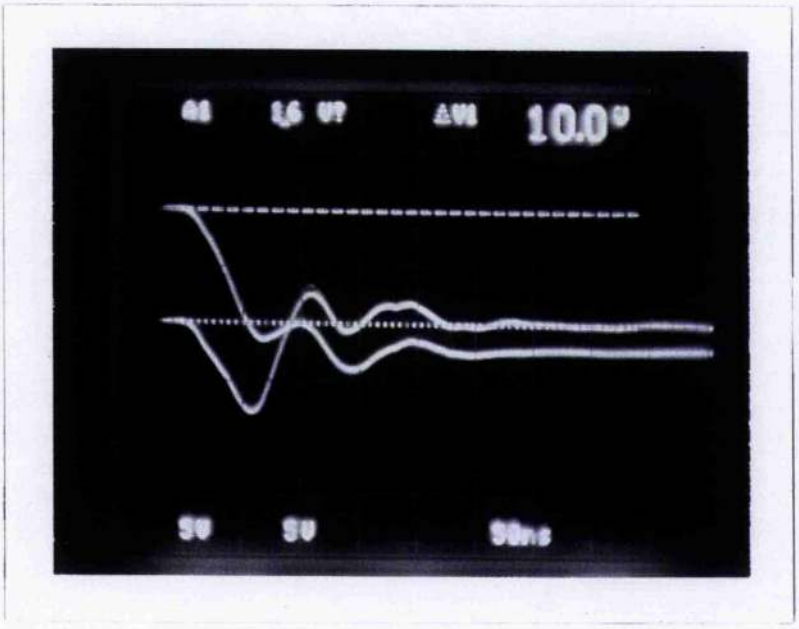

(b) $V_{ch}(t)$ and $V_t(t)$

Fig. 3.9 Oscillograms showing the charging voltage, discharge current and laser tube voltage waveforms, $V_{ch}(t)$, $i_t(t)$ and $V_t(t)$, for lasing in the CuBr-Ne laser LT regime under close to optimum conditions for P_{max} with the 0.66/0.33 nF capacitors connected. R_{Ne}, p_{total}, PRF and V_{ch} are 0.8 litre.atm.hr^{-1}, 37.5 torr, 22.5 kHz and 10 kV respectively.

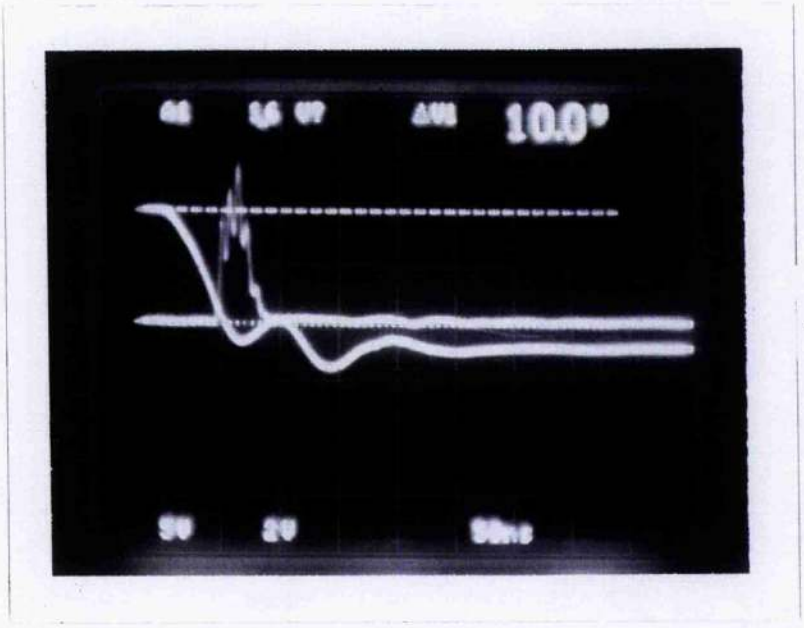

Fig. 3.10 Oscillogram showing the total laser intensity waveform, $I_l(t)$, for lasing in the CuBr-Ne laser LT regime under close to optimum conditions for P_{max} with the 0.66/0.33 nF capacitors connected. R_{Ne}, p_{total}, PRF and V_{ch} are 0.8 litre.atm.hr^{-1}, 37.5 torr, 22.5 kHz and 10 kV respectively.
(Scales: 50 ns/div. Units of intensity arbitrary.)

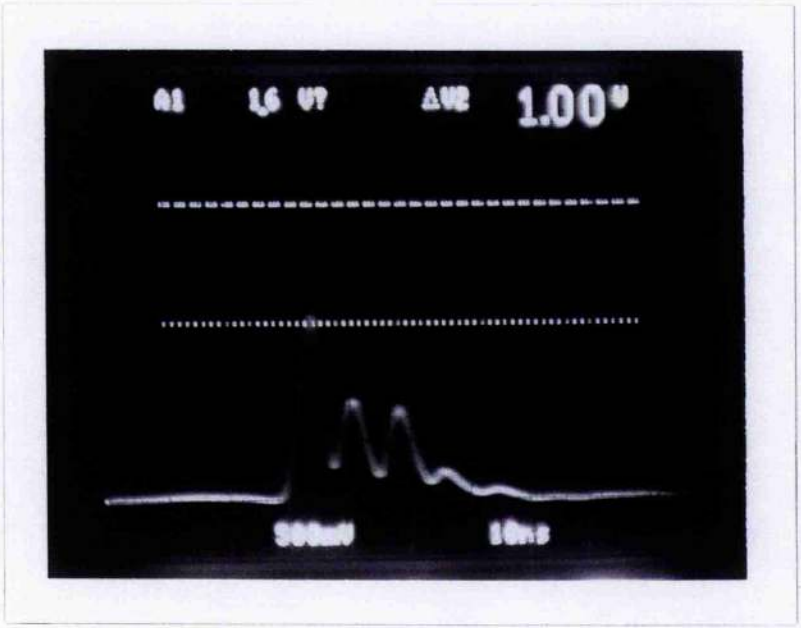

(a) $I_g(t)$

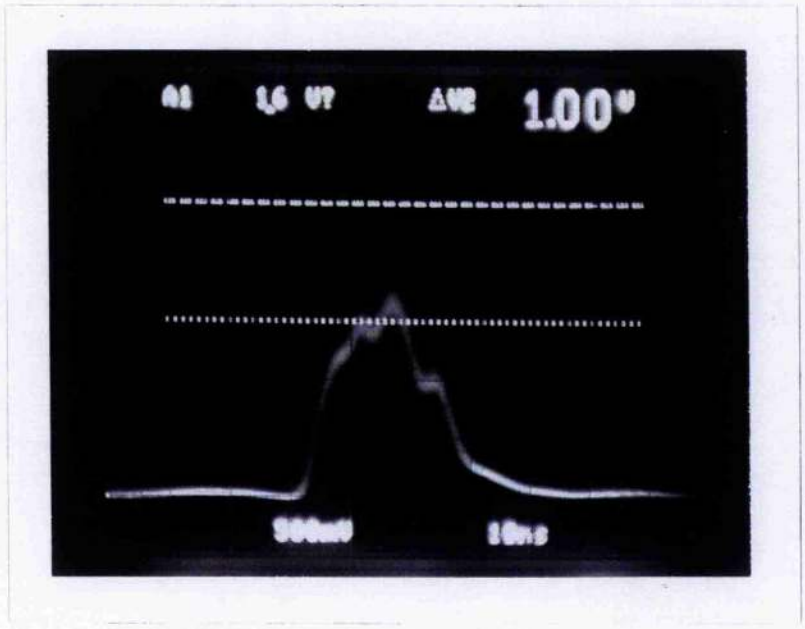

(b) $I_y(t)$

Fig. 3.11 Oscillograms showing the green and yellow laser intensity waveforms, $I_g(t)$ and $I_y(t)$, for lasing in the CuBr-Ne laser LT regime under close to optimum conditions for P_{max} with the 0.66/0.33 nF capacitors connected. R_{Ne}, p_{total}, PRF and V_{ch} are 0.8 litre.atm.hr^{-1}, 37.5 torr, 22.5 kHz and 10 kV respectively. (Scales: 10 ns/div. Units of intensity arbitrary.)

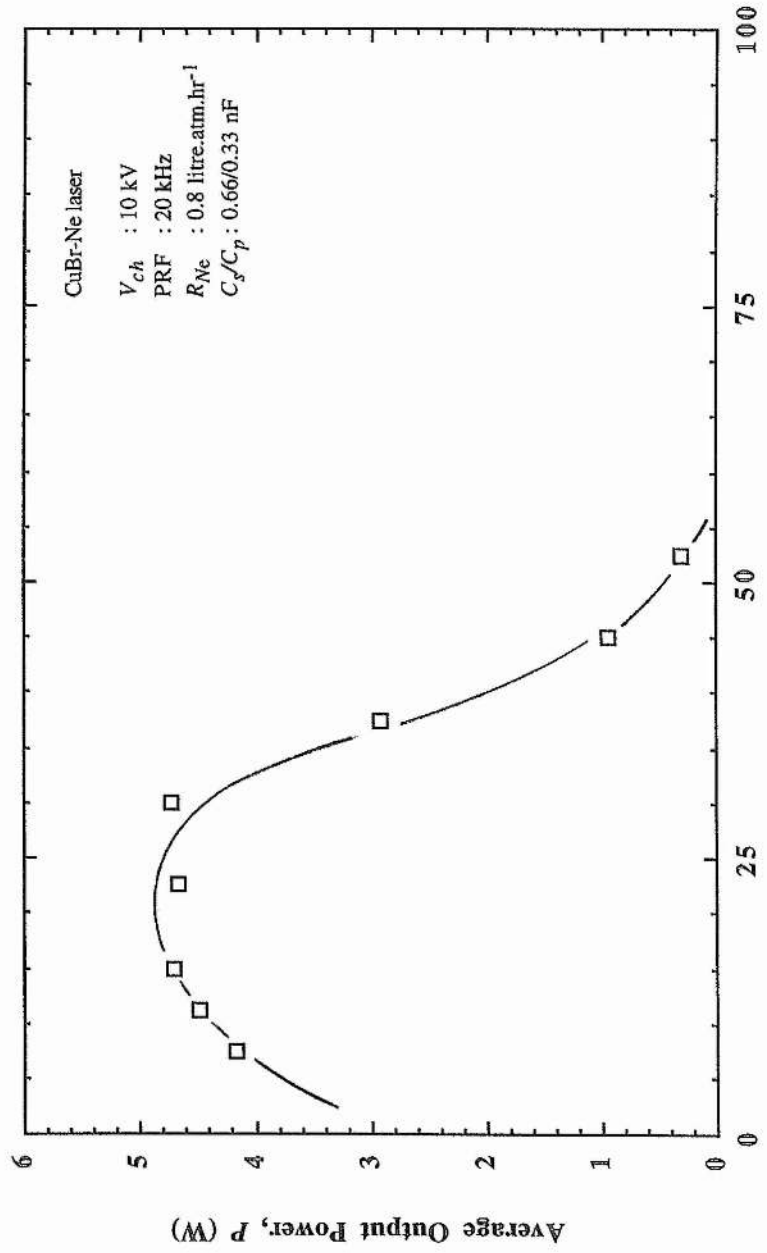

Fig. 3.12
Average output power, P, versus buffer gas pressure, p_{Ne}, in the CuBr-Ne laser HT regime.

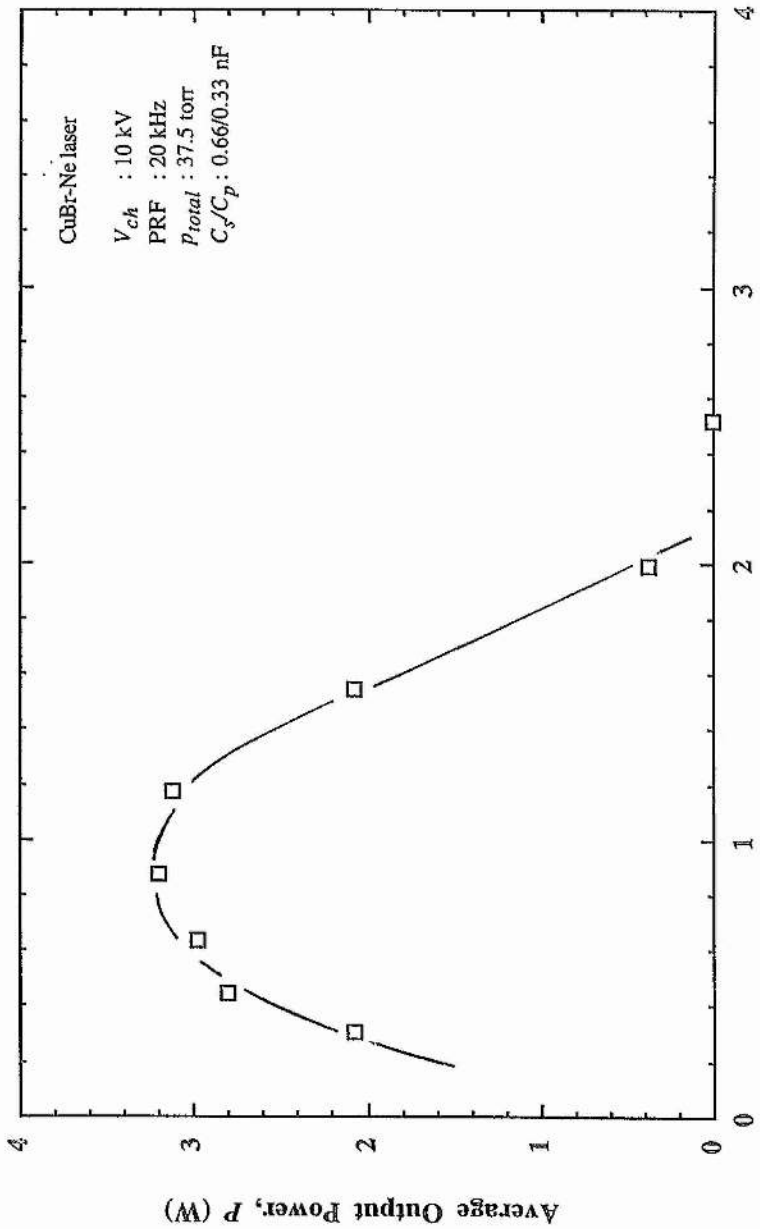

Fig. 3.13
Average output power, P, versus buffer gas flow rate, R_{Ne}, in the CuBr-Ne laser HT regime.

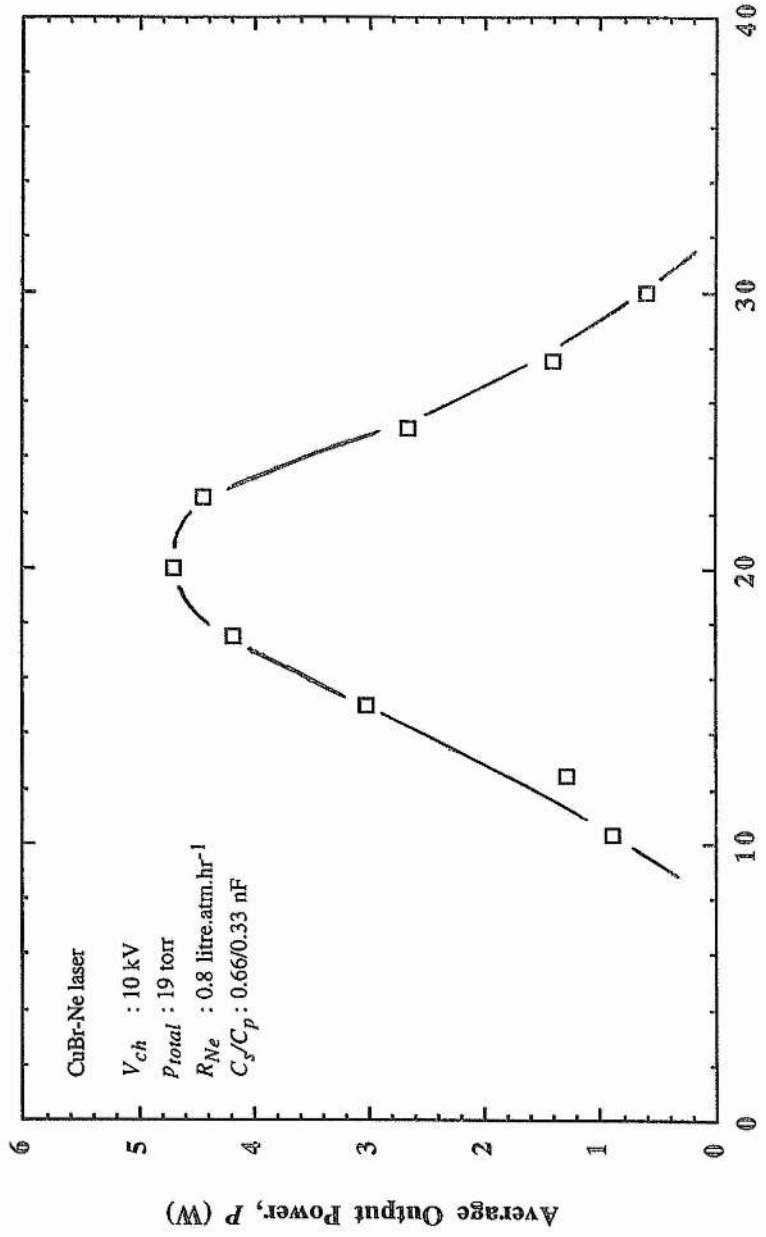

Fig. 3.14
Average output power, P, versus PRF in the CuBr-Ne laser HT regime at a total gas pressure, p_{total}, of 19 torr.

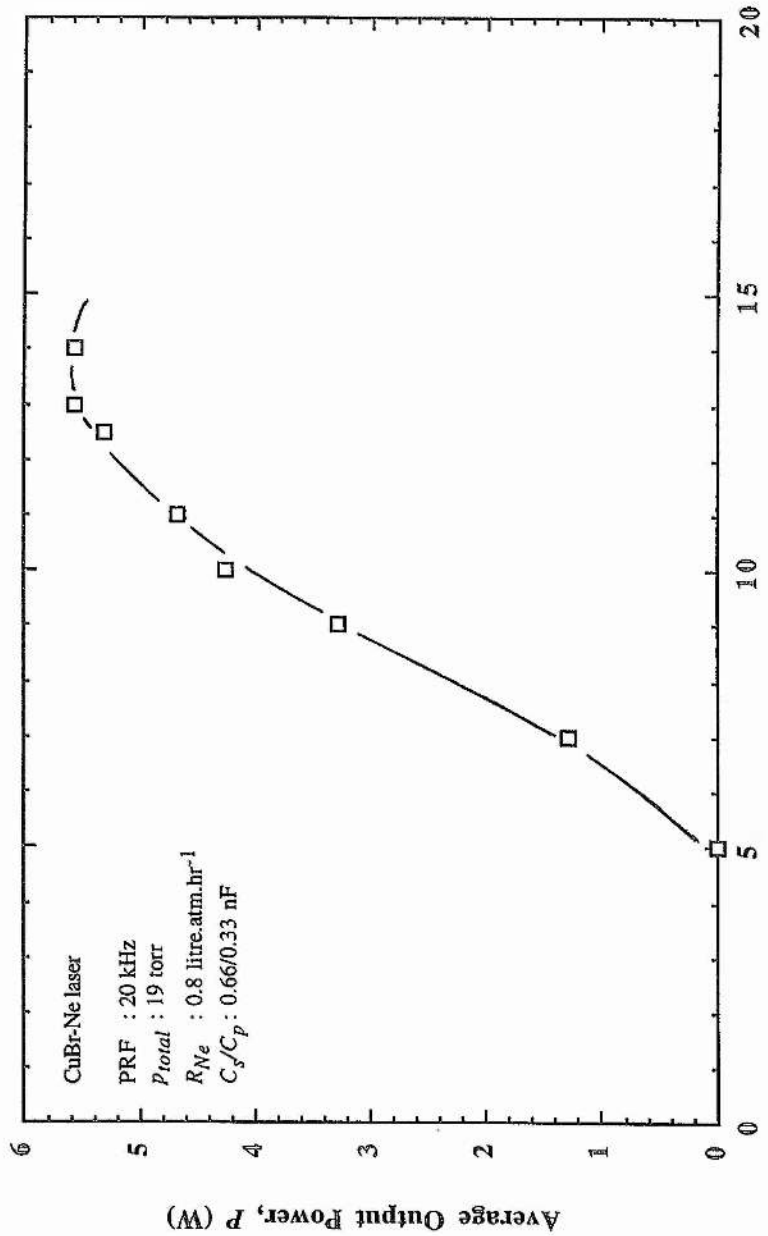

Fig. 3.15
Average output power, P, versus charging voltage, V_{ch}, in the CuBr-Ne laser HT regime at a total gas pressure, p_{total}, of 19 torr and at optimum PRF.

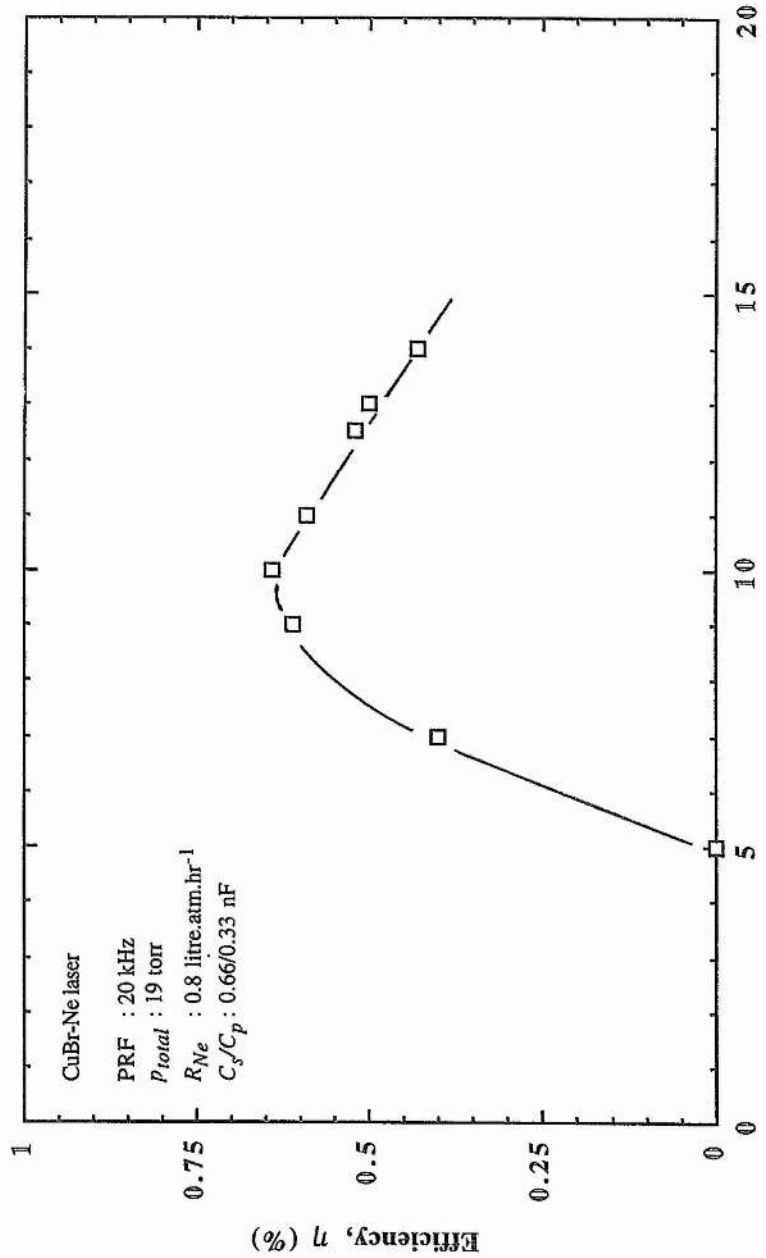

Fig. 3.16
Efficiency, η, versus charging voltage, V_{ch}, in the CuBr-Ne laser HT regime at a total gas pressure, p_{total}, of 19 torr and at optimum PRF.

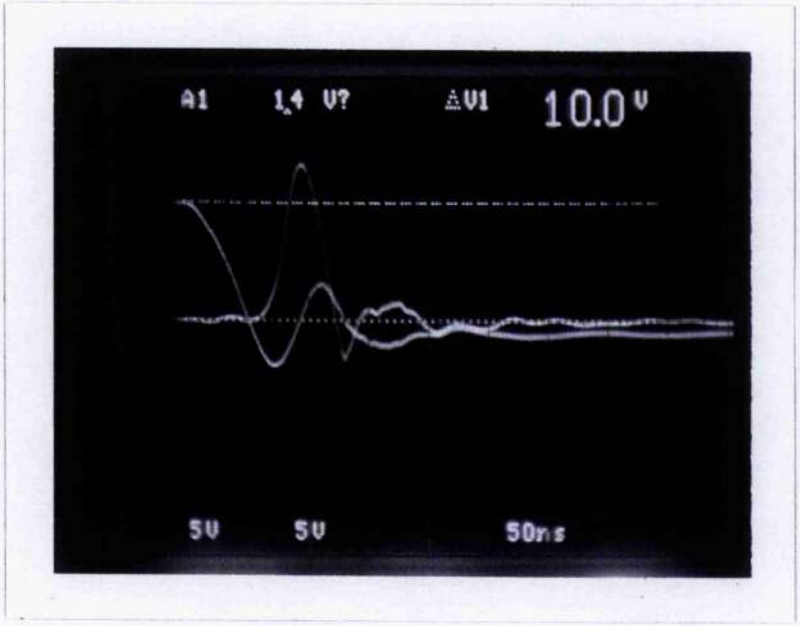

Fig. 3.17 Oscillogram showing the charging voltage and discharge current waveforms, $V_{ch}(t)$ and $i_t(t)$, for lasing in the CuBr-Ne laser HT regime under close to optimum conditions for P_{max} with the 0.66/0.33 nF capacitors connected. R_{Ne}, p_{total}, PRF and V_{ch} are 0.8 litre.atm.hr^{-1}, 19 torr, 22.5 kHz and 10 kV respectively.

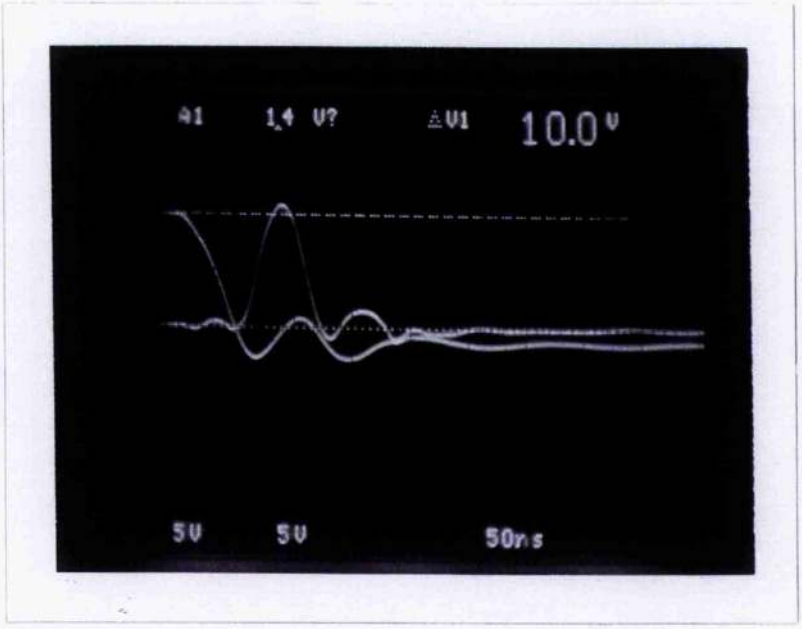

(a) $V_{ch}(t)$ and $i_t(t)$

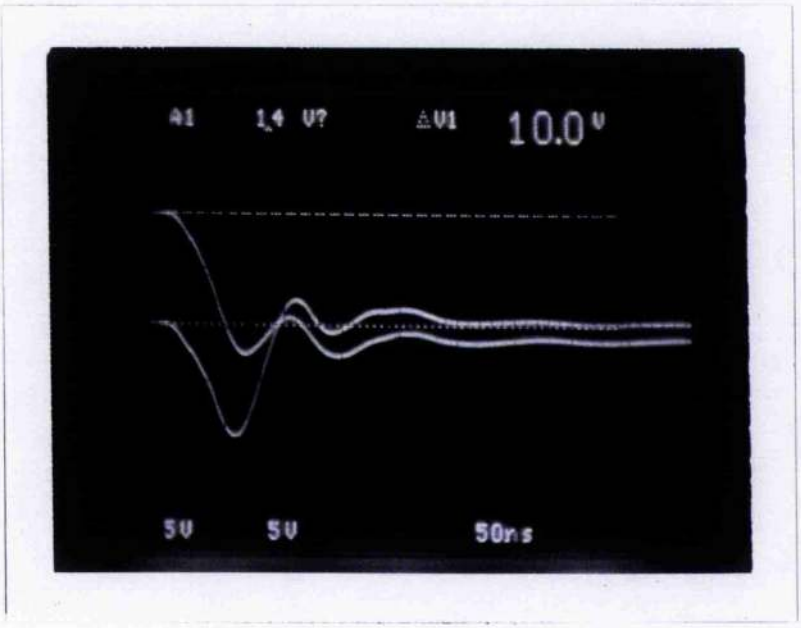

(b) $V_{ch}(t)$ and $V_t(t)$

Fig. 3.18 Oscillograms showing the charging voltage, discharge current and laser tube voltage waveforms, $V_{ch}(t)$, $i_t(t)$ and $V_t(t)$, for lasing in the CuBr-Ne laser HT regime with the 0.66/0.33 nF capacitors connected as the average output power begins to rise towards P_{max}. R_{Ne}, p_{total}, PRF and V_{ch} are 0.8 litre.atm.hr^{-1}, 19 torr, 22.5 kHz and 10 kV respectively.

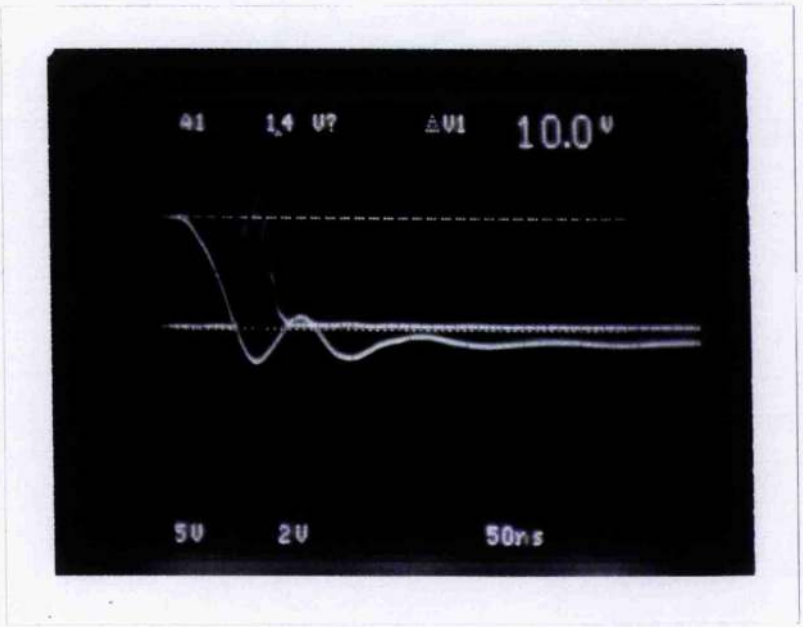

Fig. 3.19 Oscillogram showing the total laser intensity waveform, $I_l(t)$, for lasing in the CuBr-Ne laser HT regime with the 0.66/0.33 nF capacitors connected as the average output power begins to rise towards P_{max}. R_{Ne}, p_{total}, PRF and V_{ch} are 0.8 litre.atm.hr^{-1}, 19 torr, 22.5 kHz and 10 kV respectively.
(Scales: 50 ns/div. Units of intensity arbitrary.)

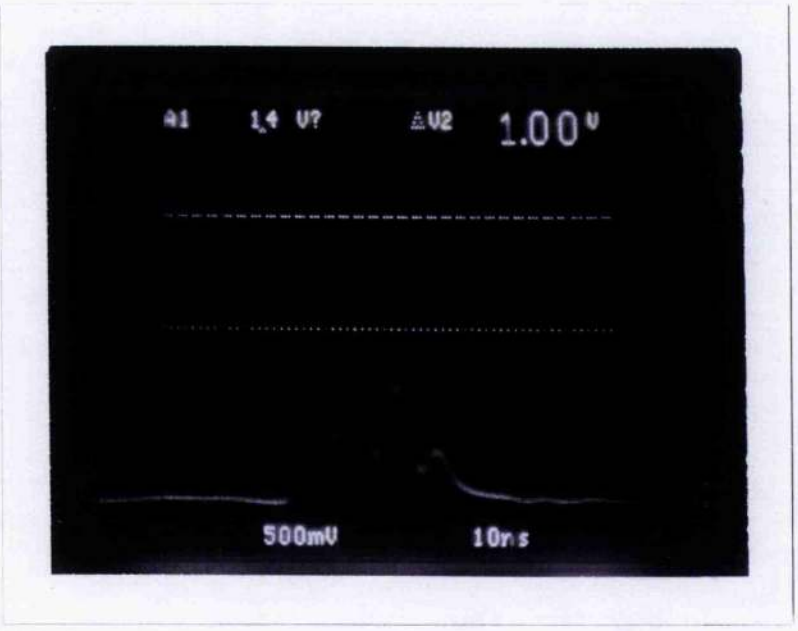

(a) $I_g(t)$

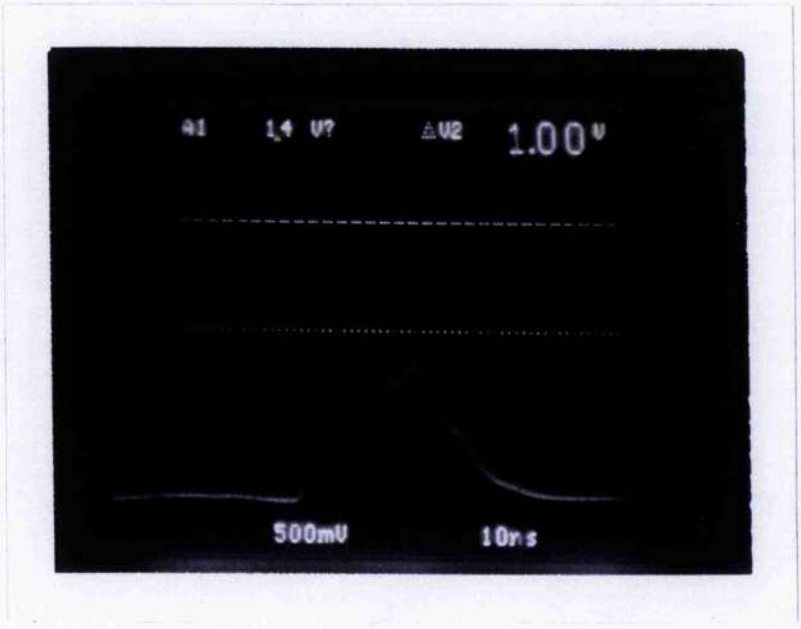

(b) $I_y(t)$

Fig. 3.20 Oscillograms showing the green and yellow laser intensity waveforms, $I_g(t)$ and $I_y(t)$, for lasing in the CuBr-Ne laser HT regime with the 0.66/0.33 nF capacitors connected as the average output power begins to rise towards P_{max}. R_{Ne}, p_{total}, PRF and V_{ch} are 0.8 litre.atm.hr^{-1}, 19 torr, 22.5 kHz and 10 kV respectively. (Scales: 10 ns/div. Units of intensity arbitrary.)

Chapter 4

Characterization of the CuBr-Ne-H_2 Laser

4.1 Introduction

In the preceding chapter, the operating characteristics of a small bore, conventional CBL, having no external source of hydrogen additive and using Ne buffer gas only, were described. In the present chapter, the altered characteristics of the CuBr-Ne laser are reported when H_2 gas is mixed with the Ne buffer gas upstream of the anode. As the CuBr-Ne and CuBr-Ne-H_2 laser tubes are identical in construction, the active volume and tube bore remain 43.5 cm^3 and 13 mm respectively. The laser tube itself is fully described in Chapter 2.

The results of this chapter illustrate the phenomenon in conventional CBLs known as the "hydrogen effect". There has been much debate as to why hydrogen addition is responsible for the enhanced output powers and efficiencies observed when it is added to the discharge gain medium of a Ne-CuBr laser. The most convincing explanation holds that the effect is due to the attributes of the hydrogen bromide (HBr) molecule, and in particular to the formation of the negative Br^- ion during the process of dissociative attachment of the HBr. Hydrogen bromide is formed in significant quantities in the discharge volume of CBLs with H_2 additive by reaction of the discharge dissociation products of the H_2 and Cu_3Br_3 molecules.

This chapter commences with some general observations concerning the performance of the CuBr-Ne-H_2 laser. An exact dependence of average output power, P, on sidearm temperature, T_s, is next provided for reference conditions of the total gas pressure, p_{total}, buffer gas flow rate, R_{Ne}, PRF and charging voltage, V_{ch}, for the two cases of no H_2 and added H_2. The resulting plots demonstrate quantitatively a single

working regime in the CuBr-Ne-H_2 laser and display its relationship to the LT and HT regimes of the CuBr-Ne laser as regards T_s.

The CuBr-Ne-H_2 laser has been broadly characterised. Trends in P, efficiency (BSE), η, and H_2 pressure, p_{H_2}, with alterations in the parameters of the electrical excitation and/or gas mixture are described in detail. Oscillograms display the time dependence of the discharge current, $i_t(t)$, the laser tube voltage, $V_t(t)$, and the total, green and yellow emission intensities, $I_l(t)$, $I_g(t)$ and $I_y(t)$, under close to optimum conditions for lasing. Finally, explanations for the experimental trends are put forward and conclusions drawn regarding the discharge mechanisms responsible. The reader may again find it useful to read the discussion section (Section 4.10) of this chapter first.

4.2 General Observations

In the CuBr-Ne-H_2 laser, oscillation again commenced within 5-10 min from a cold start as the rate determining factor was still the heating of the CuBr melt in the sidearm. Considering first the case of Cu_3Br_3 addition to a Ne-H_2 discharge mix, in which the H_2 pressure was ~ 5 % (by volume) of the total gas pressure, p_{total}, a number of phenomena were observed.

The initial addition of H_2 to the Ne discharge caused the entire sidelight spectrum to change rapidly from the bright orange-red colour of pure Ne to a dull pink as the H_2 transitions joined those of Ne. The charging voltage fell and was readjusted to compensate at this stage, an indication that H_2 addition alone was causing the discharge channel impedance to rise and the circuit-laser matching to improve. At sidearm wall temperatures of 150-300 °C (depending on p_{Ne}) sufficient Cu_3Br_3 pressures, $p_{Cu_3Br_3}$, diffused into the laser tube to cause further changes in the colour of the discharge sidelight spectrum.

Initially, the sidelight spectrum shifted to a pale green colour in the vicinity of the sidearm opening only as Cu transitions above the sidearm coalesced with the Ne and H/H_2 transitions. Towards the cathode, the spectrum alternated between pale green and dull pink as uniform lasing was established in bursts. Beyond a threshold $p_{Cu_3Br_3}$,

uniform lasing was sustainable along the entire discharge length. Average power rose suddenly in response to uniformity but still displayed signs of instability.

Peak lasing was strong at low-medium buffer gas pressures and flow rates of around 10-40 torr and 1-3 litre.atm.hr^{-1} respectively, and at reference values of PRF and charging voltage *i.e.* 20 kHz and 10 kV. Under these conditions, the beam was initially green, non-annular and full bore size and the discharge was a pale green/yellow. As T_s and $p_{Cu_3Br_3}$ were raised, the beam developed an on-axis maximum *i.e.* the Gaussian-like beam shape referred to in [70]. As $p_{Cu_3Br_3}$ increased still further, the beam became more intense and a greater balance of yellow was displayed in the output, but the discharge did not constrict. As average power peaked the beam remained full bore size. Peak P was many times greater than the powers observed in the LT regime of the CuBr-Ne laser, exceeding even the highest powers extracted in the HT regime, and there was complete stability in the vicinity of the peak.

Average output power was found to peak at that T_s at which peak power was generated in the LT mode of the CuBr-Ne laser for the same conditions of the buffer gas and electrical excitation. As T_s was raised beyond this optimum value, instability recommenced and P subsided to 0 W. No further regime of lasing was established. The maximum average power extracted depended on the partial pressure of H_2 in the discharge, and for any fixed combination of the electrical excitation and gas variables was optimum at a single p_{H_2}.

In an alternate approach, the laser was first made to oscillate in a temperature regime of the CuBr-Ne laser followed by addition and optimisation of the H_2 gas. Taking the case of H_2 addition to the CuBr-Ne laser operating at or below peak power in the LT regime under the same conditions of p_{Ne}, R_{Ne}, PRF and V_{ch} considered in the former approach then, with no H_2 added, laser action was initially of medium power, *i.e.* ≤ peak P in the LT mode, and confined to a somewhat constricted (depending on $p_{Cu_3Br_3}$) yellow/green annulus. The discharge was stable. (Unlike the case of Cu_3Br_3 addition to a Ne-H_2 discharge, Cu seeding spread uniformly and quickly through the Ne discharge as Cu_3Br_3 vapour diffused into the CuBr-Ne laser for the first time, showing no pattern of

bursts as lasing was established. There was no marked change in charging voltage either implying that the discharge impedance did not alter significantly.)

On first addition of H_2, there was some reduction in average power (the precise degree a function of p_{Ne}). The charging voltage fell sharply and required readjustment. The beam exhibited a slight increase in constriction initially (~ 5 mm OD) but was less annular. It displayed a small component of high-divergence output. A further increase in p_{H_2} caused the average power to recover rapidly, rising to a stable peak power which was many times larger than its LT regime equivalent. During this recovery phase the beam expanded to fill the entire tube bore, the annularity disappeared completely and the intensity of emission first became uniform across the beam diameter then formed an on-axis maximum.

On raising p_{H_2} still further, the power gradually declined to 0 W. The beam was reluctant to die out, remaining stable over a large range of H_2 pressures, gradually fading but not constricting. During fall off in power the beam remained yellow/green and retained an on-axis maximum throughout as evinced by the fact that the beam centre was the last region of light to disappear. Fall in power was further characterised by a diminishing discharge current though a substantial current remained even after lasing had ceased. Every increase in p_{H_2} caused the charging voltage to drop implying a continuous increase in discharge impedance, and improved circuit-laser matching, throughout. Nonetheless, when the hydrogen regime ended, the discharge impedance was still low enough to delay the onset of a wall discharge which eventually occurred on the collapse of the discharge current pulse at greatly increased H_2 levels. Turning off the H_2 supply compelled P to pass through its peak in the reverse direction and the peak of the LT mode to be re-established. Turning off the sidearm heater voltage then caused lasing to cease entirely.

The peak power achieved on addition of H_2 was noted once more to be optimum at that T_s ($p_{Cu_3Br_3}$) at which the LT regime peaked for the same combination of p_{Ne}, R_{Ne}, PRF and V_{ch}. Peak average power reduced at T_s to either side of the LT regime peak. On the low temperature side peak P was stable. The only instability observed was

that associated with non-uniform Cu metal seeding at very low $p_{Cu_3Br_3}$ which appeared to be caused by the H_2 addition itself. When the initial CuBr-Ne laser oscillations corresponded to the final phase of the LT regime, or to any phase of the HT regime, the discharge was deep blue and turbulent and displayed 'standing waves' of sidelight intensity at almost all p_{H_2} attempted. Current 'hopping' was a common phenomenon and the beam was yellow, non-annular and constricted.

In the investigation of the CuBr-Ne laser, the effects on the discharge current pulse, $i_t(t)$, of an increasing T_s were noted. A similar but not identical dependence of $i_t(t)$ was observed when either H_2 or Cu_3Br_3 was added to a Ne discharge containing significant quantities of the other.

Considering the case of H_2 addition to the CuBr-Ne discharge at T_s at or below optimum for the LT regime, the step on the main current pulse was already some way down the leading edge depending on the exact pressure of $p_{Cu_3Br_3}$ added. On first addition of H_2, the current pulse step plummeted. P remained constant as $p_{Cu_3Br_3}$, and hence the number of Cu atoms available for lasing, was not changing, but the peak current passed through a maximum as the step crossed the 10 % height as usual. Below this height the peak discharge current, $i_{t\,pk}$, and average power reduced.

At higher p_{H_2}, the step on the current pulse collapsed and the average power started to climb rapidly, reaching a peak coincidently with the current pulse. These changes occurred despite there having been no alteration in $p_{Cu_3Br_3}$ and the number of available Cu atoms. The peak current achieved was higher in this instance by ~ 50-100 A. This response of $i_t(t)$ to p_{H_2} is almost entirely consistent with its response to T_s in the HT regime of the CuBr-Ne laser except that the maximum currents are higher by ~ 20 A in the former case.

It was noted again that a step appeared on the leading edge of a secondary current pulse appended to the trailing end of the main current pulse. Once more, this step was seen to move down the leading edge of the secondary pulse with increasing p_{H_2}, touching or just crossing the ground line at peak power.

As stated earlier, the final phase of H_2 addition was characterised by a diminishing

current pulse, but lasing ceased while the primary current was still high (~100-150 A) and no wall discharge ensued. This was the only major difference between the current responses of the H_2 and HT regimes. The laser tube voltage, $V_t(t)$, was noted to rise throughout.

Finally, H_2 gas was added to a pure Ne discharge under the same conditions of gas and excitation. A similar response of $i_t(t)$ occurred but the peak currents were smaller by ~ 20 A. A ground-level step was present on the leading edge of the smaller, appended current pulse (in the position normally associated with peak power in the hydrogen and HT regimes) from the instant of its formation and remained there during all subsequent changes. $V_t(t)$ again increased throughout.

The CuBr-Ne-H_2 laser was operated continuously over a number of 12 hr intervals. The laser discharge was quite stable with some reduction in output power over long intervals of use due to dendrite formations in the active region, mainly around the semicircular aperture in the ceramic above the sidearm opening, which encroached on the beam path. The dendrites were "tree-like" in structure, grew vertically and melted on too close approach to the discharge. They were particularly common when the tube was running too hot or when high partial pressures of H_2 gas were present in the total gas mixture.

Addition of H_2 led to more effective removal of CuBr deposits so that lasing was more readily controlled by altering T_s. At switch-off, residual deposits of CuBr in the active volume were quickly removed by turning off the Cu_3Br_3 supply first. Cessation of lasing then took place over timescales comparable with the 5-10 min to lasing from a cold start even after substantial use of the discharge tube. Operation at low and high pressures still produced a build up of contaminants on the laser windows but this problem was relieved somewhat by operating solely at the lower T_s of the CuBr-Ne laser LT regime at which the hydrogen regime also peaked. Greatest stability and maximum power were achieved when H_2 was added to the CuBr-Ne laser when already operating at peak power in the LT regime.

The operating temperature of the laser tube was again a balance between that

which was hot enough to prevent CuBr deposition on the ceramic and that which was cool enough to deter dendrite formations near the sidearm opening. The presence of H_2 facilitated the removal of CuBr deposits from the laser tube, but accelerated Cu metal deposition, most probably by hydrogen reduction processes. There remained a fine scattering of copper particles across the inner surface of the alumina tube at switch-off.

4.3 Dependence of Average Output Power on Sidearm Temperature

For consistency with the CuBr-Ne laser experiments, the medium sized capacitors, C_{medium}, (0.66/0.33 nF) were again chosen to begin the quantitative investigation. By raising the sidearm temperature from 200-450 °C, and monitoring average power at 5-10 °C intervals, P versus T_s was first recorded for the case of no H_2 (*i.e.* CuBr-Ne laser). The resulting plot is shown in Figure 4.1. For the reference conditions considered, optimum T_s is 335 °C and 450 °C in the LT and HT regimes respectively, a difference of 115 °C. The respective peak powers are 2.6 W and 2.95 W.

Hydrogen was subsequently admitted to the laser tube and optimised at a number of T_s, at and to either side of the optimum T_s (of 335 °C) established for the LT regime. In this way an equivalent dependence of P on T_s was procured for the CuBr-Ne-H_2 laser. Average output power versus sidearm wall temperature for the CuBr-Ne-H_2 laser is plotted in Fig. 4.1 alongside the curve for the CuBr-Ne laser. The plot confirms the general observation of a single regime of operation in the CuBr-Ne-H_2 laser whose peak average power (7.4 W in this case) is extractable at the same sidearm temperature at which the LT regime peaks.

Figure 4.1 demonstrates that the "hydrogen effect" can, in some regards, be viewed as an augmentation of the LT regime of the CuBr-Ne laser, except that the hydrogen regime extends to sidearm temperatures associated with the HT regime of operation and increasingly displays characteristics peculiar to the HT regime with increasing T_s beyond optimum. When the plot corresponding to the CuBr-Ne-H_2 laser is extrapolated to 450 °C (*i.e.* to optimum T_s for the HT regime), the difference in the average powers extractable from each laser is < 1 W (Fig. 4.1). This suggests that the HT

regime of the CuBr-Ne laser results from the release of H_2 containing impurities from the sidearm at elevated T_s.

The HT regime appears therefore to be a localised "hydrogen effect" which is optimal at a T_s dictated by a number of different factors:

1) the temperature range (usually elevated) over which H or H_2 is released in appropriate concentrations from the CuBr melt;
2) the buffer gas and excitation variables p_{Ne}, R_{Ne}, PRF and V_{ch} on which optimum T_s, in both regimes, was seen to depend in Chapter 3;
3) the Cu_3Br_3 pressure (much larger at the elevated T_s at which the HT regime optimises) which can lead to premature termination of the regime if too large.

The limits imposed by these factors enable lasing in the HT regime to take place over narrow temperature ranges only. By contrast, the CuBr-Ne-H_2 laser, which has available to it a variable and sufficient supply of H_2 gas at all conditions of p_{Ne}, R_{Ne}, PRF, V_{ch} and $p_{Cu_3Br_3}$ considered, is broad in temperature range.

As a result of the above dependence of P on T_s, and of earlier observations regarding the stability of the system, in the characterisation of each aspect of CuBr-Ne-H_2 laser performance, T_s was first set for peak power in the LT regime of the CuBr-Ne system and H_2 gas was admitted and optimised thereafter. This ensured that lasing was stable and that the recorded powers were representative of the true average powers achievable under all conditions studied.

Finally, it should be noted that the sidearm wall temperatures of Fig. 4.1 are not synonymous with those shown in Fig. 3.1 of Chapter 3 (P versus T_s in the CuBr-Ne laser at 19 and 34 torr). The laser tube was dissembled for cleaning and for replenishment of the CuBr on a number of occasions between taking these sets of results so that the thermocouple position and degree of thermal contact were not the same in each case.

4.4 Optimum H_2 Pressure Versus Buffer Gas Pressure

The influence of buffer gas pressure over the H_2 pressures required for optimal lasing was determined at a number of total gas pressures in the range 7.5 to 90 torr. The medium

sized capacitors were employed.

As the H_2 molecule is of very small diameter, it was difficult to achieve fine control over the H_2 pressure with the needle valves available. An alternative method of measuring H_2 pressure, other than by flow rate calibration, had to be used. With p_{Ne} set to 90 torr initially and T_s adjusted for peak power in the LT regime, p_{H_2} was increased in stages until peak average power was established. The total gas pressure was readjusted to 90 torr at each stage. When the optimum p_{H_2} was attained, the sidearm heater voltage was switched off and lasing allowed to cease. The laser supply voltage was interrupted and the Ne inlet line sealed off. As the gases were flowing, all Ne was duly extracted from the tube, and when the gas pressure had settled, its value was noted as the optimum pressure of H_2 for a total gas pressure of 90 torr. The Ne inlet was reopened, and when a p_{total} of 90 torr had been re-established, the laser supply voltage was switched on and the discharge tube allowed to reheat. The entire procedure was repeated at a number of smaller p_{total}.

The dependence of optimum p_{H_2} on p_{Ne} is shown in Fig. 4.2. Ne pressures were calculated simply by subtracting the recorded p_{H_2} from the corresponding p_{total}. The plot is a straight line through the origin. H_2 pressures of up to 4.5 torr are required with increasing buffer gas pressures to ~ 86 torr.

4.5 Average Output Power Versus Buffer Gas Pressure

With the 0.66/0.33 nF capacitors connected, the response of average output power to changing buffer gas pressure was obtained for total gas pressures in the range 3.75 to 90 torr. The experiment was conducted in two stages.

In stage 1, p_{Ne} was set to 15 torr initially and T_s was carefully adjusted for peak power in the LT regime of the CuBr-Ne laser. The H_2 pressure was then optimised in stages and p_{total} readjusted to 15 torr at each stage. When optimum p_{H_2} was established, the gas flow control valve (Fig. 2.4) was opened fully to give the lowest possible pressure (3.75 torr) at the reference R_{Ne} of 0.8 litre.atm.hr^{-1}. Average power was recorded at the reduced total gas pressure. By gradual closure of the gas flow control valve, p_{total} was

slowly returned to 15 torr in steps of 0.75 torr and average power recorded at each stage. The H_2 flow rate, R_{H_2}, and the sidearm wall temperature, both optimised for peak power at 15 torr, were maintained constant throughout the rise in pressure. This approach to measuring P was possible because of the linear nature of the dependence of p_{H_2} on p_{Ne} (Fig. 4.2).

In the final stage of the experiment, p_{H_2} was optimised again, this time for a p_{total} of 90 torr. The gas flow control valve was then opened gradually and average power recorded in steps of 7.5 or 15 torr down to a total gas pressure of 15 torr. The H_2 flow rate and sidearm wall temperature, both optimised for peak power at 90 torr, were again maintained constant throughout the reduction in p_{total}.

For each total gas pressure investigated, the corresponding pressures of H_2 (and Ne) were obtained from the plot of p_{H_2} versus p_{total} used in the calculation of p_{Ne} for Fig. 4.2 (p_{H_2} versus p_{Ne}). Average power versus buffer gas pressure is plotted in Fig. 4.3. Average power rises with increasing p_{Ne} to a maximum of 7.2 W at ~ 25 torr. Increasing the buffer gas pressure to ~ 86 torr causes P to fall by ~ 37.5 %.

When lasing at or below optimum p_{Ne}, and under reference conditions of the other variables, the laser beam is yellow/green, non-annular and unconstricted. When p_{Ne} is increased beyond its optimum value, the ratio of yellow:green in the beam is raised. The average power falls but the discharge remains stable and the beam full bore size.

4.6 Average Output Power Versus Buffer Gas Flow Rate

The dependence of average output power on buffer gas flow rate was obtained for R_{Ne} in the range 0.3 to 6.4 litre.atm.hr^{-1} with C_{medium} connected. As p_{H_2} was not being measured during this experiment, the experimental techniques of Chapter 2 were applied.

Fig. 4.4 demonstrates that lasing is strong at most R_{Ne} considered. Average power at the smallest flow rate of 0.3 litre.atm.hr^{-1} is a bold 88 % of its peak value. The rise in average power with increasing R_{Ne} to the optimum flow rate of ~ 2 litre.atm.hr^{-1} is very gradual. Powers at flow rates beyond 2 litre.atm.hr^{-1} also reduce gradually and are still high at the maximum flow rate of 6.4 litre.atm.hr^{-1} considered. The point at 3.7

litre.atm.hr^{-1} was always down in power despite repeated attempts to prove otherwise. This is considered due to turbulence at that point which does not favour release of Cu_3Br_3 from the sidearm into the main body of the discharge tube. The yellow appearance of the discharge at that particular flow rate supports this assumption. Increases in flow rate result in changes in beam and discharge comparable with those noted on raising p_{Ne}.

4.7 Average Output Power Versus PRF for Three Values of the Storage/Peaking Capacitors

The influence of PRF on average power was subsequently considered for each of C_{small} (0.52/0.24 nF), C_{medium} (0.66/0.33 nF) and C_{large} (0.97/0.45 nF). With the charging voltage fixed at 10 kV, the PRF was varied in increasing multiples of approximately 5 kHz alternately higher then lower than its reference value. Sidearm temperature and H_2 pressure were adjusted at the reference PRF only.

Average output power versus PRF is plotted in Fig. 4.5 for all three capacitor pairs. The PRF curves are almost parabolic in nature. The optimum PRFs are 35, 30 and 27 kHz for the 0.52/0.24 nF, 0.66/0.33 nF and 0.97/0.45 nF capacitors respectively, thus showing a clear tendency for optimum PRF to decrease with increasing capacitance. When the PRF run for C_{large} commenced, the power at 20 kHz plunged on initial variation of PRF, settling at a much reduced value of 5.6 W. Similar, if less pronounced, dips are also visible on the curves for C_{small} and C_{medium} at 20 kHz. Changing the PRF appeared to alter the Cu_3Br_3 distribution in the laser tube and the point at 20 kHz entered a dip due to resonances blocking the release of Cu_3Br_3 from the reservoir.

4.8 Average Output Power and Efficiency Versus Charging Voltage for Three Values of the Storage/Peaking Capacitors

In investigating average power as a function of charging voltage, the PRF was fixed in the vicinity of its optimum value for each capacitor set. The charging voltage was then varied in increasing multiples of approximately 1 kV alternately higher then lower than its reference value of 10 kV. Sidearm wall temperature and H_2 pressure were adjusted at the

reference V_{ch} of 10 kV only.

Plots of average power versus charging voltage are displayed for all three capacitor pairs in Fig. 4.6. Average power rises steeply and linearly at low V_{ch}, peaking at approximately 11 kV and 10 kV for C_{small} and C_{medium} respectively. In the case of C_{large}, average power had still to peak at the maximum V_{ch} of 12 kV attempted. The plots also reveal the maximum power levels which can be extracted from the CuBr-Ne-H_2 laser. The curves suggest that this laser favours the small capacitors. The maximum average output power, P_{max}, is 11.4 W and was obtained at 11 kV and 30 kHz with C_{small} connected.

The charging voltage run with C_{large} was performed at a fixed PRF of 20 kHz and demonstrates an average power of 8.5 W at 10 kV and 20 kHz. This is consistent with the initial observations of a relatively high average power at 20 kHz before PRF variation caused the power to decline at this point during the PRF run reported in Section 4.7.

When the PRF, charging voltage or both were increased beyond their optimum values, the yellow component of beam and sidelight spectrum became increasingly intense. To either side of optimum PRF or V_{ch} the beam reduced in power. 'Standing waves' of sidelight intensity appeared with increasing frequency as the electrical excitation became very non-optimal. The non-annular nature of the beam and its on-axis maximum prevailed throughout.

By applying equation (3.1) to the data of Fig. 4.6, plots of efficiency (BSE) versus V_{ch} at close to optimum PRF were obtained for each of C_{small}, C_{medium} and C_{large}. These plots are shown in Fig. 4.7. The characteristic steep rise to peak η at the lower charging voltages is apparent in each case. Efficiency peaks at 9 kV for C_{small} and at 8 kV for both C_{medium} and C_{large}. Beyond optimum V_{ch} there is the more gradual, almost linear decline in efficiency with increasing charging voltage. At low and high charging voltages, the efficiency curves tend to merge becoming spaced out in the vicinity of optimum charging voltage.

Peak efficiencies are 1.47, 1.24 and 1.02 % for C_{small}, C_{medium} and C_{large} respectively. The CuBr-Ne-H_2 laser quite clearly favours the small capacitors in terms of

both average output power and efficiency. The maximum efficiency, η_{max}, is therefore 1.47 % for this laser. From the plots of P versus V_{ch} (Fig. 4.6) and η versus V_{ch} (Fig. 4.7) for C_{small}, we see that η at that V_{ch} corresponding to P_{max}, *i.e.* 11 kV, is 1.21 % while P at that V_{ch} corresponding to η_{max} , *i.e.* 9 kV, is 9.3 W.

4.9 Features of the Discharge Current, Laser Tube voltage and Total, Green and Yellow Intensity Waveforms

Oscillograms of discharge current, laser tube voltage, and emission intensity were taken, together with the charging voltage waveform, $V_{ch}(t)$, under approximate conditions for P_{max} with the 0.66/0.33 nF capacitors connected. Although the actual P_{max} was extracted with the small capacitors (0.52/0.24 nF) connected, for any comparison to be useful, the oscillograms should all reflect the same capacitance. For C_{medium} then, a P_{total}, R_{Ne}, V_{ch} and PRF of 26 torr, 0.8 litre.atm.hr^{-1}, 10 kV and 29 kHz respectively, gave close to optimum discharge conditions.

The discharge current, laser tube voltage and charging voltage waveforms are shown in Fig. 4.8. Oscillogram (a) shows $i_t(t)$ and $V_{ch}(t)$. The step on the leading edge of the current pulse has clearly collapsed and the peak current is ~ 300 A. Oscillogram (b) displays the $V_t(t)$ and $V_{ch}(t)$ waveforms. The peak value of $V_t(t)$ is 12 kV. It therefore exceeds $V_{ch}(t)$ by 2 kV. Comparing oscillograms (a) and (b) reveals a ~ 50 ns delay between first rise of $V_t(t)$ and the subsequent rise of $i_t(t)$. There is some delay after onset of the current pulse before the current avalanche proper begins, but this delay is not due to the original prepulse current step which commenced ~ 20 ns after $V_t(t)$ and collapsed as the hydrogen regime was entered. The delay in the current avalanche, t_{da} , relative to onset of the current pulse is ~ 19 ns and $V_t(t)$ is peaking when the avalanche begins. Likewise $V_t(t)$ is almost zero when $i_t(t)$ peaks. The total current pulse risetime, t_{ri}, and the avalanche risetime, t_{ra}, are ~ 44 ns and 25 ns respectively.

Fig. 4.9 shows the total intensity waveform, $I_l(t)$. Lasing begins on the leading edge of the current pulse, a few nanoseconds before avalanche proper begins. The risetime to peak intensity, t_{rl}, is ~ 13 ns. Fall off in intensity beyond the main peak,

occurs at similar rates to the rise. Peak intensity occurs before the current pulse has peaked but just after the tube voltage peaks. Smaller peaks are displayed to either side of the principal peak. The total intensity pulse duration, t_l, is ~ 37 ns. The delay in $I_l(t)$, t_{dl}, relative to the onset of the current pulse is 15 ns, *i.e.* lasing commences just before the current avalanche proper begins.

Fig. 4.10 shows the green and yellow intensity waveforms, $I_g(t)$ and $I_y(t)$. The green and yellow pulses begin at different times. The start of the green pulse is coincident with the beginning of the total intensity pulse, with its main peak occurring ~ 13 ns into the pulse. Successive peaks occur at regular intervals of ~ 7 ns. The total duration of the green pulse, t_g, its risetime, t_{rg}, and its delay, t_{dg}, relative to the onset of the current pulse, are 33, 13 and 15 ns respectively.

The yellow pulse begins ~ 3 ns after the green pulse and its main peak occurs ~ 14 ns into the total intensity pulse. The smaller peaks have almost completely merged with the sides of the main peak. The total duration of the yellow pulse, t_y, its risetime, t_{ry}, and its delay, t_{dy}, relative to the onset of the current pulse, are 34, 11 and 18 ns respectively. The above information relating to the discharge current, laser tube voltage and total, green and yellow intensity waveforms at close to optimum conditions for P_{max} is summarised in Table 4.1.

4.10 Discussion

It is again appropriate to comment on the general observations first. When Cu_3Br_3 was added to a Ne-H_2 discharge, the beam was Gaussian in profile and full bore size from the outset, provided that p_{H_2} was sufficiently large. With rising T_s, the yellow:green ratio increased. The peak powers were always greater than in either the LT or HT regimes of the CuBr-Ne laser and peak power always occurred at optimum $p_{Cu_3Br_3}$ for the LT mode under equivalent discharge conditions.

H_2 addition to a Ne-Cu_3Br_3 discharge always caused some initial reduction in power while the discharge impedance rose. The beam also constricted initially but was less annular. During the recovery in power, the beam expanded to fill the entire bore and

developed its Gaussian profile. An increasing p_{H_2} did not alter the yellow:green intensity ratio in favour of the yellow transition. The impedance was noted to increase throughout the rise in p_{H_2}.

These observations can be explained in terms of the effect of hydrogen on the discharge. One of the main effects of H_2 in the discharge is the reduction of CuBr to free Cu atoms in the active volume. Astadjov et al. [76] showed that when hydrogen is absent from the CuBr-Ne system, most of the excitation is confined to the near vicinity of the laser tube axis with very little occurring near the wall. On addition of H_2 the level of excitation reduces in the laser tube centre but flattens out overall to become more uniform across the tube bore. Keeping this in mind we can assume that if in the CuBr-Ne system (with no H_2) most of the excitation occurs on axis then so too must most of the ionization. Similarly, there will be very little ionization occurring near the wall. The result of this constriction (discussed in Chapter 3) is that the majority of ions are created on axis and are driven out by cataphoresis to form a black hole in the centre. Furthermore, the ground state is depleted faster in the presence of fast ionization during each excitation pulse and so the laser pulse is shorter. The added H_2 can react with Cu_3Br_3 near the wall to form Cu atoms and HBr. There is now a readily ionizable species near the wall also so that the current is able to spread out thereby reducing the constriction and enabling uniform or Gaussian lasing. When Cu_3Br_3 is added to a discharge already containing hydrogen the beam is full bore size and gaussian from the outset. When H_2 is added last, the initial annularity is observed to fill in and the constriction to disappear.

Another effect of H_2 addition is the production of HBr by reactions in the discharge and the action of dissociative attachment to counter cataphoretic depletion of Cu atoms. The increase in plasma impedance with H_2 addition is consistent with the much faster removal of electrons and ions from the active volume and the delay of the electron avalanche by dissociative attachment at the beginning of the excitation pulse (see Chapter 1).

The peak powers are always greater in the hydrogen regime because the reaction of the H_2 with the Cu_3Br_3 increases the ground state density of Cu atoms, n_{Cu}, for the

same level of $p_{Cu_3Br_3}$, and HBr delays the electron avalanche by attachment until the peak tube voltage is reached, which is close to optimum for producing an inversion on the Cu levels. However, peak power occurs at the same $p_{Cu_3Br_3}$ as for the LT regime of the CuBr-Ne laser because the turnover in power is still due to reduction in peak T_e. This fall in peak T_e is caused by inelastic collisions with Cu_3Br_3 and its discharge dissociation products. Thus, the effectiveness of pumping to the green upper laser level relative to the yellow is reduced. Although the relative concentrations of the dissociation products may change because of the introduction of H_2, the overall numbers of Cu and Br do not so that power turns over at the same $p_{Cu_3Br_3}$ as before. The rising yellow:green ratio with rising T_s, but not with increasing p_{H_2}, is evidence that the same process of peak T_e reduction by inelastic electron collisions with Cu and Cu_xBr_x is more effective than collisions with hydrogen. (Certainly, the H atom has much higher excited electronic states (≥10.2 eV) and a higher ionization potential (13.6 eV) than all species except Ne and H_2, so the only inelastic losses are to rovibrational excitation of H_2.)

Dendritic deposits were also found around the aperture in the ceramic. These were of a crystalline nature, grew vertically into the discharge, and were rounded at the ends where they had been melted on too close approach to the discharge. The dendrites were formed when the tube was too hot or when large concentrations of H_2 had been used. This is consistent with deposition by hydrogen reduction of copper bromide vapour at the wall (see Chapter 7).

The power was observed to peak at p_{Ne} of 20-30 torr. Greater $p_{Cu_3Br_3}$ and p_{H_2} were required at higher Ne pressures in order to reach peak power. Optimum p_{H_2} rose linearly from 0 to 4.5 torr with increasing p_{Ne} from 0 to 86 torr. This is consistent with a higher CuBr density at higher p_{Ne}, and the need to add more hydrogen to form HBr and free Cu atoms by reaction of hydrogen with the extra Cu bromide. The output beam was also weighted more heavily in favour of the yellow transition at the higher p_{Ne}. This again is related to the raised $p_{Cu_3Br_3}$, which reduces the peak T_e due to inelastic electron collisions thus favouring the yellow transition more compared to the green one. (The CuBr laser acts like an overheated elemental Cu vapour laser.)

There was a clear tendency for optimum PRF to decrease with increasing capacitance. A rising optimum $p_{Cu_3Br_3}$ accompanied the rising PRFs and the beam was more intensely yellow. High PRFs lead to more Cu depletion (or more accurately less recovery between pulses) and therefore $p_{Cu_3Br_3}$ needs to be increased. But this reduces the peak T_e and so the beam becomes more yellow.

The fast charging voltage runs revealed the maximum power of which the device was capable to be 11.4 W with the small capacitors connected. A rising $p_{Cu_3Br_3}$ accompanied the rising charging voltages. The beam was increasingly yellow and unstable with increasing p_{Ne}, R_{Ne}, PRF and V_{ch} beyond optimum, but the full bore size of the beam and the on-axis maximum persisted. This last fact is a result of the effectiveness of H_2 reduction to free Cu atoms and counter cataphoresis and axial Cu depletion.

4.11 Conclusion

There is only one mode of operation with hydrogen added to the CuBr-Ne tube. Maximum power is produced by the CuBr laser with added H_2 at the same CuBr concentration as in the LT mode of the CuBr-Ne laser. The efficacy of the addition of H_2 to enhance output power and efficiency of a CuBr laser has been demonstrated. Its influence is due to the combined actions of dissociative attachment of HBr (on plasma relaxation and electron avalanche) and hydrogen reduction of CuBr and its polymers (to free Cu atoms, especially away from the tube axis). The HT mode of the CuBr laser appears to be an unstable operating condition created by release of hydrogen or hydrogen-bearing impurity from the CuBr sidearm at temperatures at which the CuBr pressures are too high to give stable lasing. The hydrogen concentrations in the HT mode also seem to be too low for the power to reach full value.

A peak power of 11.4 W corresponding to a specific average output power of 262 $mW.cm^{-3}$ was obtained from a CuBr-Ne-H_2 laser of 43.5 cm^3 active volume. Average output power is shown to peak at buffer gas pressures in the region of 25 torr. The system demonstrates strong lasing over an extensive range of buffer gas flow rates, peaking at

around 2 litre.atm.hr^{-1} under the conditions studied. Optimum PRF is within the range 25 to 35 kHz for the storage and peaking capacitors tried.

Maximum power and efficiency were observed with the 0.52/0.24 nF capacitors connected. The maximum power of 11.4 W was seen at 30 kHz and 11 kV. This corresponds to an efficiency (BSE) of 1.21 %. At 9 kV, the average power was 9.3 W and the efficiency reached 1.47 %.

Quantity	CuBr-Ne-H_2 Laser
V_{ch} (kV)	10
$V_{t\,pk}$ (kV)	12
$i_{t\,pk}$ (A)	300
t_{ri} (ns)	44
t_{ra} (ns)	25
t_{da} (ns)	19
t_l (ns)	37
t_{rl} (ns)	13
t_{dl} (ns)	15
t_g (ns)	33
t_{rg} (ns)	13
t_{dg} (ns)	15
t_y (ns)	34
t_{ry} (ns)	11
t_{dy} (ns)	18

Table 4.1
Characteristics of $V_{ch}(t)$, $V_t(t)$, $i_t(t)$, $I_l(t)$, $I_g(t)$ and $I_y(t)$ at close to optimum conditions for P_{max} in the 13 mm bore CuBr-Ne-H_2 Laser.

(R_{Ne} and V_{ch} reference at 0.8 litre.atm.hr^{-1} and 10 kV respectively. p_{total} and PRF close to optimum at 26 torr and 29 kHz respectively. C_s/C_p 0.66/0.33 nF.)

Quantity	CuBr-Ne-H_2 Laser
Tube bore (mm)	13
Tube length (cm)	32.8
Active volume (cm^3)	43.5
P_{max} (W)	11.4
Maximum specific P ($mW.cm^{-3}$)	262
η at P_{max} (%)	1.21
C_s/C_p for P_{max} (nF)	0.52/0.24
PRF for P_{max} (kHz)	30
V_{ch} for P_{max} (kV)	11
Specific P_{in} at P_{max} ($W.cm^{-3}$)	21.7
η_{max} with C_{small} (%)	1.47
P at η_{max} (W)	9.3
V_{ch} at η_{max} (kV)	9
Specific P_{in} at η_{max} ($W.cm^{-3}$)	14.5

Table 4.2

P_{max}, η_{max}, electrical excitation and related quantities for the 13 mm bore CuBr-Ne-H_2 Laser.

(p_{total} and R_{Ne} reference at 37.5 torr and 0.8 litre.atm.hr^{-1} respectively.)

P	Peaks at a single $p_{Cu_3Br_3}$ (~ 0.33 torr in 15 torr Ne)
	Peaks at a single p_{H_2} (~ 0-4.5 torr for p_{Ne} in the range 0-86 torr, reference R_{Ne}, PRF and V_{ch} and for C_{medium})
	Peaks at a single p_{Ne} (25 torr for reference R_{Ne}, PRF and V_{ch} and for C_{medium})
	Peaks at a single R_{Ne} (2 litre.atm.hr^{-1} for reference p_{total}, PRF and V_{ch} and for C_{medium})
	Peaks at high V_{ch}
$p_{Cu_3Br_3}$ **for Peak *P***	Increases with increasing p_{Ne}, R_{Ne}, PRF and V_{ch}
p_{H_2} **for Peak *P***	Increases linearly with increasing p_{Ne}
PRF for Peak *P*	Decreases with increasing C_s/C_p
η	Peaks at low V_{ch}

Table 4.3

Additional characteristics of the 13 mm bore CuBr-Ne-H_2 laser.

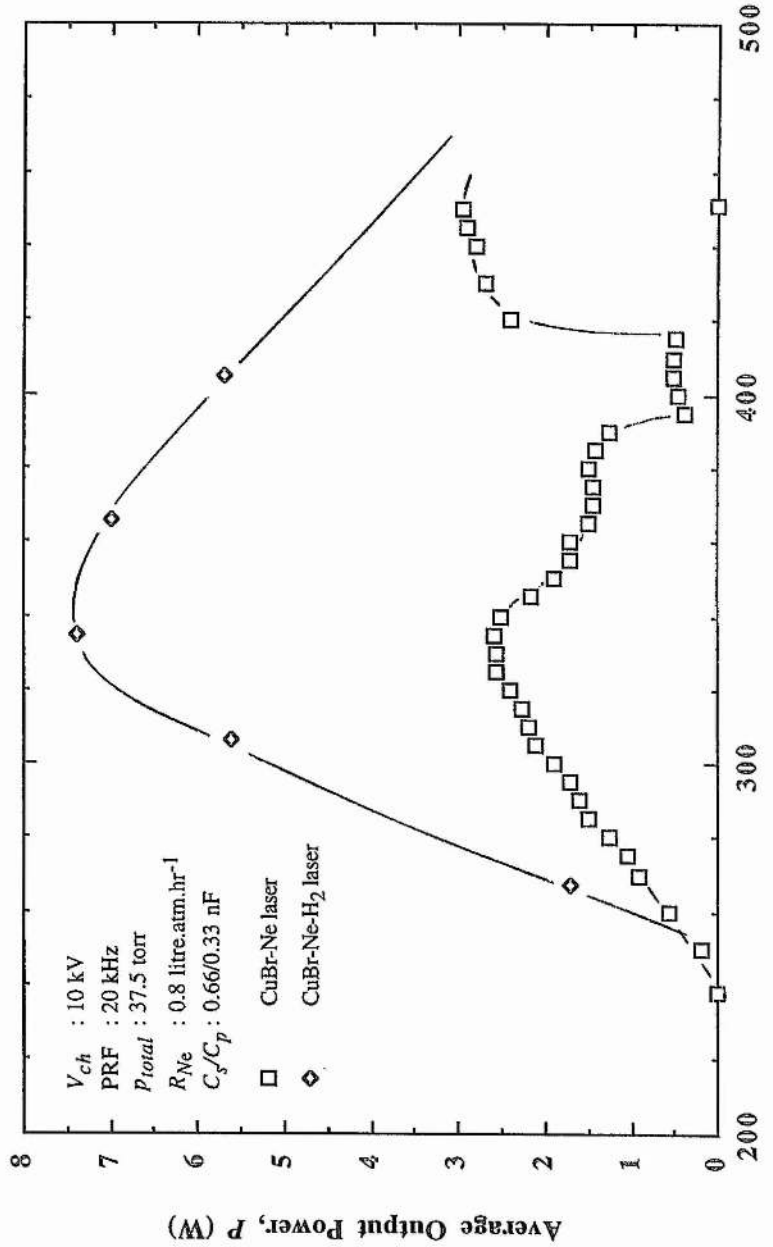

Fig. 4.1
Average output power, P, versus sidearm wall temperature, T_s, in the CuBr-Ne and CuBr-Ne-H_2 lasers.

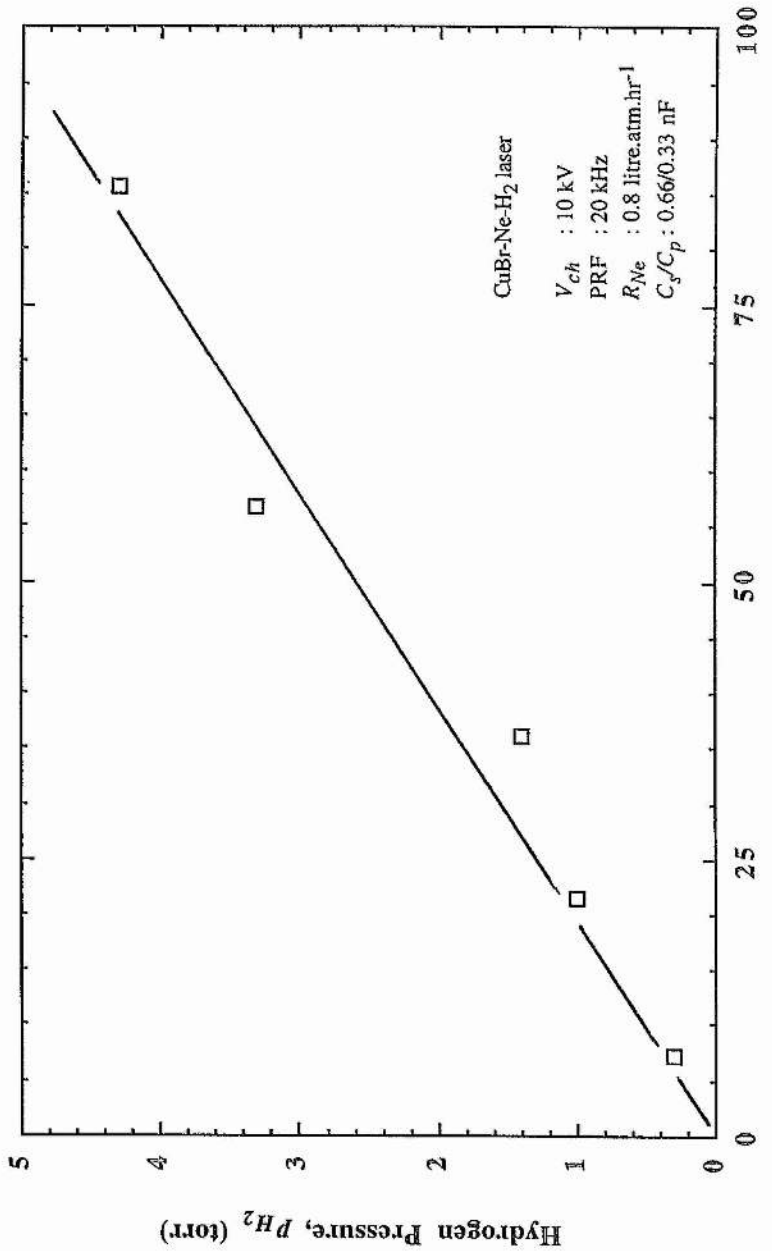

Fig. 4.2
Hydrogen pressure, p_{H_2}, versus buffer gas pressure, p_{Ne}, in the CuBr-Ne-H_2 laser.

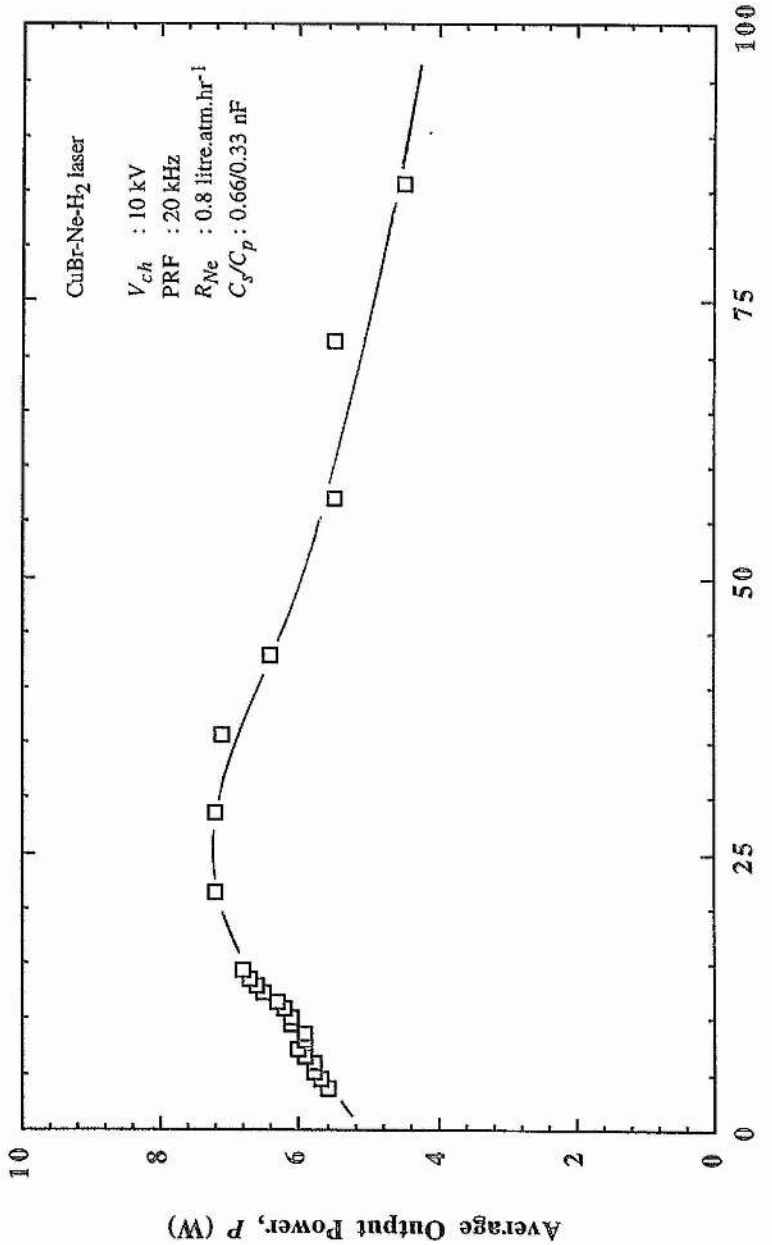

Fig. 4.3
Average output power, P, versus buffer gas pressure, p_{Ne}, in the CuBr-Ne-H_2 laser.

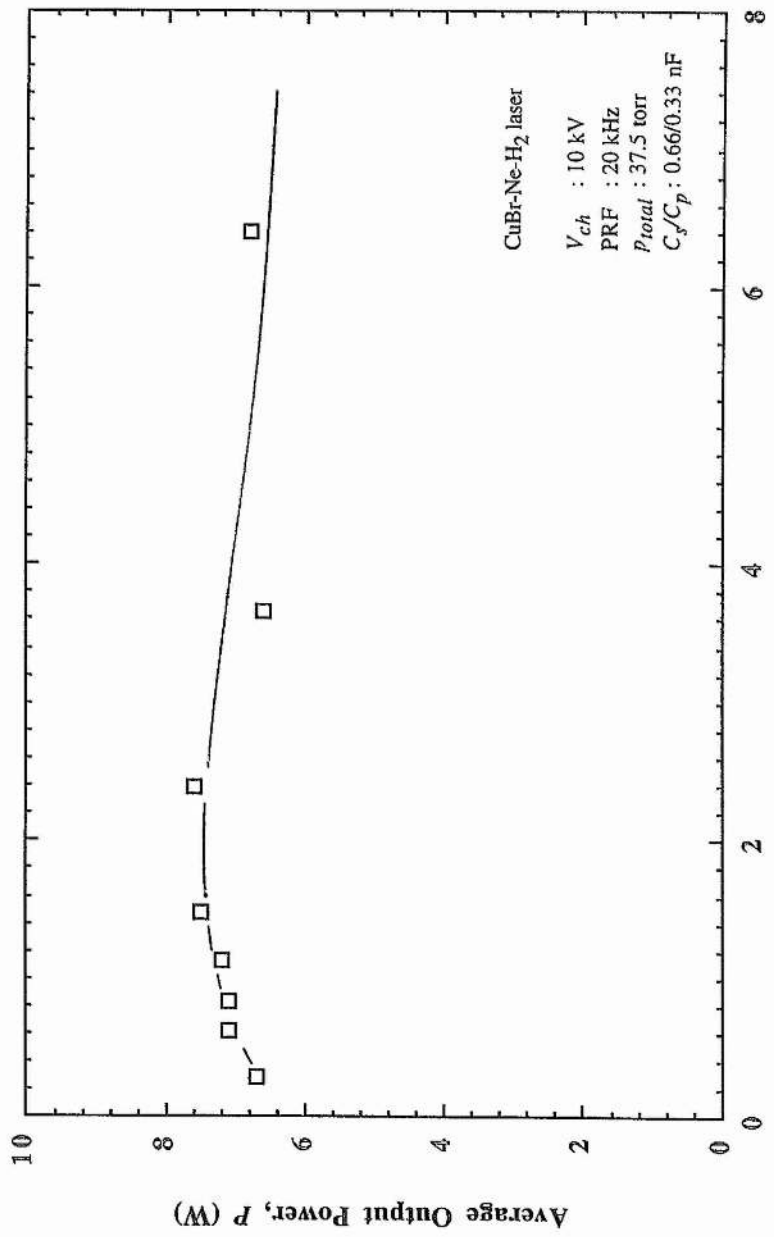

Fig. 4.4
Average output power, P, versus buffer gas flow rate, R_{Ne}, in the CuBr-Ne-H_2 laser.

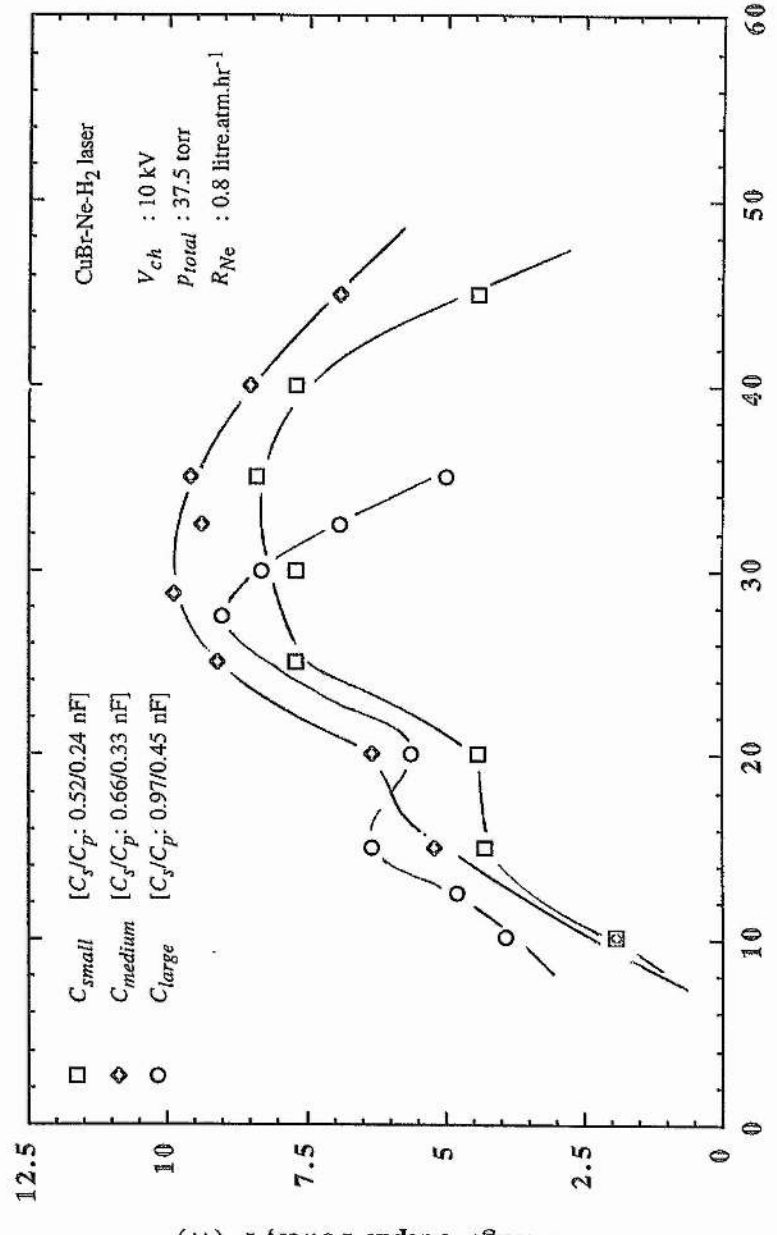

Fig. 4.5
Average output power, P, versus PRF in the CuBr-Ne-H_2 laser for three values of the storage/peaking capacitors.

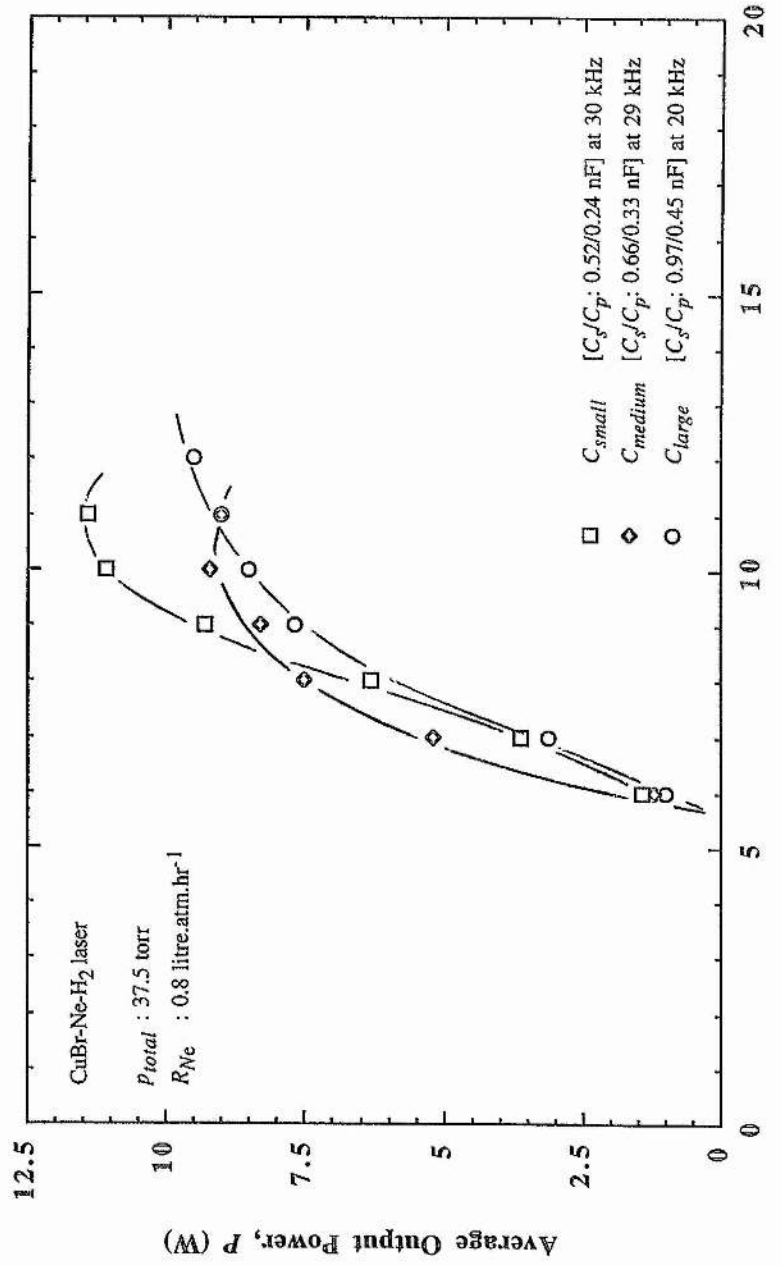

Fig. 4.6
Average output power, P, versus charging voltage, V_{ch}, in the CuBr-Ne-H_2 laser for three values of the storage/peaking capacitors, and at close to optimum PRF for each.

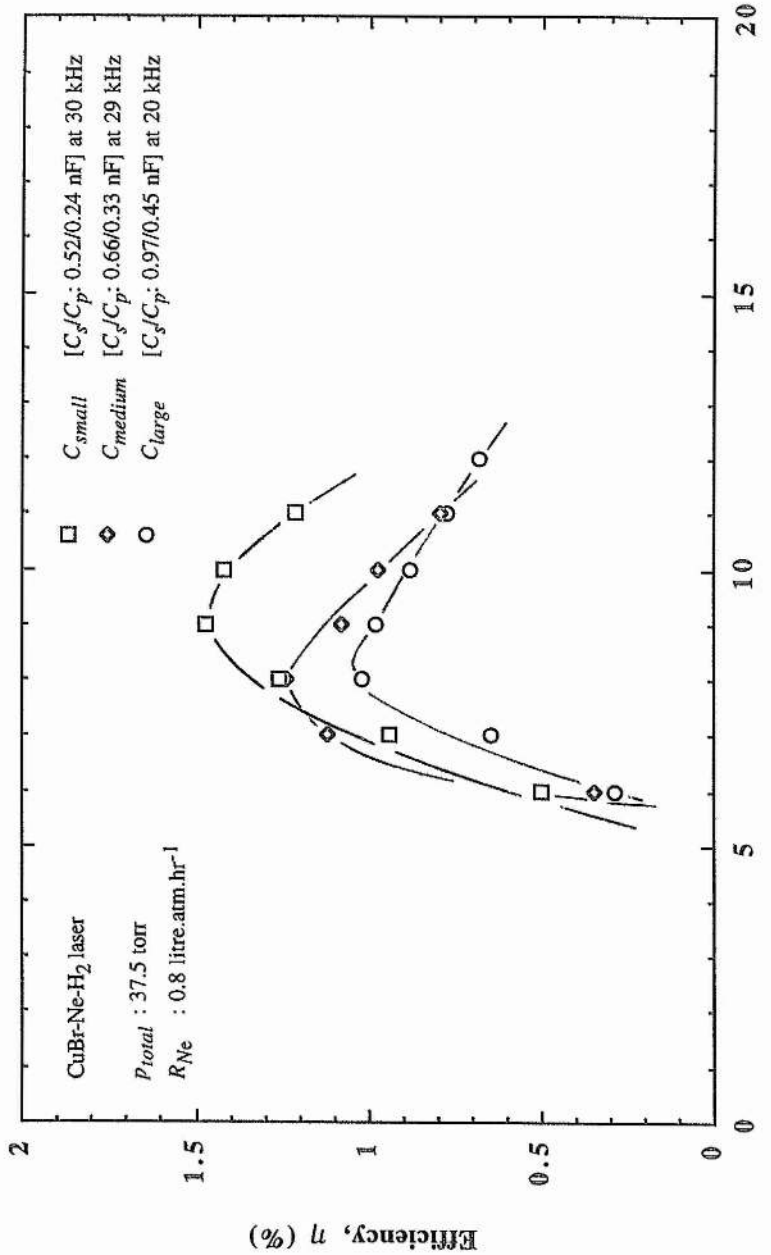

Fig. 4.7
Efficiency, η, versus charging voltage, V_{ch}, in the CuBr-Ne-H_2 laser for three values of the storage/peaking capacitors, and at close to optimum PRF for each.

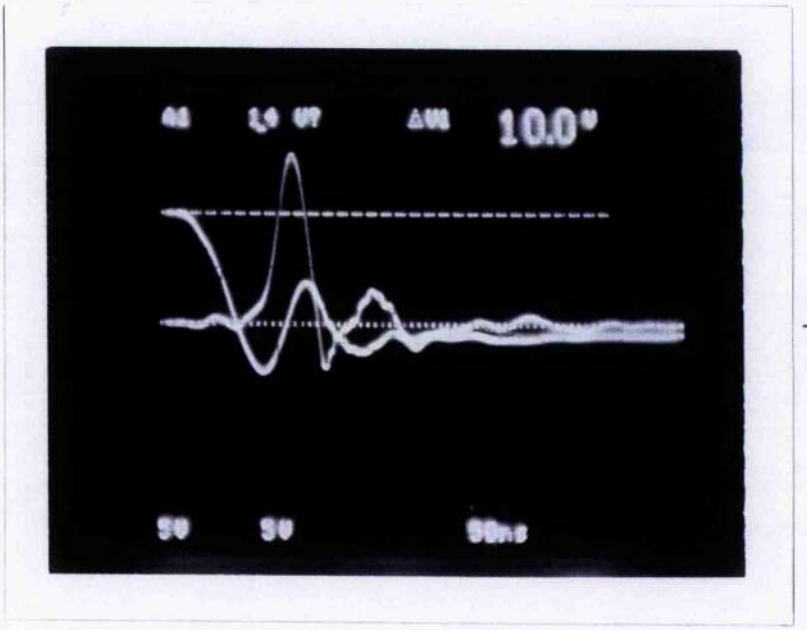

(a) $V_{ch}(t)$ and $i_t(t)$

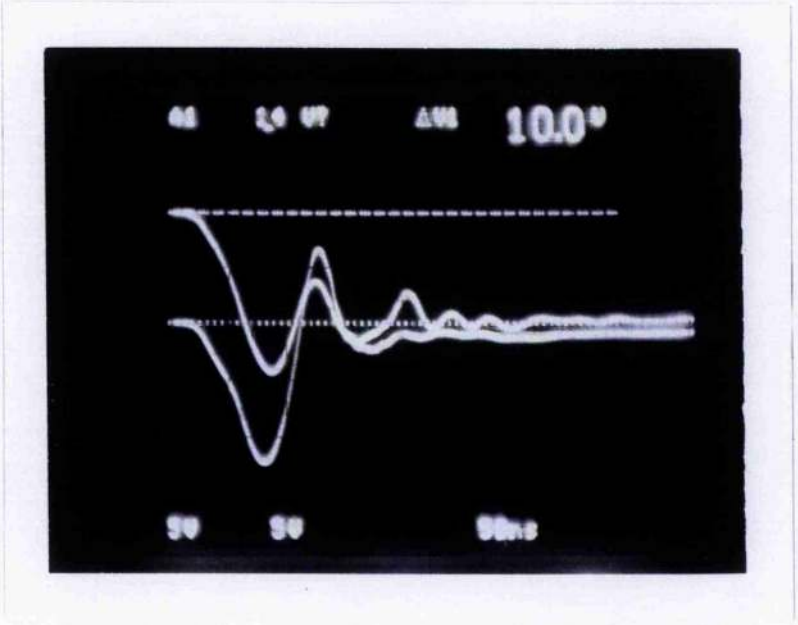

(b) $V_{ch}(t)$ and $V_t(t)$

Fig. 4.8 Oscillograms showing the charging voltage, discharge current and laser tube voltage waveforms, $V_{ch}(t)$, $i_t(t)$ and $V_t(t)$, for lasing in the CuBr-Ne-H_2 laser under close to optimum conditions for P_{max} with the 0.66/0.33 nF capacitors connected. R_{Ne}, p_{total}, PRF and V_{ch} are 0.8 litre.atm.hr^{-1}, 26 torr, 29 kHz and 10 kV respectively.

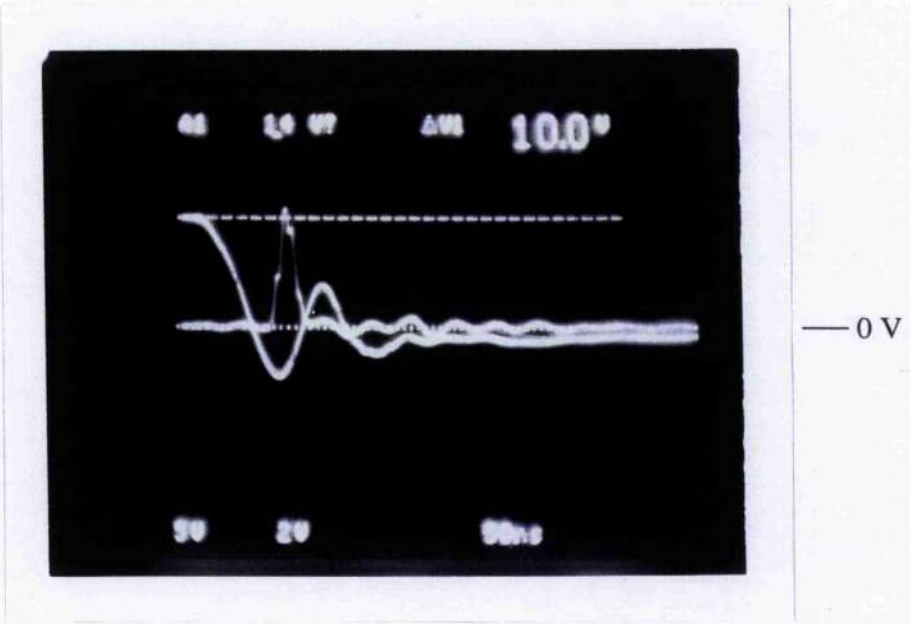

Fig. 4.9 Oscillogram showing the total laser intensity waveform, $I_l(t)$, for lasing in the CuBr-Ne-H_2 laser under close to optimum conditions for P_{max} with the 0.66/0.33 nF capacitors connected. R_{Ne}, p_{total}, PRF and V_{ch} are 0.8 litre.atm.hr^{-1}, 26 torr, 29 kHz and 10 kV respectively.
(Scales: 50 ns/div. Units of intensity arbitrary.)

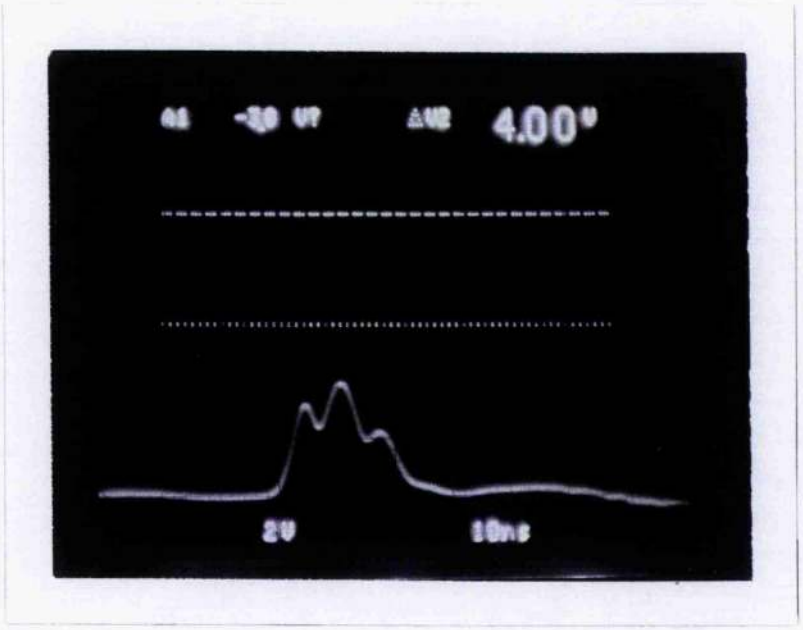

(a) $I_g(t)$

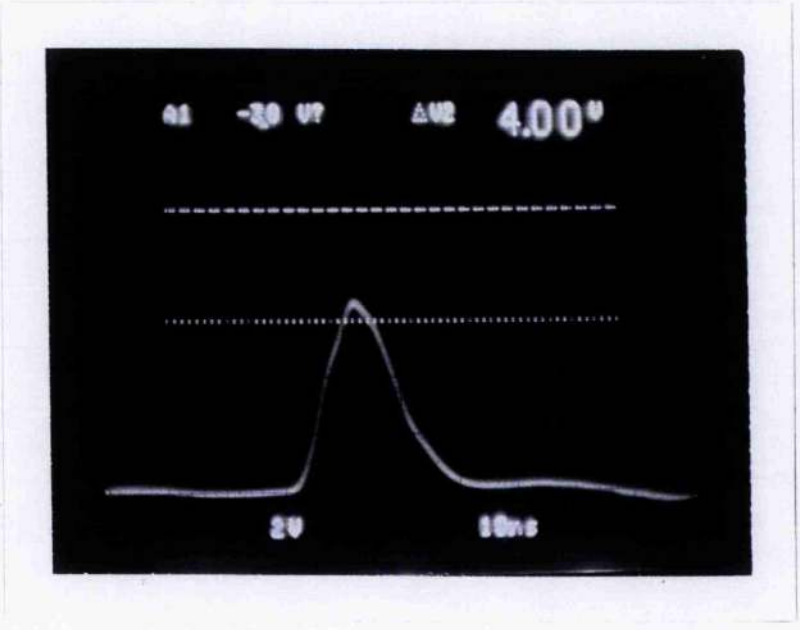

(b) $I_y(t)$

Fig. 4.10 Oscillograms showing the green and yellow laser intensity waveforms, $I_g(t)$ and $I_y(t)$, for lasing in the CuBr-Ne-H_2 laser under close to optimum conditions for P_{max} with the 0.66/0.33 nF capacitors connected. R_{Ne}, p_{total}, PRF and V_{ch} are 0.8 litre.atm.hr^{-1}, 26 torr, 29 kHz and 10 kV respectively. (Scales: 10 ns/div. Units of intensity arbitrary.)

Chapter 5

Characterization of the Cu Hybrid Laser

5.1 Introduction

Analogous with their CuBr-Ne and CuBr-Ne-H_2 laser counterparts, Cu hybrid lasers rely on electron-impact dissociation of Cu_3Br_3 vapour in the active volume of the laser tube to provide the liberated Cu atoms for lasing on the 510.6 and 578.2 nm cyclic transitions. Nevertheless, the means by which Cu_3Br_3 vapour is added to the discharge sets these lasers apart from conventional CBLs.

Cu metal sourced in the active region of a Cu hybrid laser is heated to medium wall temperatures (500-800 °C *cf.* 1500-1600 °C in CVLs) by a buffer gas discharge to which HBr gas has been added. The copper is acted on by the discharge dissociation products of the HBr which is mixed with the buffer gas in relatively small concentrations. The monomeric CuBr so formed polymerises above the Cu surface and diffuses into the discharge volume where electron impact dissociation of the polymers generates the free Cu atoms for lasing.

In this chapter, the attributes of a small, self-heated Cu hybrid laser tube, of 36.8 cm^3 active volume and 12.5 mm bore, employing a distributed configuration of the Cu metal, are discussed. In common with the other lasers investigated, the buffer gas was Ne, and a full description of the laser tube can be found in Chapter 2. The Cu hybrid laser makes an interesting comparison with the CuBr-Ne-H_2 laser, as both lasers rely on dissociative attachment of HBr and H_2 reduction for their high output powers and efficiencies. Nevertheless, there are some distinct differences in the operating characteristics of the two lasers.

A detailed study of the Cu hybrid regime of lasing has been undertaken. In the Cu

hybrid laser the HBr pressure, p_{HBr}, controls the Cu_3Br_3 pressure, $p_{Cu_3Br_3}$, in, and the extractable average output power, P, from, the laser, via the HBr/Cu reaction. After opening with some general observations on Cu hybrid laser performance, dependences of P on p_{HBr} are presented for three total gas pressures, p_{total}, for reference conditions of the buffer gas flow rate, R_{Ne}, PRF and charging voltage, V_{ch}, in order to demonstrate a single regime of operation in the Cu hybrid laser also. The dependence of P on discharge tube wall temperature, T_w, is then considered to determine the effect of wall temperature on the efficacy of the HBr/Cu reaction.

To enable useful comparisons to be made with the CuBr-Ne and CuBr-Ne-H_2 laser systems, dependences of P, efficiency (BSE), η, and p_{HBr} on the parameters of the electrical excitation and/or gas mixture have been established. Oscillograms displaying the time dependence of the discharge current, $i_t(t)$, the laser tube voltage, $V_t(t)$, and the total, green and yellow emission intensities, $I_l(t)$, $I_g(t)$ and $I_y(t)$, under close to optimum conditions for lasing are presented. Finally, the experimental trends are explained in terms of the discharge mechanisms thought to be occurring. The reader may again find it useful to read the discussion section (Section 5.12) of this chapter first.

5.2 General Observations

In the Cu hybrid laser, oscillation commenced within 1 min from a cold start as a consequence of having no sidearm to heat. The Cu_3Br_3 was generated solely in the active region which was heated very quickly by the discharge to the temperatures necessary for the Cu/HBr reaction to take place. On first addition of HBr to the discharge, the sidelight spectrum changed from bright orange-red to yellow/green as Cu atoms were liberated and excited in the discharge volume. It was necessary to adjust the charging voltage as HBr addition caused the circuit-laser matching to improve.

Peak lasing was strong at intermediate values of buffer gas pressure, p_{Ne}, (50-70 torr), at low R_{Ne} (~ 1 litre.atm.hr^{-1}) and at reference values of PRF and V_{ch}, *i.e.* 20 kHz and 10 kV. Under these conditions, laser action was initially within a narrow green annular region near the tube wall and the discharge sidelight spectrum was a uniform pale

green. With rising p_{HBr}, the annularity filled in causing the lasing intensity to become first uniform across the beam diameter and then to display an on-axis maximum. The beam was bright green and full bore size, the discharge still uniform green and stable.

On further addition of HBr, average power passed through a single peak. The yellow component of the beam intensified but the beam showed no signs of contraction. The discharge was stable and the sidelight spectrum echoed the change in beam colour. After peaking, P decreased to 0 W with further increase in p_{HBr}. There was some instability due to the increased halogen concentrations but the beam showed little constriction and faded slowly. No further regime of operation was established. The average power achieved depended on the HBr pressure, and for any fixed combination of the electrical excitation and buffer gas parameters, was optimum at a single p_{HBr}.

In Chapters 3 and 4 the effects on $i_t(t)$ of adding Cu_3Br_3 vapour to a pure Ne discharge and H_2 gas to a Ne-CuBr discharge were described in detail. In brief, addition of Cu_3Br_3 vapour to the pure Ne discharge caused a step to move down the leading edge of the main current pulse and the peak current and average power to increase simultaneously. When the step fell to ~ 10-20 % of the peak current, both current and power passed through maxima which corresponded to peak power in the LT regime. From the 10 % level to the eventual collapse of the step both discharge current and average power diminished. The effect of adding H_2 gas to the CuBr-Ne discharge was to trigger the collapse of the step if this had not yet occurred. The power remained constant until the prepulse electron current, *i.e.* the current pulse step, was 10 % of the peak current. As the step passed below this level, both current and power passed through minima before rising to greater levels than before H_2 was added. Further H_2 addition caused the current to pass through a maximum simultaneously with average power (*i.e.* peak of hydrogen regime) before diminishing and finally collapsing at p_{H_2} well beyond that at which lasing was observed to cease.

When HBr was added to the pure Ne discharge the above effects were combined as hydrogen and bromine were introduced together in a one-to-one ratio. A step was observed to move down the leading edge of the current pulse coincidently with the rise of

the peak current and average output power to even greater levels than observed in the CuBr-Ne-H_2 laser. When the step on the current pulse fell to the 10 % level, both the discharge current and average power passed through a single peak, reducing along with the step height with increasing p_{HBr} thereafter. No further spell of lasing occurred on collapse of the step.

In common with the CuBr-Ne and CuBr-Ne-H_2 systems, the Cu hybrid laser lased continuously over a number of intervals of up to 12 hr each. The laser discharge was stable but the average power reduced somewhat over long time intervals due to dendrite formations in the active region. Dendrites grew vertically from the edges and centres of the Cu pieces and were 'tree-like' in structure, occurring somewhat numerously due to the increased availability of deposition sites, *i.e.* the discharge-facing surfaces of the Cu pieces. The dendrites would melt periodically on too close approach to the discharge resulting in the periodic reinstatement of peak P. Their growth was noted to accelerate when the tube was operating at high wall temperatures or when the HBr pressure was large.

During operation, greatest consumption of Cu took place at the anode. Downstream pieces displayed marginal erosion or growth, essentially at random. As hydrogen and bromine were introduced to the system in a one-to-one ratio, the need to optimise first one then the other was alleviated, leading to simpler control of the laser output. There was still evidence of window contamination at very high and very low buffer gas pressures and flow rates. On shutting off the HBr supply, the average power peaked in the reverse direction before falling to 0 W. Cessation of lasing always occurred within timescales comparable to those at start up, *i.e.* within 1 min.

The operating temperature of the tube was, as usual, a balance between those temperatures hot enough to prevent CuBr formation in active region and those cool enough to discourage Cu dendrite formation. The ceramic remained clean of CuBr and Cu deposits, indicating that the wall temperatures of typically 500-800 °C were sufficient. Insulation was increased near the inlet to prevent copper bromide formation and deposition, and thus Br removal, at such a crucial location.

At non-optimum conditions of the gas and excitation parameters, discharge and beam effects were encountered which were similar to those occurring in the CuBr-Ne-H_2 laser tube, *i.e.* beam/discharge instability, 'standing waves' of sidelight intensity, lack of beam directionality, high-divergence beam components and current 'hopping', but these were less pronounced and more easily controlled. The one-to-one ratio of hydrogen to halogen atoms, a virtual absence of CuBr deposits on the ceramic and an ability to control the CuBr concentration by simple control of the HBr pressure account for this. Peak power was not found to be critical on a single wall temperature, and could be achieved quite readily over a 500-800 °C range.

In instances where the wall temperature was excessive (> 800 °C), a fluctuating average power was occasionally observed for fixed gas/excitation conditions. With increasing insulation, output powers turned over at reduced charging voltages and PRFs indicating a maximum tube temperature for effective lasing.

5.3 Dependence of Average Output Power on HBr Pressure

The medium sized capacitors, C_{medium}, (0.66 nF/0.33 nF) were again selected to illustrate the general trends. The dependence of average output power on HBr pressure was established at three different total gas pressures of 15, 52.5 and 97.5 torr. HBr gas was added in stages to a Ne discharge operating at each of these pressures in turn. There was no difficulty in controlling p_{HBr} via a needle valve (because of the large molecular diameter of HBr) and both p_{Ne} and p_{HBr} were calculated by considering the ratio of one flow rate, say R_{Ne}, to the sum of both flow rates, at each p_{total}. After each addition of HBr, p_{total} was readjusted to its initial value and average output power recorded.

The resulting plots of P versus p_{HBr} are shown in Fig. 5.1 for each p_{total} considered. Average output power passes through a single peak in each case at a critical p_{HBr} which rises with increasing total gas pressure. This confirms the earlier assertion that only one regime of lasing exists as regards HBr pressure. Similar dependences of P on p_{HBr} are readily attained over an extensive range of buffer gas and electrical excitation conditions. The highest power was observed at 52.5 torr in the above examples.

5.4 Dependence of Average Output Power on Wall Temperature

As the HBr/Cu reaction takes place at the discharge tube wall it is important to consider the effect of wall temperature, T_w, on the efficacy of the lasing process. With the medium sized capacitors connected and p_{total} returned to its reference value of 37.5 torr, the HBr pressure was increased and found to be optimum at ~ 2 torr.

The influence of T_w on P was next determined. The laser tube was wrapped in heavy thermal insulation and the buffer gas discharge repetitively pulsed at a PRF of 35 kHz (shown in Section 5.8 below to be close to optimum for C_{medium} at reference values of the other parameters). When the outside wall temperature reached 440 °C, 2 torr HBr was added and lasing commenced instantaneously. With p_{HBr} still fixed at 2 torr, average output power was recorded at ~ 10-20 °C intervals as T_w continued to increase up to the maximum temperature of 830 °C considered. The time interval over which T_w increased from 400 to 830 °C was 15-20 min. Average output power versus wall temperature is plotted in Fig. 5.2. Lasing saturated at an average power of almost 11 W at ~ 550 °C. The power remained within a ± 1 W spread up to the maximum temperature of 830 °C.

5.5 Optimum HBr Pressure Versus Buffer Gas Pressure

With the 0.66/0.33 nF capacitors connected, optimum HBr pressure was established at a number of total gas pressures in the range 15 to 97.5 torr. The actual values of p_{HBr} and p_{Ne} at each p_{total} were found from flow rate and total gas pressure considerations as before. HBr pressure versus buffer gas pressure is shown in Fig. 5.3. HBr pressure increases linearly with increasing p_{Ne}, rising from 1.4 to 3.2 torr over the 13.6-94.5 torr range of p_{Ne} considered. The slope of the plot is not steep and, if extrapolated, will cross the p_{HBr} axis at a finite value of ~ 1.2 torr (*cf.* the plot of p_{H_2} versus p_{Ne} for the CuBr-Ne-H_2 laser which passes through the origin).

5.6 Average Output Power Versus Buffer Gas Pressure

When the HBr pressure was optimised at each total gas pressure considered in the

investigation of p_{HBr} versus p_{Ne} (Section 5.5), the average output power achieved was also noted. Average output power versus buffer gas pressure is shown in Fig. 5.4. The average powers all lie on a smooth curve which rises steadily from ~ 5.5 W at 13.6 torr p_{Ne} to ~ 8.4 W at 50 torr p_{Ne}, peaks in the region of 60 torr and then gradually reduces as the maximum p_{Ne} of 94.5 torr is reached.

5.7 Average Output Power Versus Buffer Gas Flow Rate

With the 0.66/0.33 nF capacitors connected, the dependence of average power on buffer gas flow rate was obtained for R_{Ne} in the range 0.5 to 7.7 litre.atm.hr^{-1}. Average power versus buffer gas flow rate is shown in Fig. 5.5. The plot demonstrates that the Cu hybrid laser favours low R_{Ne} in the region of 1 litre.atm.hr^{-1}. There is a sharp rise in power with increasing flow rate to 1 litre.atm.hr^{-1} but the reduction in power with increasing flow rate beyond 1 litre.atm.hr^{-1} is more gradual. At the maximum R_{Ne} of 7.7 litre.atm.hr^{-1} power is less than 50 % of its peak value.

5.8 Average Output Power Versus PRF for Three Values of the Storage/Peaking Capacitors

Average output power versus PRF was next considered for each of the small, medium and large capacitor pairs. The PRF was varied in increasing multiples of approximately 2.5 kHz alternately higher then lower than the reference PRF of 20 kHz. The HBr pressure was readjusted as necessary at 20 kHz only. The input powers at 20 kHz were 0.89, 1.02 and 1.24 kW for the small, medium and large capacitors respectively.

Plots of P versus PRF are shown in Fig. 5.6 for all three capacitor pairs. The optimum PRFs are 41, 38 and 32 kHz for C_{small}, C_{medium} and C_{large} respectively showing the by now familiar tendency for optimum PRF to decrease with increasing capacitance.

5.9 Average Output Power and Efficiency Versus Charging Voltage for Three Values of the Storage/Peaking Capacitors

For each set of capacitors, average output power was studied as a function of charging voltage. In each case the PRF was close to optimum. Charging voltage was varied in increasing multiples of approximately 1 kV alternately higher then lower than its reference value of 10 kV. The HBr pressure was readjusted as necessary at the reference V_{ch} of 10 kV only.

Plots of P versus V_{ch} at close to optimum PRF are presented for all three pairs of capacitors in Fig. 5.7 and reveal the maximum power levels which may be extracted from the Cu hybrid laser. A maximum average output power, P_{max}, of 12.8 W was achieved at 35 kHz and 11 kV with the 0.66/0.33 nF capacitors connected and exceeds the maximum powers obtained with C_{small} and C_{large} by almost 3 W in either case. Average power rises rapidly at low charging voltages and peaks in the vicinity of 11, 10.5 and 10 kV for C_{small}, C_{medium} and C_{large} respectively.

Using equation (3.1) and the data from Fig. 5.7, efficiency was calculated at each V_{ch} considered during the P versus V_{ch} experimental runs. Plots of η versus V_{ch} at close to optimum PRF are shown in Fig. 5.8 for all three capacitor pairs. Fig. 5.8 demonstrates a rapid rise in efficiency at lower charging voltages. Efficiency peaks at 7 kV and 6 kV for the medium and large capacitors respectively. Few points were taken with C_{small} connected so that the peak cannot be seen in this case. Beyond optimum V_{ch}, efficiency reduces gradually and linearly with increasing charging voltage. The efficiency curves merge at low V_{ch} but spread out in the vicinity of optimum V_{ch}. At large charging voltages there is some indication that the curves will eventually merge. Peak efficiencies are 1.66 and 1.09 % for the medium and large capacitor pairs respectively.

The Cu hybrid laser appears to favour the 0.66/0.33 nF capacitors in terms of both average power and efficiency. From the plots of P versus V_{ch} and η versus V_{ch} for C_{medium} we find that η at that V_{ch} corresponding to P_{max}, *i.e.* 11 kV, is 0.92 % while P at that V_{ch} corresponding to η_{max} (1.66 %), *i.e.* 7 kV, is 9.4 W.

5.10 Average Output Power and Efficiency Versus Charging Voltage at Five Values of the PRF

With the optimum capacitors (0.66/0.33 nF) connected, charging voltage runs were carried out at several additional PRFs, 15, 20, 25, and 30 kHz, all lower than the optimum PRF of 38 kHz for the medium capacitors. Average power was recorded as a function of charging voltage at each PRF and the resulting plots are shown in Fig. 5.9 together with the plot of P versus V_{ch} at 35 kHz discussed in Section 5.9. Optimum charging voltage is > 16, 15, 14, 12 and 11 kV at 15, 20, 25, 30 and 35 kHz respectively. Optimum charging voltage therefore decreases with increasing PRF.

From the data of Fig. 5.9, efficiency was calculated at each V_{ch} considered during the P versus V_{ch} experimental runs at 15, 20, 25, 30 and 35 kHz. The resulting plots of η versus V_{ch} are shown in Fig. 5.10. Efficiency peaks at 9 kV for a 15 kHz PRF, at 7.5 kV for a 20 kHz PRF and at 7 kV for the remaining PRFs. Hence the optimum charging voltage for maximum efficiency shows some tendency to decrease with increasing PRF. The curves have the same general form as in Fig. 5.8. but are scattered at ≤ optimum V_{ch}. The curves cross at higher V_{ch} at which power is optimum.

5.11 Features of the Discharge Current, Laser Tube voltage and Total, Green and Yellow Intensity Waveforms

To complete the study of the Cu hybrid laser, oscillograms of discharge current, laser tube voltage, and emission intensity were taken, together with the charging voltage waveform, $V_{ch}(t)$, under approximate conditions for P_{max}. The 0.66/0.33 nF capacitors were connected while p_{total}, R_{Ne}, V_{ch} and PRF were 37.5 torr, 0.8 litre.atm.hr^{-1}, 10 kV and 35 kHz respectively.

The discharge current, laser tube voltage and charging voltage waveforms are shown in Fig. 5.11. Oscillogram (a) shows $i_t(t)$ and $V_{ch}(t)$. The step on the leading edge of the current pulse has just fallen below ~ 10 % of the peak current of ~ 300 A but is still visible. Oscillogram (b) displays the $V_t(t)$ and $V_{ch}(t)$ waveforms. $V_t(t)$ reaches ~ 82 % of $V_{ch}(t)$, *i.e.* 8.2 kV. Comparing oscillograms (a) and (b) reveals a delay of only ~ 20 ns

between first rise of $V_t(t)$ and the subsequent rise of $i_t(t)$ because of the step. The delay in the current avalanche, t_{da} , relative to the onset of the current pulse is long at ~ 40 ns because of the step (*cf.* ~ 19 ns in the CuBr-Ne-H_2 laser) and $V_t(t)$ is already peaking when it begins. Likewise $V_t(t)$ is zero when $i_t(t)$ peaks. The total current pulse risetime, t_{ri}, is ~ 65 ns yielding a figure for the avalanche risetime, t_{ra}, of ~ 25 ns (*cf.* 25 ns in the CuBr-Ne-H_2 laser also).

Fig. 5.12 shows the total intensity waveform, $I_l(t)$, together with its ground level. Lasing begins on the leading edge of the current pulse. The risetime to peak intensity, t_{rl}, is ~ 11 ns. The rise to and fall from peak intensity occur at approximately the same rate. Peak intensity occurs well before the current pulse has peaked and some nanoseconds after the laser tube voltage pulse has peaked. Smaller peaks are displayed to either side of the principal total intensity peak. The total intensity pulse duration, t_l, is ~ 27 ns. The delay in $I_l(t)$, t_{dl}, relative to the onset of the current pulse is ~ 36 ns *i.e.* lasing commences ~ 4 ns before the current avalanche proper begins.

Fig. 5.13 shows the green and yellow intensity waveforms, $I_g(t)$ and $I_y(t)$, together with their ground lines. The green and yellow pulses begin at different times. The start of the green pulse is coincident with the beginning of the total intensity pulse and its main peak occurs ~ 11 ns into the pulse. Smaller peaks occur at regular intervals of ~ 7 ns to either side of the main peak. The total duration of the green pulse, t_g, its risetime, t_{rg}, and its delay, t_{dg}, relative to the onset of the current pulse, are 26, 11 and 36 ns respectively.

The yellow pulse begins ~ 1 ns after the green pulse and its main peak occurs ~ 13 ns into the total intensity pulse. It displays a small peak to one side of the main peak at an interval of ~ 7 ns. The total duration of the yellow pulse, t_y, its risetime, t_{ry}, and its delay, t_{dy}, relative to the onset of the current pulse, are 26, 12 and 37 ns respectively. The above information relating to the discharge current, laser tube voltage and total, green and yellow intensity waveforms at close to optimum conditions for P_{max} is summarised in Table 5.1.

5.12 Discussion

Addition of HBr caused the discharge impedance to rise and matching to improve. This was evinced by the rise in tube temperature of ~ 100 °C. Though lasing was initially annular, the annularity filled in with increasing p_{HBr}, becoming uniform, then Gaussian on approach to peak power. The beam was increasingly yellow towards the peak, but unconstricted. Beyond peak power there was still very little constriction and the beam faded slowly with rising p_{HBr}.

Dendrites were more common in the Cu hybrid laser because there were more deposition sites (the Cu pieces, which were hotter than the wall). The dendrites grew into the discharge and were 'tree-like' in nature. They were most numerous when the tube was running too hot or when the HBr levels were high. However, the inner wall of the ceramic was clean on cessation of lasing.

The current pulse exhibited a step which moved down the leading edge with increasing p_{HBr}. At the 10 % height, the current and power were maximum, demonstrating values similar to those of the CuBr-Ne-H_2 laser (after collapse of the step). On collapse of the step both the power and current reduced and did not recover. This behaviour is consistent with the increasing removal of prepulse electrons by attachment and recombination processes as HBr pressure was raised, and an increase in discharge impedance.

For the parameters PRF or V_{ch}, any increase in their values causes a depletion of Cu atoms by one of a number of mechanisms, which must be remedied by increasing the pressure of HBr, as found in practice. The laser beam was very yellow at high PRFs (> 30 kHz) which might indicate a reduced peak T_e.

At higher p_{Ne}, the influence of HBr on the peak T_e (T_e at electron avalanche) counters any fall in the parameter as Ne pressure is raised. The power was observed to peak at a buffer gas pressure of 60 torr, which was considerably larger than the optimum pressures of the CuBr-Ne and CuBr-Ne-H_2 lasers. Output power was still high at 100 torr. This indicates that the action of HBr on the EEDF is more effective in the hybrid laser. In Chapter 6, we will see that the partial pressure of HBr in a hybrid laser is higher than that

in a CuBr-Ne-H_2 laser.

The peak power was not critical on a single wall temperature. The power was within ± 1 W over a 550-830 °C temperature range, becoming maximum at 550 °C. With increasing insulation, the PRFs turned over at reduced V_{ch} so that there is a maximum temperature for effective lasing which must be beyond the wall temperature of 830 °C. The dependence of power on wall temperature shows that the copper bromide equilibrium pressure above the copper surfaces and the kinetic processes are independent of wall temperature in the range 550-830 °C.

The pressure p_{HBr} increased linearly from 1.4 to 3.2 torr with increasing p_{Ne} from 13.6-94.5 torr, but the slope of the plot is not steep and does not go through the origin. It rather crosses the axis at ~ 1.2 torr. This implies that there is a minimum p_{HBr} needed for the reaction to produce sufficient Cu atoms for the inversion, and is related to the fact that the HBr performs two roles in the discharge: first to seed the volume with Cu atoms by the in situ formation of CuBr, and second to enhance the kinetics by dissociative attachment and hydrogen reduction.

There was a clear tendency for optimum PRF to decrease with increasing capacitance C_s and charging voltage V_{ch}. The same arguments apply here as for the CuBr-Ne and CuBr-Ne-H_2 lasers, where there is a trade-off between PRF, V_{ch} and C_s for maximum power as a result of the increase with all three parameters of the depletion of Cu atoms from the centre of the discharge. The efficiency peaked at low charging voltages (where Cu depletion was small) and was much reduced at those charging voltages where maximum power was observed in each case.

As in the cases of the CuBr-Ne laser and the CuBr-Ne-H_2 laser, lasing occurs on the leading edge of the current pulse primarily during the current avalanche, because that is when the applied tube voltage peaks and T_e is highest so that the upper laser levels are pumped the fastest.

5.13 Conclusion

A laser power of 12.8 W is reported from a Cu hybrid laser tube of 36.8 cm^3 active

volume and 12.5 mm bore. This corresponds to a record specific average output power of 348 $mW.cm^{-3}$ for any copper laser of ≥12.5 mm bore, which is a factor of 4.3 improvement over the CuBr-Ne laser and a factor of 1.3 improvement over the CuBr-Ne-H_2 laser tube. In the Cu hybrid laser, the optimum gas pressure was 60 torr for the conditions studied. The system favours low buffer gas flow rates of ~ 1 $litre.atm.hr^{-1}$. Optimum PRF is within the range 30 to 45 kHz for the values of storage and peaking capacitance tried.

Peak power and efficiency were observed with the 0.66/0.33 nF capacitors connected. The peak power of 12.8 W was observed at a PRF of 35 kHz and at a charging voltage of 11 kV. This corresponds to an efficiency (BSE) of 0.92 %. At 7 kV, the average power was 9.4 W and the efficiency reached 1.66 %. This represents a factor of 2.3 improvement over the peak efficiency of 0.71 % found for the CuBr-Ne system and a factor of 1.1 improvement over the peak efficiency of 1.47 % achieved in the CuBr-Ne-H_2 system.

Quantity	Cu Hybrid Laser
V_{ch} (kV)	10
$V_{t\,pk}$ (kV)	8.2
$i_{t\,pk}$ (A)	300
t_{ri} (ns)	65
t_{ra} (ns)	25
t_{da} (ns)	40
t_l (ns)	27
t_{rl} (ns)	11
t_{dl} (ns)	36
t_g (ns)	26
t_{rg} (ns)	11
t_{dg} (ns)	36
t_y (ns)	26
t_{ry} (ns)	12
t_{dy} (ns)	37

Table 5.1
Characteristics of $V_{ch}(t)$, $V_t(t)$, $i_t(t)$, $I_l(t)$, $I_g(t)$ and $I_y(t)$ at close to optimum conditions for P_{max} in the 12.5 mm bore Cu hybrid laser.

(p_{total}, R_{Ne} and V_{ch} reference at 37.5 torr, 0.8 litre.atm.hr^{-1} and 10 kV respectively. PRF close to optimum at 35 kHz. C_s/C_p 0.66/0.33 nF.)

Quantity	Cu Hybrid Laser
Tube bore (mm)	12.5
Tube length (cm)	30
Active volume (cm^3)	36.8
P_{max} (W)	12.8
Maximum specific P ($mW.cm^{-3}$)	348
η at P_{max} (%)	0.92
C_s/C_p for P_{max} (nF)	0.66/0.33
PRF for P_{max} (kHz)	35
V_{ch} for P_{max} (kV)	11
Specific P_{in} at P_{max} ($W.cm^{-3}$)	38
η_{max} with C_{medium} (%)	1.66
P at η_{max} (W)	9.4
V_{ch} at η_{max} (kV)	7
Specific P_{in} at η_{max} ($W.cm^{-3}$)	15.4

Table 5.2

P_{max}, η_{max}, electrical excitation and related quantities for the 12.5 mm bore Cu hybrid laser.

(p_{total} and R_{Ne} reference at 37.5 torr and 0.8 litre.atm.hr^{-1} respectively)

P	Peaks at a single p_{HBr} (~ 1.4-3.2 torr for p_{Ne} in the range 13.6-94.5 torr, reference R_{Ne}, PRF and V_{ch} and for C_{medium})
	Peaks at a single p_{Ne} (~ 60 torr for reference R_{Ne}, PRF and V_{ch} and for C_{medium})
	Peaks at a single R_{Ne} (~ 1 litre.atm.hr^{-1} for reference p_{total}, PRF and V_{ch} and for C_{medium})
	Peaks at high V_{ch}
	Constant to within ± 1 W with increasing T_w from ~ 550-830 °C
p_{HBr} for Peak P	Increases with increasing p_{Ne}, PRF and V_{ch}
	Increases linearly with increasing p_{Ne}
PRF for Peak P	Decreases with increasing C_s/C_p
V_{ch} for Peak P	Decreases with increasing PRF
η	Peaks at low V_{ch}
V_{ch} for Peak η	Decreases with increasing PRF

Table 5.3

Additional characteristics of the 12.5 mm bore Cu hybrid laser.

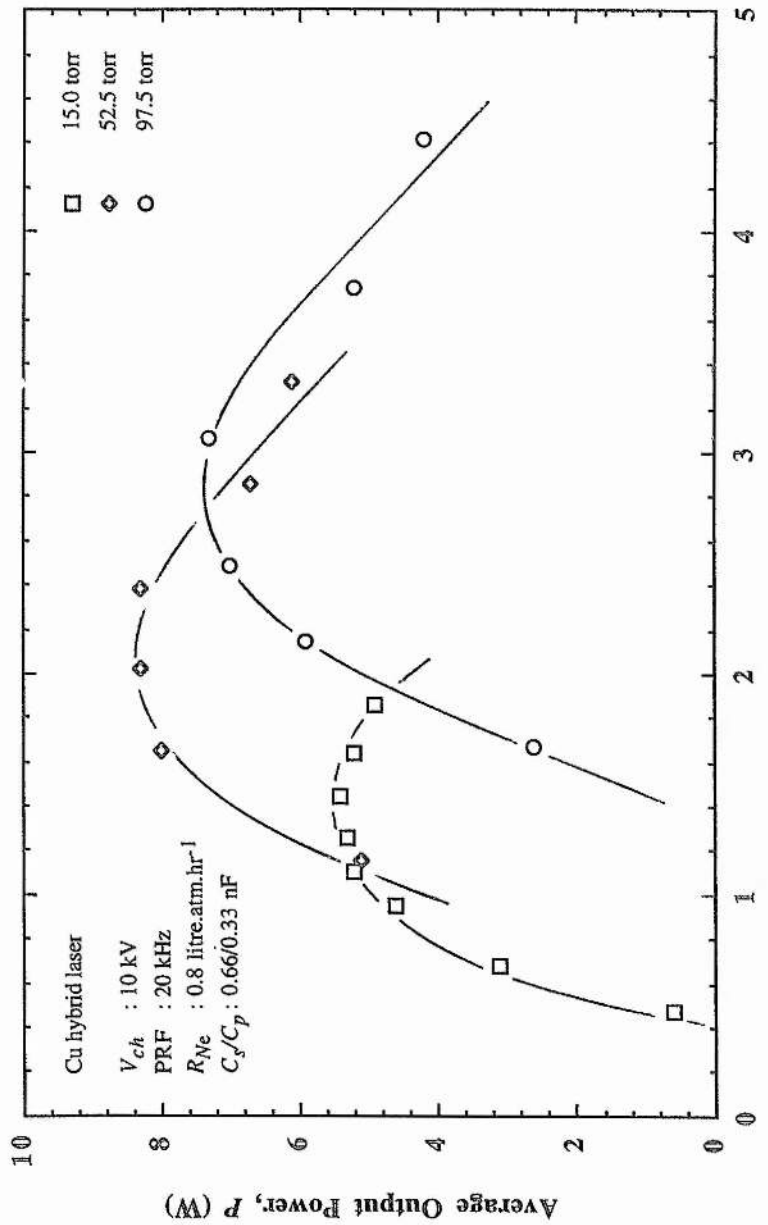

Fig. 5.1

Average output power, P, versus hydrogen bromide pressure, p_{HBr}, in the Cu hybrid laser at three values of the total gas pressure, p_{total}.

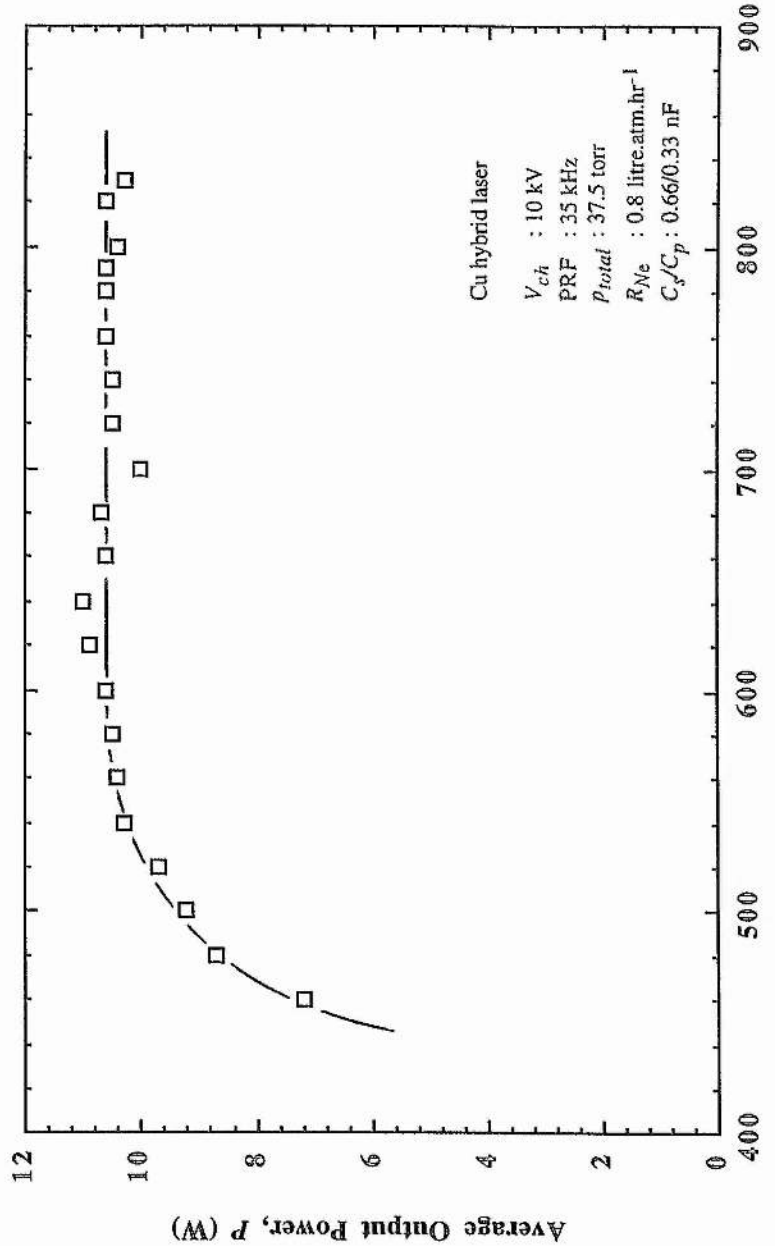

Fig. 5.2
Average output power, P, versus discharge tube wall temperature, T_w, in the Cu hybrid laser.

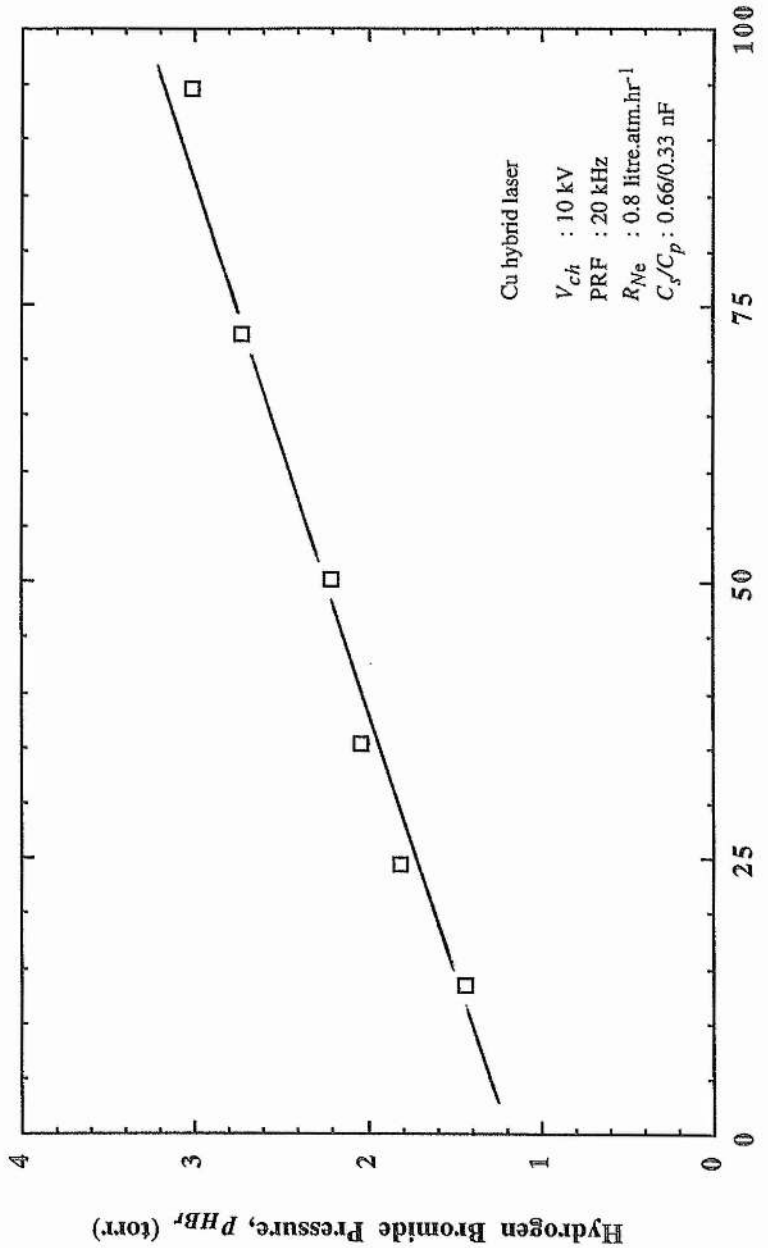

Fig. 5.3
Hydrogen bromide pressure, p_{HBr}, versus buffer gas pressure, p_{Ne}, in the Cu hybrid laser.

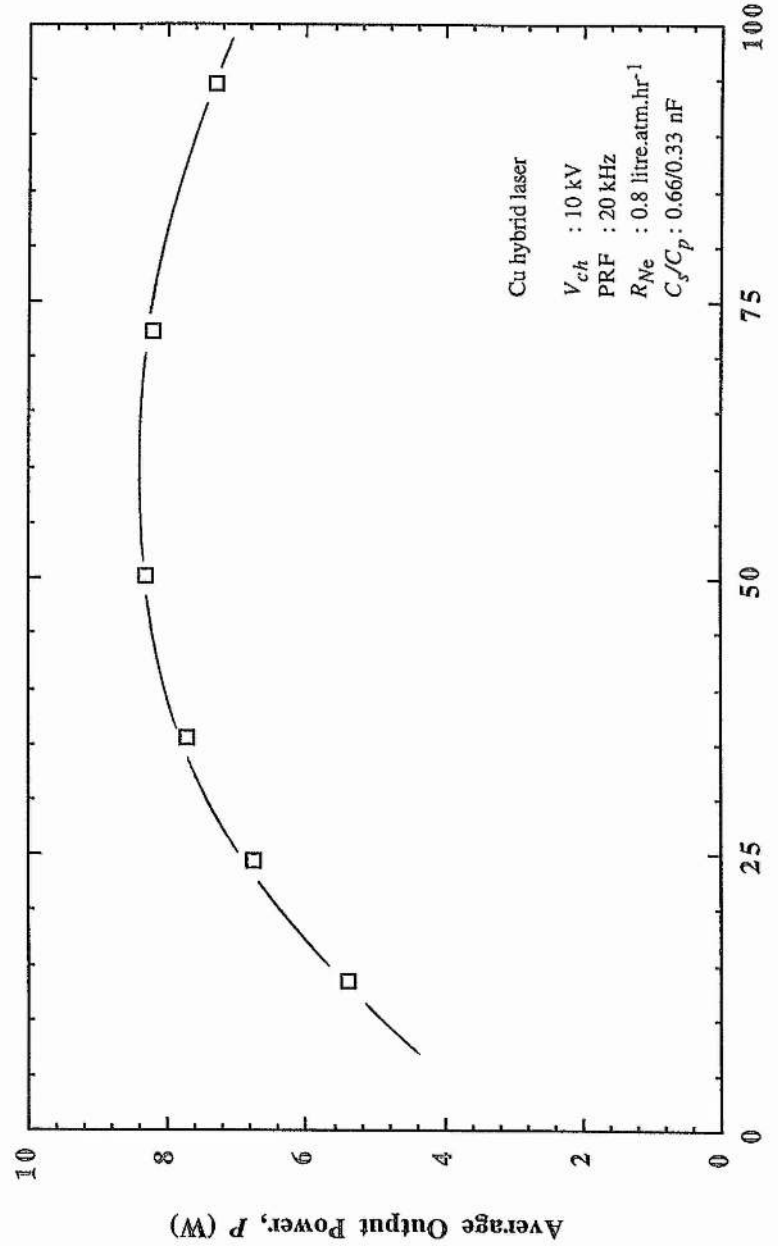

Fig. 5.4
Average output power, P, versus buffer gas pressure, p_{Ne}, in the Cu hybrid laser.

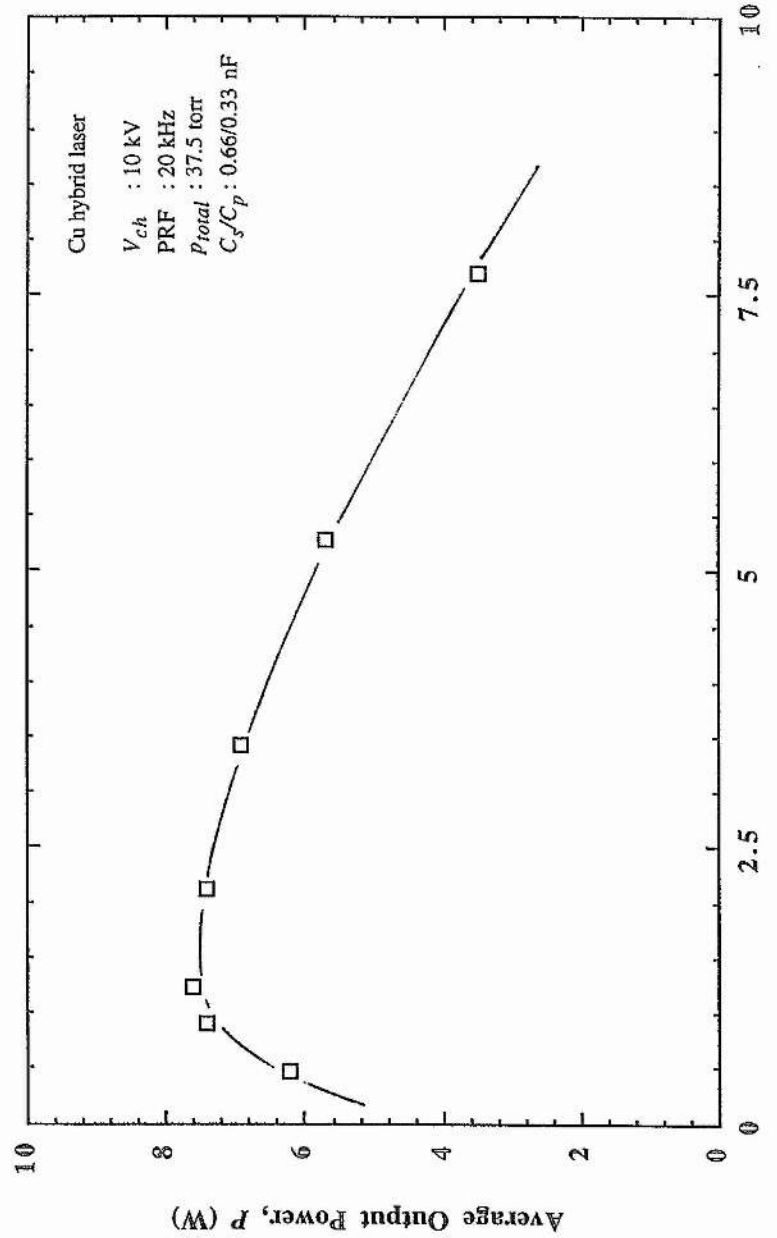

Fig. 5.5
Average output power, P, versus buffer gas flow rate, R_{Ne}, in the Cu hybrid laser.

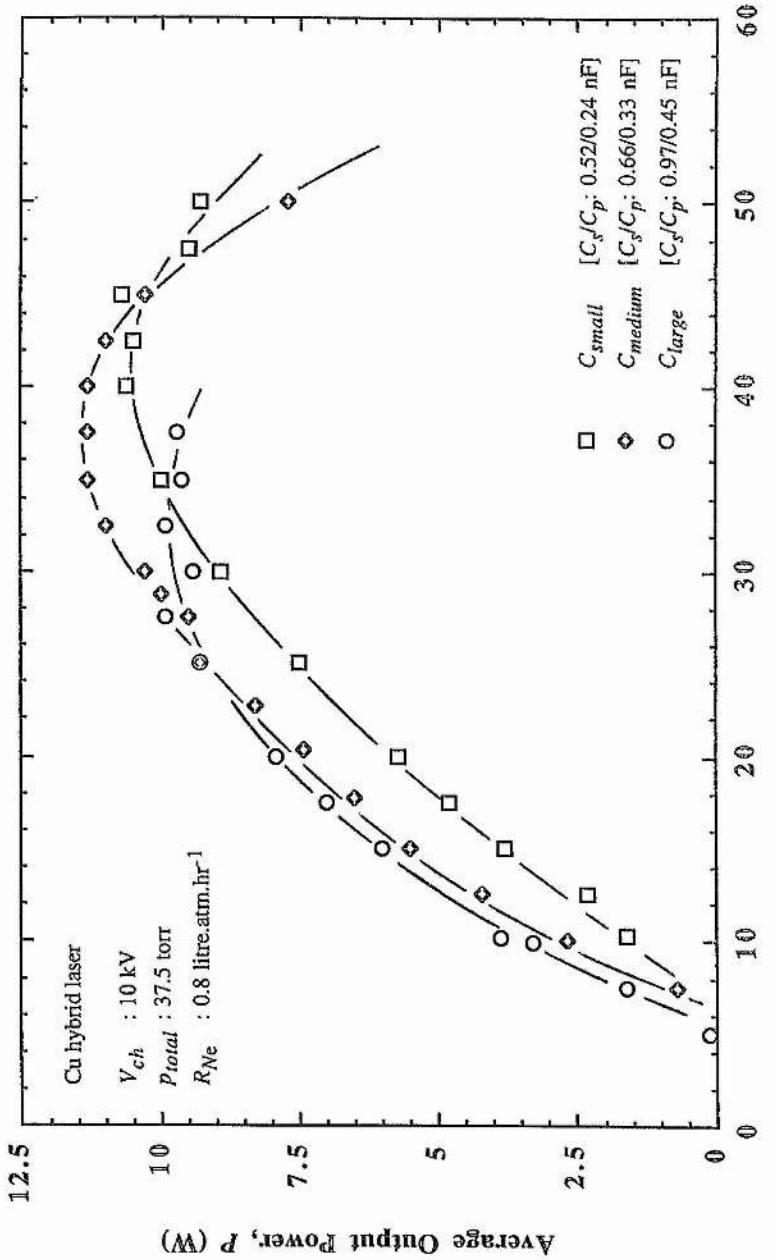

Fig. 5.6
Average output power, P, versus PRF in the Cu hybrid laser for three values of the storage/peaking capacitors.

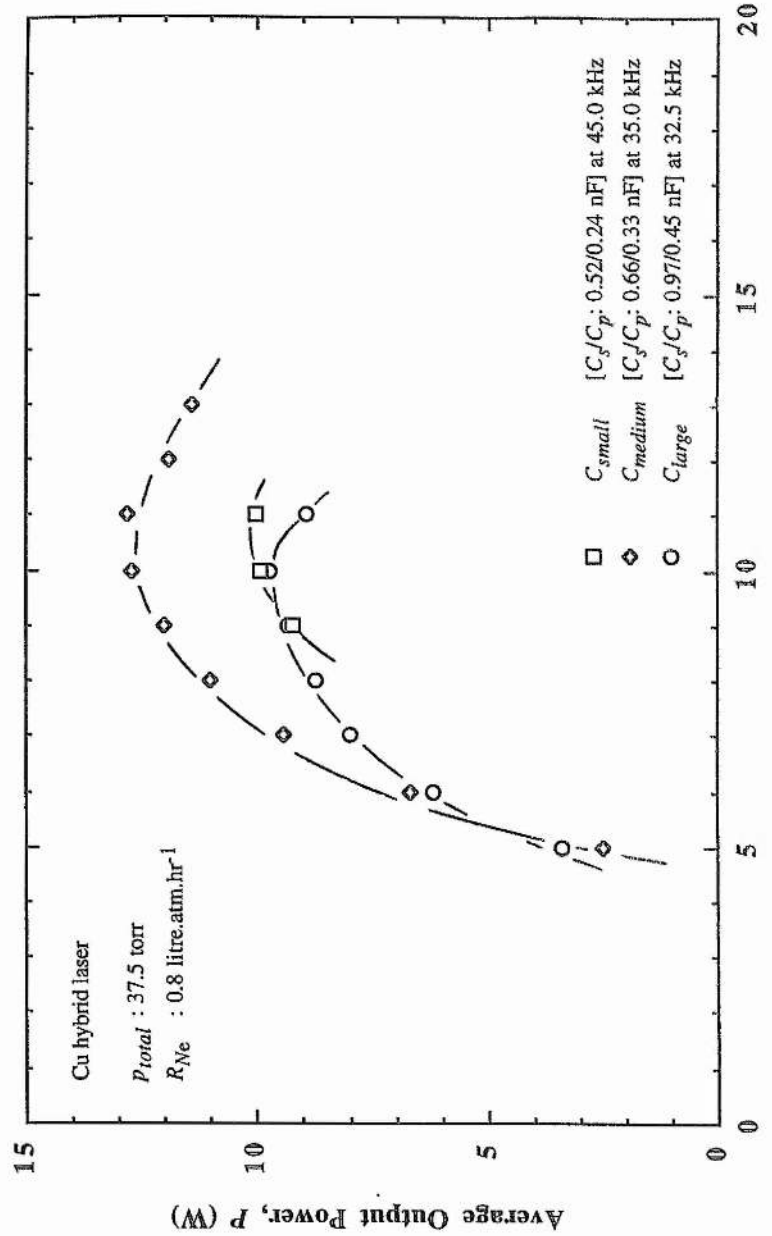

Fig. 5.7
Average output power, P, versus charging voltage, V_{ch}, in the Cu hybrid laser for three values of the storage/peaking capacitors, and at close to optimum PRF for each.

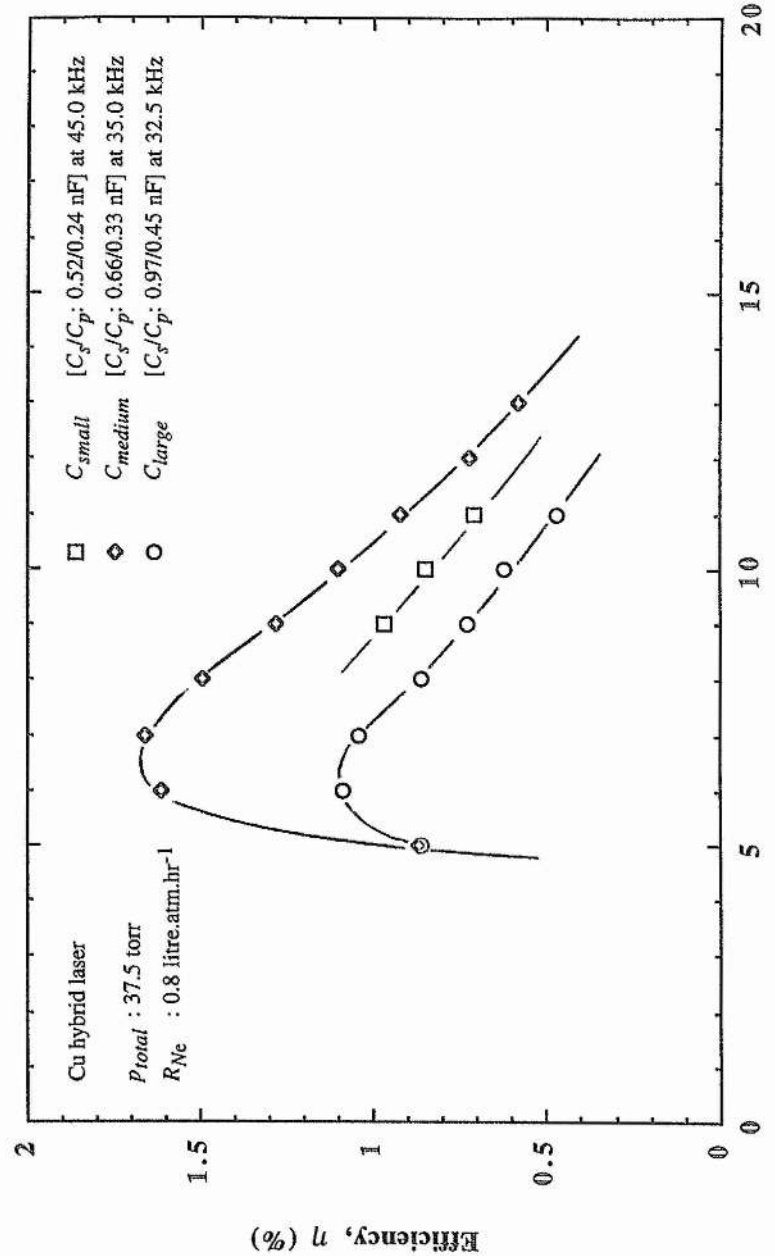

Fig. 5.8
Efficiency, η, versus charging voltage, V_{ch}, in the Cu hybrid laser for three values of the storage/peaking capacitors, and at close to optimum PRF for each.

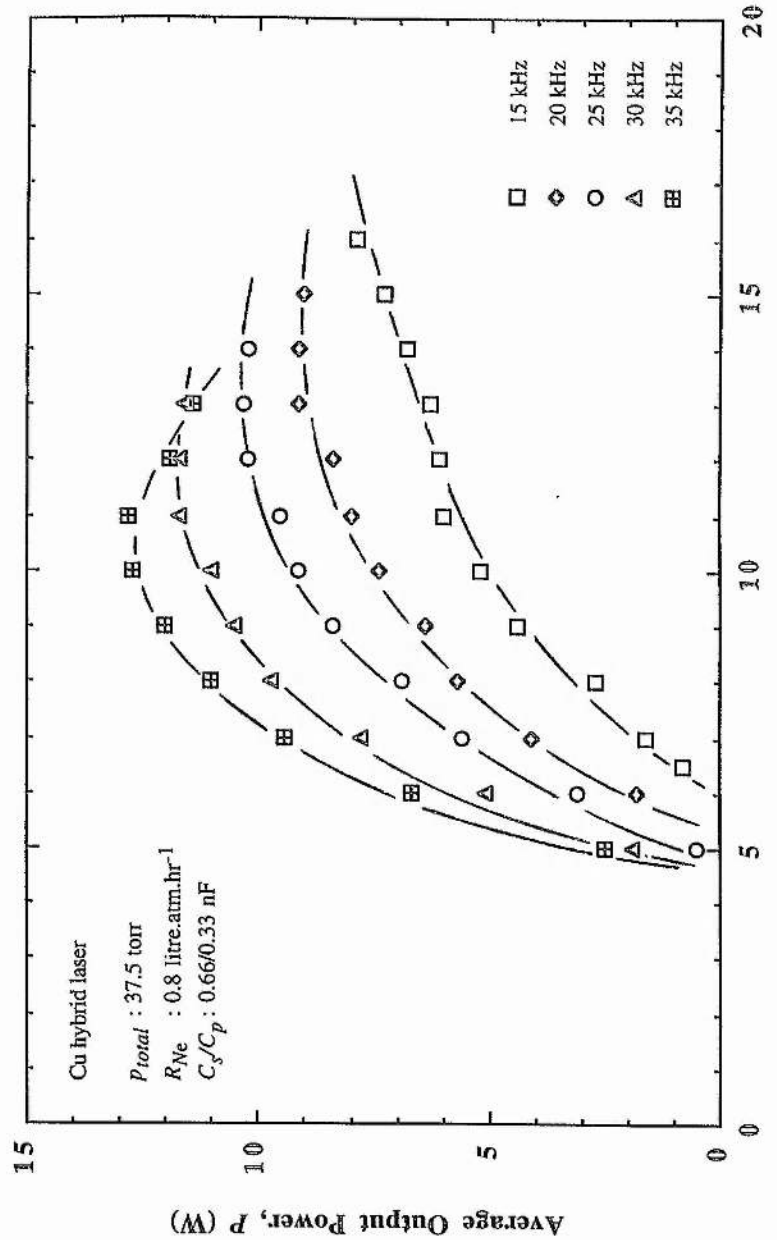

Fig. 5.9
Average output power, P, versus charging voltage, V_{ch}, in the Cu hybrid laser at five values of the PRF.

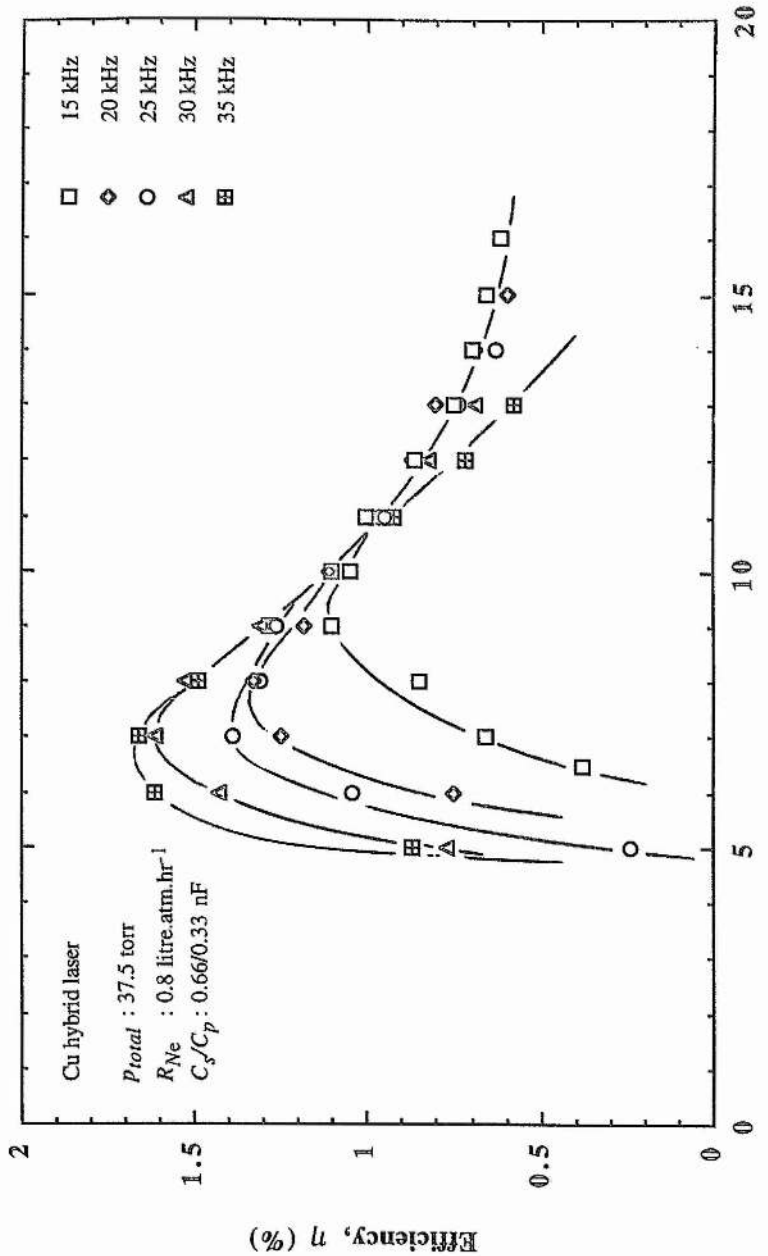

Fig. 5.10
Efficiency, η, versus charging voltage, V_{ch}, in the Cu hybrid laser at five values of the PRF.

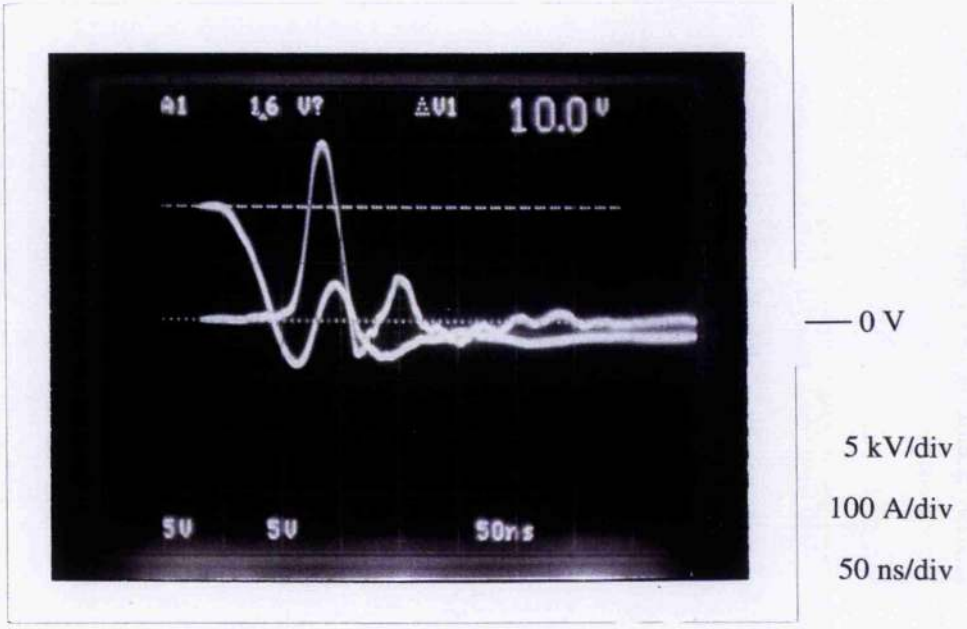

(a) $V_{ch}(t)$ and $i_t(t)$

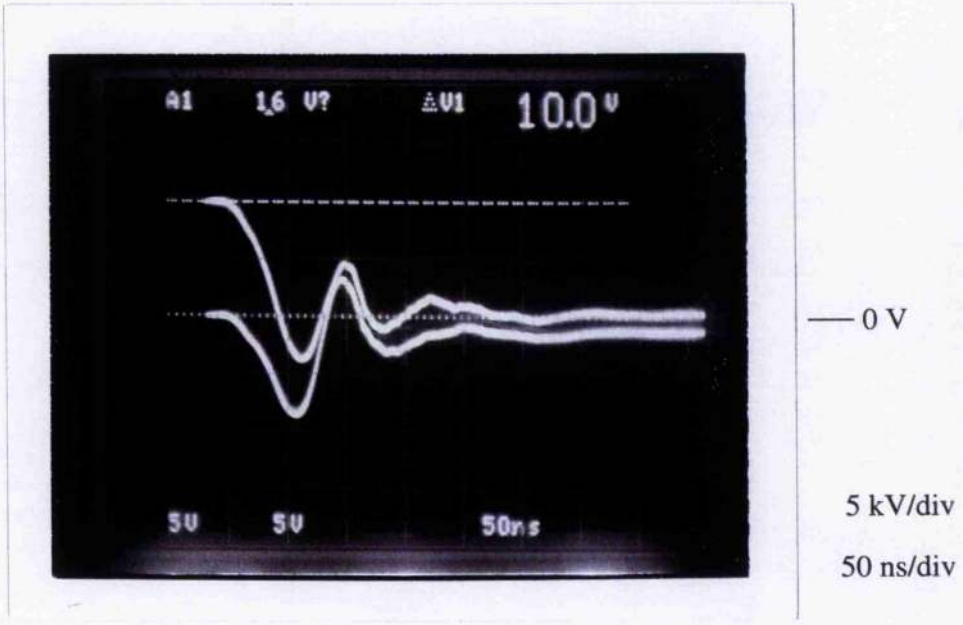

(b) $V_{ch}(t)$ and $V_t(t)$

Fig. 5.11 Oscillograms showing the charging voltage, discharge current and laser tube voltage waveforms, $V_{ch}(t)$, $i_t(t)$ and $V_t(t)$, for lasing in the Cu hybrid laser under close to optimum conditions for P_{max} with the 0.66/0.33 nF capacitors connected. R_{Ne}, p_{total}, PRF and V_{ch} are 0.8 litre.atm.hr^{-1}, 37.5 torr, 35 kHz and 10 kV respectively.

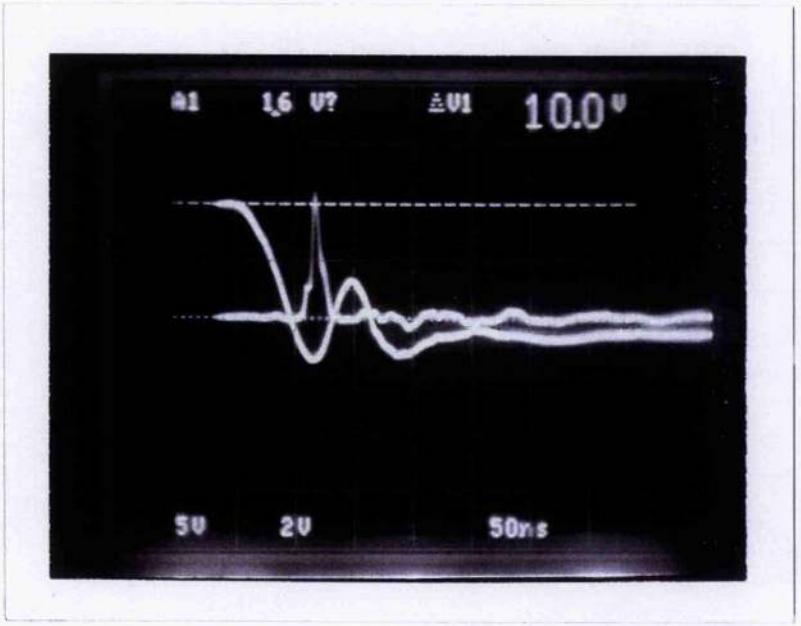

Fig. 5.12 Oscillogram showing the total laser intensity waveform, $I_l(t)$, for lasing in the Cu hybrid laser under close to optimum conditions for P_{max} with the 0.66/0.33 nF capacitors connected. R_{Ne}, p_{total}, PRF and V_{ch} are 0.8 litre.atm.hr^{-1}, 37.5 torr, 35 kHz and 10 kV respectively.
(Scales: 50 ns/div. Units of intensity arbitrary.)

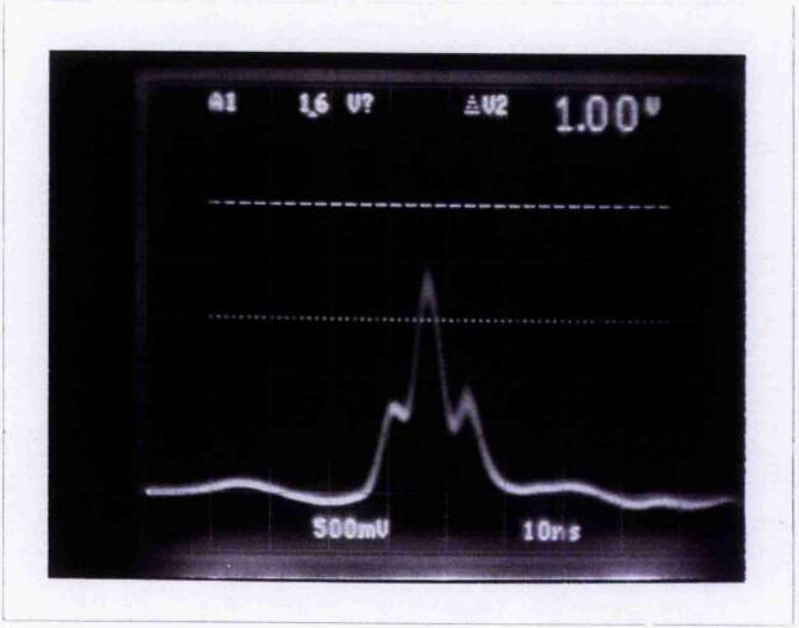

(a) $I_g(t)$

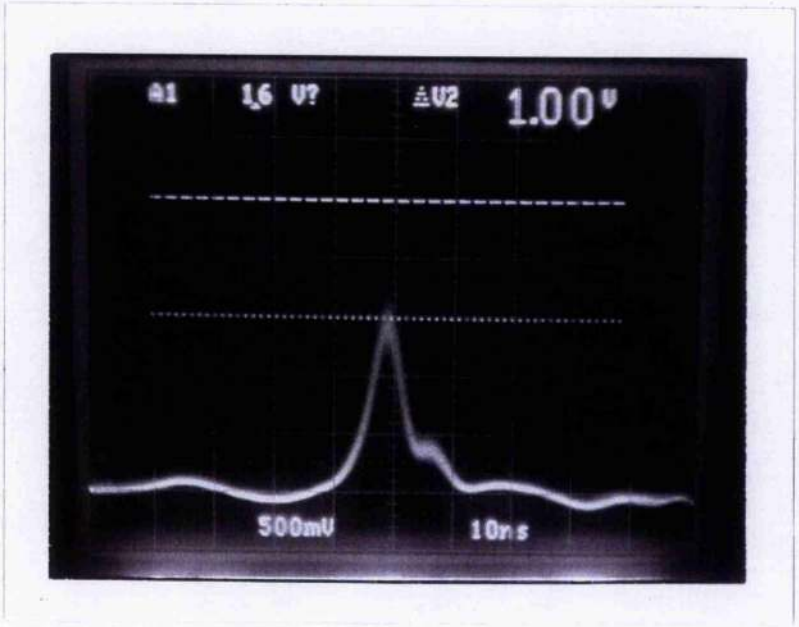

(b) $I_y(t)$

Fig. 5.13 Oscillograms showing the green and yellow laser intensity waveforms, $I_g(t)$ and $I_y(t)$, for lasing in the Cu hybrid laser under close to optimum conditions for P_{max} with the 0.66/0.33 nF capacitors connected. R_{Ne}, p_{total}, PRF and V_{ch} are 0.8 litre.atm.hr^{-1}, 37.5 torr, 35 kHz and 10 kV respectively. (Scales: 10 ns/div. Units of intensity arbitrary.)

Chapter 6

Comparison of CuBr-Ne, CuBr-Ne-H_2 and Cu Hybrid Laser Characteristics

6.1 Introduction

To date, independent experimental studies of CuBr-Ne, CuBr-Ne-H_2 and Cu hybrid lasers have identified some of their properties, *e.g.* annular and Gaussian-like beam profiles, but few investigators have compared the performance of tubes of like geometry, which were also operated with identical excitation circuitry, gas handling, optics and diagnostics. In 1988, Astadjov et al. [70] compared sealed-off CuBr-Ne and CuBr-Ne-H_2 lasers using the same discharge tube and proposed an explanation for their differing behaviours, however their characterisations were not exhaustive, concentrating mainly on the electric parameters of the discharge during the excitation pulse. Those experiments were conducted just before Cu hybrid lasers emerged as a technology, and so hybrid lasers did not feature in the discussion.

The first experimental comparison of a Cu hybrid laser with conventional CBL technologies was not made until 1995 when Isaev et al. [71] compared all three types of lasers in an identical experimental set-up. This study concentrated mainly on the temporal behaviours of the discharge current waveforms. An alternative explanation of CuBr-Ne-H_2 laser behaviour was given in terms of dissociative attachment of HBr (Section 1.9).

Chapters 3 to 5 of this thesis contain accounts of the individual responses of similarly sized CuBr-Ne, CuBr-Ne-H_2 and Cu hybrid lasers to a much wider range of test conditions including scanning of the buffer gas variables (pressure and flow rate) and of the parameters of the electrical excitation (PRF, charging voltage and storage/peaking

capacitances). It was possible to vary HBr, H_2 and Cu_3Br_3 pressures independently in the same flowing-gas, experimental set-up so that the true dependences of output power and additive gas pressures on the parameters of the buffer gas and electrical excitation could be studied for the first time. Reasons for the lasers' performance characteristics were proposed in terms of the possible effects on the discharge kinetics of reactions involving the species added to the active volume of each device. In this chapter, the similarities and differences in the main findings for the CuBr-Ne, CuBr-Ne-H_2 and Cu hybrid lasers are highlighted and discussed in order to shed light on the true differences in the mechanisms of operation of the lasers, and ultimately to explain why the output power increases in the order CuBr (3.55 W), CuBr-H_2 (11.4 W) and Cu hybrid (12.8 W). In what follows, reference to the 'CuBr laser' implies the normal or 'LT' operating mode of the Ne-CuBr laser.

6.2 General Comparison of CuBr, CuBr-H_2 and Cu Hybrid Lasers

The conditions under which P_{max} was obtained in each laser are compared in Table 6.1. The highest powers were obtained with the hybrid laser and the efficiency at maximum power was highest for the CuBr-H_2 laser. The maximum specific average output power of the Cu hybrid laser exceeded that of the CuBr-H_2 laser by a factor of 1.3. The efficiency at maximum power was greatest for the CuBr-H_2 laser by a factor of 1.3 over that of the hybrid laser.

Both the CuBr-H_2 laser and the hybrid laser were much more powerful and efficient than the CuBr laser. Maximum average output power and maximum specific average output power increased when H_2 was added to the CuBr laser. Output power in the CuBr-H_2 regime exceeded that of the CuBr regime by a factor of 3.2. The efficiency at maximum power was greatest in the CuBr-H_2 laser by 3.7 times over that of the CuBr laser. At maximum efficiency the power extractable from the CuBr-H_2 laser was larger by a factor of 4. The maximum specific average output power of the Cu hybrid laser exceeded that of the CuBr laser by a factor of 4.3. The efficiency at maximum power of the hybrid laser exceeded that of the CuBr laser by a factor of 2.8.

6.3 Shared Characteristics of the Three Laser Types

The first important result to emerge from the study of these lasers is that an increase in the partial pressure of all additive gases to each regime of lasing was necessary to re-establish peak power with increasing buffer-gas pressure, PRF or charging voltage. The higher p_{Ne} is, the faster electrons are cooled in the interpulse period towards T_g. The plasma relaxes (ions/electrons recombine) faster, and the cumulative depletion of Cu atoms on the tube axis by cataphoresis is smaller (due to reduced Cu^+ lifetimes), so higher PRFs are enabled. The largest p_{Ne} that can be tolerated before power falls off is determined by the influence of Ne on the EEDF, *i.e.* on peak T_e. Too high a n_{Ne} (or p_{Ne}) reduces peak T_e for effective inversion, just as too much n_{Cu} or $n_{Cu_3Br_3}$ will. However, much larger quantities of Ne can be tolerated because its excited energy states are all > 16.7 eV, *i.e.* greater than the excited levels and the ionization potential (7.73 eV) of Cu and much greater than the rovibrational levels of Cu_3Br_3 etc.

At higher PRFs there is increasing depletion of Cu from the discharge centre due to cumulative gas heating effects so that greater Cu_3Br_3 or HBr additive concentrations are necessary to replace the missing copper atoms. At higher charging voltages higher additive concentrations can be tolerated before T_e falls below that required for efficient pumping of the upper laser levels, as the peak applied tube voltage generally increases with charging voltage.

Increasing the buffer-gas pressure allows additive concentrations to increase, as the raised tube impedance afforded by higher p_{Ne} lets peak T_e be maintained. However this can only be maintained so far before Ne itself acts to reduce peak T_e by inelastic collisions. As the PRF is raised, n_{Cu} depletion on axis requires $p_{Cu_3Br_3}/p_{HBr}$ to be increased to maintain n_{Cu} on axis. As the overall additive concentration increases, peak T_e falls. As charging voltage is raised, peak T_e rises, but gas heating and cataphoresis also increase causing depletion of n_{Cu}. The only way to counter this is to increase $p_{Cu_3Br_3}$ or p_{HBr}, but this also increases $n_{Cu_3Br_3}$ etc. near the wall. Overall, larger additive concentrations end up reducing peak T_e.

As the peak electron temperature falls in every case, pumping of the green upper

laser level becomes less effective before pumping of the smaller energy yellow upper level is affected. Hence, the beam becomes more yellow at each parameter extreme. This behaviour is completely analogous to the behaviour of the green:yellow intensity ratio in a CVL as it overheats, *i.e.* as n_{Cu} rises too high [77]. One exception to the above rule was the HT regime of the CuBr laser. This regime led on from the final stages of an earlier regime (the LT regime) and the beam began with a very high yellow content. It was noted to become greener on approach to peak before turning yellow again as is usual when peak power is passed through (due to lowered electron temperatures) and the lasing begins to diminish. This suggests that peak T_e initially increased (beam became greener) and then decreased (beam became yellow again), probably due to the increase in peak tube voltage that accompanied the ingress of the H_2 'impurity'.

For the cases of the CuBr laser (LT), the CuBr-H_2 laser and Cu hybrid laser, optimum PRF was always observed to decrease with increasing capacitance. No result was taken for the CuBr (HT) regime which was characterised in less detail. This trend was explained in terms of gas heating and cataphoresis. At higher capacitance, larger input energies could be supplied to the discharge for the same charging voltage so that cumulative gas heating and cataphoresis effects (fractional ionization of Cu) worsened and PRFs had to be lowered to enable sufficient relaxation times between pulses for n_{Cu} to recover on the tube axis.

With the CuBr and Cu hybrid lasers, the charging voltage for peak power decreased with increasing PRF. Results were not taken for the CuBr (HT) laser or for the CuBr-H_2 laser but the trend is expected to be the same. The effect is again linked to a trade-off between relaxation time (PRF) and fractional ionization and gas heating (voltage) to prevent the gas from overheating and to minimize cataphoretic effects. An increase in the free electron density remaining at the end of each interpulse period as PRF is raised means that the gas can also provide less voltage hold-off before breaking down, which can reduce peak T_e. Although the dependence of charging voltage on capacitance was not obtained, voltage is expected to decrease with increasing capacitance. As a larger capacitance gives increased input energy for the same charging voltage, the voltage must

be reduced if the PRF is fixed.

The charging voltage for peak efficiency decreased with increasing PRF with the CuBr and hybrid lasers. Again, results were not taken for the CuBr (HT) laser or for the CuBr-H_2 laser, but they are expected to be similar. This is also likely to be a gas heating/cataphoresis effect, as for efficient pumping a large n_{Cu} is needed. High voltages and PRFs tend to reduce n_{Cu}, and so there is a trade-off for maximum efficiency.

The properties of the charging voltage, discharge current, laser tube voltage and total, green and yellow intensity waveforms when lasing close to P_{max} (with C_{medium} connected) with each laser are compared in Table 6.2. Lasing always occurred on the leading edge of the current pulse and as a general rule commenced simultaneously with the avalanche suggesting that T_e was close to optimum for creation of the inversion when the avalanche began. (The laser tube voltage was always near its peak when the current avalanche and lasing began.) Before the avalanche commenced there was some or no current depending on the laser tested. The leading step in the discharge current was small in each type of laser, because there were few free electrons to accelerate and T_e was held too low for avalanche (ionization).

As a general rule, during lasing the yellow pulse commenced some few nanoseconds after the green with the exception of the HT regime where these commenced almost simultaneously. This is because when T_e is high, the green transition goes into gain first. Although the upper levels are close in energy (3.78 eV and 3.81 eV), the dependence of the stimulated emission coefficient on wavelength favours the green line over the yellow line.

6.4 Comparison of CuBr (HT) and CuBr-H_2 Lasers

It is convenient to begin with a comparison of the HT and H_2 regimes. It was suggested in Chapter 3 that the HT regime in the CuBr laser is caused by the release of H_2-containing impurities from the CuBr melt at elevated sidearm temperatures, and that the HT regime is in fact a manifestation at excessive sidearm temperatures of the "hydrogen effect". In chapter 4, peak power in the HT regime was demonstrated to occur at a

sidearm temperature of 450 °C under reference conditions of all gas and excitation parameters and with the 0.66/0.33 nF capacitors connected. In apparent confirmation of the above hypothesis, under those same conditions of gas and excitation, average power in the CuBr-H_2 laser was shown to be approximately equal to the peak power observed in the HT regime when the appropriate plot was extrapolated to this same sidearm temperature of 450 °C. There were also shown to be similarities in the response of the discharge current to an increase in H_2 pressure and sidearm temperature in the H_2 and HT regimes respectively. Comparison of the performance characteristics of both regimes now enables us to examine whether the hypothesis of equivalence holds true for all results taken.

Reviewing the general observations first. The HT regime quite clearly attempts to emulate the beam pattern observed in the CuBr-H_2 laser. With increasing sidearm temperature on approach to peak power the beam becomes less annular, less constricted and displays a higher green:yellow ratio. There are marked improvements in discharge impedance as evinced by a falling charging voltage which requires readjusting and a rise in discharge tube voltage to peak values well beyond those seen in either the LT or hybrid regimes but approaching those of the H_2 regime.

The same initial drop in power of the LT regime, accompanied by a slight increase in beam constriction and an increased intensity of the yellow transition, as seen when H_2 is added to the CuBr laser, was observed in the CuBr laser just prior to the onset of the HT regime of lasing. When unstable, both regimes demonstrated the same signs of turbulence.

The response of the current pulse was also similar. Peak currents were very much higher than those of the LT regime, by ~ 45 A and 85 A at maximum power in the HT and H_2 regimes respectively. The lower currents in the HT regime relative to the H_2 regime are probably due to the effects of excess bromine, *e.g.* increased electron attachment as Br^-, in the former case. Both regimes showed a requirement for the current step to collapse before any increase in power could take place. In the case of the HT regime, collapse of the step below the 10 % height in the LT regime signalled a fall in

power and in peak current which were not reversed until the step collapsed and the HT regime took over. The power and peak current then reached higher values than before. In the case of H_2 addition to the LT regime, power remained constant at that of the LT regime until the 10 % step height was reached. Below this the power and peak current were again reduced, recovering after collapse of the step to reach higher values than before.

There was a difference in the final response of the current pulse, in that the HT current ended suddenly in a wall discharge on cessation of lasing while the H_2 regime maintained a sizeable current (of ~ 100 A) at greatly increased H_2 pressures after the cessation of lasing. In Chapter 3, the wall discharge was attributed to an overload of Cu_3Br_3 at sidearm temperatures associated with the final phase of the HT regime. The resulting increase in discharge impedance caused by discharge bending and constriction under the influence of so much bromine causes the current to view the discharge tube wall as the lower impedance path. When H_2 was added to the CuBr laser discharge in far greater concentrations than possible in the CuBr laser HT regime (in which hydrogen was bonded to the Cu_3Br_3 molecules and could not have existed in greater concentrations than these), the discharge impedance increased but no wall discharge resulted. The fact that the discharge current collapse coincided almost exactly with the abrupt termination of lasing in the HT regime probably shows that discharge bending/constriction was responsible for both. It was noted that the beam was only 2-3 mm in diameter, bright yellow and extremely unstable when lasing ceased. Hence premature ending of the regime and therefore its narrow temperature band is a bromine effect which is less pronounced at lower buffer-gas pressures where the Cu_3Br_3 pressures are also lower. When taking results in the H_2 regime, the Cu_3Br_3 pressures and sidearm temperatures involved were optimum for the LT regime. If H_2 had been added at optimum sidearm temperature for the HT regime then the response might also have been to terminate in a wall discharge. Certainly when H_2 was added at sidearm temperatures beyond optimum in the LT regime, in order to obtain the sidearm temperature dependence of the H_2 regime, other signs of instability generally associated with the HT regime were present.

However it was very difficult to control the H_2 regime at sidearm temperatures associated with the HT regime so that no experimental comparison could be made in this case.

In the HT regime the output powers and efficiencies were higher than in the LT regime, as would be expected if H_2 addition was responsible, but the powers and efficiencies attained were less than 50 % of those obtained when lasing in the H_2 regime. This deficiency can also be attributed to the higher Cu_3Br_3 pressures which, in excessive quantities, constrict the beam and reduce the pumping efficiency of the upper laser levels by reducing the peak electron temperature in the discharge via collisions.

The dendritic deposits observed after lasing in the HT regime were less numerous but of similar form to those found in the CuBr-H_2 laser. This again suggests hydrogen to be the common factor as similar structures were not found after lasing in the LT regime. This is consistent with hydrogen reduction as the main deposition process (see Chapter 7, Section 7.2). There was CuBr deposition on the ceramic after lasing in the HT regime which was not observed in the CuBr-H_2 laser, but then the concentrations of Cu_3Br_3 being added to the discharge were also much higher in the former case so that this observation is not entirely unexpected.

Fig. 6.1 shows average power versus buffer-gas pressure for all four regimes of lasing. Clearly the HT and H_2 regimes favour similarly low pressures (~ 20-30 torr), however as the plot of Fig. 6.2 comparing trends in average output power with buffer-gas flow rate shows, the HT regime peaks at approximately half the flow rate favoured by the H_2 regime (1 versus 2 litre.atm.hr^{-1}). The pressure and flow rate curves plotted for the HT regime both terminate prematurely at ~ 55 torr and ~ 2.2 litre.atm.hr^{-1} respectively. In Chapter 3 these effects were interpreted as being due to the even higher Cu_3Br_3 pressures which must be tolerated at higher buffer gas pressures and flow rates. As the flow rate at which the pressure curve was established was relatively low, the curve lasts long enough to show approximately the same dependence of power on pressure as in the H_2 regime before the Cu_3Br_3 pressure forces the demise of the regime. At the reference pressure at which the flow rate curve was obtained, the powers are already low because of increased bromine concentrations. The further increase necessary at the higher flow rates, together

with extra turbulence induced by the higher flow rates themselves, accounts for the sudden turn over in response at relatively small rates of flow. Before the turn over occurs, the power is rising steeply and linearly so that it is possible that under optimal conditions of pressure this rise would have continued, eventually showing the same dependence of power on flow rate as in the H_2 regime but this is not conclusively so.

As Fig. 6.3 reveals, there is a difference of ~ 10 kHz between the optimum PRFs of the H_2 and HT regimes, the higher value corresponding to the former. The HT PRF of 20 kHz is probably realistic because the pressure was reduced to 19 torr before taking the result, however, the premature turn over may again be explained by a lack of tolerance of the increased bromine pressures at the higher PRFs which does not affect the H_2 regime to such an extent as it normally operates at lower Cu_3Br_3 pressures and so can tolerate a larger increase.

From Fig. 6.4, lasing is possible in the H_2 regime at zero concentrations of H_2 because it simply reduces to the peak output of the CuBr laser LT regime. It is difficult to say if this is the case in the HT regime. It depends on whether the fall off in power from the LT peak is precipitated by H_2 addition or bromine effects. In the former case, the complete absence of H_2 contamination by locking it up in some non-reacting molecular structure (*e.g.* by addition of a salt with which it reacts) will prevent the occurrence of the "hydrogen effect" and might enable the CuBr LT regime to continue on to greater powers at higher sidearm temperatures. If however the fall in the CuBr LT regime is a bromine effect then the effect would still occur and there could be no lasing at elevated sidearm temperatures without some presence of hydrogen.

Other than commenting on the fact that maximum powers and efficiencies at maximum power are higher in the H_2 regime than in the HT regime little more can be said about output characteristics as the capacitances at which maximum power and efficiency were obtained in the HT regime were not optimised. It can be said however that for the same capacitances, the maximum efficiency and power at maximum efficiency in the HT regime were below 50 % of those of the H_2 regime and exceeded those of the LT regime. The voltages at which efficiency was optimum were higher in

both the HT and H_2 regimes and highest in the HT regime. The specific input energy was also slightly higher in the HT regime.

From the comparison of the HT and H_2 regimes it is consistent that hydrogen addition causes the increased output powers and efficiencies (over the LT regime) in both. The sole difference is the levels of Cu_3Br_3 present in the discharge which lead to increased instabilities and premature termination of some of the features of the HT regime. For the green to recover as the laser enters the HT regime and to begin coincidentally with the yellow, the fall off in power from the LT regime cannot occur because of increased metastable population or no such recovery would be possible.

Two temperature regimes of operation (LT and HT) were discovered by another set of investigators but the effect was never properly explained [31]. Their observations of continuous power where there were previously two regimes on the addition of alkali-chlorides to the discharge [33] might be indicative of the form which the hydrogen must take during the "hydrogen effect" if we assume that hydrogen was also the source of the peculiar sidearm temperature dependence of their output powers. Other species had reduced effects on the two regimes.

6.5 Comparison of CuBr and CuBr-H_2 Lasers

In the CuBr laser, the beam pattern was annular at all times due, as has been said, to the copper density being highest near the wall (because of on-axis gas heating) so that this part of the discharge goes into gain first. The CuBr-H_2 laser output commenced with an annular or uniform intensity profile depending as H_2 was added to the CuBr laser operating in the LT regime or Cu_3Br_3 was added to a Ne-H_2 discharge. In either case the beam always became uniform, then bell-shaped or pseudo-Gaussian, with increasing Cu_3Br_3 or H_2 pressure. The CuBr laser showed increasing constriction from first addition of Cu_3Br_3 right through to the final fall in power. The CuBr-H_2 laser showed little or no constriction at any stage of lasing.

There was no improvement in circuit-laser matching when operating in the CuBr regime except during the final phase after the output power had peaked. Matching

improved throughout the CuBr-H_2 regime. H_2 addition has been shown to raise the impedance of the discharge considerably (either via H or HBr). The rising impedance in the final phase of the CuBr regime is likely to be due to excessive electron attachment to bromine atoms or to the onset of H_2 diffusion from the sidearm into the active volume. The increased constriction, increasing intensity of yellow and instability are indicative of bromine.

In the CuBr laser, the step was at the 10-20 % height when power was maximum. Below this the average output power and peak current dropped. In the H_2 regime the step had to collapse before power and discharge current increased. This is interesting because it means that virtual removal of all free electrons took place before the H_2 regime was established. The peak currents are larger in the CuBr-H_2 laser than in the CuBr laser (by ~ 85 A), so that in addition to more effective removal of electrons at the end of the interpulse period by dissociative attachment of HBr, the effect of hydrogen is also to increase the peak current due to an increase in n_{Cu} caused by hydrogen reduction of Cu_xBr_x.

In the CuBr laser the dendrites were lumpy, non-crystalline solids. There was a fine scattering of CuBr and Cu particles across the inner wall of the ceramic. In the CuBr-H_2 laser, the dendrites were crystalline and grew into the discharge, exhibiting rounded ends where they had melted on too close approach to the discharge. The dendrites were numerous around the aperture in the ceramic. There was Cu but no CuBr scattered across the ceramic. These observations indicate that the Cu deposition process is different when hydrogen is present, *i.e.* thermal dissociation in the CuBr laser and hydrogen reduction in the CuBr-H_2 laser.

From Fig. 6.1 showing the dependences of all regimes on increasing buffer gas pressure, the CuBr laser and CuBr-H_2 laser prefer the same low buffer gas pressures in the range ~ 25-30 torr. From the flow rate dependences plotted in Fig. 6.2, the LT and H_2 regimes both favour a flow rate of ~ 2 litre.atm.hr^{-1}.

The PRF dependences of Fig. 6.3 show the optimum PRF for the CuBr laser to be 22.5 kHz, 7.5 kHz lower than the CuBr-H_2 laser optimum PRF of 30 kHz.

The optimum capacitances are smaller in the case of the CuBr-H_2 laser indicating a higher impedance discharge. As explained earlier, operation with smaller capacitances allows higher PRFs to be used due to small cumulative effects. The charging voltage at maximum specific output power is higher in the CuBr laser by 1 kV so that it requires a larger specific input energy at the lower PRFs. However, it was also noted that the PRF increases afforded by the presence of H_2 were over and above those based on purely thermal considerations, *i.e.* interpulse relaxation of the plasma is faster when H_2 is present. The smaller capacitances used with H_2 also allowed faster rising current pulses.

Looking at the comparison of the current, voltage and intensity waveforms for maximum power in each regime (Table 6.2) we see that the laser tube voltage is highest in the CuBr-H_2 laser and lowest in the CuBr laser at 12 and 7.5 kV respectively. The total current pulse risetime is greater in the CuBr laser (67 ns) because of the step and lower in the CuBr-H_2 laser at 44 ns. The risetime of the current avalanche is ~ 40 ns in the CuBr laser but only approximately half that at 25 ns in the CuBr-H_2 laser. Again, these observations are consistent with a higher discharge impedance in the CuBr-H_2 laser.

6.6 Comparison of Cu Hybrid and CuBr Lasers

From Fig. 6.1, the CuBr laser and Cu hybrid laser are shown to favour different gas pressure regimes. The CuBr laser prefers pressures of the order ~ 30 torr while the hybrid laser gives greater powers at double that pressure (~ 60 torr).

From the flow rate dependences plotted in Fig. 6.2, the CuBr and hybrid lasers favour buffer-gas flow rates of ~ 2 litre.atm.hr^{-1} and ~ 1 litre.atm.hr^{-1} respectively so that the optimum flow rate for the hybrid laser is approximately one half of that for the CuBr laser. Although the CuBr laser demonstrates a fairly steep rise to maximum flow rate it exhibits a very gradual decline thereafter, whereas the Cu hybrid laser exhibits a much steeper decline in power at increasing rates of flow.

Fig. 6.3 shows optimum PRF for the CuBr and hybrid lasers to be 22.5 and 38 kHz respectively, a difference of 15.5 kHz. The optimum capacitances were the same (0.66/0.33 nF) in both cases. The PRF increase is therefore entirely due to the presence of

HBr, *i.e.* interpulse relaxation of the plasma is faster when HBr is present. The charging voltage at maximum specific output power is higher in the CuBr laser by 1 kV so that the CuBr laser requires a larger specific input energy at the lower PRFs. It was also noted that not only did PRF decrease with increasing capacitance but that the amount by which the PRF dropped on moving from C_{small} to C_{medium} to C_{large} was greater in the hybrid laser.

The CuBr beam was observed to display an annular intensity profile at all times. The beam of the Cu hybrid laser was initially annular at small HBr pressures, but at larger pressures of HBr this annularity filled in. The hybrid laser also differed from the CuBr laser in that it showed little or no beam constriction at most HBr pressures.

Whereas in the CuBr laser the current step was at the 10-20 % height when the power was maximum, in the Cu hybrid laser the step was at the 10 % height at maximum power. Both regimes fell in current and power when the step fell below the 10 % height. Therefore neither of these lasers required complete removal of residual electrons and found it beneficial to have some present. The peak currents are much larger in the hybrid regime (by ~ 85 A), indicating a larger n_{Cu}.

Dendrites were most numerous in the Cu hybrid laser. Compared with the lumpy, non-crystalline, dendritic deposits in the CuBr laser, these were crystalline, grew into the discharge and exhibited rounded ends where they had melted on too close approach to the discharge. The dendrites grew from the edges or centres of the Cu pieces and were spaced at random along the length of the active volume. The ceramic was clean in the hybrid regime.

Looking at the comparison of the current, voltage and intensity waveforms (Table 6.2) we see that the laser tube voltage is slightly higher in the Cu hybrid laser (8.2 versus 7.5 kV) but that both are low in comparison to the charging voltage. The total current pulse risetime is ≥ 65 ns in both the hybrid and CuBr lasers due to the presence of the current step in each case. The risetime of the all-important current avalanche is ~ 40 ns in the CuBr laser but only 25 ns in the hybrid laser. The laser pulse width is greatest in the CuBr laser and smallest in the hybrid laser at 49 and 27 ns respectively, presumably due

to the different excitation pulse lengths.

6.7 Comparison of Cu Hybrid and CuBr-H_2 Lasers

Generally, the output characteristics (power, efficiency, PRF) of the Cu hybrid and CuBr-H_2 lasers are very similar. Nevertheless, despite the fact that the same species are present in the two lasers, there are a number of significant differences between them. This can largely be traced to a larger HBr concentration in the hybrid laser. In 15 torr Ne we require ~ 1 torr CuBr which is 1 torr Cu and 1 torr Br. For maximum power in the H_2 regime we require 0.64 torr H_2 (or 1.28 torr H). For maximum power in the Cu hybrid laser we require ~ 1.57 torr HBr at the same Ne pressure, which is equivalent to 1.57 torr H and 1.57 torr Br. Hence in the Cu hybrid laser, there is 0.29 torr extra H and 0.57 torr extra Br. Given the fact that the hybrid laser optimizes at approximately twice the Ne pressure of the CuBr-H_2 laser and p_{HBr} increases linearly with p_{Ne}, the HBr concentration will be significantly greater in the hybrid laser at maximum power for each due to the hybrid laser's higher Br content (2.5 torr HBr at 60 torr Ne compared to 1.25 torr H_2 and 1-1.7 torr CuBr at 25 torr Ne).

From Fig. 6.1 showing the dependences of all regimes on increasing buffer-gas pressure, the H_2 and hybrid regimes are shown to favour different regions of the pressure range. The H_2 regime prefers pressures of the order ~ 25 torr while the hybrid regime gives greater powers at more than double that pressure (~ 60 torr). This difference in performance indicates a higher peak T_e in the Cu hybrid laser as the upper limit on p_{Ne} beyond which n_{Ne} reduces peak T_e through inelastic collisions with electrons is clearly higher in the hybrid case.

From the flow rate dependences plotted in Fig. 6.2, the H_2 and hybrid regimes favour buffer-gas flow rates of ~ 2 litre.atm.hr^{-1} and ~ 1 litre.atm.hr^{-1} respectively so that the optimum flow rate for the hybrid laser is approximately one half of that for the H_2 regime. Following its rise to maximum power at low rates of flow, the H_2 regime exhibits a very gradual decline with increasing flow rate thereafter. The Cu hybrid laser exhibits a much steeper decline in power at increased flow rates, similar in fact to the HT regime

which also favours a flow rate of ~ 1 litre.atm.hr^{-1} but falls to 0 W by 2.2 litre.atm.hr^{-1}.

The difference in PRF between the Cu hybrid and H_2 regimes is, from Fig. 6.3, 8 kHz in favour of the hybrid regime, but both PRFs are high. This indicates a basic similarity between the lasers in the interpulse relaxation period which suggests that differences between the two lasers take place during the excitation pulses rather than between them.

Looking at the comparison of the current, voltage and intensity waveforms (Table 6.2) for maximum power in each regime we see that the laser tube voltage is highest in the CuBr-H_2 laser at 12 kV, and is smaller in the hybrid regime at 8.2 kV. The peak currents are high and equal. The total current pulse risetime is greater in the hybrid regime (65 ns) because of the step and ~ 21 ns smaller at 44 ns in the H_2 regime. The risetime of the current avalanche is ~ 25 ns in both regimes. The optimum capacitances were smaller in the case of the CuBr-H_2 laser indicating a larger impedance. The charging voltage at maximum specific output power is the same in both regimes so that the hybrid laser can tolerate a larger specific input power and the maximum specific output power is large as a result.

In the H_2 regime the step collapsed completely before power and discharge current increased. In the Cu hybrid laser the step was at the 10 % height at maximum power. This means that virtual removal of all free electrons had to take place before the hydrogen regime could be established. There was in fact no power increase with added H_2 until this stage was reached unlike in the Cu hybrid laser where increasing power and reduction in step height were strongly coupled.

An obvious difference between hybrid and CuBr-H_2 lasers is the method of Cu seeding, which is the topic of Chapter 7. However, it can be mentioned here that there was accelerated copper loss in both the CuBr-H_2 and Cu hybrid lasers. In the first case this took the form of a scattering of Cu particles on the ceramic and Cu dendrites around the ceramic aperture. In the second case the loss occurred on the controlled locations of the Cu pieces, indicating that the Cu pieces in the tube catalysed the Cu deposition.

The H_2 and hybrid regimes of lasing were also similar in that neither showed any

great degree of beam constriction. Beam constriction is caused by excessive attachment of free electrons to Br atoms which causes the electrons to remain close to the point of their origin in the centre of the discharge at all times and forces successive pulses to adhere ever closer to the centre of the discharge as that is where the pre-ionization is. The constriction is thought to disappear on addition of H_2 or HBr to the discharge because hydrogen reduction of CuBr and Cu_3Br_3 molecules,

$$H + CuBr \rightarrow Cu + HBr$$

$$H + Cu_3Br_3 \rightarrow Cu + HBr + 2CuBr$$

frees easily ionizable Cu atoms (the main ion species in the discharge) at the edges of the discharge and thus effectively widens the discharge channel. It is the removal of the constriction, which eases Cu ionization and depletion on the tube axis, which causes the black hole to disappear, that is the annular beam to be replaced by one which has peak intensity on the tube axis.

Hydrogen reduction also generates HBr. The presence of significant quantities of HBr in a CuBr-H_2 laser was demonstrated by the mass spectrometric measurements of Isaev et al. [71]. HBr is added directly to the hybrid laser. The benefits of HBr to discharge kinetics were discussed in Chapter 1.

It is known that the H_2 addition must act to increase the number of ground state Cu atoms from the results of HCl addition to a copper laser [27] where HCl was seen to raise the laser energy by 15 %. The Cu ground state density is also flattened across the tube bore by the reduction in cataphoresis that results from the shortened Cu^+ lifetimes due to dissociative attachment of HBr followed by ion-ion (Cu^+-Br^-) neutralization

$$Cu^+ + Br^- \rightarrow Cu^* + Br.$$

H_2 addition in the CuBr-H_2 laser raised its discharge impedance to a greater degree (greater laser tube voltages and similar currents) than did HBr in the hybrid laser, again

suggesting that more Cu atoms are available in the hybrid laser than in the halide laser. If the electron impact dissociation of the H_2 molecules on entry to a Ne-CuBr discharge produces atomic and ionic hydrogen, then HBr can form by the processes:

$$H + Br + M \rightarrow HBr + M,$$
$$H + CuBr \rightarrow Cu + HBr .$$

There is a minimum of 1.2 torr HBr necessary for lasing to even occur in the Cu hybrid laser. This is because even at the lowest output powers, there must be a minimum Cu concentration. In the hybrid laser the HBr has two roles: to seed the discharge and to enhance the kinetics (speed the recovery of Cu and delay the current avalanche). Therefore HBr must be present even when the laser first begins to oscillate.

Finally, the higher output powers of the hybrid laser compared to the CuBr-H_2 laser are attributable to the larger concentrations of HBr that can be tolerated in its discharge (see the beginning of this section). The higher n_{HBr} leads to more effective dissociative attachment and all the benefits that follow. The partial dissociation of HBr in the discharge also produces H_2 which can react with Cu_3Br_3 to reduce it to free Cu atoms, HBr, Cu_2Br_2 etc. As HBr delays the electron avalanche more effectively, a larger p_{Ne} can be tolerated for a given peak T_e. This allows higher PRFs to be used (faster plasma relaxation and recovery of n_{Cu}). The ability of hybrid lasers to produce the highest output powers per unit volume makes them the main contender for volumetric scaling to high average output powers. This is discussed in Chapter 8 in relation to the attainment of kilowatt average powers.

6.8 Conclusions

The Cu hybrid laser demonstrates the highest output power and efficiency, and most strongly resembles the CuBr-H_2 laser in terms of the overall character of it emission. In its dependence on buffer-gas pressure and flow rate it echoes neither of the other two systems, favouring pressures in the range 50-70 torr and flow rates of approximately 1

litre.atm.hr^{-1}. It also tolerates optimum HBr pressures of the order of 1.4-3.2 torr over a 13.6-94.5 torr buffer-gas pressure range in contrast to around 0.3 torr of Cu_3Br_3 vapour in both the CuBr and CuBr-H_2 lasers. These differences most probably relate to the different mechanism of Cu seeding in Cu hybrid lasers. Seeding in hybrid lasers is discussed in Chapter 7.

The HT regime of the CuBr laser has been shown to be most probably an emission anomaly arising from impurities in the laser tube. Neglecting the HT regime and assuming the LT regime to be the correct regime of operation, the CuBr and CuBr-H_2 lasers peak at similar buffer-gas (and halide) pressures and flow rates (25-30 torr and 2 litre.atm.hr^{-1} respectively), but the optimal values of the excitation parameters (PRF and charging voltage), and the overall powers, efficiencies and pattern of laser emission, are strongly affected by the presence or lack of H_2.

Finally, the above discussion shows why H_2 addition to a conventional CVL does not give the benefits of Br_2 or HBr addition simply by virtue of the fact that the active species in bromide lasers with hydrogen added is HBr and not H_2. The recent development of 'kinetically enhanced' CVLs [2], where HBr is added instead of H_2, highlights this fact.

Quantity	CuBr-Ne Laser		CuBr-Ne-H_2 Laser	Cu Hybrid Laser
	LT Regime	HT Regime		
Tube bore (mm)	13	13	13	12.5
Tube length (cm)	32.8	32.8	32.8	30
Active volume (cm^3)	43.5	43.5	43.5	36.8
P_{max} (W)	3.55	5.7	11.4	12.8
Maximum specific P ($mW.cm^{-3}$)	82	131	262	348
η at P_{max} (%)	0.33	0.46	1.21	0.92
C_s/C_p for P_{max} (nF)	0.66/0.33	0.66/0.33	0.52/0.24	0.66/0.33
PRF for P_{max} (kHz)	22.5	20	30	35
V_{ch} for P_{max} (kV)	12	13.5	11	11
Specific P_{in} at P_{max} ($W.cm^{-3}$)	24.6	27.7	21.7	38
η_{max} (%)	0.56	0.64	1.47	1.66
P at η_{max} (W)	2.30	4.1	9.3	9.4
V_{ch} at η_{max} (kV)	7.5	10	9	7
Specific P_{in} at η_{max} ($W.cm^{-3}$)	9.6	15.2	14.5	15.4

Table 6.1

Comparison of P_{max}, η_{max}, electrical excitation and related quantities for all four laser regimes.

Quantity	CuBr-Ne Laser		CuBr-Ne-H_2 Laser	Cu Hybrid Laser
	LT Regime	HT Regime		
V_{ch} (kV)	10	10	10	10
$V_{t\,pk}$ (kV)	7.5	9.5 (~ 12 kV at peak)	12	8.2
$i_{t\,pk}$ (A)	215	215 (260 A at peak)	300	300
t_{ri} (ns)	67	40	44	65
t_{ra} (ns)	40	40	25	25
t_{da} (ns)	27	0	19	40
t_l (ns)	49	46	37	27
t_{rl} (ns)	16	13	13	11
t_{dl} (ns)	27	0	15	36
t_g (ns)	41	40	33	26
t_{rg} (ns)	6	3	13	11
t_{dg} (ns)	27	0	15	36
t_y (ns)	46	45	34	26
t_{ry} (ns)	16	11	11	12
t_{dy} (ns)	30	< 1	18	37

Table 6.2
Comparison of the characteristics of $V_{ch}(t)$, $V_t(t)$, $i_t(t)$, $I_l(t)$, $I_g(t)$ and $I_y(t)$ at close to optimum conditions for P_{max} in all four laser regimes.

(Note that that the data shown for the HT regime was recorded as the average output power began its ascent towards P_{max}.)

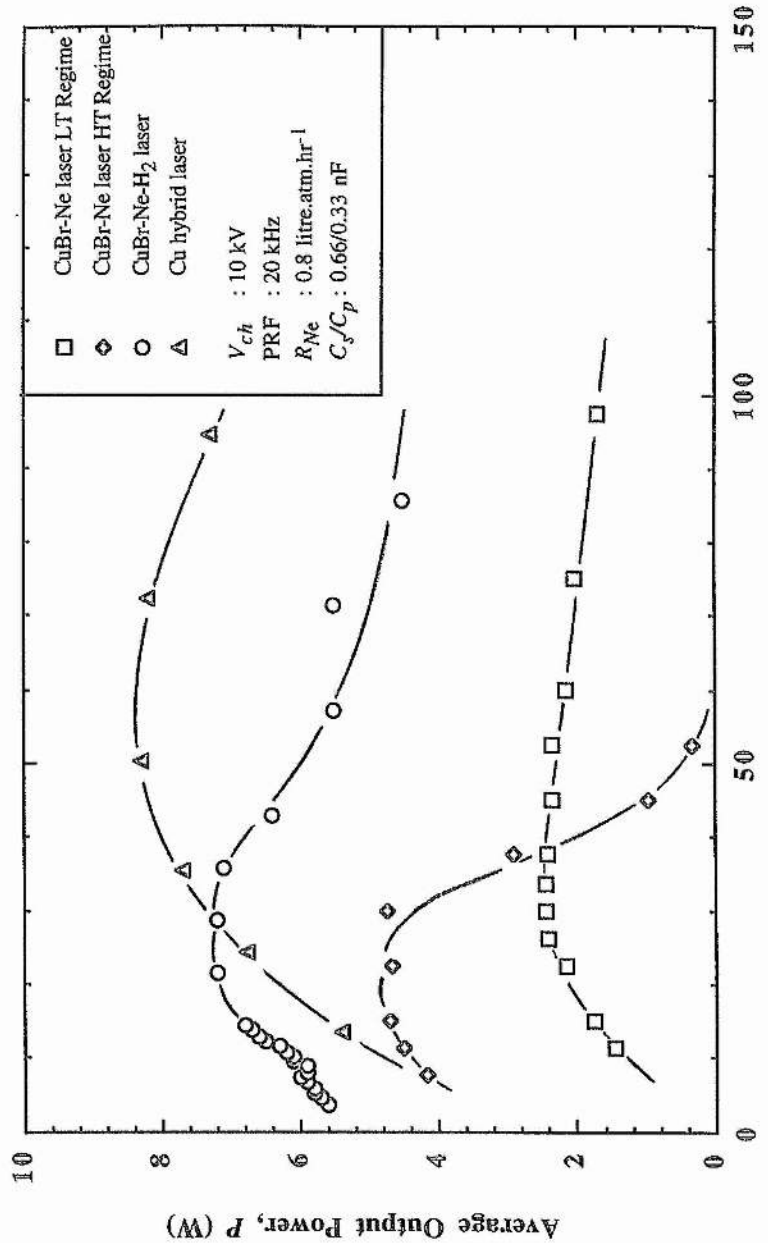

Fig. 6.1
Average output power, P, versus buffer gas pressure, p_{Ne}, for all four laser regimes.

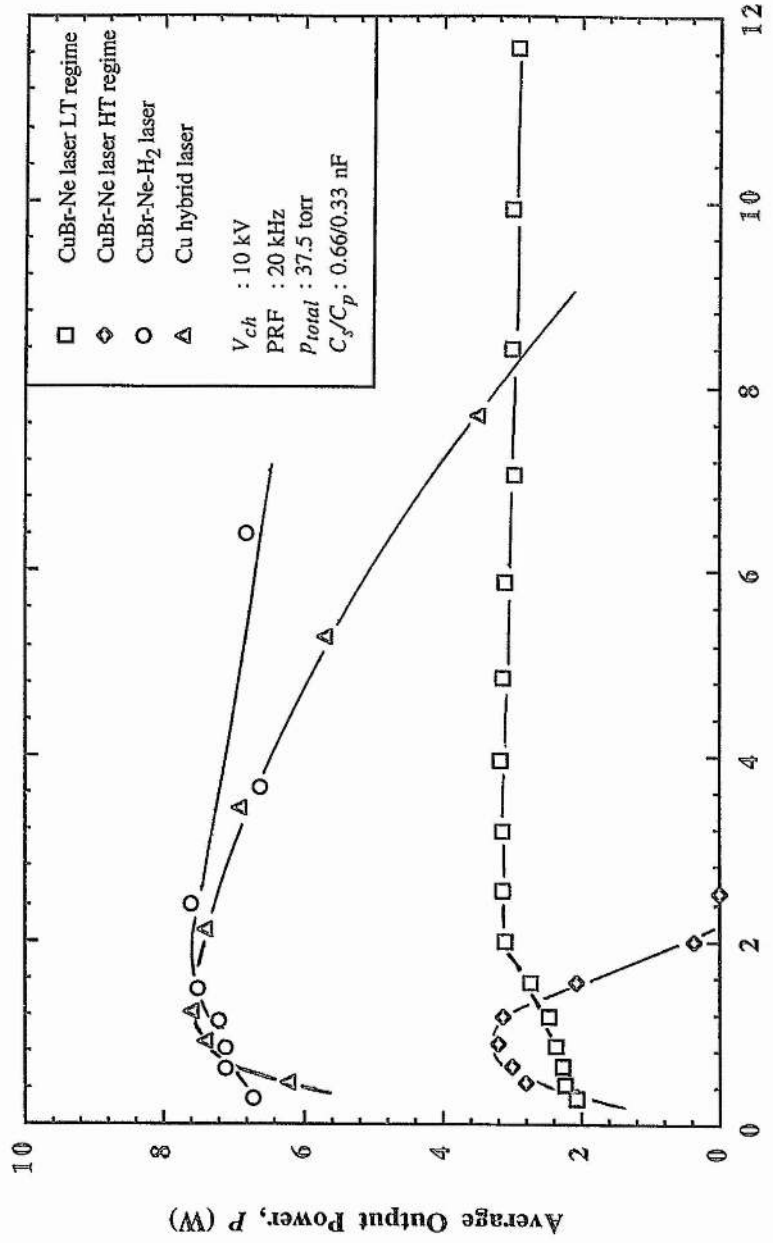

Fig. 6.2
Average output power, P, versus buffer gas flow rate, R_{Ne}, for all four laser regimes.

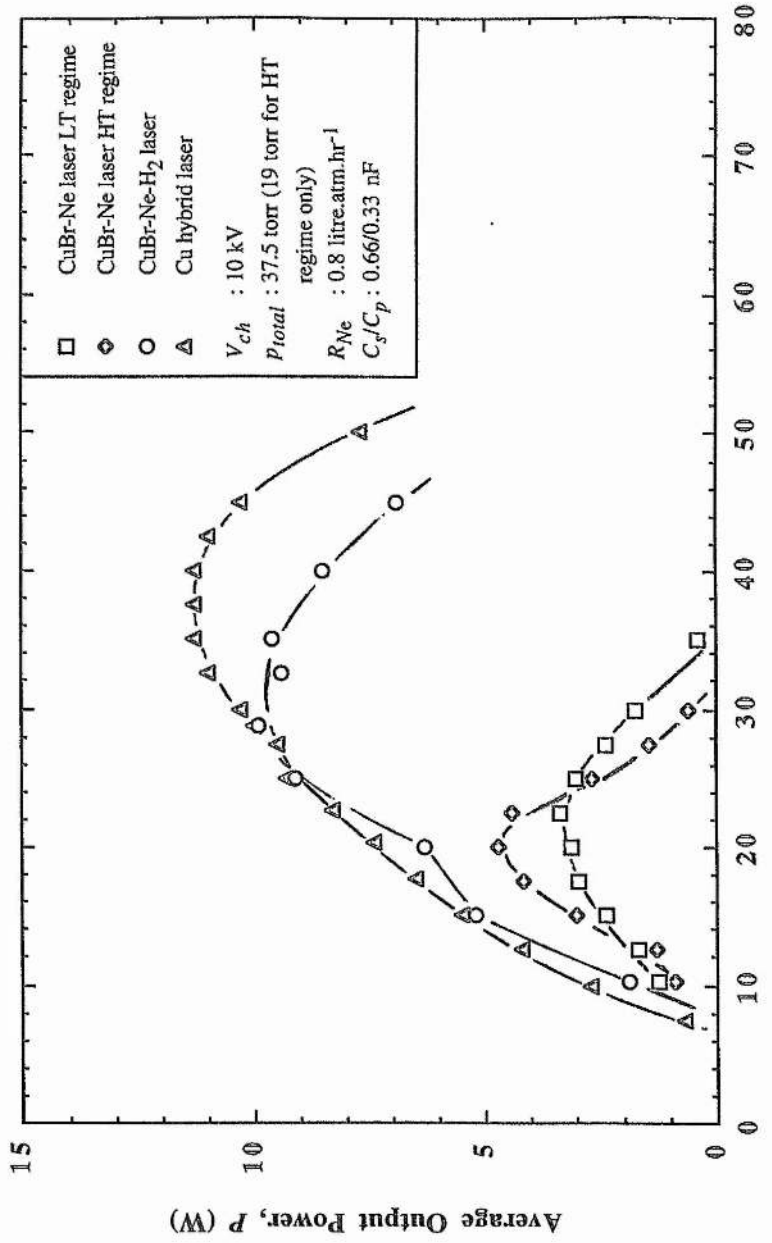

Fig. 6.3
Average output power, P, versus PRF for all four laser regimes.

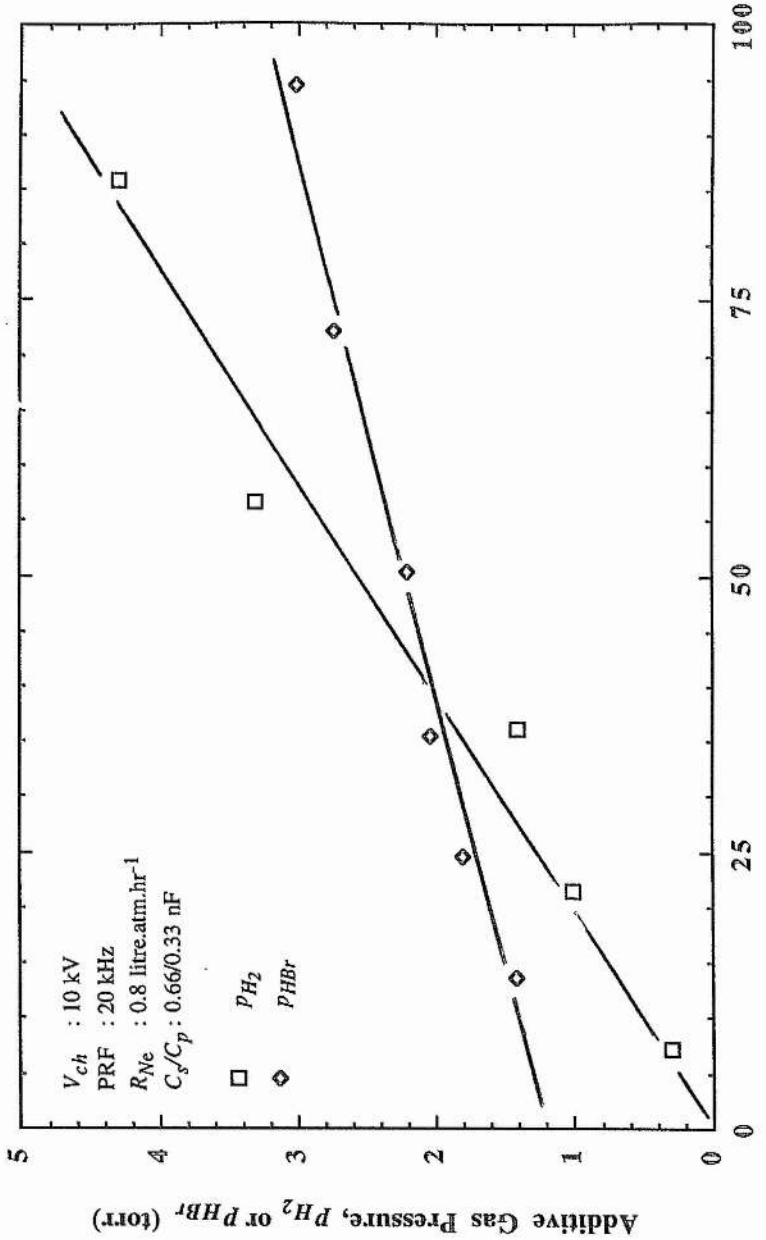

Fig. 6.4
Hydrogen pressure, p_{H_2}, and hydrogen bromide pressure, p_{HBr}, versus buffer gas pressure, p_{Ne}, in the CuBr-Ne-H_2 and Cu hybrid lasers respectively.

Chapter 7

Studies of Metal Seeding in the Cu Hybrid Laser

7.1 Introduction

The process of introducing free metal atoms into the gain medium of a metal vapour laser is designated 'metal seeding' and proceeds differently in each of the copper lasers discussed so far. In CVLs, copper metal in the laser tube is vaporised by waste heat generated by the gas discharge to be seeded. Insulation is wrapped around the tube so that temperatures in the range 1400-1600 °C, which are necessary to generate the required 0.1-1 torr of Cu vapour, can be obtained. In the LT regime of the CuBr-Ne laser, vaporisation of solid CuBr at temperatures of around 490 °C, and subsequent dissociation of the gaseous Cu_3Br_3 and Cu_4Br_4 polymers by electron impact in the buffer-gas discharge volume, produces the free Cu atoms for lasing. Seeding occurs by a similar mechanism in the HT mode of the CuBr-Ne laser and in the CuBr-Ne-H_2 laser, but in these cases, hydrogen reduction of the Cu salt might also assist in the dissociation process.

In the copper hybrid laser, HBr molecules are entrained in the flowing buffer gas and are decomposed in the discharge region to produce a variety of species of which the most important are undoubtedly Br_2, Br, Br^-, H_2, H and H^-. An active species in the discharge, thought to be atomic bromine [78], reacts with the source Cu in the laser tube at temperatures of approximately 500-800 °C to produce gaseous CuBr. The CuBr molecules polymerize [81] to Cu_3Br_3 and Cu_4Br_4 above the copper surface from whence they diffuse into the discharge volume and are dissociated by electron impact and hydrogen reduction into free Cu atoms and a mixture of Br, H and HBr. The species CuH

may also be present (see Section 7.6). The Cu seeding process in the copper hybrid laser has been likened to the 'iodide' or 'hot-filament' process of metal purification [75] except that in the latter case a heated filament takes the place of the discharge plasma as the decomposition element.

During their investigation of a 60 mm bore copper hybrid laser, Jones and Little noted that the sidelight spectrum was uniform from cathode to anode [78]. A 5 cm^2 area of copper near the gas inlet was sufficient to ensure optimum laser operation and there was greatest consumption of copper near the anode. Equilibrium was established close to the point of entry of the gas and maintained along the tube length with reactions at subsequent pieces serving only to redress the equilibrium. An optimum gas flow rate was also observed, and equilibrium over the first few pieces was consistent with this rate. As copper hybrid lasers have produced high output powers with the highest efficiencies so far recorded, it is desirable to study the Cu seeding process further. The process lends itself well to investigation as the HBr pressure and Cu loss are readily measured. In this chapter the results of the first quantitative experimental study of the Cu seeding mechanism in a copper hybrid laser are reported.

The effects of varying buffer-gas flow rate, exposed surface area of Cu metal and the location of the source metal in the active volume on the efficacy of the Cu seeding process are investigated in the same 12.5 mm bore copper hybrid laser which produced an average output power of 12.8 W at a PRF of 35 kHz for a gas flow rate of around 1 litre.atm.hr^{-1} and an HBr pressure of approximately 2 torr in 35.5 torr Ne (Chapter 5). It is demonstrated that characteristic laser operation can be achieved when small surface areas (< 100 mm^2) of copper metal are located at the upstream end of the laser tube only.

The distribution of copper in the laser tube was determined before and after lasing for a 3 hour period. The removal rate of copper from the laser tube was estimated using a single cylindrical source of copper adjacent to the anode. The atomic Br pressure at the tube wall and the number density of Cu in atomic and molecular forms, averaged throughout the tube, have been estimated.

From considerations of the energies and cross-sections of kinetic processes

involving the most likely discharge species, the most probable chemical reactions are identified. The estimated number density of Cu in the active volume together with relevant vapour pressure data then enable the actual types and concentrations of gas species to be postulated. Finally, evidence is cited for the theory that dendritic Cu deposits are the result of a secondary, non-optimal 'iodide' process wherein the source Cu metal itself acts as a deposition site for some of the liberated Cu atoms. The local effects of dendrites on the competing processes of Cu salt formation and Cu metal deposition are discussed.

7.2 Basis of the Metal Seeding Process

A recent account of the seeding process in metal hybrid lasers suggests that the mechanisms at work during gaseous metal halide formation and diffusion to the centre of the discharge are the same as those in the 'iodide' process of metal purification [78]. The 'iodide' technique [75] was developed to provide robust metals of high purity for the aerospace and military sectors. It is alternately designated 'hot-filament', 'de Boer' and 'van Arkel' after the process details and the scientists who pioneered the technique.

The central principle of the 'iodide' process is one of halogen (or hydrogen halide) gas reacting with hot metal to form a metal halide vapour which then diffuses to a hot filament. There, it is decomposed back into pure metal and halogen gas by thermal dissociation or by hydrogen reduction in a H_2 atmosphere. The newly formed halogen gas can then diffuse back to the hot source metal where the process is repeated. Cu is one of a number of metals which have been successfully deposited by this technique. Very small concentrations of halogen are required to deposit quite substantial amounts of metal. Although the list of halogens tried includes bromine and chlorine, iodine has had the highest success rate, hence the name.

In the 'iodide' process halide formation at the source metal and decomposition at the filament may be treated separately. At the metal, halogen gas is thermally dissociated above the surface to form atomic halogen, *e.g.* for iodine

$$I_2 \text{ (vapour)} \rightarrow 2I \text{ (vapour)}.$$

Liberated halogen atoms react with the metal to form a volatile halide, *e.g.*

$$M \text{ (solid)} + I \text{ (vapour)} \rightarrow MI \text{ (vapour)}.$$

Together, these reactions give the first two criteria for the 'iodide' process: 1) the halogen must be unstable at the source metal temperature; 2) the halogen must be able to react with the metal to form a stable, volatile halide at the source metal temperature. If the halide is not stable then the rate of removal always falls to the evaporation rate of the metal. At the hot filament there is only one criterion of major importance to the study of the hybrid laser seeding mechanism: 3) the volatile halide must be readily decomposed at the higher temperature of the hot filament. There are other conditions to be met at the filament [75], but these are of relevance only where crystal growth is the primary objective.

When a suitable halogen has been identified, *i.e.* one with a stable halide at the desired temperature of the source metal, then at any fixed pressure of the halogen gas the reactions at the metal surface pass through four distinct regimes with increasing temperature. Taking iodine as an example together with a general metal, M, these are: *Regime 1.* The metal vapour pressure exceeds the halide vapour pressure and the metal surface becomes coated with solid halide; *Regime 2.* The halide vapour pressure just exceeds the metal vapour pressure and metal is removed at the evaporation rate of the halide; *Regime 3.* The rate of arrival of halogen atoms falls below the rate of removal of halogen atoms as halide and the rate of removal of metal atoms as MI_x is simply $1/x$ times the rate of arrival of halogen atoms; *Regime 4.* The halide is no longer stable. More than x halogen atoms are required to form one gaseous MI_x molecule. The rate of removal decreases until it becomes equal to the evaporation rate of the metal from whence it increases monotonically.

The removal rate of metal as gaseous metal halide therefore has a maximum at

relatively low temperatures (regime 3) and a minimum at elevated temperatures (regime 4). Lower temperatures are always required to thermally dissociate a metal halide in the presence of hydrogen. The metal surface temperature is set to give operation in regime 3 where removal of metal atoms is a maximum. For the case of copper, CuI_2 is not stable but Cu(I)I is readily formed at a surface temperature of around 400 °C. In contrast, the filament temperature is set for operation in regime 4 where a minimum number of metal atoms can be sustained as metal halide vapour. Pure metal is deposited due to the instability of the halide at the filament temperature. For CuI, deposition most readily occurs at filament temperatures in the region of 900 °C.

The 'iodide' process has been demonstrated in both sealed-off and flowing-gas systems. In the sealed-off apparatus the crude metal to be purified is usually confined to a volume between the bulb wall and a perforated metal cylinder surrounding the hot filament. The cylinder metal is chosen so that it will not react with the other species at the necessary temperatures and pressures. The perforations in the cylinder enable a uniform distribution of metal halide vapour to be achieved around the deposition site. The volatile halide is continuously formed and decomposed within the unit. The flowing-gas method involves the vaporisation of halide in an auxiliary chamber and diffusion of the gaseous halide molecules so formed into the deposition chamber containing the filament. There, the halide vapour is entrained in a flowing buffer gas. Undecomposed halide and its reaction products are continuously removed from the second chamber. In the flowing-gas system the vapour pressure of halide sustained depends not only on the rate of reaction at the metal surface but also on the flow rate of the gas.

In the copper hybrid laser to which HBr is added, the Cu donor species is copper bromide and the optimum pressures of HBr are sustained at Cu metal and plasma edge temperatures of 500-800 °C and 900-1000 °C respectively. In the 'iodide' process, Cu metal was deposited from CuI, albeit in dendritic form, using source metal and hot filament temperatures of 400 °C and 900 °C respectively. As the molecular properties of CuBr and CuI are quite similar, this comparison is good evidence that the 'iodide' process is at work in both systems. As mentioned in the introduction to this chapter, the

main difference between the 'iodide' and 'metal seeding' processes is in the dissociative stage of each though both techniques are cyclic. In the former case, dissociation of the metal halide occurs thermally or by hydrogen reduction on a hot element. In the laser tube, decomposition of the halide occurs primarily in the high-temperature, non-localised plasma of the buffer-gas discharge by electron impact and by hydrogen reduction. In either case, after the metal salt is dissociated, the halogen is free to react with more of the source metal.

Although the copper hybrid laser is a flowing-gas system, the halide is created by reaction of bromine with a distribution of copper metal in the same chamber where 'deposition' takes place. The hybrid laser discharge tube therefore contains elements of both the sealed-off and flowing-gas versions of the 'iodide' process. The source metal itself can also act as a site for the dissociation of halide in the hybrid laser, and deposition of the metal is usually in the form of dendrites. In examining the metal seeding process in the copper hybrid laser, it is again possible to treat as separate the reaction at the source metal to form volatile CuBr and the dissociation of the bromide at the sites identified above, *i.e.* on source copper and in plasma.

Although CuBr formation proceeds in the same fashion in both the copper hybrid laser and 'iodide' process, the laser has the additional requirement that it must lase. For this, the partial pressure of halide generated must to sufficient to enable lasing but not so great that discharge constriction or instabilities set in. In the copper hybrid laser the appropriate criteria at the Cu metal are [78]: 1) the halogen/hydrogen halide should have a low thermal stability; 2) the halogen/hydrogen halide should react with copper at accessible temperatures to form a volatile copper halide which is relatively stable in the vapour state; 3) the volatile halide should have a ratio of metal to halogen atoms close to unity or greater than unity (monohalides or subhalides); 4) the decomposition temperature should be greater than the wall temperature to maintain the halide at vapour pressures required for lasing (a few tenths of a torr); 5) The halide should be readily dissociated in the gaseous discharge.

Confining the discussion to a Cu-Ne-HBr gas mixture with a distributed copper

configuration (Br_2, HCl, Cl_2, and SF_6 halogen donor molecules and He buffer gas have also been tried), the first reaction that can occur is thermal dissociation of the HBr molecule to yield Br:

$$\text{HBr (vapour)} \underset{\text{wall}}{\rightarrow} \text{H (vapour)} + \text{Br (vapour)}.$$

In the laser tube volume this dissociation takes place by electron impact. The reactions most likely to remove Cu in the form of CuBr from its initial source are:

$$\text{Cu (solid)} + Br_2\text{ (vapour)} \underset{\text{wall}}{\rightarrow} \text{CuBr (vapour)} + \text{Br (vapour)},$$

$$\text{Cu (solid)} + \text{Br (vapour)} \underset{\text{wall}}{\rightarrow} \text{CuBr (vapour)},$$

$$\text{Cu (solid)} + \text{HBr (vapour)} \underset{\text{wall}}{\rightarrow} \text{CuBr (vapour)} + \text{H (vapour)}.$$

The largest contribution is thought to be made by the second reaction [78], *i.e.* by the action and/or mediation of Br. Electrons, ions, and H will make some contribution depending on their mean paths for recombination near the tube edge whereas HBr and Br_2 are less likely to be involved. That the reacting species is chemically active is demonstrated by the fact that only that copper immediately adjacent to the discharge is consumed. This is a reproducible result which occurs despite the fact that the copper pieces are often raised slightly above the alumina floor so that the gas mixture can circulate beneath them.

As demonstrated in Chapter 5, for buffer-gas pressures in the range 13.6-94.5 torr an upper limit of 1.4-3.2 torr is placed on HBr pressure. Above these pressures, average power falls and discharge constriction and instabilities can set in. The temperature of the source metal is chosen to give the desired halide vapour pressure. At 1.4-3.2 torr HBr there are three temperature ranges to consider.

Below 450 °C corresponds to regimes 1 and 2 of the 'iodide' process. HBr, Br_2

and Br react slowly with the surface to produce solid CuBr and H/H_2. If the rate of arrival of halogen atoms exceeds the evaporation rate of CuBr then the copper is coated. If not, then the rate of removal is the evaporation rate of CuBr. If the metal surface temperature exceeds 450 °C but is less than 800-900 °C then operation in regime 3 is possible. The evaporation rate of CuBr is higher than the rate of arrival of Br bearing species. No surface CuBr layer forms and the rate of production of CuBr depends on the rate of arrival of the reactants. The metal is clean and the evaporation rates do not depend on transport through a condensed layer. Above 900 °C the CuBr is no longer stable and the removal rate of copper falls until equal to the evaporation rate of copper at that temperature. The removal rate of copper therefore exhibits the characteristic minimum at around 900-1000 °C which is the filament temperature used in the sealed-bulb deposition of copper from CuI. As illustrated by the 450-800 °C operating temperature range of the laser, the temperature of the copper pieces is not too critical as the HBr pressures can be readily adapted to any changes in the rates of the forward and reverse reactions to maintain the necessary density of ground state copper atoms.

When solid copper is reacted with HCl vapour, Cu_3Cl_3 trimers are found to be present in greater numbers above the metal surface than are CuCl molecules [79]. In his studies of CuI, Loonam suggested that as the reaction

$$MI\ (vapour) \rightarrow M\ (solid) + I\ (vapour)$$

has one mole of vapour on either side of the equation, gives no pronounced increase in entropy and shows no marked lowering of free energy on heating it was therefore unlikely to occur [75]. In his opinion, any element that formed a stable gaseous monomeric monoiodide could not be deposited by thermal dissociation. However, if the gaseous metal iodide was polymeric then the reaction

$$M_3I_3\ (vapour) \rightarrow 3M(solid) + 3I\ (vapour)$$

would permit a considerable increase in entropy. According to Loonam, the fact that a metal can be deposited from its iodide by thermal dissociation itself implies that the iodide exists in polymeric form. CuBr is of similar entropy to CuI which suggests that it might also exist mainly in the polymeric form. The presence of CuBr polymers in a copper hybrid laser has been demonstrated quite recently [66].

It is assumed then that polymerization of CuBr must occur above the copper pieces:

$$Cu_{x-1}Br_{x-1} + CuBr + M \rightarrow Cu_xBr_x + M \ldots$$

Copper bromide molecules diffuse towards the centre of the laser tube. In the discharge, the copper bromide is depolymerized and the copper atoms are freed by electron impact and hydrogen reduction processes:

$$e + Cu_xBr_x \rightarrow Cu_{x-1}Br_{x-1} + CuBr + e,$$

$$e + CuBr \rightarrow Cu + Br + e$$

$$e + CuBr \rightarrow Cu + Br^-$$

$$Cu_xBr_x + H \rightarrow Cu_{x-1}Br_{x-1} + Cu + HBr, \text{ etc.}$$

As there is an ongoing process of dissociation in the centre of the discharge, there is a permanent number density gradient in favour of diffusion of copper bromide to the discharge centre. Halide molecules continuously diffuse from the wall to replace those which have been dissociated, thereby delivering further copper atoms to the discharge as required. The density of Cu atoms in the discharge can exceed the numbers available when copper is sourced as solid CuBr (as in the CuBr-Ne and CuBr-Ne-H_2 lasers for example), as the numbers of halogen atoms, which transport copper atoms into the discharge, are larger (by 2-3 times) in a hybrid laser (2.5 torr added HBr versus ~0.3 torr $Cu_{3.5}Br_{3.5}$ vapour in a conventional halide laser [70]). Therefore, the specific output pulse energy can also be higher in a hybrid laser than in a halide laser.

In the steady state, the rate of loss of Cu atoms by condensation on the tube wall and by diffusion out of the end-flanges with the gas flow, together with loss of CuBr by thermal dissociation, dendrite growth and condensation, equals the rate of removal of Cu from the copper surface and from the alumina wall by reaction with halogen. As the alumina is clean during normal operation and the copper pieces consistently drop in weight and are clean, the rate of supply of copper to the discharge is limited by the rate of reaction of halogen with the copper pieces. In [78], the results of Frommer and Polyani [80] were interpreted as meaning that the maximum collision yield is 0.3 for reaction of Cu with Cl.

In the interpulse period, the number of free Cu atoms are reduced by reassociation with bromine to the monomeric and polymeric forms of copper bromide, and by diffusion to the wall of the tube. As in the 'iodide' process, the copper bromide molecules are removed from the gaseous phase on the copper surface (or any hot surface) by thermal dissociation

$$Cu_xBr_x(g) \rightarrow Cu(s) + Cu_{x-1}Br_{x-1}(g) + Br(g),\ x=1,2,3,4,\ldots$$

and by hydrogen reduction

$$Cu_xBr_x(g) + H(\text{or } H_2)(g) \rightarrow Cu(s) + Cu_{x-1}Br_{x-1}(g) + HBr(g) + (H(g)),\ x=1,2,3,4,\ldots$$

Where deposition is faster than removal (near the cathode, for example), the resulting deposits are dendritic in form.

7.3 Dependence of Average Output Power on Buffer Gas Flow Rate for Distributed and Cylindrical Copper Metal Configurations

To determine the ideal surface area and location of the Cu metal for lasing in the 12.5 mm bore copper hybrid laser tube, the average output power of the laser was recorded as a function of buffer-gas flow rate in the range 0.3-7.7 litre.atm.hr^{-1} for each of five

configurations of the copper metal. The 0.66/0.33 nF capacitors were used and the total gas pressure, charging voltage and PRF were fixed at their reference values of 37.5 torr (2 torr HBr), 10 kV and 20 kHz respectively.

The first configuration tried was that used in the general experiments reported in Chapter 5. Twelve copper pieces 5 mm x 10 mm x 0.25 mm were placed end-to-end in pairs at 5 cm intervals along the floor of the alumina tube. The anode facing edge of the first copper piece was located approximately 10 mm in from the edge of the ceramic. In the other configurations, the copper source was a single cylinder which was rolled from 85 mm wide by 0.25 mm thick copper sheet, moulded to the inside of the alumina tube and located at the upstream end of the laser tube, immediately adjacent to the anode. Cylinders of 1 mm, 2 mm, 10 mm and 20 mm length were used.

On completion of each investigation of average output power versus flow rate, the remaining Cu metal was inspected to ascertain the actual reaction area which the copper had presented to the discharge including, for example, reaction around the edges of the copper pieces and cylinders. The approximate area of reaction for each copper piece was 55 mm^2 giving a total reaction area in the laser tube of around 660 mm^2. Areas of exposure were 79 mm^2, 113 mm^2, 408 mm^2 and 758 mm^2 for the 1 mm, 2 mm, 10 mm and 20 mm cylinders respectively.

Average output power versus gas flow rate is shown in Fig. 7.1 for all configurations attempted and can be fitted with a single curve. Whether distributed or confined to the upstream end of the laser tube, the copper configuration makes little difference to laser performance. In each case, an output power of 6-8 W was obtained for a flow rate of ~1 litre.atm.hr^{-1}. For a tube 12.5 mm in bore and 36.8 cm^3 in active volume, a 1 mm long copper cylinder (79 mm^2 reaction area) supplies sufficient concentrations of copper bromide to the discharge for optimum power to be achieved.

When a single copper cylinder was used in place of distributed copper pieces, there were some instances of instability at very low flow rates ($\leq$ 0.5 litre.atm.hr^{-1}) due to sporadic lasing (*i.e.* improper seeding) at the cathode end of the tube, but these instabilities were only observed when the shorter copper cylinders (1 and 2 mm lengths)

were in use. When the copper metal was all located upstream, cessation of lasing was noted to take longer between HBr additions than when the copper metal was distributed. Dendrites grew vertically upwards and downwards from cylinder edges, and from the centres and edges of the copper pieces. When the copper was distributed, dendrite growth appeared to occur at random along the length of the tube.

7.4 Dependence of Optimum HBr Pressure on Buffer Gas Flow Rate for Distributed and Cylindrical Copper Metal Configurations

Along with average output power, HBr pressure was noted for optimal lasing at each buffer-gas flow rate attempted. As for average output power, HBr pressure versus flow rate (Fig. 7.2) can be fitted with a single curve for all configurations of the copper metal. At low flow rates, the required HBr pressure is 3-4 torr (corresponding to 8-11 % of the gas mixture) and, according to Fig. 7.1, the output power is low at 5.5-6 W. At 1 litre.atm.hr^{-1} flow rate, the requisite pressure of HBr drops to only 2 torr for a maximum output power of 6-8 W. At the highest flow rates considered the maximum HBr pressure was marked by the onset of discharge instabilities. Near 8 litre.atm.hr^{-1} only ~ 0.5 torr HBr could be tolerated, and the average output power was greatly reduced at 3-5 W.

7.5 Copper Distribution Versus Time for Distributed and Cylindrical Copper Metal Configurations

The laser was operated for a period of 185 min. with the distributed copper configuration. The buffer-gas flow rate was 0.9 litre.atm.hr^{-1} and the HBr pressure was optimised at 2 torr for the entire 185 min. The total gas pressure, charging voltage and PRF were 37.5 torr, 10 kV and 20 kHz as before. The 12 pieces of copper were weighed before and after lasing. Fig. 7.3 shows the weights of the 6 pairs of copper pieces as functions of position in the laser tube, before and after the 185 min. period. Change in weight with position is shown in Fig. 7.4. The weights of copper dendrite formations found attached to the pieces are included in the figures for weights after lasing in Fig. 7.3.

Figs. 7.3 and 7.4 show that the first pair of copper pieces was consumed entirely

in the seeding process. Some of the consumed copper was deposited near the cathode while the remainder was lost as copper bromide in the end-flanges. There are small, essentially random fluctuations in weight nearer the cathode indicating clearly that these pieces maintain the equilibrium pressure of copper bromide.

The dendrites were observed to be short, thick, 'tree-like' structures with rounded tips. A grey, porous, powder-like deposit was also seen on some of the copper pieces after lasing. This was especially noticeable on those pieces closest to the anode where the copper metal was cooler. Dendrites grew at essentially random locations throughout the tube, but it was noted that where a dendrite had grown on a copper piece close to the cathode there was also increased consumption of the original piece although there was no great change in its overall weight.

The rate of reaction of copper with HBr and its dissociation products was quantified by determining the amount of copper removed from the laser tube over a fixed period of time when it was fitted with a 10 mm long copper cylinder near the anode. The cylindrical configuration was chosen to give an even distribution of copper around the discharge (as in the sealed-off 'iodide' process apparatus), and so that removal of copper was not complicated by reactions at other sites downstream. A weight of 0.19 g copper was consumed in 132 min. when the buffer-gas flow rate and total gas pressure were 0.9 litre.atm.hr^{-1} and 37.5 torr respectively. The HBr partial pressure was measured as 3.4 torr on this occasion.

At the flow rate of 0.9 litre.atm.hr^{-1}, the active volume was replaced every 7.26 seconds. Over a 132 min. period 0.19 g of Cu was removed from the metal surface. The rate of removal of Cu atoms from the copper metal is just,

$$Rate\ of\ removal\ of\ Cu\ atoms = \frac{Total\ no.\ of\ atoms}{Cu\ area \times time}, \qquad \text{----------(7.1)}$$

and is 5.6 x 10^{16} cm^{-2}.s^{-1} in this example. Using the calculated figure for the removal rate of Cu and an estimated gas temperature of 600 °C we can find the number density of atomic bromine, n_{Br}. The rate of Br collisions on the Cu surface is given by

$$Br\ collisions/cm^2.s = \frac{n_{Br}\bar{v}_{Br}}{4} \qquad \text{----------(7.2)}$$

from the kinetic theory of gases. Here, $\bar{v}_{Br}$ is the average velocity of the Br atom given by,

$$\bar{v}_{Br} = \sqrt{\frac{8kT_g}{\pi M_{Br}}}, \qquad \text{----------(7.3)}$$

where k is Boltzmann's constant, T_g is gas temperature (K) and M_{Br} is the mass of the atom (kg).

Then, assuming that the results of Frommer and Polyani's experiments with HCl [80] also hold for HBr, every third collision of a Br atom must lead to a CuBr molecule so that we can calculate that the number density of atomic bromine must be 1.4 x 10^{13} cm^{-3} or just 1.3 mtorr if we use the ideal-gas expression for the atomic bromine pressure, p_{Br}, in Pa:

$$p_{Br} = n_{Br}kT_g. \qquad \text{----------(7.4)}$$

As significant deposition of copper bromide occurred in the anode region due to diffusion against the slow gas flow, it was not possible to obtain an accurate value for copper density in the laser tube. Assuming that half the copper generated by reaction at the copper piece was immediately lost from the tube in this manner (true for very slow flow rates) then the number density of copper (in atomic/molecular forms) averaged radially may be calculated as 2.2 x 10^{16} cm^{-3}.

7.6 Discussion of Results

The dependence of average output power and optimum HBr pressure on buffer-gas flow rate in Figs. 7.1 and 7.2 can be interpreted thus. At the lowest flow rates, CuBr diffuses

backwards against the gas flow into the tube. The output power is low, probably because of the subsequent loss of CuBr by condensation upstream of the anode. Increased pressures of HBr are necessary to compensate for this loss. Deposits of copper bromide near the anode were noted for the lowest flow rates. At flow rates above 3 litre.atm.hr^{-1}, back diffusion of CuBr is less of a problem but the gas temperature can fall and copper bromide vapour can condense in the active volume of the laser tube instead. This leads to discharge instabilities and non-uniformities and lower output powers. There is a tendency to tolerate smaller HBr pressures as the levels of CuBr in the tube are already high. The largest variation in output powers was recorded at the highest flow rates. It is likely that turbulence was induced in the tube. The wall temperature dependence of average output power is plotted in Fig. 5.2 of Chapter 5 for the small-bore copper hybrid laser and shows that output power is constant with wall temperature in the range 550-830 °C. The dependence of output power on flow rate must therefore be due to changes in copper entrainment (low flows) and gas temperature (high flows), rather than to tube temperature.

The weights of copper before and after lasing in Fig. 7.3 clearly demonstrate that in small-bore copper hybrid lasers the upstream pieces supply the free copper atoms for lasing. The smaller increases and reductions in the weights of pieces nearer to the cathode serve only to maintain the equilibrium of free copper atoms. Powers are therefore unaffected by placing all of the copper metal near the anode. Lasing was sporadic at low flow rates when the short cylinders (1-2 mm length) were used because up to half of the relatively small densities of free Cu atoms was lost due to back diffusion at the anode and there were no copper sites downstream to replenish the density near the cathode. If metal seeding was a volumetric effect then we might expect to observe a different response from the 60 mm bore copper hybrid laser in which volumetric effects should play a larger role. The similar behaviours of the 12.5 mm and 60 mm bore tubes demonstrate that metal seeding is a wall effect.

For the large calculated concentration of copper atoms to exist, a significant amount of the copper must be locked up as Cu_xBr_x polymers in the discharge with x

being weighted between 3 and 4, as suggested by the results of [81]. This supports the view that the CuBr monomers polymerize very quickly above the copper pieces. As HBr is known to have been added to the tube at a partial pressure of 3.4 torr in this example, an *upper* limit of 5.2 x 10^{15} cm^{-3} may be placed on the radially averaged number density of Cu_xBr_x polymers, for x = 3.5. This upper limit can only account for 80 % of the copper atoms in the tube. It is likely therefore that the balance of copper atoms are present as free atoms and in CuH molecules, which are relatively stable (dissociation energy of 2.73 eV [82]).

In one previous investigation of a 25 mm bore copper hybrid laser [83], the axial density of Cu atoms was measured as 9.4 x 10^{14} cm^{-3}. The ratio of specific average output pulse energies between the 12.5 mm and 25 mm bore lasers is ~2 (see Chapter 8). Assuming therefore that the average number density of Cu atoms in the 12.5 mm bore laser is ~ 2 times higher than in the 25 mm bore laser, the average density of atomic copper should be of the order of 4 x 10^{15} cm^{-3} in the 12.5 mm bore laser.

Assuming from the above analysis that the densities of Br, H and Br_2 can be neglected (the former two species being highly reactive and the latter unstable), and that the HBr density is equal to the H_2 density, we can estimate the number densities of $Cu_{3.5}Br_{3.5}$ polymers, CuH, Cu and HBr in the laser tube. The equations of atom conservation may be stated as:

$$\text{Br: } n_{HBr} + 3.5\left(n_{Cu_{3.5}Br_{3.5}}\right) = n_{HBr}(\text{original}) = 1.8\times10^{16}\,\text{cm}^{-3}, \qquad \text{----------(7.5)}$$

$$\text{Cu: } 3.5\left(n_{Cu_{3.5}Br_{3.5}}\right) + n_{Cu} + n_{CuH} = n'_{Cu}(\text{total}) = 2.2\times10^{16}\,\text{cm}^{-3}, \qquad \text{----------(7.6)}$$

$$\text{H: } n_{HBr} + 2n_{H_2} + n_{CuH} = n_{HBr}(\text{original}) = 1.8\times10^{16}\,\text{cm}^{-3}. \qquad \text{----------(7.7)}$$

Having shown that 1.8 x 10^{16} cm^{-3} of HBr was added to the tube, and assuming that the average Cu density is 4 x 10^{15} cm^{-3}, we find from the above equations that the following number densities (radial averages) fit the data: 4.4 x 10^{15} cm^{-3} (HBr), 4.4 x 10^{15} cm^{-3}

(H_2), 4 x 10^{15} cm^{-3} (Cu), 3.9 x 10^{15} cm^{-3} ($Cu_{3.5}Br_{3.5}$) and 5.0 x 10^{15} cm^{-3} (CuH). There are evidently significant number densities of both $Cu_{3.5}Br_{3.5}$ and CuH in the discharge of the 12.5 mm bore copper hybrid laser to account for the Cu removed during operation.

Finally, for the sake of completeness, it is important not to overlook the secondary deposition site for copper - the copper source metal itself. Dendrite growth is noticeably faster in small-bore tubes. Studies of small-bore hybrid lasers have concluded that dendrites form on the hottest areas by thermal decomposition and hydrogen reduction, and that the deposition of metal is accelerated as it grows into the discharge. That deposition is much faster in discharges containing H_2 indicates that H_2 reduction is the main deposition process in those discharges.

There is evidence in the nature of the deposit that it forms via a thermally driven mechanism. Copper whisker formations have been reported in the deposition of copper from copper iodide [75]. At filament temperatures of 430-700 °C these were straight and narrow with little overgrowth. At temperatures of around 900-1000 °C (and at high supersaturation of the metal vapour) the whiskers formed were thickened by two-dimensional nucleation to form short thick spikes. Near the melting point of copper (1083 °C) the edges became rounded. The reduction process occurred at growth steps on the tips of the whiskers. With bulb and filament temperatures of 400 and 900 °C respectively (typical temperatures for the copper hybrid laser) the deposit was described as dendritic. Further, when the filament was too cool, the deposit was a grey, loosely bound powder of high surface area. Briefly then, very low temperatures caused the metal halide vapour to be deposited as solid metal iodide. At intermediate temperatures coarse, crystalline, metallic growths formed, and at just below the melting point of the metal the deposition had smooth crystalline faces. All of these observations are consistent with the earlier descriptions of deposition on the copper metal in the copper hybrid laser. Although the copper metal temperature may be 600-900 °C (100° higher than the wall temperature of 500-800 °C) in the copper hybrid laser, this is low with respect to the melting point of 1083 °C. Grey powder was only observed on copper pieces near the anode where temperatures were at the lower end of the scale.

Finally, in the normal 'iodide' process, a surface projection from the deposited metal is at a lower temperature than the rest of the deposit [75]. Halogen which contacts the projection reacts with it to form metal halide at its cooler surface and causes it to disappear. When the filament temperature is high enough, even the projection tip is hot enough to decompose the halide. In the copper hybrid laser, the protrusions (*i.e.* dendrites) are always hotter than the source copper, and continue to increase in temperature towards the tips because of increased proximity to the discharge. Dendrite growth is accelerated at the tips until a point is reached where the temperature at the tips approaches the melting point of copper. The tips then fuse and become rounded. Increased bromine concentrations at the copper pieces below the dendrites will speed up the formation of copper bromide and increase the deposition on the dendrites attached to the pieces. It was noted in the present study that where dendrites formed on those pieces near the cathode, greater removal of metal from the original surface had also occurred. As the copper metal is nearer to the discharge centre in smaller bore tubes and therefore hotter, this is an alternative explanation of accelerated dendrite growth in small-bore Cu hybrid lasers.

7.7 Conclusions

In the 12.5 mm bore copper hybrid laser, less than 100 mm^2 of copper metal is necessary for optimum lasing and this need only be placed at the upstream end of the active volume. For all configurations of the copper metal, average output power is maximum at a single buffer-gas flow rate (~ 1 $litre.atm.hr^{-1}$). Reduction in output power at flow rates to either side of optimum are due to back diffusion of CuBr (low flows) and reduced gas temperatures (high flows). Optimum HBr pressure falls exponentially with increasing flow rate and again may be fitted with a single curve for all copper metal configurations attempted.

The atomic bromine pressure at the wall needed to account for the observed copper metal removal rate is estimated as ~1.3 mtorr; the number density of copper in atomic and molecular forms averaged throughout the tube is 2.2×10^{16} cm^{-3}. Significant

numbers of Cu_xBr_x polymers and CuH must exist in the laser discharge to lock up the large quantity of copper atoms that exists in the active region. This is the first quantitative study to suggest the existence of CuH molecules in halide laser media.

Finally, the accelerated growth of copper dendrites in the small-bore tubes is caused mainly by hydrogen reduction of the bromide at the hot tips of the dendrites. In CuBr lasers in the absence of H_2, the slower process of thermal dissociation is probably responsible for Cu deposition on hot spots in the tube.

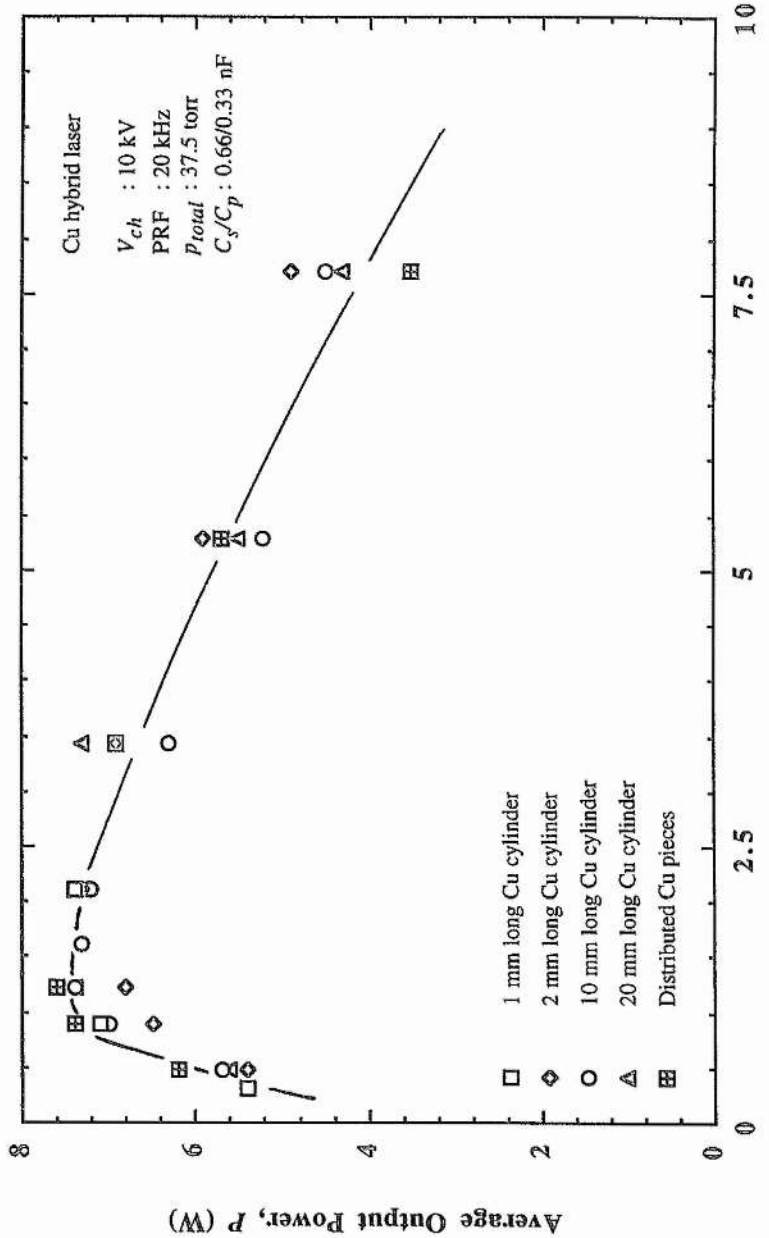

Fig. 7.1
Average output power, P, versus buffer gas flow rate, R_{Ne}, in the Cu hybrid laser for cylindrical and distributed configurations of the Cu metal.

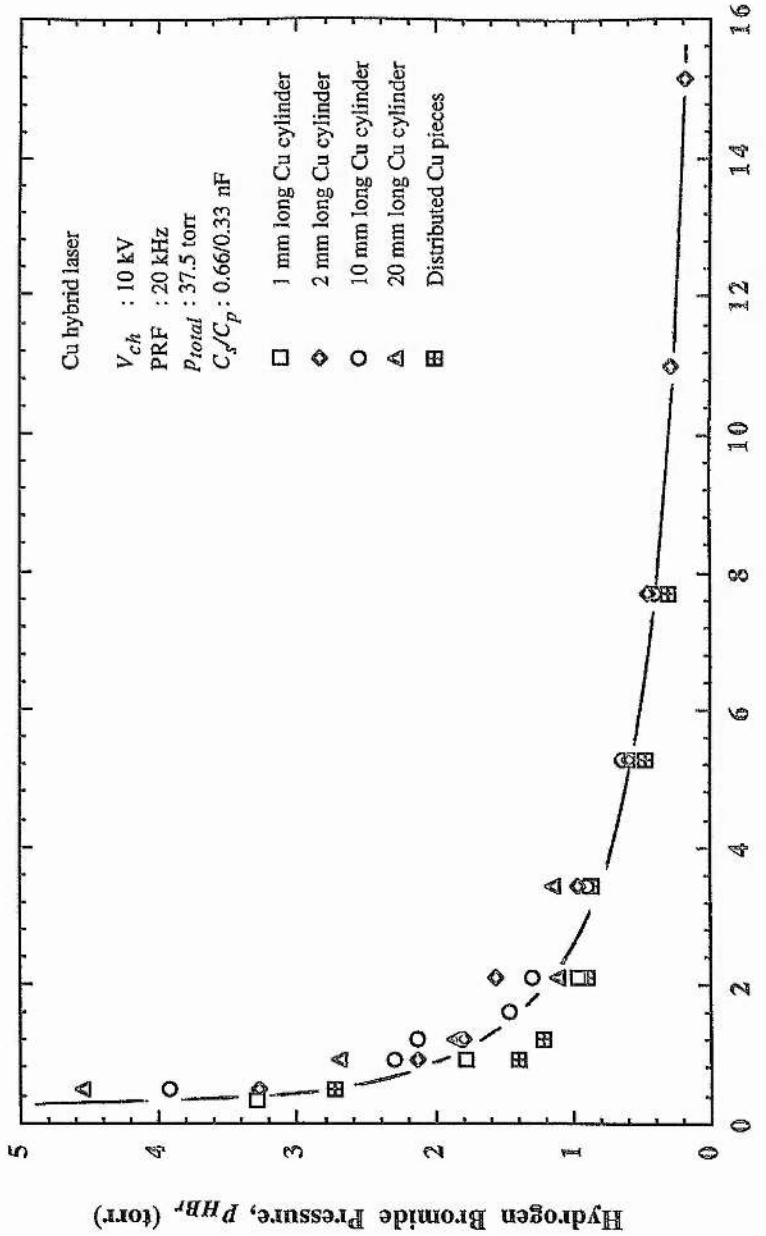

Fig. 7.2

Hydrogen bromide pressure, p_{HBr}, versus buffer gas flow rate, R_{Ne}, in the Cu hybrid laser for cylindrical and distributed configurations of the Cu metal.

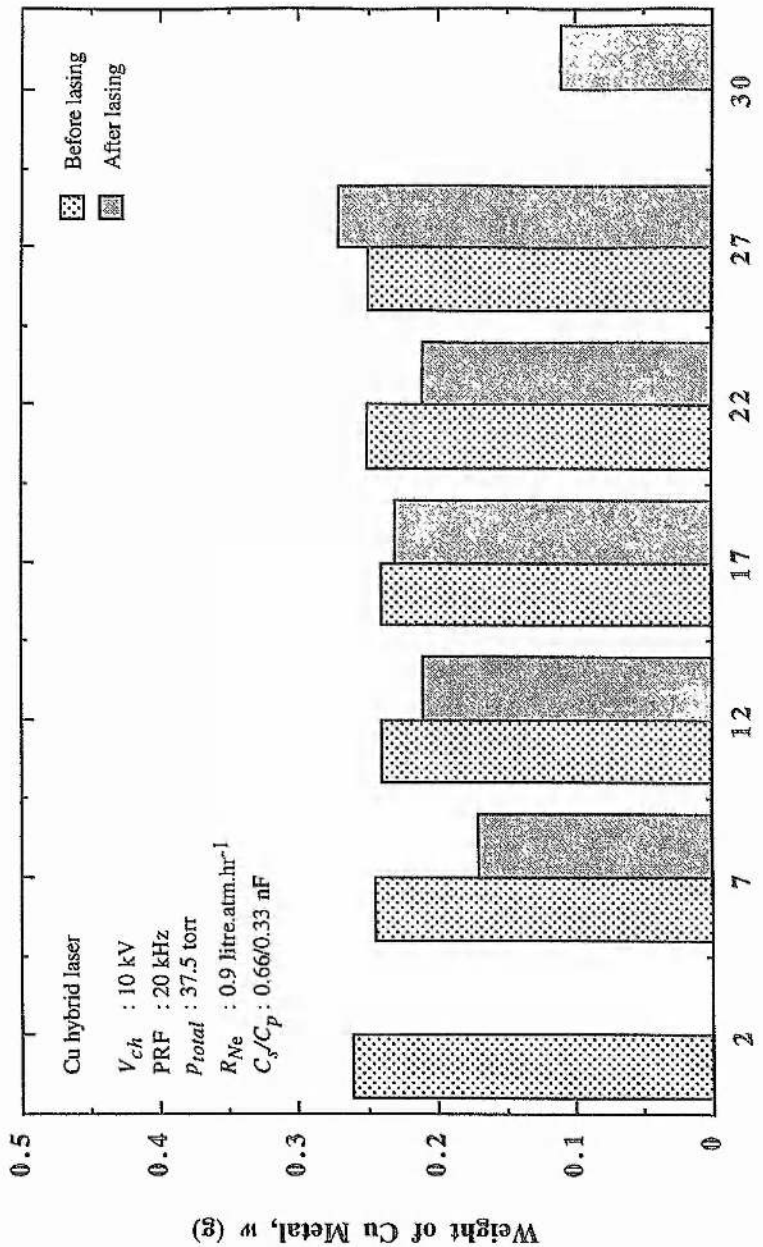

Fig. 7.3
Weight of Cu metal, w, versus mean distance from anode, d_a, before and after a 185 min. period of lasing.

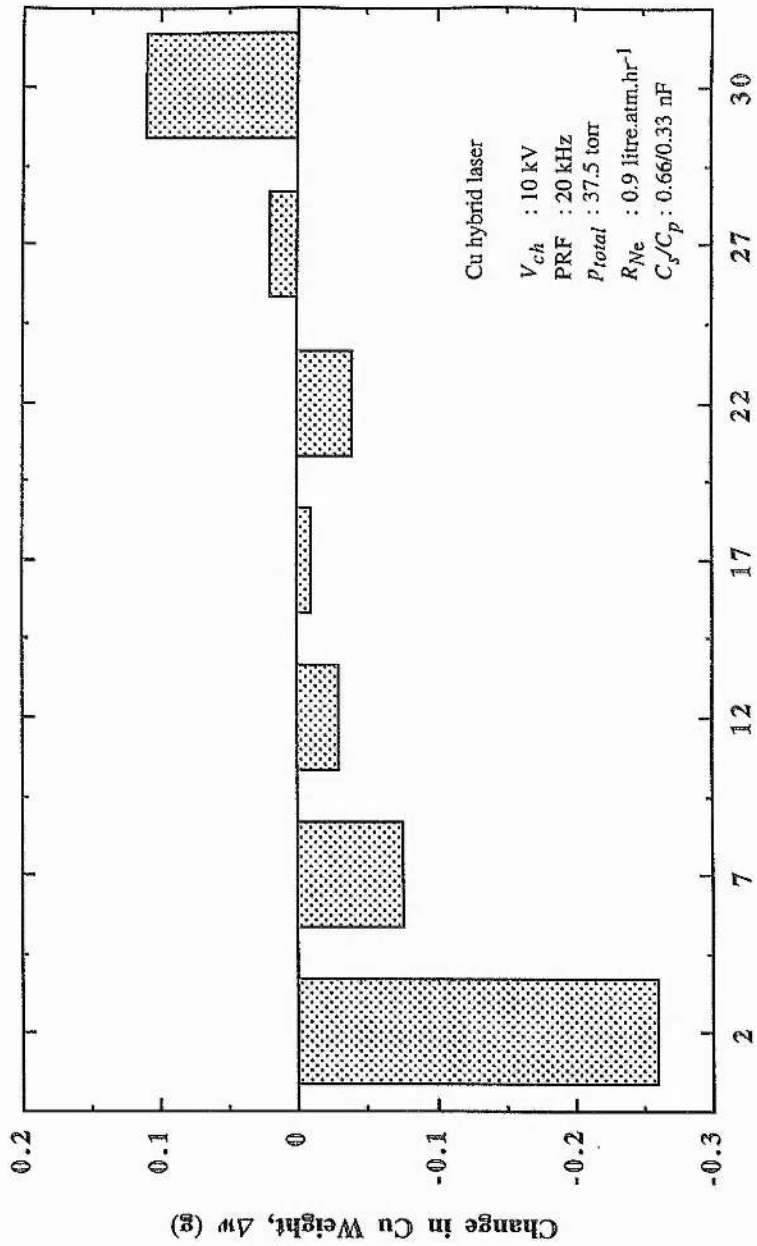

Fig. 7.4
Change in Cu weight distribution over a 185 min. period of lasing.

Chapter 8

Volumetric Scaling of Cu Hybrid Lasers

8.1 Introduction

In the introduction to this thesis it was pointed out that laser systems composed of CVLs in MOPA configurations have produced the highest output powers and energies of all Cu lasers to date. Specific examples are a 1.4 kW MOPA chain (with a 25 W MO and 3 PAs, each supplying an output power of 400-450 W) and a 650 W, 1 % efficiency PA, of unspecified design, both of which were reported by Warner [16] in 1991. More recently, Konagai et al. extracted 550 W from a single oscillator tube [15].

Two further developments deserve a mention. In 1995, Chang et al. [84] reported gas cooling on the discharge axis of an 80 mm bore PA by a distribution of Mo plates or 'septa' placed along the inside of the discharge tube. An increase in output power from 255 W to 325 W was realized. In common with the first two examples of high-power lasing these output powers were achieved using conventional CVL technology in which Cu seeding of the discharge was by vaporization of Cu metal in the active region and a small (0.5-1 %) amount of H_2 was added to the Ne buffer gas. In a recent publication, Bokhan and Molodykh [85] examined numerically the possibility of scaling MVLs in average power. Average powers of the order of kilowatts per metre were envisaged if the traditional longitudinal discharge excitation was dispensed with and the concept of runaway-electron beam excitation applied instead.

The Cu hybrid laser is a much more recent development. Although the basic principle of its operation (*i.e.* reaction of an active species in the discharge with source metal in the discharge tube to form a volatile compound of the metal which can then be dissociated by electron impact in the discharge to produce free atomic metal for lasing) has been used in a number of isolated examples of lasers since the mid-1970s, the Cu

hybrid laser has only emerged as a technology in its own right since the late 1980s/early 1990s. Nevertheless, at the time of this writing, the Cu hybrid laser is the most efficient of all atomic Cu lasers (and of all high-power visible lasers) and has been known to produce up to 201 W average power with 1.9 % efficiency (BSE) and 120 W with 3.2 % efficiency [86].

Cu hybrid laser performance differs markedly from that of elemental CVLs and from conventional CBLs with no H_2 additive. As the work presented in this thesis has verified, Cu hybrid lasers also perform better than CBLs with H_2 additive. In common with H_2-CBLs, Cu hybrid lasers have almost no plasma skin effect, exhibit long gain duration (~ 100 ns), and demonstrate rapid plasma relaxation in the interpulse periods. With its additional advantages of higher output powers and record efficiencies, Cu hybrid lasers are well placed for scaling in tube bore, active length and PRF to kilowatt average output powers with efficiencies of ~ 2 %, and to ~ 600 W at 3.5 % efficiency.

An even more recent development in atomic copper laser technology is the addition of HBr and other hydrogen halide donors to a CVL operating at the more usual 1500-1600 °C wall temperature (*cf.* typical wall temperatures of 500-800 °C in the Cu hybrid laser). This has improved the output characteristics of these CVLs, which now approach the lower temperature Cu hybrid lasers in performance [87]. CVLs with added hydrogen halide have been termed 'kinetically enhanced' CVLs by their investigators. The atomic Cu density is a function of tube temperature, *i.e.* of input power, because the discharge is seeded by vaporization of Cu liquid in the tube, however, the mechanisms responsible for much of its improved performance are essentially the same as those occurring in the Cu hybrid laser, and to a lesser extent in the CBL with H_2 additive.

The purpose of the present chapter is to evaluate the possibility of constructing atomic Cu lasers of kilowatt-scale average output powers using current technology. The presence of hydrogen halides in the discharge volumes of Cu hybrid lasers make these lasers particularly well suited to volume scaling in order to achieve high output powers. The prospects for increasing the average output power from single or double tube Cu hybrid devices into the kilowatt regime are discussed in this chapter. We shall see that

their as yet unrealized capacity for volume scaling makes it possible for a double-tube MOPA or ICO system to deliver at least 1 kW average output power.

8.2 Volume Scaling of Elemental CVLs

Conventional CVLs may be scaled in active bore, D, or length, L. In the case of increasing the tube bore, one of three major factors limiting the amount of scaling which conventional CVLs can tolerate before their output characteristics begin to deteriorate is the plasma skin effect. The plasma skin effect can degrade performance in laser tubes with bores as low as 42 mm [72]. At D ~ 42 mm, the skin effect causes a radially dependent longitudinal electric field to develop which is a maximum near the discharge tube wall and a minimum on-axis. As well as giving the beam an on-axis minimum, through more effective excitation near the wall where the electric field is strongest, the peculiar nature of the electric field pattern is also responsible for a noticeable delay between the onset of excitation and lasing near the wall and on the tube axis. In the conventional CVL of 42 mm bore (no HBr), the prepulse electron density was measured as ~ 30 % of the peak electron density, and the prepulse conductivity was 4800 $\Omega^{-1}.m^{-1}$ [72]. Although the skin effect in CVLs is reduced by operating at higher buffer-gas pressures, and by on-axis cooling of the atomic Cu-Ne gas mixture by locating septa in that region [88, 89], no functional CVLs of > 80 mm bore have thus far been reported.

In addition to its contribution to the skin effect, an increasing gas temperature in the discharge volume restricts radial scaling of conventional devices via its control over the prepulse metastable lower laser level populations. High prepulse metastable densities reduce the maximum possible inversion density, and the (already short) time interval during which the plasma medium is in gain. For constant efficiency, if a laser tube is scaled in bore then output power can only increase if the input power per unit length increases (for fixed discharge length). However, this implies an increase in on-axis temperature [90]. The higher input powers dictate that the PRF must be reduced to enable sufficient gas/plasma relaxation to take place between pulses. Scaling in bore beyond a critical size therefore gives no advantage and may even lead to a deterioration in laser

performance.

The third factor which can pose problems for radial scaling is the loading of the switch/modulator excitation circuit which can become excessive at larger tube bores at which input pulse energy and peak current requirements are greatly increased whilst 'fast' ($\leq$ 100 ns risetime) discharge excitation must be maintained. In addition, the conductivity of the CVL discharge channel is always high so that impedance matching is difficult even for tube bores of 60 mm and will be more so at larger tube bores.

Finally, scaling in length should be considered. The largest length is determined by the rather short gain duration. As it is desirable to have 4 or more cavity round-trips during gain in order to reduce the time-averaged divergence, the longest CVL oscillators and amplifiers reported have discharge lengths of 300 cm [91].

8.3 Advantages of Hydrogen Halide Additives for Volume Scaling

The high discharge channel impedance afforded by the presence of HBr in a hybrid laser leads to many advantages over conventional CVLs for scaling. First, there is almost no skin effect in a hybrid laser. In a 60 mm bore hybrid laser [86], lasing at the wall and on the tube axis began within 3 ns of each other. The penetration of the longitudinal electric field into the active medium is highlighted by the fact that the output beam intensity profile of the 60 mm bore laser is close to Gaussian in form, *i.e.* there is a strong central maximum in laser beam intensity. The pseudo-Gaussian intensity profile is maintained throughout the pulse duration, which is important for machining applications.

We can use the data of [71] to calculate typical plasma skin depths and electric field penetration times in a 25 mm bore hybrid laser. Current and voltage data lead to a tube conductivity of 0.8 $\Omega^{-1}.m^{-1}$ during application of the tube voltage. (This corresponds to a remanent electron density of 10^{10}-10^{11} cm^{-3}, or 0.01-0.1% of the peak electron density in the same laser; *cf.* 30% of the peak electron density remaining in a CVL [83].) Therefore, the plasma skin depth in the hybrid laser is 350 mm (independent of tube bore assuming the same conductivity), and the penetration time for an 80 mm bore hybrid laser is 0.25 ns. These figures should be compared with 30 mm and 43 ns, respectively, for an

80 mm bore CVL [92]. Therefore, because of the efficient removal of free electrons between excitation pulses in a hybrid laser, the electric field can penetrate 100's mm depth of plasma in less than a nanosecond.

The lower wall temperature of Cu hybrid lasers is an advantage in keeping gas temperature effects at bay, especially in large-bore devices, where the axis is far removed from the wall. Even the output beam of a 60 mm bore hybrid laser displays a strong central maximum in its transverse intensity profile, indicating no deterioration in gain on the tube axis due to gas temperature effects, even at PRFs of 15-20 kHz [86]. The 2-3 times higher efficiency of hybrid lasers means 2-3 times more output power can be achieved from those devices compared to CVLs for the same input power per unit length. Specific input powers of ~ 15 $kW.m^{-1}$ can be applied to large-bore ($\geq$ 80 mm) CVLs [93].

The improved matching of the modulator to the laser tube with HBr at high impedances, together with the faster plasma relaxation, means that these lasers can be operated with smaller capacitances at higher PRFs than their non-HBr counterparts. This also makes for more effective excitation as the current pulse risetime can be shorter, and the input excitation pulse better temporally matched to the gain period in a hybrid laser. The more effective excitation contributes to higher laser efficiency. The input pulse energy and, in general, the peak current density required are lower in hybrid lasers, making scaling of hybrid lasers in tube bore more practical from the point of view of the modulator/switch requirements.

Finally, the laser pulse duration is longer with added HBr. While a 60 mm bore CVL produces a laser pulse lasting ~ 40 ns (FWHM), a 60 mm bore hybrid laser generates a laser pulse lasting 60 ns (FWHM). The hybrid laser can therefore afford longer cavities than conventional CVLs when operated as an oscillator.

Copper lasers with hydrogen halides in the gas mixture therefore have some attractive features additional to their high specific average output powers and efficiencies. The very weak plasma skin effect allows the tube bore to be increased by 100's mm. The longer gain period means long optical cavities can be fitted without great detriment to beam quality, making scaling by length more feasible compared to CVLs, which have

already been scaled to 300 cm discharge length. The rapid and volumetric nature of plasma relaxation between pulses enables high-PRF (15-20 kHz) operation of tubes with large bore sizes (≥ 60 mm). The ability to operate with lower input energies and peak currents also favours scaling by tube bore in hybrid lasers as opposed to CVLs.

8.4 Volume Scaling Behaviour of Cu Hybrid Lasers

The results of experiments on hybrid lasers with 4.5 mm [94], 12.5 mm, 45 mm [95] and 60 mm [86] bores are summarized in Fig. 8.1, where average output power per unit length is plotted versus tube bore. Included in that figure is also a point corresponding to a 40 mm bore 'kinetically enhanced' CVL [87]. It can be seen that the output power per unit length is a good linear function of tube bore. The true dependence is probably slightly steeper, as the output powers of the 45 and 60 mm bore lasers did not saturate completely with the highest charging voltages used. If it is assumed that the hybrid laser can be scaled up to at least 300 cm discharge length, as has been demonstrated for CVLs, then Fig. 8.1 shows that an average output power of 1 kW is predicted for a tube bore of 250 mm, well within the plasma skin depth limit. The field penetration time for such a tube would be 2-3 ns.

The dependence on tube bore of the PRF for maximum average output power is shown in Fig. 8.2. There are two regimes of operation: a small-bore (≤ 25 mm) regime, where diffusion and volumetric processes play major roles in determining the upper limit to PRF; and a large-bore (≥ 25 mm) regime, where the PRF is determined entirely by volumetric processes, *i.e.* the PRF (~ 17 kHz) is independent of tube bore. The 250 mm bore tube is therefore expected to optimize at a PRF of 17 kHz. It is likely that the diffusive process which limits the PRF is the return of Cu atoms against radial cataphoresis. In large-bore tubes, the current densities are much smaller and so is the radial electric field. Cataphoresis is unlikely to be a problem. The volumetric regime is thus a regime where cataphoresis no longer limits PRF. The limit is very likely to be excessive prepulse metastable densities in the hotter central zone of the tube.

In order to determine the other operating parameters, the dependences of the

characteristic parameters $(p_{Ne}D)/2$ and E_{max}/p_{Ne} are plotted, where p_{Ne} is the buffer-gas pressure and E_{max} is the maximum applied field, assuming, as is usually found to be the case, that the charging voltage is similar to the maximum tube voltage. Fig. 8.3 shows these two parameters calculated as functions of tube bore. A transition from a diffusion-dominated regime at low tube bores to one where volumetric processes dominate is again apparent. In the case of a 250 mm bore tube, E_{max}/p_{Ne} tends to 500 V.m^{-1}.torr^{-1} and $(p_{Ne}D)/2$ tends to 1500 torr.mm. The value for $(p_{Ne}D)/2$ sets the Ne pressure at ~ 12 torr, which in turn specifies the maximum applied (or charging) voltage over 300 cm as ~ 18 kV. Assuming the same volumetric processes control the operating efficiency in the 250 mm bore laser as in the 60 mm and 45 mm bore lasers, it is found that the laser efficiency (BSE) at maximum power will be ~ 2%. Then, the input power to the laser will be 50 kW, so that the storage capacitance C_s must be 19 nF for the given PRF and charging voltage.

We can do the following check on storage capacitance. The impedance of the 60 mm bore, 200 cm active length tube can be related through the change in bore and length to the impedance of the 250 mm bore, 300 cm long laser by the factor 0.086. As the optimum peaking capacitance C_p for the 60 mm tube was 0.95 nF, the peaking capacitor suitable for matching into the 250 mm bore laser will be ~ 11 nF. Based on previous studies of hybrid lasers, the optimum storage capacitance will be approximately twice the peaking capacitance, *i.e.* ~ 22 nF, which compares favourably with our independent calculation above of a C_s of ~ 19 nF.

Finally, it is necessary to check that the tube inductance does not prevent the current pulse risetime from being ≤ 100 ns for efficient copper excitation. The inductance per unit length of coaxial conductors is

$$\frac{1}{2\pi}\mu_o \ln\frac{b}{a}, \qquad \text{----------(8.1)}$$

where b is the radius of the coaxial current return, and a is the radius of the inner conductor. Assuming the bulk of the discharge current to be carried in the central half

(125 mm) of the laser tube, and a diameter for the coaxial current return of 350 mm, then the inductance, L_h, of the 300 cm long discharge tube is found to be ~ 200 nH. The excitation pulse risetime is given by

$$\frac{\pi}{4}\sqrt{L_h C_p}. \qquad \text{----------(8.2)}$$

Allowing for placement of peaking capacitors etc., setting L_h as 300 nH gives an excitation pulse risetime of 45 ns, which is well suited to excitation of the atomic copper transitions.

The 50 kW input power required by the 1 kW hybrid laser can be handled by 3-5 thyratrons operating in parallel. Note that 3 thyratrons are used in parallel to drive present-day commercial 100 W CVLs. Gabay et al. [96] have operated a 120 W CVL with a single-thyratron circuit, where 10 kW power was delivered to the laser head (80 mm bore, 150 cm active length) in a circuit with magnetic assist and 3-stage magnetic pulse compression. Pulse energies of 3.6 J (1.8 J to the laser tube) were switched at 5.5 kHz in the circuit. By contrast, the 1 kW copper hybrid laser requires pulse energies of 3.1 J to be delivered to the discharge tube at 17 kHz PRF. All-solid-state modulators are used to drive CVL PAs at Lawrence Livermore National Laboratory with input powers of 30 kW and PRFs of 4-5 kHz [97]. With modifications for high-PRF operation, a similar system could also be applied to the copper hybrid laser.

For 50 kW total input power, the specific input power required is 16-17 $kW.m^{-1}$, which is similar to that already known to be applied to CVLs (~ 15 $kW.m^{-1}$) [93]. Bearing in mind the 600-700 °C lower wall temperature of hybrid lasers, we can see that gas heating will be less problematic, although the input power is radially more uniform in a CVL. The 15 $kW.m^{-1}$ CVL uses septa placed vertically along the middle of the discharge tube to cool the gas at the centre of the tube, and reduce the remanent metastable state density there. By making use of septa in a (~ 800 °C) hybrid laser, it is estimated that it is possible to obtain 1 kW output power from a 300 cm long discharge tube of 230 mm bore. The temperature profile in the gas should be similar to that expected in a laser with

only 8-9 $kW.m^{-1}$ input power, as the temperature of the septa in the middle of the tube should be close to the wall temperature. The PRF would be 17 kHz, the gas pressure 13 torr, the charging voltage 19.5 kV, and the storage and peaking capacitances 15 nF and 7.5 nF, respectively. The laser would still require ~ 50 kW input power, of course. If the septa were made of copper, they could double as the copper reservoir in the tube. Alternatively, ceramic (BeO, alumina) septa could be used.

We therefore see that development of a kilowatt average power copper hybrid laser tube is a practical proposition. In order to ensure that the beam is of high quality (≤ 2 times the diffraction limit), and to prevent parasitic depletion of the inversion by photons which do not contribute to the output beam, it is necessary to extract the output power using the tube as either a PA or as an injection-controlled oscillator (ICO). As a PA, around 25% extra output power should be available, giving 1.25 kW extractable power. For the ICO configuration, as long as the cavity is flooded with high quality light (1-2 times the diffraction limit) for at least 10-20 ns corresponding to the onset of gain in the tube, the majority of the light output should also be of high quality.

Finally, it should be mentioned that hybrid lasers also tend to operate at maximum efficiency with around 60 % of the maximum output power. The trend for maximum efficiency (based on stored energy) as tube bore is varied is shown in Fig. 8.4. It can be seen that the efficiency reaches a maximum of ~ 3.5 %. We can therefore expect the scaled hybrid lasers discussed here to generate ~ 600 W at ~ 3.5 % efficiency, *i.e.* with an electrical input power of only 17 kW. Such a laser is realizable now.

8.5 Conclusions

Copper lasers with hydrogen halide additives are well suited to scaling in volume to tube bores around 350 mm and discharge lengths of at least 300 cm. The rapid and volumetric nature of relaxation of the active medium in the interpulse period enables high-PRF (15-20 kHz) operation, even at larger ($\geq$ 60 mm) bore sizes. Evidence has been presented that the parameters E_{max}/p_{Ne}, $(p_{Ne}D)/2$ and the PRF are effectively constant for tube bores larger than 25-40 mm. This is a result of most of the key laser kinetics being determined

by volumetric processes in large-bore tubes. The output power per unit length is a linear function of tube bore.

Kilowatt average output powers appear possible using only current technology. As a starting point for the development of kilowatt-class copper hybrid lasers, the recommended laser tube dimensions for 1 kW output power are 250 mm bore and 300 cm discharge length. The laser should have a buffer-gas pressure of 10-15 torr, and be driven at 15-20 kHz with ~ 20 kV charging voltage. The storage and peaking capacitances should be 15-20 nF and ~ 7.5-10 nF. Between 3 and 5 thyratrons could be used with magnetic assist and multi-stage magnetic pulse compression to drive the laser with 50 kW input power. It may be necessary to cool the gas at the centre of the tube by radiation to the wall using septa.

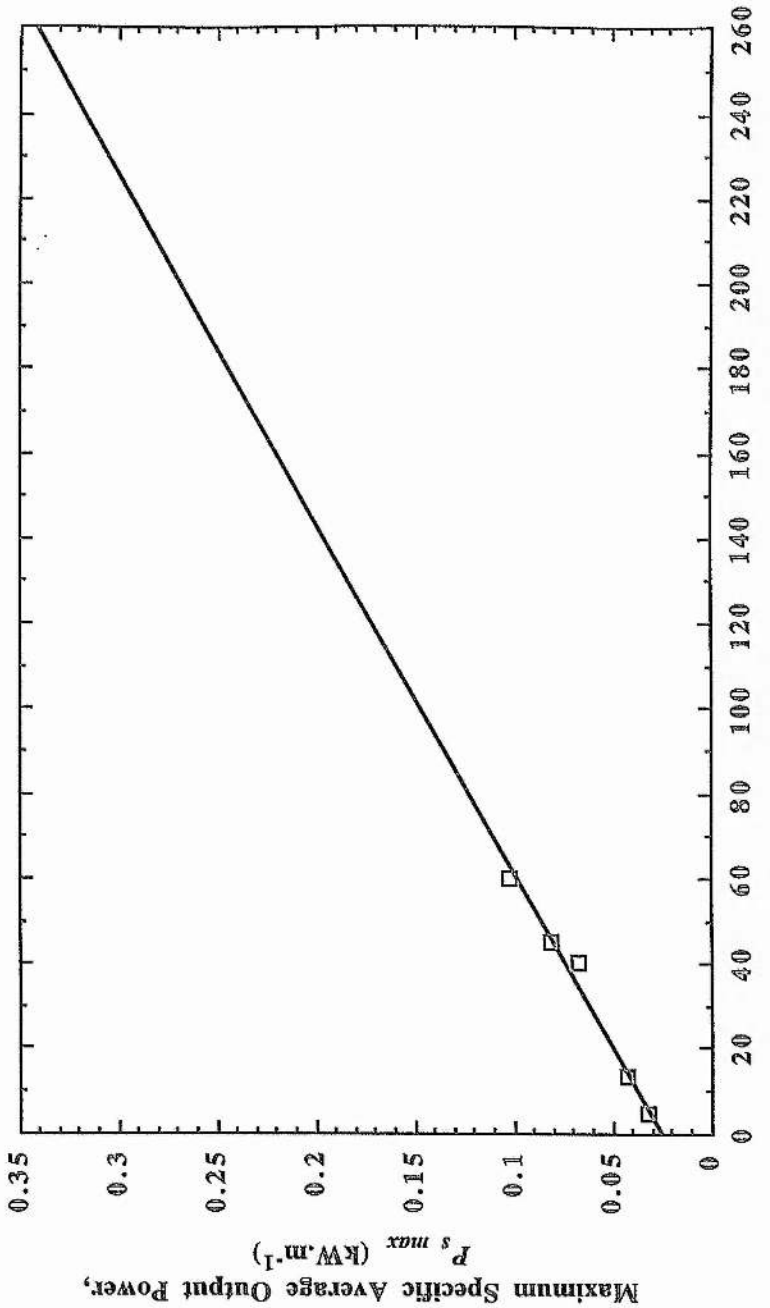

Fig. 8.1
Maximum specific average output power, $P_{s\ max}$, versus discharge tube bore, D, for a number of Cu hybrid lasers reported in the literature.
(Note that one point for a CVL with HBr additive is included in the figure.)

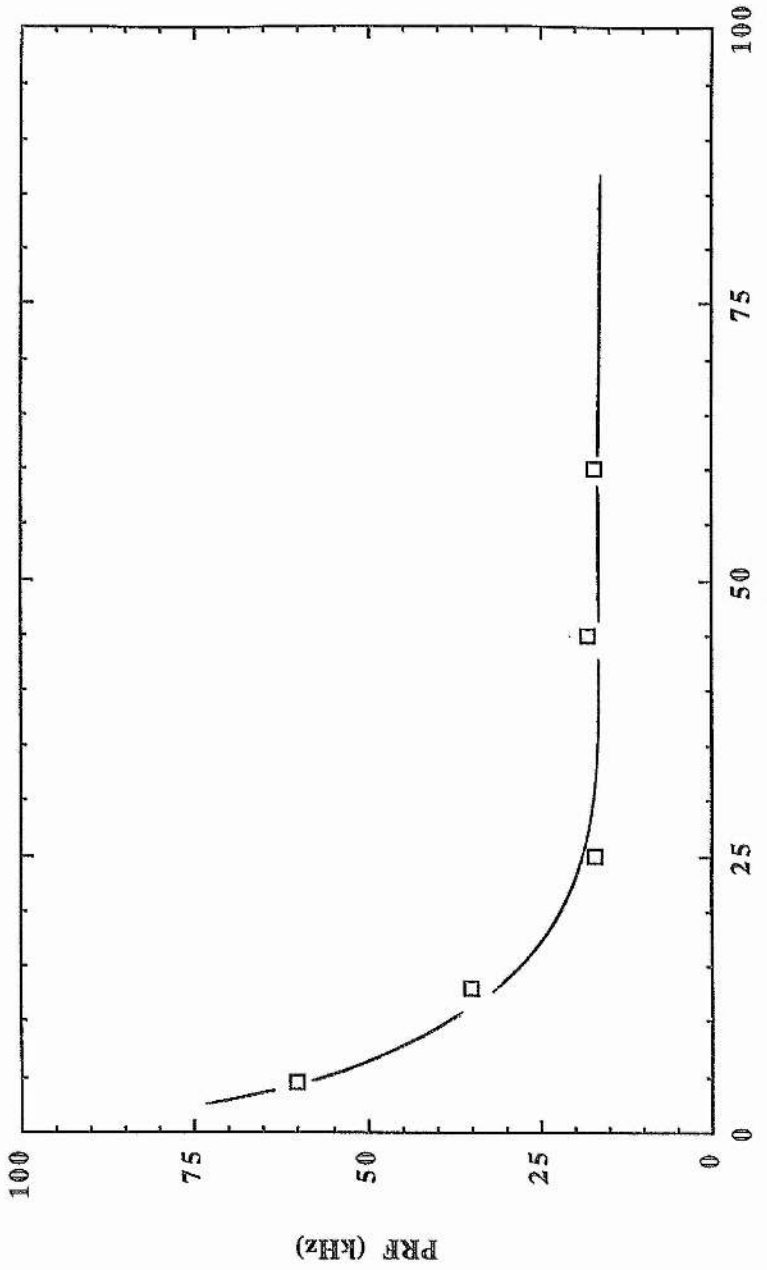

Fig. 8.2
PRF for maximum specific average output power, $P_{s\,max}$, versus discharge tube bore, D, for a number of Cu hybrid lasers reported in the literature.

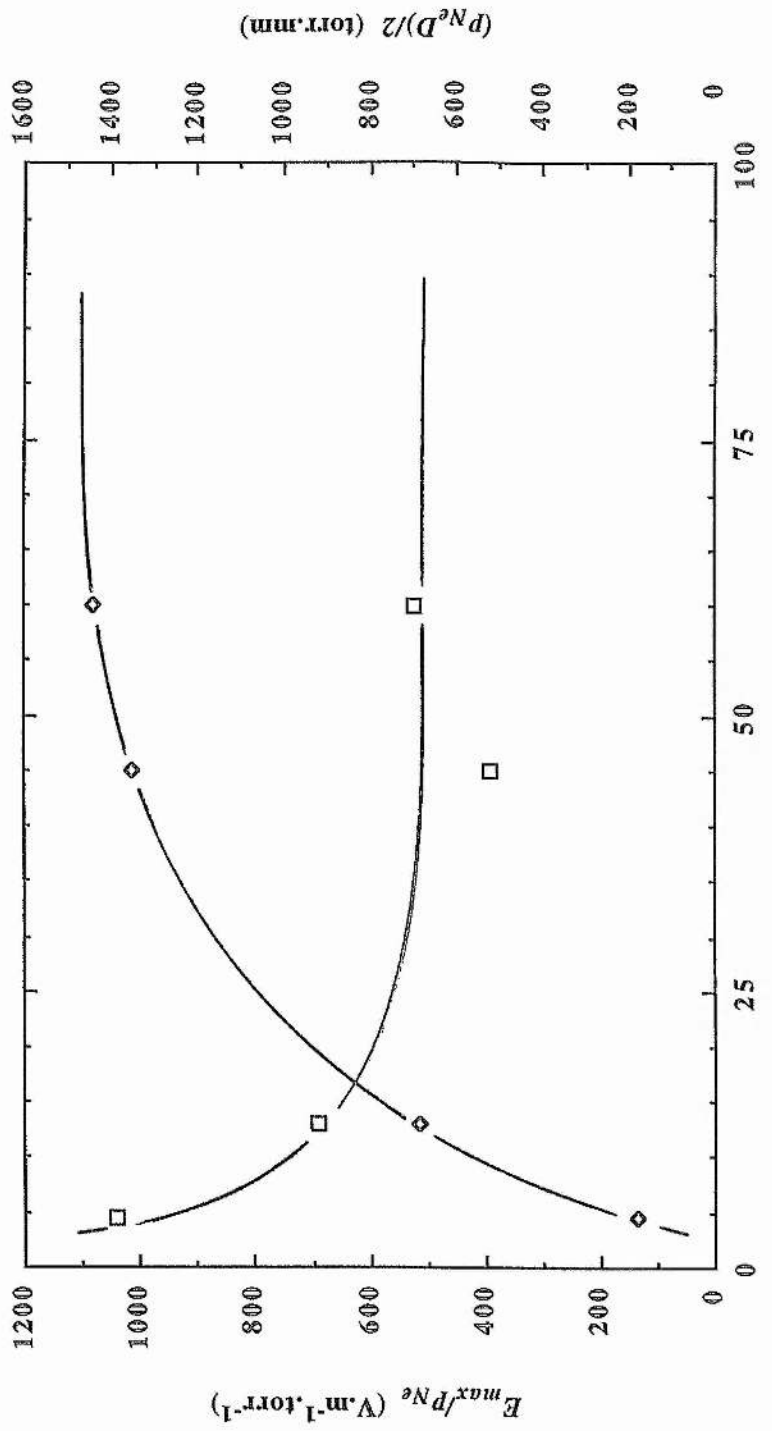

Fig. 8.3
Dependences of the operating characteristics E_{max}/p_{Ne} and $(p_{Ne}D)/2$ on discharge tube bore, D, for a number of Cu hybrid lasers reported in the literature.

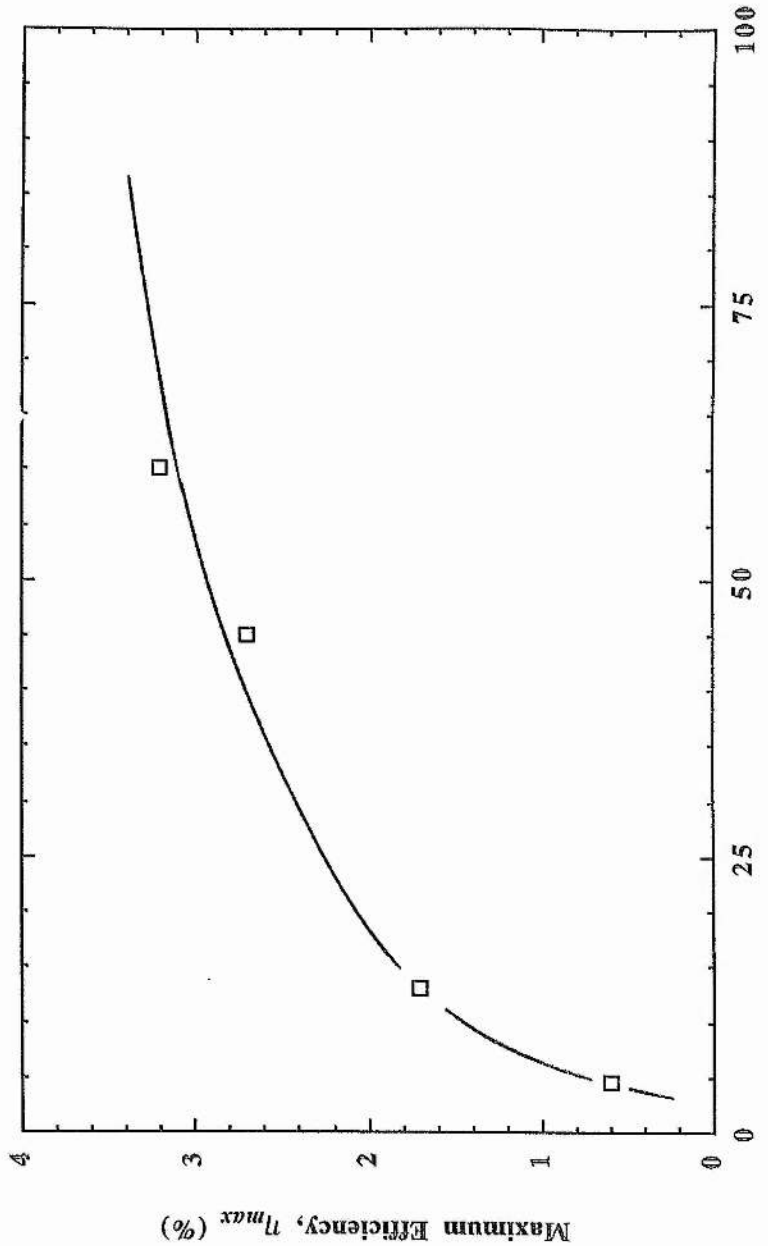

Fig. 8.4
Maximum efficiency, η_{max}, versus discharge tube bore, D, for a number of Cu hybrid lasers reported in the literature.

Chapter 9

Conclusions

A comprehensive experimental comparison of conventional CuBr and Cu hybrid laser technologies has been conducted using the same experimental rig. This is the first time that such a comparison has been attempted. Conclusions have been drawn regarding the mechanisms responsible for the observed behaviours of the lasers. Results were also presented of the first quantitative experimental study of the metal seeding mechanism in a Cu hybrid laser. As Cu hybrid lasers are the highest efficiency high average power visible lasers (510.6 and 578.2 nm), the prospects for raising the average output power into the kilowatt regime by scaling these devices in active volume was also discussed here for the first time.

An average output power of 3.55 W was found for a CuBr-Ne laser of 43.5 cm^3 active volume and 13 mm bore. This corresponds to a specific average power of 82 $mW.cm^{-3}$. Average power was shown to peak at buffer-gas pressures in the region of 30 torr. The system was further shown to favour buffer-gas flow rates of around 2 $litre.atm.hr^{-1}$. Optimum PRF was within the range 20 to 24 kHz for the combinations of storage and peaking capacitors tried. The maximum power of 3.55 W was observed at 22.5 kHz and 12 kV with the 0.66/0.33 nF capacitors connected. This corresponds to an efficiency (BSE) of 0.33 %. At 7.5 kV, the average power was 2.30 W and the efficiency reached 0.56 %. The highest efficiency of 0.71 % was obtained at 22.5 kHz and 7 kV with the 0.52/0.24 nF capacitors connected.

Whilst establishing the characteristics described above, a second regime of operation was discovered at higher sidearm temperatures. Average powers were higher over smaller spans of buffer-gas pressure and flow rate, but less stable, and the regime

existed over a much narrower range of sidearm temperatures. The regime was argued to result from the release of hydrogen-containing impurities (probably H_2O) from the CuBr in the sidearm at elevated temperatures. A similar phenomenon has been reported [31] but not explained by other investigators.

A peak power of 11.4 W, corresponding to a specific average output power of 262 $mW.cm^{-3}$, was obtained from a CuBr-Ne-H_2 laser of 43.5 cm^3 active volume and 13 mm bore. Maximum power was produced by the CuBr-Ne-H_2 laser at the same CuBr concentration as the CuBr-Ne laser. The efficacy of the addition of H_2 to enhance output power and efficiency of a CuBr laser was demonstrated. Its influence is due to the combined actions of dissociative attachment of HBr (on plasma relaxation and electron avalanche) and hydrogen reduction of CuBr and its polymers (to free Cu atoms, especially away from the tube axis). Average output power was shown to peak at buffer-gas pressures in the region of 25 torr. The system demonstrated strong lasing over an extensive range of buffer-gas flow rates, peaking at around 2 $litre.atm.hr^{-1}$ under the conditions studied. Optimum PRF was within the range 25 to 35 kHz. Maximum power and efficiency were observed with the 0.52/0.24 nF capacitors. The maximum power of 11.4 W was obtained at 30 kHz and 11 kV. This corresponds to an efficiency (BSE) of 1.21 %. At 9 kV, the average power was 9.3 W and the efficiency reached 1.47 %.

An average output power of 12.8 W was obtained from a Cu hybrid laser tube of 36.8 cm^3 active volume and 12.5 mm bore. This corresponds to a record specific average output power of 348 $mW.cm^{-3}$ for copper lasers of $\geq$ 12.5 mm bore, which is a factor of 4.3 times larger than that of the CuBr-Ne laser and 1.3 times more than that of the CuBr-Ne-H_2 laser. In the Cu hybrid laser, the optimum gas pressure was 60 torr for the conditions studied. The system favoured low buffer-gas flow rates of around 1 $litre.atm.hr^{-1}$. Optimum PRF was within the range 30 to 45 kHz. Maximum power and efficiency were observed with the 0.66/0.33 nF capacitors connected. The maximum power of 12.8 W was observed at a PRF of 35 kHz and at a charging voltage of 11 kV. This corresponds to an efficiency (BSE) of 0.92 %. At 7 kV, the average power was 9.4 W and the efficiency reached 1.66 %. This represents a factor of 2.3 improvement over

the peak efficiency of 0.71 % found for the CuBr-Ne system and a factor of 1.1 improvement over the peak efficiency of 1.47 % achieved in the CuBr-Ne-H_2 system.

The Cu hybrid laser demonstrated the highest output power and efficiency, and most strongly resembled the CuBr-Ne-H_2 laser in terms of the overall character of its emission. In its dependence on buffer-gas pressure and flow rate it echoes neither of the other two systems. It also tolerates optimum HBr pressures of the order of 1.4-3.2 torr over a 13.6-94.5 torr buffer-gas pressure range in contrast to around 0.33 torr of Cu_3Br_3 vapour in both the CuBr and CuBr-Ne-H_2 lasers. These differences most probably relate to the different mechanism of Cu seeding in Cu hybrid lasers.

Neglecting the HT regime and assuming the LT regime to be the correct regime of operation, the CuBr-Ne and CuBr-Ne-H_2 lasers peaked at similar buffer-gas (and halide) pressures and flow rates (25-30 torr and 2 litre.atm.hr^{-1} respectively), but the optimal values of the excitation parameters (PRF and charging voltage), and the overall powers, efficiencies and pattern of laser emission, are strongly affected by the presence or lack of H_2.

It is clear from the discussions in this thesis why H_2 addition to a conventional CVL does not give the benefits of Br_2 or HBr addition: the active species in bromide lasers with added hydrogen is HBr and not H_2. The recent development of 'kinetically enhanced' CVLs, where HBr is added instead of H_2, highlights this fact [2].

In the 12.5 mm bore copper hybrid laser, less than 100 mm^2 of copper metal is necessary for optimum lasing and this need only be placed at the upstream end of the active volume. For all configurations of the copper metal, average output power is maximum at a single buffer-gas flow rate (~ 1 litre.atm.hr^{-1}). Reductions in output power at flow rates to either side of optimum were due to back diffusion of CuBr (low flows) and reduced gas temperatures (high flows). Optimum HBr pressure fell exponentially with increasing flow rate and could be fitted with a single curve for all Cu metal configurations attempted.

The atomic bromine pressure at the wall needed to account for the observed copper metal removal rate was estimated as ~1.3 mtorr; the number density of copper in

atomic and molecular forms averaged throughout the tube was 2.2 x 10^{16} cm^{-3}. Significant numbers of Cu_3Br_3 and Cu_4Br_4 polymers and of CuH must exist in the laser discharge to lock up the large quantity of copper atoms that exists in the active region. This is the first quantitative study to suggest the existence of CuH molecules in halide laser media.

The accelerated growth of Cu dendrites in the small-bore tube was postulated to be due to one of two mechanisms. Depletion of copper bromide at the source metal caused by decomposition and reduction of the bromide at the hotter dendrite, leads to increased removal of metal from the source and accelerated deposition at the tip. This is especially true in small-bore devices where the metal is closer to the hot discharge centre. The other mechanism operates by transport of Cu to the dendrite as ions in the radial electric field, and deposition by condensation. It is not possible to distinguish between these mechanisms at present, but the much faster dendrite growth when H_2 is added to the discharge suggests that the first mechanism is the most important where H_2 is present.

Copper lasers with hydrogen halide additives are well suited to scaling in volume to tube bores of around 350 mm and to discharge lengths of at least 300 cm. The rapid and volumetric nature of relaxation of the active medium in the interpulse period enables high-PRF (15-20 kHz) operation, even at larger (≥ 60 mm) bore sizes. Evidence has been presented that the parameters E_{max} / p_{Ne} and $(p_{Ne}D)/2$, and the PRF, are effectively constant for tube bores larger than 25-40 mm. This is a result of most of the key laser kinetics being determined by volumetric processes in large-bore tubes. The output power per unit length is a linear function of tube bore.

Kilowatt average output powers appear possible using only current technology. As a starting point for the development of kilowatt-class copper hybrid lasers, the recommended laser tube dimensions for 1 kW output power are 250 mm bore and 300 cm discharge length. The laser should have a buffer-gas pressure of 10-15 torr, and be driven at 15-20 kHz with ~ 20 kV charging voltage. The storage and peaking capacitances should be 15-20 nF and ~ 7.5-10 nF. Between 3 and 5 thyratrons could be used with magnetic assist and multi-stage magnetic pulse compression to drive the laser with 50 kW

input power. It may be necessary to cool the gas at the centre of the tube by radiation to the wall using septa.

Finally, as for future work, there need to be measurements made of temporally and spatially resolved densities of HBr, CuBr polymers, H_2 molecules, Cu atoms, Cu^+, H^- and Br^- ions and electrons in order to fully understand the kinetics of these lasers. At present, this is not possible due to the complexity of such comprehensive measurements. It is hoped that the study presented in this thesis will have formed a useful basis from which to conduct some of those investigations in the future.

Chapter 10

References

1. O. S. Akirtava, V. L. Dzhikiya and Yu. M. Oleinik, "Laser utilizing Cu I transitions in copper halide vapors," *Sov. J. Quantum Electron.*, vol. 5, no. 8, pp. 1001-2, 1975.

2. R. J. Carman, M. J. Withford, D. J. W. Brown and J. A. Piper, "Performance enhancement of elemental copper vapour lasers by bromine and hydrogenated bromine additives," *SPIE 3092, Proc. XI International Symposium on Gas Flow and Chemical lasers and High Power Laser Conference*, Edinburgh, UK, 25-30 August 1996, ed. H. J. Baker, pp. 68–71, 1997.

3. G. R. Fowles and W. T. Silfvast, "High-gain laser transitions in lead vapor," *Appl. Phys. Lett.*, vol. 6, pp. 236-7, 1965.

4. W. T. Walter, M. Piltch, N. Solimene and G. Gould, "Pulsed laser action in atomic copper vapor," *Bull. Am. Phys. Soc.*, vol. 11, no. 1, p. 113, 1966.

5. W. T. Walter, N. Solimene, M. Piltch and G. Gould, "Efficient pulsed gas discharge lasers," *IEEE J. Quantum Electron.*, vol. QE-2, pp. 474-9, 1966; Fourth Int. Conf. on Quantum Electron., Phoenix, AZ, April 1966.

6. A. A. Isaev, M. A. Kazaryan and G. G. Petrash, "Effective pulsed copper-vapor laser with high average generation power," *JETP Lett.*, vol. 16, no. 1, pp. 27-9, 1972.

7. A. A. Isaev, M. A. Kazaryan and G. G. Petrash, "Pulsed lasers with high repetition frequency using lead, manganese, copper, and gold vapor," *J. Appl. Spectrosc.*, vol. 18, no. 3, pp. 357-8, 1973.

8. G. G. Mitin, O. P. Maksimov, V. S. Gorelik, A. A. Isaev, M. A. Kazaryan and M. M. Sushchinnskii, "Application of the copper vapor laser to the investigation of Raman

spectra in crystals," *J. Appl. Spectrosc.*, vol. 21, no. 2, pp. 1097-8, 1974.

9. K. I. Zemskov, A. A. Isaev, M. A. Kazaryan and G. G. Petrash, "Laser projection microscope," *Sov. J. Quantum Electron.*, vol. 4, no. 1, p. 5, 1974.

10. C. D. Decker, T. S. Fahlen and J. Falk, "Amplification and lasing action on a laser dye pumped by a copper-vapor laser," *J. Appl. Phys.*, vol. 46, no. 5, pp. 2308-9, 1975.

11. R. C. Stern and B. B. Snavely, "The laser isotope separation program at Lawrence Livermore Laboratory," *Ann. NY Acad. Sci.*, vol. 267, pp. 71-80, 1976.

12. I. Smilanski, A. Kerman, L. A. Levin and G. Erez, "Scaling of the discharge heated copper vapor laser," *Opt. Comm.*, vol. 25, no. 1, pp. 79-82, 1978.

13. R. E. Grove, G. W. Coutts, R. S. Anderson, R. J. Homsey and T. W. Karras, "100 watt copper vapor laser," *CLEOS/ICF'80 Technical Digest*, vol. 88, 1980.

14. B. G. Bricks, T. E. Buczacki, T. W. Karras, R. S. Anderson and C. E. Anderson, "5-watt copper vapor laser study," General Electric Co., Final Report, *University of California Radiation Laboratory Report No. UCRL 13700*, 4 Aug. 1976.

15. C. Konagai, H. Kimura, N. Aoki, N. Kobayashi, S. Iizuka and Y. Baba, "Development of high-power copper vapor laser amplifier," *Proc. 15th Ann. Meeting Laser Soc. Jap.*, Osaka, vol. 15, p. 112, 1995.

16. B. E. Warner, "Status of copper vapor laser technology at Lawrence Livermore National Laboratory," *CLEO'91 Technical Digest*, pp. 516-18, 1991.

17. C. H. Corliss, W. R. Bozman and F. O. Westfall, "Electrodeless metal-halide lamps," *J. Opt. Soc. Am.*, vol. 43, no. 5, pp. 398-400, 1953.

18. L. A. Weaver, C. S. Liu and E. W. Sucov, "Superradiant laser emission at 5106 Å in pulsed copper iodide discharges," CLEA'73, *IEEE J. Quantum Electron.*, vol. QE-9, no. 6, pp. 645, 1973.

19. C. J. Chen, N. M. Nerheim and G. R. Russell, "Double-discharge copper vapor laser with copper chloride as a lasant," *Appl. Phys. Lett.*, vol. 23, no. 9, pp. 514-15, 1973.

20. I. Liberman, R. V. Babcock, C. S. Liu, T. V. George and L. A. Weaver, "High-repetition-rate copper iodide laser," *Appl. Phys. Lett.*, vol. 25, no. 6, pp. 334-5, 1974.

21. J. A. Piper, "A copper iodide laser excited by transverse discharge," *Opt. Comm.*,

vol. 14, no. 3, pp. 296-300, 1975.

22. R. S. Anderson, B. G. Bricks and T. W. Karras, "Copper oxide as the metal source in a discharge-heated copper vapor laser," *Appl. Phys. Lett.*, vol. 29, no. 3, pp. 187-8, 1976.

23. A. J. Andrews, C. E. Webb, R. C. Tobin and R. G. Denning, "A copper vapour laser operating at room temperature," *Opt. Comm.*, vol. 22, no. 3, pp. 272-4, 1977.

24. G. Chakrapani, T. A. Prasada Rao, A. A. N. Murty and D. Ramachandra Rao, "Laser action in copper with copper acetate as a lasant," *Appl. Phys. Lett.*, vol. 31, no. 12, pp. 832-3, 1977.

25. A. M. Shukhtin, V. G. Mishakov and G. A. Fedotov, "Production of copper vapor from Cu_2O dust in a pulsed discharge," *Sov. Tech. Phys. Lett.*, vol. 3, pp. 304-5, 1977.

26. S. Gabay, I. Smilanski, L. A. Levin and G. Erez, "Comparison of CuCl, CuBr and CuI as lasants for copper-vapor lasers," *IEEE J. Quantum Electron.*, vol. QE-13, no. 5, pp. 364-6, 1977.

27. A. A. Vetter and N. M. Nerheim, "Addition of HCl to the double-pulse copper chloride laser," *Appl. Phys. Lett.*, vol. 30, no. 8, pp. 405-7, 1977.

28. N. M. Nerheim, A. A. Vetter and G. R. Russell, "Scaling a double-pulsed copper chloride laser to 10 mJ," *J. Appl. Phys.*, vol. 49, no. 1, pp. 12-15, 1978.

29. J. A. Piper, "A transversely excited copper halide laser with large active volume," *IEEE J. Quantum Electron.*, vol. QE-14, no. 6, pp. 405-7, 1978.

30. N. K. Vuchkov, G. G. Petrash and N. V. Sabotinov, "Service life of a CuBr vapor laser," *Sov. J. Quantum Electron.*, vol. 12, no. 9, pp. 1228-9, 1982.

31. W. Winiarczyk and L. Krause, "Temperature effects in the double-pulsed CuCl laser," *Appl. Opt.*, vol. 21, no. 15, pp. 2659-60, 1982.

32. W. Winiarczyk and L. Krause, "Effects of Na and K addition on the operating characteristics of the CuCl laser," *Opt. Comm.*, vol. 43, no. 1, pp. 47-9, 1982.

33. S. W. Kim, R. J. Niefer, J. B. Atkinson and L. Krause, "Effects of alkali-chlorides on the performance of the double-pulsed CuCl laser," *Optics Comm.*, vol. 63, no. 4, 1987.

34. D. Astadjov, G. Petrash, N. Sabotinov and N. Vuchkov, "Physical processes

limiting the CuBr laser lifetime," *SPIE 473 Symposium OPTIKA'84*, pp. 211-14, 1984.

35. D. N. Astadzhov, N. K. Vuchkov, G. G. Petrash and N. V. Sabotinov, "Investigation of the factors limiting the service life of a CuBr vapor laser," *Sov. J. Quantum Electron.*, vol. 14, no. 4, pp. 544-7, 1984.

36. D. N. Astadjov, N. V. Sabotinov and N. K. Vuchkov, "Effect of hydrogen on CuBr laser power and efficiency," *Opt. Comm.*, vol. 56, no. 4, pp. 279-82, 1985.

37. K. Kuroda, H. Takahashi, M. Chihara and I. Ogura, "Radial distribution of the gain of a CuBr laser," *J. Appl. Phys.*, vol. 52, no. 1, pp. 87-90, 1981.

38. H. Saito and H. Taniguchi, "Pulse broadening of laser oscillation on the $4p\ ^2P^o_{3/2} - 4s^2\ ^2D_{5/2}$ transition in the neutral copper atom by cesium vapors," *Appl. Phys. Lett.*, vol. 47, no. 5, pp. 440-2, 1985.

39. K. Oouchi, Y. Yato, N. Sasao and K. Fujii, "Enhancement and relaxation control of CuBr-AgBr green-yellow laser," *CLEO'89 Technical Digest*, pp. 184-6, 1989.

40. N. K. Vuchkov, N. V. Sabotinov and D. N. Astadjov, "High-efficiency CuBr laser with interacting peaking circuits," *Opt. Quantum Electron.*, vol. 20, pp. 433-8, 1988.

41. N. V. Sabotinov, N. K. Vuchkov and D. N. Astadjov, "High power and high efficiency copper bromide lasers," *SPIE 1041 Metal Vapor, Deep Blue and Ultraviolet Lasers*, pp. 110-16, 1989.

42. N. K. Vuchkov, D. N. Astadjov and N. V. Sabotinov, "A new circuit for CuBr laser excitation," *Opt. Quantum Electron.*, vol. 23, pp. S549-53, 1991.

43. D. N. Astadjov, K. D. Dimitrov, D. R. Jones, V. Kirkov, C. E. Little, N. V. Sabotinov and N. K. Vuchkov, "Copper bromide laser of 120 W average output power," *IEEE J. Quantum Electron.*, vol. QE-33, no. 5, pp. 705-9, 1997.

44. N. K. Vuchkov, N. V. Sabotinov and K. A. Temelkov, "Two-arm CuBr laser with a central electrode," *IEEE J. Quantum Electron.*, vol. QE-33, pp. 541-4, 1997.

45. N. K. Vuchkov, D. N. Astadjov and N. V. Sabotinov, "A copper vapor laser utilizing pure copper with an admixture of other metal chlorides," *Opt. Comm.*, vol. 42, no. 3, pp. 199-200, 1982.

46. H. Saito and H. Taniguchi, "Low-temperature operation of copper-vapor lasers by

using vapor-complex reaction of metallic copper and metal halide," *IEEE J. Quantum Electron.*, vol. QE-21, no. 9, pp. 1308-9, 1985.

47. E. S. Livingstone and A. Maitland, "A low temperature, segmented metal, copper vapour laser," *J. Phys. E: Sci. Instrum.*, vol. 22, p. 63, 1989.

48. E. S. Livingstone and A. Maitland, "A high power, segmented metal, copper bromide laser," *Meas. Sci. Technol.*, vol. 2, pp. 1119-20, 1991.

49. D. R. Jones and C. E. Little, "A Lead Bromide Laser Operating at 722.9 and 406.2 nm," *IEEE J. Quantum Electron.*, vol. QE-28, no.3, pp. 590-3, 1992.

50. C. E. Little and J. A. Piper, "Average-power scaling of self-heated Sr^+ afterglow recombination lasers," *IEEE J. Quantum Electron.*, vol. QE-26, no. 5, pp. 903-10, 1990.

51. E. S. Livingstone, D. R. Jones, A. Maitland and C. E. Little, "Characteristics of a copper bromide laser with flowing Ne-HBr buffer gas," *Opt. Quantum Electron.*, vol. 24, pp. 73-82, 1992.

52. D. R. Jones and C. E. Little, "A self-heated iron bromide (λ=452.9 nm) laser with Ne-HBr buffer gas," *Opt. Quantum Electron.*, vol. 24, pp. 67-72, 1992.

53. D. R. Jones and C. E. Little, "A compact, high-power, fast start-up manganese bromide laser (λ 534-554 nm, 1.29-1.40 mm)," *Opt. Comm.*, vol. 89, pp. 80-87, 1992.

54. D. R. Jones and C. E. Little, "A 472.2 nm bismuth halide laser," *Opt. Comm.*, vol. 91, pp. 223-228, 1992.

55. D. R. Jones, A. Maitland and C. E. Little, "A high efficiency, fast start–up, 100 W average-power copper bromide laser," *CLEO'92 Technical Digest*, pp. 548-9, 1992.

56. D. R. Jones, N. V. Sabotinov, A. Maitland and C. E. Little, "A high-power high-efficiency Cu-Ne-HBr (λ =510.6, 578.2 nm) laser," *Optics Comm.*, vol. 94, no. 4, pp. 289-99, 1992.

57. D. R. Jones, A. Maitland and C. E. Little, "200 W average power copper hybrid laser," XI Nat. Quantum Electronics Conf., Queens University of Belfast, Belfast, 30 Aug. - 2 Sept. 1993, *Technical Digest*, 1993.

58. D. R. Jones, S. N. Halliwell and C. E. Little, "Influence of remanent electron density on the performance of copper HyBrID lasers," *Opt. Comm.*, vol. 111, pp. 394-

402, 1994.

59. D. R. Jones, A. Maitland and C. E. Little, "Kinetic processes in copper HyBrID lasers," *CLEO/Europe'94 Technical Digest*, pp. 187-8, 1994.

60. N. V. Sabotinov, D. R. Jones, F. Akerboom, A. Maitland and C. E. Little, "9.5-W copper HyBrID laser with a specific average output power of 2.0 W/cm^3," *CLEO'94, Technical Digest*, pp. 402-3, 1994.

61. P. Coutance, G. Naylor and J. P. Pique, "A copper "HyBrID" laser of high-beam quality using an axial unstable cavity," *IEEE J. Quantum Electron.*, vol. QE-31, no. 10, pp. 1747-52, 1995.

62. Lei J., Liang P., Shen Q., Ji Y., Ye R. and Ren H., "Study on the properties of a Cu-Ne-HBr laser and its operation parameters," *Chin. J. Lasers*, vol. A22, no. 6, pp. 411-14, 1995. (In Chinese.)

63. P. Blau, Y. Achiam, I. Smilanski and I. Hen, "Large bore copper HyBrID laser excited by magnetically compressed pulses," *IQEC'96 Technical Digest*, pp. 188-9, 1996.

64. C. G. Whyte, C. E. Little, G. P. Hogan and C. E. Webb, "Temporally and spatially resolved measurements of electron density in a copper HyBrID laser," *CLEO'95 Technical Digest*, p. 284, 1995.

65. D. J. W. Brown, C. G. Whyte, D. R. Jones and C. E. Little, "High power, high beam quality copper HyBrID laser systems," *IQEC'96 Technical Digest*, p. 205, 1996.

66. P. Coutance, G. Sitja and J. P. Pique, "Copper bromide polymers concentration in a Cu/HBr laser," *IQEC'96 Technical Digest 239*, 1996.

67. A. A. Isaev, D. R. Jones, C. E. Little, G. G. Petrash, C. G. Whyte and K. I. Zemskov, "1.3 W average power at 255 nm by second harmonic generation in BBO pumped by a copper HyBrID laser," *Opt. Comm.*, vol. 132, pp. 302-6, 1996.

68. W. T. Silfvast, *Laser Fundamentals*, Cambridge University Press, New York, USA, 1996, p. 414.

69. R. A. J. Shelton, "Vapour pressures of the solid copper (I) halides," *Trans. Faraday Soc.*, vol. 57, p. 2113, 1961.

70. D. N. Astadjov, N. K. Vuchkov and N. V. Sabotinov, "Parametric study of the CuBr

laser with hydrogen additives," *IEEE J. Quantum Electron.*, vol. QE-24, no. 9, pp. 1927-35, 1988.

71. A. A. Isaev, D. R. Jones, C. E. Little, G. G. Petrash, C. G. Whyte and K. I. Zemskov, "Characteristics of pulsed discharges in CuBr and copper HyBrID lasers," *IEEE J. Quantum Electron.*, vol. QE-33, no. 6, pp. 919-26, 1997.

72. G. P. Hogan and C. E. Webb, "Pre-ionization and discharge breakdown in the copper vapor laser: The phantom current," *Opt. Comm.*, vol. 117, pp. 570-579, 1995.

73. L. A. Weaver, C. S. Liu and E. W. Sucov, "Superradiant emission at 5106, 5700 and 5782 Å in pulsed copper iodide discharges," *IEEE J. Quantum Electron.*, vol. QE-10, no. 2, pp. 140-7, 1974.

74. D. N. Astadjov, K. D. Dimitrov, D. R. Jones, V. Kirkov, L. Little, C. E. Little, N. V. Sabotinov and N. K. Vuchkov, "Influence on operating characteristics of scaling sealed-off CuBr lasers in active length," *Opt. Comm.*, vol. 135, pp. 289-94, 1997.

75. R. F. Rolsten, *Iodide Metals and Metal Iodides*, John Wiley and Sons, New York, 1961.

76. D. N. Astadjov, A. A. Isaev, G. G. Petrash, I. V. Ponomarev, N. V. Sabotinov and N. K. Vuchkov, "Temporal and radial evolution of the populations of Cu I levels in the CuBr vapor laser," *IEEE J. Quantum Electron.*, vol. QE-28, no. 10, pp. 1966-9, 1992.

77. R. R. Lewis, "The operating regime of longitudinal discharge copper vapour lasers," *Opt. Quantum Electron.*, vol. 23, pp. S493-512, 1991.

78. D. R. Jones and C. E. Little, "Kinetics of copper HyBrID lasers," *SPIE 2619 Int. Conf. on Atomic and Molecular Pulsed Lasers*, Tomsk, Russia, 27-30 March, ed. V. F. Tarasenko, G. V. Mayer and G. G. Petrash, pp. 52–67, 1995.

79. L. Brewer and N. L. Lofgren, "The thermodynamics of gaseous cuprous chloride, monomer and trimer," *J. Am. Chem. Soc.*, vol. 72, no. 7, pp. 3038-45, 1950.

80. L. Frommer and M. Polyani, "Über heterogene Elementarreaktionen I. Einwirkung von Cl_2 auf Cu," *Z. Physik. Chem.*, vol. 137A, pp. 201-8, 1928.

81. M. Guido, G. Balducci, G. Gigli and M. Spoliti, "Mass spectrometric study of the vaporization of cuprous chloride and the dissociation energy of Cu_3Cl_3, Cu_4Cl_4, and

Cu_5Cl_5," *J. Chem. Phys.*, vol. 55, no. 9, pp. 4556-4572, 1971.

82. K. P. Huber and G. Herzberg, *Molecular Spectra and Molecular Structure. IV. Constants of Diatomic Molecules*, Van Nostrand Reinhold Co., New York, 1979.

83. G. P. Hogan, C. E. Webb, C. G. Whyte and C. E. Little, "Experimental studies of CVL kinetics," in *Pulsed Metal Vapour Lasers - Physics and Emerging Applications in Industry, Medicine and Science*, ed. C. E. Little and N. V. Sabotinov (Kluwer Academic Publishers: Dordrecht), pp. 67-72, 1996.

84. J. J. Chang, B. E. Warner, C. D. Boley and E. P. Dragon, "High-power copper vapour lasers and applications," in *Pulsed Metal Vapour Lasers - Physics and Emerging Applications in Industry, Medicine and Science*, ed. C. E. Little and N. V. Sabotinov (Kluwer Academic Publishers: Dordrecht), pp. 101-112, 1996.

85. P. A. Bokhan and E. I. Molodykh, "Output limiting mechanisms and the prospects for metal vapour lasers with average output power above 1 kW/m," *op. cit.*, pp. 137-48, 1996.

86. D. R. Jones, A. Maitland and C. E. Little, "A high-efficiency 200 W average power copper HyBrID laser," *IEEE J. Quantum Electron.*, vol. QE-30, no. 10, pp. 2385-2390, 1994.

87. M. J. Withford, D. J. W. Brown, R. J. Carman and J. A. Piper, "Kinetic enhancement in copper vapour lasers using halogen donor gas additives," *IQEC'96 Technical Digest*, p. 238, 1996.

88. J. J. Chang, C. D. Boley, M. W. Martinez, W. A. Molander and B. E. Warner, "Beam characteristics of a large-bore copper laser with radiatively cooled plasma," *SPIE 2118 Gas, Metal Vapor and Free Electron Lasers and Applications*, ed. V. N. Smiley and F. K. Tittel, pp. 2-8, 1994.

89. Y. Iseki, K. Hayashi, I. Watanabe, E. Noda and S. Suzuki, "Characteristics of a large-bore copper vapor laser with gas-cooling plates," *Jap. J. Appl. Phys.*, vol. 33, Part 2(6B), pp. L860-2, 1994.

90. G. G. Petrash, "Diagnostics of CVL plasma," *SPIE 2619 Int. Conf. on Atomic and Molecular Pulsed Lasers, Tomsk, Russia, 27-30 March, 1995*, ed. V. F. Tarasenko, G. V.

Mayer and G. G. Petrash, pp. 68–75, 1995.

91. N. Aoki, H. Kimura, C. Konagai, S. Shirayama, T. Miyazawa and T. Takahashi, "High-power copper vapor laser development," *SPIE 1412 Gas and Metal Vapor Lasers and Applications*, ed. J. J. Kim and F. K. Tittel, pp. 2-11, 1991.

92. M. J. Kushner and B. E. Warner, "Large-bore copper-vapor lasers: kinetics and scaling issues," *J. Appl. Phys.*, vol. 54, no. 6, pp. 2970-82, 1983.

93. W. A. Molander, "Measurement of ground state copper density using hook spectroscopy," *SPIE 1041 Metal Vapor, Deep Blue and Ultraviolet Lasers*, pp. 11-18, 1989.

94. N. V. Sabotinov, F. Akerboom, D. R. Jones, A. Maitland and C. E. Little, "A copper HyBrID laser with 2 W/cm^3 specific average output power," *IEEE J. Quantum Electron.* vol. QE-31, no. 4, pp. 747-53, 1995.

95. D. R. Jones, A. Maitland and C. E. Little, "A copper HyBrID laser of 120 W average output power and 2.2% efficiency," *Opt. Quantum Electron.* vol. 25, pp. 261-9, 1993.

96. S. Gabay, P. Blau, M. Lando, I. Druckman, Z. Horvitz, Y. Yfrah, I. Hen, E. Miron and I. Smilanski, "Stabilization of high-power copper vapour laser," *Opt. Quantum Electron.* vol. 23, pp. S485-92, 1991.

97. E. G. Cook, D. G. Ball, D. L. Birx, J. D. Branum, S. E. Peluso, M. D. Langford, R. D. Speer, J. R. Sullivan and P. G. Woods, "High average power magnetic modulator for copper lasers," *Proc. 8th IEEE Int. Pulsed Power Conf.*, San Diego, CA, 17-19 Jun. 1991, 1991.

Papers Arising From This Work

1. L. Little and C. E. Little, "Dynamics of the metal seeding process in copper hybrid lasers," *SPIE 3092, Proc. XI International Symposium on Gas Flow and Chemical lasers and High Power Laser Conference*, Edinburgh, UK, 25-30 August 1996, ed. H. J. Baker, pp. 285–8, 1997.

2. L. Little and C. E. Little, "Average power scaling of copper hybrid lasers," *SPIE 3092, Proc. XI International Symposium on Gas Flow and Chemical lasers and High Power Laser Conference*, Edinburgh, UK, 25-30 August 1996, ed. H. J. Baker, pp. 62–7, 1997.